Diesel fuel and Diesel fuel with Water Emulsions Spray and Combustion Characterization

David Robert Emberson
School of Engineering and Material Sciences
Queen Mary University of London

Primary Supervisor: Professor Theodosios Korakianitis
(a.k.a. Theodosios Alexander)
Secondary Supervisor: Professor R. J. Crookes

A thesis submitted in conformity with the requirements
for the degree of Doctor of Philosophy
University of London

Statement of Conformity

I, David Robert Emberson, confirm that the research included within this thesis is my own work or that where it has been carried out in collaboration with, or supported by others, that this is duly acknowledged below and my contribution indicated. Previously published material is also acknowledged below.

I attest that I have exercised reasonable care to ensure that the work is original, and does not to the best of my knowledge break any UK law, infringe any third partys copyright or other Intellectual Property Right, or contain any confidential material.

I accept that the College has the right to use plagiarism detection software to check the electronic version of the thesis.

I confirm that this thesis has not been previously submitted for the award of a degree by this or any other university.

Signature:

Date:

Abstract

The legislative demand to simultaneously reduce nitrogen oxide(s) emissions and particulate matter emissions from compression ignition engines is proving difficult to achieve in the real world. One promising strategy is the use of Diesel fuel emulsified with water. There is little work concerning the effect of emulsification on fuel injection sprays. This work details an experimental campaign to characterize non-vaporizing sprays of Diesel fuel and Diesel emulsions, with 10% and 20% water by mass. Characterization of the fuel sprays has been done using: high speed photography, applying focused shadowgraphy and a diffused back-lighting technique and; hydraulically using a force transducer placed 0.5mm from the injector nozzle to measure spray momentum flux. All measurements have been made in an optically accessible high pressure chamber filled with nitrogen, resulting in an ambient gas density of 22.6 kg/m^3 and 34.5 kg/m^3, with injection pressures of 500, 700 and 1000bar used.

The images collected have been used to determine the spray cone angle, the tip penetration and the tip velocity. The signal from the force transducer has been used to determine spray momentum flux, instantaneous mass flow rate, dimensionless nozzle coefficients and injection velocity. The injection pressure had no discernible influence on the spray cone angle for the Diesel fuel sprays but did for the emulsified fuels. Increasing the ambient density resulted in an increase in the spray cone angle for Diesel fuel, this was not always the case for the emulsified fuel sprays. The spray tip emerged from the nozzle and accelerated for a very short period after the start of injection until a maximum velocity was reached.

The momentum flux for each fuel was almost the same for corresponding conditions. Increasing the chamber gas density reduced the measured spray momentum. The total mass of fuel injected for Diesel fuel was larger than for the emulsions for the equivalent conditions and duration, although emulsions had a larger density and viscosity. The emulsions had a higher injection velocity. The nozzle discharge coefficient for Diesel was higher than for the emulsions. The velocities measured hydraulically are much higher than the maximum tip velocities measured optically.

The study has been completed by some preliminary combustion studies of the fuels in an optically accessible combustion chamber. The emulsion tested exhibited much lower natural flame luminosity, used to determine the spatially integrated natural luminosity of the flame which may be useful as a soot indicator. There was no evidence that the microexplosion phenomenon was present in these tests.

Acknowledgements

First and foremost I thank my wife, Harriet Emberson for her support throughout the process of producing this thesis. I thank my supervisor, Professor Theodosios Alexander, Sc.D. (aka T. Korakianitis) for giving me the opportunity to undertake this project and the guidance and support he has offered. I thank Professor. Roy Crookes for his support and technical assistance throughout the project. I also thank Dr. Alvaro Diez for his guidance throughout the work. A special thanks goes to Balazs Ihracska for his design and manufacturing work and Vincent Ford, without whom, this work would not have been possible.

This work has been fully funded by Advanced Engine Research (A.E.R, Basildon, Essex, UK) with the principal investigator Professor Theodosios Alexander.

Nomenclature

Subscripts

a	air
amb	ambient
B	backlit
$crit$	critical
eff	effective
f	fuel
geo	geometric
i	inlet
inj	injection
l	liquid
o	outlet
S	shadowgraph
v	vapor

Symbols

A	amps
Ca	cavitation number
CAD	computer aided design
C_d	discharge coefficient
D	characteristic length scale
ϵ	deflection angle
F	force
Hz	Hertz
K	cavitation number
L	nozzle length
m	mass
$\dot{m}$	instantaneous mass flow rate
$\dot{M}$	momentum flux
μ	dynamic viscosity
Oh	Ohnesorge number
P	pressure
Pa	Pascal
Re	Reynolds number
ρ	density
S	tip penetration
σ	surface tension

t	time
θ	cone angle
V	voltage
v	velocity
We	Webber number

Abbreviations

ATDC	after top dead center
CAD	crank angle degrees
CI	compression ignition
CN	cavitation number
CVC	constant volume chamber
D10	Diesel fuel and 10% water
D20	Diesel fuel and 20% water
DAQ	data acquisition
DPF	diesel particulate filter
ECU	engine control unit
EOI	end of injection
EU	European Union
FFT	fast Fourier transform
fps	frame per second
HLB	hydrophillic-lipophililic balance
ICE	internal combustion engine
ID	ignition delay
LED	light emitting diode
NL	natural luminosity
NO_x	nitrogen oxides
OACC	optical accessible combustion chamber
PM	particulate matter
QE	quantum efficiency
QMUL	Queen Mary University of London
rpm	revolutions per minute
RSD	relative standard deviation
SINL	spatially integrated natural flame luminosity
SOI	start of injection
TAM	trapped air mass
TDC	top dead center
TTL	transistor transistor logic

Contents

List of Figures

List of Tables

1. Introduction

Introduction

The internal combustion engine continues to be the dominant form of motive power across the globe. With developing countries feeding the growing demand for vehicles, the number of internal combustion engines in operation continues to increase. China is an excellent example to demonstrate the global growth in demand of motor vehicles in recent years where the market for passenger vehicles rose by a factor of 18 between 1990 and 2008 from 0.51 to 9.38 million vehicles sold per year, for the first time selling more than 10 million cars in one year in 2009 [1]. The total vehicle population in China in 1990 was 5.5 million which by 2012 had increased to 109.4 million (excluding motorcycles, electric bikes and rural trucks)[2]. The growth in the use of the internal combustion engine is accompanied by a growth in demand for fuel. The two main fuels used by internal combustion engines is petroleum and Diesel fuel, both derived from crude oil. Global oil consumption has increased year upon year, with a 1.4% increase in the year 2013 to 2014 [3] with developing countries accounting for 51% of consumption. Of particular relevance is the growth in the consumption of the light and middle distillates, the range that petroleum and Diesel fuel is found. Fig.1.1 shows the growth in consumption of the two distillates over the last 10 years [3]. The growth is evident in the Asia Pacific region resulting from extensive economic growth in that period. The overarching fact concerning this increased demand and dependency on fossil derived fuels is the finite nature of the resource and the looming possibility of reaching peak oil production. Peak oil production is a concept that was realized in the early days of crude exploitation and is defined as the point in time at which conventional oil production will reach its maximum after which it will permanently decrease. There is much speculation as to when this point will occur, with optimistic claims falling in the 2030s [4] and more pessimistic claims stating it has already been inadvertently reached [5]. It would seem the dymaxion view promoted by Buckminster Fuller, to “do more with less” [6] is a sensible route to

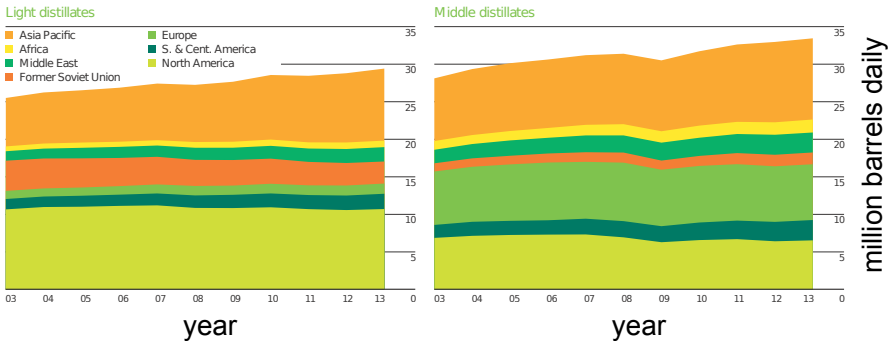

Figure 1.1: Light and middle distillate crude oil consumption in million barrels used each day by region [3].

follow when it comes to fossil fuel usage.

While it may be sensible to look to the growing economies to see how the number of internal combustion engines will grow and fossil fuel demand increase, the route that future engine development may take is most likely described in more economically developed countries where the technology is mature and their use is fully integrated into most aspects of the society. Using Europe as the example, it is seen that the nature of engine development has been informed by customer desire and legislation. Of prime concern to the customer is a desire to reduce fuel costs which has been met by the engine designer by improving thermal efficiency, allowing sales data to quote high distance to volume (of fuel) figures. Legislation has been primarily concerned with emissions as understanding and concern about environmental pollution has drastically increased [7].

Carbon dioxide emissions have come under legislative control in attempts to curb anthropogenic climate change. Mainly controlled via increasing vehicle efficiency (distance travelled per volume of fuel) and are usually reported as grams emitted per unit distance. The European Union (EU) has made a firm independent commitment to achieve at least a 20% reduction of greenhouse gas emissions by 2020 (compared to 1990 levels), irrespective of reductions achieved by other developed countries [8]. Transport has been identified as a major contributor to total CO_2 emissions, estimated to account for 20% of global primary energy consumption and for about 18% of the total anthropogenic greenhouse gas emissions [9]. The EU commitment aimed to reduce CO_2 emissions to 140 g/km by 2008 to 2009 with a new policy implemented to further reduce this to 120 g/km by 2015. It was envisaged that by 2015, the average would be 130 g/km (from type approval tests) with the remaining 10 g/km accomplished by other means not directly linked to the vehicle energy performance such as use of biofuels , efficiency requirements for mobile air-conditioning systems and tyre pressure monitoring systems [9] [10]. In

meeting the commitment engine thermal efficiencies needed to improve which has resulted in a shift of the European passenger car fleet towards higher efficiency compression ignition (Diesel) cars and an effort to promote smaller less fuel consuming models [9]. It is believed under current trends the 130 g/km target will be met [11]. Being a leader in vehicle development, production and exports it is expected that the EU's policy on passenger car and light duty truck energy efficiency will affect several non-European countries as well[9].

Air quality environmental concerns and human health concerns have driven the legislation of other internal combustion engine emissions, with considerable attention payed to nitrogen oxides, and particulate matter (NO_x, PM). Short-term exposure to high concentrations of NO_2 can cause inflammation of the airways and longer term exposure to lower levels increases susceptibility to respiratory infections and to allergens and nitrogen oxides are a known precursor to photochemical smog [12]. Exposure to PM_{10} (the fraction of aerosol particles with the aerodynamic diameter less than 10 μm) and $PM_{2.5}$ is linked to a range of respiratory, cardiovascular illnesses and increased mortality rates [13] also impacting anthropomorphic climate change, acidification and eutrophication [12]. In parallel with CO_2 abatement, the EU initiated a regulation regime for NO_x and PM along with hydrocarbon emissions. It is of interest that Diesel fueled compression ignition engines are known to have higher emissions of both NO_x and PM compared to petroleum engined cars. It is possible that the move to compression ignition vehicles in the passenger car fleet poses higher environmental pressures than a gasoline vehicle would have and the incentives associated with Diesel fueled vehicle purchase in Europe may need to be re-evaluated [11]. The emissions regulations have moved through a number of stages, typically refereed to as Euro 1, Euro 2, Euro 3, Euro 4, Euro 5 and Euro 6 (coming into effect 2014). The standards are different for different vehicle types, the standards for passenger compression ignition vehicle are shown in Fig.1.2.

Vehicle manufactures test new engine models during production according to the new European drive cycle, designed to simulate real world engine operational conditions. Whilst the type approval in this manner is producing positive results with the emissions of related air pollutants decreasing across the EU, it is estimated that up to 20% of Europe's population still live in areas where pollution concentrations (focussed on NO_x and PM) exceed air quality standards [15]. There is growing concern that the type approval testing that is passed in laboratory conditions is not transferring into real world driving emissions with Euro vehicle emission standards for Diesel fueled vehicles tunable to deliver the anticipated reductions in emissions in real world driving. The high NO_x emissions of Diesel fueled vehicles under real-

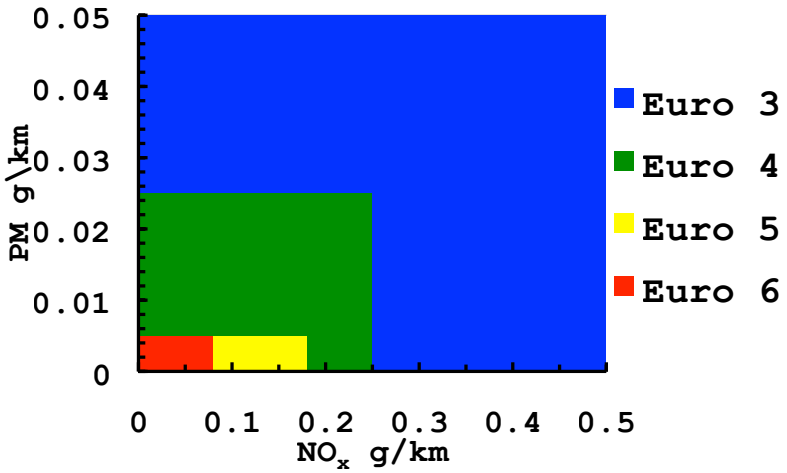

Figure 1.2: EU nitrogen oxides and particulate matter emissions legislation development through the so called Euro stages. Emission are quoted in grams per kilometer covered by the vehicle under a test European test drive cycle. [14, 7]

world driving conditions remain the main cause for environmental concern regarding the emission profile of Euro 5 passenger cars. Measured emissions of NO_x exceeded the type-approval limits (up to 5 times in extreme cases) and presented significantly increased average values (0.35 g/km for urban driving and 0.56 g/km for motorway driving) have been observed [16]. According to the 2013 air pollution report produced in the UK by Department for Environment, Food and Rural Affairs (DEFRA) a number of UK cities, most notably London are breaching EU air pollution standards consistently. The report states that NO_x emissions from Diesel fueled cars have decreased little in the past 15-20 years and that the Euro Standards have failed to deliver the expected improvements for these vehicles [12]. It seems that even in the relatively mature regulatory environment of the EU, real world use of the internal combustion engine, and its continued long term future use, will be dependent on not just further improvements of efficiencies and reduction of emissions, but a guarantee that current regulations can be consistently met across a range of operational ranges and environments. As there is currently no viable alternative to the internal combustion engine ready for large scale market penetration, the primacy of the research field focussed on increasing understanding of the complex processes taking place in the internal combustion engine should not be doubted and looks set to continue for a great many years.

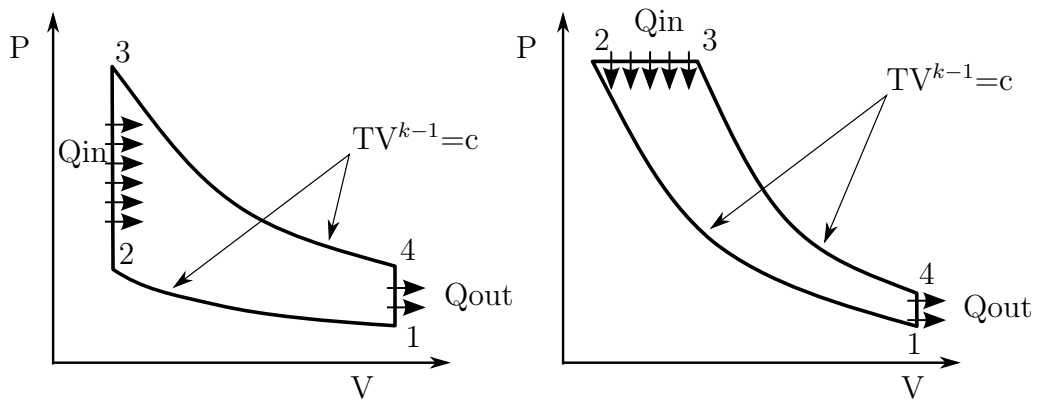

Figure 1.3: Pressure volume diagram of the air standard Otto cycle (left) and the Diesel cycle (right)

1.1 The Internal Combustion Engine

There are a number of ways to categorize a reciprocating ICE, broadly speaking, the two most common and useful means of classification are the working cycle and the method of ignition. Working cycle refers to the number of revolutions of the crankshaft per power stroke. Four and two stroke engines are by far the most common. Spark ignition engines (SI), make use of an electrical discharge between to two contacts (a spark across a gap) to initiate combustion, usually fueled by petrol. Compression ignition engines (CI) use the high temperatures achieved upon rapid adiabatic compression of a gas and are usually fueled with Diesel fuel (the engine is most often referred to as a Diesel engine).

The most basic form of reciprocating internal combustion engine analysis is described by air standard cycles. The working fluid is treated as air throughout the cycle; during combustion the energy received by the working fluid is equal to the combustion enthalpy transferred to the working fluid via heat transfer and; the working fluid specific heat and specific heat ratio is assumed constant throughout the cycle, hence the air standard models are highly idealized but provide a basis for the thermodynamic analysis of both SI and CI engines. The spark ignition engine is described by the Otto cycle while the compression ignition engine is described by the Diesel cycle. Fig1.3 shows a graphical representation of the two cycles in the form of a pressure volume plot. The compression (1 to 2) and expansion (3 to 4) portions of each cycle is modeled as isentropic, therefore TV^{k-1}=constant. This results in an expression of the thermal efficiency in terms of the ratio of volume displaced by the piston, the compression ratio r_v given by V_1/V_2. The Otto cycle

efficiency is given by

$$\eta = 1 - \frac{1}{r_v^{k-1}} \tag{1.1}$$

while the Diesel cycle efficiency is given by

$$\eta = 1 - \frac{1}{r_v^{k-1}} \left[\frac{r_c^k - 1}{k(r_c - 1)} \right] \tag{1.2}$$

where r_c is the cutoff ratio or load ratio which is the ratio of the volume at the start and end of combustion (V_3/V_2). It is evident from Eqn.1.1 and 1.2 that efficiency is increased with increasing compression ratio. The Diesel cycle efficiency depends on the cutoff as well as the compression ratio.The cutoff ratio is always greater than unity and thus the term in square brackets in Eqn.1.2 is always greater than unity, hence for the same compression ratio, the Otto cycle is always more efficient than the Diesle cycle [17].

In reality, the compression ratio of an Otto cycle, spark ignition engine has always been limited due to the tendency for the fuel and air mixture in the engine cylinder to detonate prematurely during the compression stroke in a process known as knock [18] . This is a consequence of the fuel and air mixing prior to entering the cylinder/combustion chamber, usually in the inlet manifold either by carburetion or port fuel injection [19]. Diesel cycle, compression ignition engines inject fuel directly into the cylinder (combustion chamber) during the compression stroke of the engine, the fuel forms a spray, mixes with surrounding air and ignites due to the high temperatures achieved under compression, hence the higher compression ratio is a perquisite of operation. This explains the reason behind the shift to compression ignition Diesel fueled engines in Europe which are generally viewed as being able to achieve higher efficiencies and hence better fuel consumption.

1.1.1 The Compression Ignition Engine

Air alone is inducted into the cylinder through an un-throttled inlet port. This is another source of efficiency gain over an SI engine which will usually have a throttle in the air inlet system increasing pumping losses (reduced volumetric efficiency). As the piston moves up the cylinder towards TDC the air is compressed, accompanied by an increase in temperature. The piston nears TDC, fuel is injected under high pressure through a nozzle with one or several holes into the combustion chamber.

The fuel may be injected directly into the main chamber (direct inject, DI) or injected into a section of the combustion chamber divided from the main chamber

(indirect injection, IDI). Older injectors are supplied with fuel from an injector pump, mechanically driven off the crank, with injection controlled by injection line pressure. These injectors consist of a needle which acts as a valve, opening and closing allowing high pressure fuel (around 60-75MPa) to enter the chamber. The needle opening pressure is determined by the spring load and the projected area of the needle [17, 18, 20].

Modern diesel engine design has moved away from these mechanically driven and timed injectors to precise and accurate electronically controlled injectors. The modern common rail injector system allows the fuel to be injected into the combustion chamber directly at high pressure at precise times and precise quantities [21]. The common rail (CR) in these systems acts as a pressure accumulator which stores high pressure fuel supplied from a high pressure pump, driven off the crankshaft. Injection needle control is by electronically controlled solenoid or the latest generation of piezo electric injectors, allowing extremely accurate injection with multiple injections per combustion event possible [22].

The fuel is injected into the combustion chamber and forms of a fine spray. The fuel spray must penetrate and disperse through the charge of hot compressed air in the combustion chamber, with fuel droplet atomization and evaporation occurring. The fuel and air mixture is heterogenous, there will be regions of rich, lean and near stoichiometric mixture depending on the position and the time after the start of injection (SOI). From the time of the SOI to the time of start of combustion (SOC) there is a significant period referred to as the ignition delay. Discussion of the ignition delay period is divided into two components, physical delay and a chemical delay [23]. It should be noted that this division can be deceptive as the processes outlined happen simultaneously [24]. The physical delay period includes

- Time for the fuel spray to leave the injector
- Entrainment of hot air into the spray plume.
- Vaporization of the fuel droplets caused by the entrained hot air
- Mixing of the fuel vapor with air

The fuel spray fluid dynamic behavior and properties are critical to the physical delay period as is the fluid dynamic nature of the air charge in the combustion chamber during the injection process. The chemical delay is the short period before the fuel and air mixture begins energy release [23] which is kinetically controlled [25]. The initial ignition position and time, unlike in a SI engine, is unknown and difficult to define.

Ignition detection can be roughly broken down into two methods; rapid combustion chamber pressure measurements or light based assessment, making use of optical combustion chambers. At the end of the delay period, there will be a region of premixed fuel/air that has formed during the delay period. This will initial ignite and burn rapidly, producing a peak in the cylinder pressure (pre-mixed burn fraction). The remainder of the fuel will burn as a diffusion flame, much more slowly and is controlled by the rate of fuel and air mixing in the chamber [26].

1.1.2 CI engine Emissions

During the heterogenous combustion in the engine cylinder a wide range of products are produced that will be released into the atmosphere in the engine's exhaust stream. These products are the engine emissions. Other emissions from the engine such as noise and heat are not generally implied when discussing emissions. The gaseous emissions of concern are;

- **Unburnt Hydrocarbons (HC)** The heterogenous nature of the fuel air mixture and the range of equivalence present results in some incomplete combustion. This leads to a mixture of hydrocarbons in the exhaust gas stream. The mixture of HC compounds in a CI engine exhaust stream is of a large range of molecular size. Not all of the HC will be in the gaseous phase.

- **Carbon Monoxide (CO)** A lack of oxygen present during combustion results in a higher concentration of CO. The main influence on CO emissions is therefore the air/fuel ratio. As with HC, the heterogeneous nature of the mixture can lead to locally fuel rich zones which will produce higher CO concentrations. Post oxidation then occurs which then reduces these concentrations. CI engines usually run with excess air, operating within the low smoke limit, hence CO emissions in CI engines are not usually significant.

- **Nitrogen Oxides (NO_x)** Nitrogen from the air is oxidized during the combustion process to form nitrogen oxides. Fuel bound nitrogen plays a very small role. The N_2 and O_2 react with the equilibrium concentration of the NO_x compounds at around 2000K-3000K [20]. Nitrogen oxide is the predominant oxide of nitrogen formed during combustion with subsequent oxidation forming the NO_2. The NO_x formation is highly dependent on temperature through the so called Zeldovich mechanism along with the duration of combustion and the local oxygen concentration [17]. NO_x is mainly formed on the lean side of the diffusion combustion region where temperatures are high as

local equivalence ratio is approaching unity and oxygen concentration is high [26, 27].

- **Carbon Dioxide CO_2** Considered one of the primary causes of anthropogenic climate change, a result of the complete oxidation of the carbon in the hydrocarbon fuel.

The main non-gaseous emission of concern is soot. Soot is not a clearly defined substance, but in general terms, soot is a solid substance consisting of roughly eight parts carbon and one part hydrogen [28]. Soot in a CI engine is a product of pyrolysis or incomplete combustion of hydrocarbons which nucleates from the vapor phase to a solid phase in the locally fuel rich region of the reaction zone [28]. The primary carbon particles formed may agglomerate to form larger particles until they reach the fuel lean zone, where they can be oxidized. The final rate of soot released depends on the difference between the rate of formation and the rate of oxidation.

While carbon is the main constituent of the soot particles other substances may be adsorbed or condense on the surface of the particle [28]. The formation of the primary soot particles is largely dependent on; fuel chemical composition; the oxygen availability in the reaction zone; the temperature, with higher temperatures promoting complete combustion. The production of soot particles in a flame is inherently a chemically-controlled phenomenon which the thermodynamic state of the system alone cannot describe [29]. The oxidation of the primary particles will be a function of available oxygen, temperature, residence time and structure of the primary particle . Soot formation and oxidation is an extremely complex sequence of reactions with a number of precursors and subspecies determining what is ultimately emitted in the engines exhaust stream [30].

Particulate matter (PM) is the combination of soot and other liquid or solid-phase materials contained in the exhaust stream. Particulate matter is often separated into a soluble and an insoluble portion, with soot making up the insoluble portion. The fraction of particulate matter which is soot, is often estimated by finding the insoluble portion of the particulate and is typically higher than 50%. Other particulate matter constituents include: un/partially burned fuel/lubricant oil, bound water, wear metals and fuel-derived sulfate [28]

Fig.1.4 shows a conceptual model developed by Dec [31] which is used extensively across CI engine literature to describe the combustion of a typical Diesel fuel injection spray (often termed a jet). The model deals with the quasi steady phase of combustion of a free jet (no surface or other jet impingement). The injected fuel

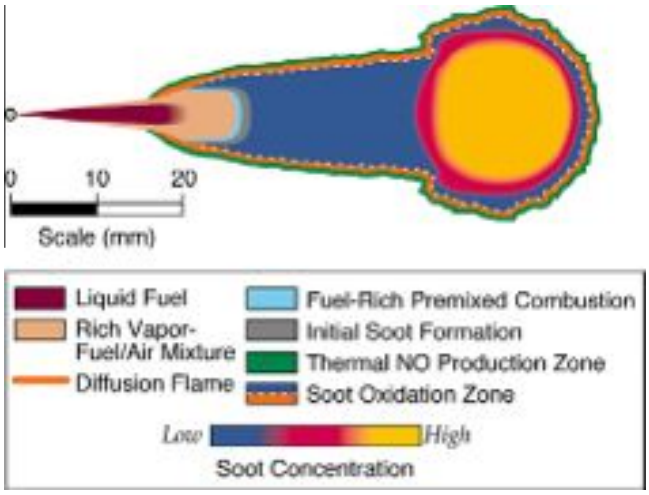

Figure 1.4: Schematic of the conceptual model of fuel jet combustion in a CI engine developed by Dec [31]

forms a cone shaped spray, the liquid phase of the spray scales with the energy entrained (hot air) into the conical zone which is dependent on the spray cone angle. The maximum penetration of liquid fuel is the liquid length. A diffusion flame surrounds the entire region downstream of the liquid penetration and extends upstream to a fixed distance from the nozzle tip termed the lift-off length. The model is useful when conceptualizing the heterogeneous combustion taking place in a CI engine and to help identify the regions where the emissions of concern may be being produced. The model also introduces the concept that the fuel spray dynamics are themselves important, the spray cone angle.

1.1.3 Emission control

Control of the NO_x and PM, is of primary importance in meeting the Euro legislative constraints. Due to the thermal dependency of the formation of NO and therefore NO_x compounds, most of the NO_x control strategies rely on reducing the temperature of combustion or reducing the duration of the diffusion flame period [32]. Retarding injection has been shown to give useful reductions in NO_x emissions. The onset of combustion is also retarded, peak flame temperatures are reduced leading to a reduction in NO concentration.

During the ignition delay, a portion of the fuel has time to mix with the surrounding air. The mixture is closer to stoichiometric and this "premixed" mixture burns rapidly with a high temperature producing a considerable portion of the NO [27]. An increased injection rate due to higher injection pressure results in more fuel

undergoing improved mixing during the ignition delay, increasing the temperature further [33] so there is a trade off with improved engine efficiency.

Re-circulation of exhaust gases into the cylinder has become an essential method for reduction of NO_x emissions from CI engines [34]. Exhaust gas recirculation (EGR) results in a lowering of the peak in cylinder temperatures. The introduction of carbon dioxide into the cylinder displaces oxygen, reducing the available oxygen for combustion. With the local oxygen concentration reduced, a proportion of the fuel will have to diffuse over a wider volume to form a stoichiometric mixture. This enlarged volume will also contain non-reacting gases such as carbon dioxide, water and nitrogen. These gases will "absorb" energy released by combustion, leading to lower flame temperature and lower NO_x generation [35]. One major disadvantage with the use of EGR is the balance that must be made between the reduction of NO_x emissions and the increase in PM that occurs with increasing EGR concentrations. Reducing the flame temperature in order to reduce NO_x causes the balance between soot formation and burnout to move in the direction of increasing PM emissions [36].

The addition of water into the combustion chamber with the aim of reducing local temperatures leading to a reduction in thermal NO_x has also been applied [37, 38]. The advantage of the addition of water compared to EGR is that it is not accompanied by an increase in PM emissions. The water may be introduced to the combustion chamber by

- Addition of water into the air inlet stream/manifold (fumigation)
- Direct injection into the cylinder
- Addition of water to the fuel forming an emulsion

A number of strategies for injecting water into the inlet manifold have been examined. Multiple injections near the inlet valve, single point upstream of the compressor inlet (relevant to turbocharged engines) and downstream of the compressor have all been examined [38]. Water to fuel ratio has been increased up to 50% with reductions in NO_X accompanied by only a minor increase in PM [37]. Direct injection into the combustion chamber has been shown to require less water compared to fumigation with the water present in regions where it is more effective [39].

fthe Diesel fuel and water with water content generally ranging from 10% to 20%. The mixture is injected into the cylinder as standard Diesel fuel would be. This is a significant advantage of emulsions over other methods of introducing water into

the combustion chamber in that the engine and fuel injection system would require little or no modification.

PM formation may be reduced with improved fuel air mixing resulting in more complete oxidation, this is accompanied by an increase in temperature, increasing thermal NO_x. For this reason in modern engines, PM is generally dealt with using an exhaust "after-treatment" diesel particulate filter (DPF). The addition of a DPF increases the complexity in the engine after-treatment system and further complication is that DPFs need to be regenerated periodically to avoid excessive back pressure in the engine. [40]. This regeneration is the oxidation of the captured PM, requiring high temperatures in the DPF. These may be achieved through additional heating (burners) and scheduled high engine speed operation. The speeds required for regeneration are generally higher than those achieved in urban areas.

1.2 Diesel and Water Emulsions

The introduction of water into the combustion chamber with the fuel in the form of a Diesel fuel and water emulsion has shown promise to reduce both NO_x and PM with out the trade off that is usually encountered i.e higher temperature-less soot more NO_x, lower temperature reduces NO_x but soot production and PM emission increases. In an extensive review of the topic, A.Lif reported a reduction of up to 35% NO_x emissions when using an emulsified fuel [41]. In an emissions review article, Tree and Svensson [28] state it has been consistently demonstrated in engine experiments that Diesel fuel and water emulsions reduce NO_x. They note that the percent reduction is typically approximately equal to the percent of water added by mass to the fuel. In a review of previous work conducted here [42, 43, 44, 45, 46, 47], the majority of tests have been conducted in the 5% to 10% water addition range. Some tests have been carried out with up to 40%, all showing a reduction in NO_x, CO, HC's and PM emissions, though not always quoted in a percentage reduction basis. The PM emission reduction has been observed to be accompanied by a reduction in the amount of hydrocarbons adsorbed by the soot particles [42, 43] as determined by the soluble organic fraction,insoluble organic fraction ratio (SOF/ISF). As with all fuels, the effect of emulsification on combustion and the extent of emission reduction depends on injection strategy and operating conditions [44]. The use of Diesel fuel and water emulsions in CI engine has been observed, in some cases, to lead to a small improvement in brake thermal efficiency [41, 43, 45, 48, 49].

1.2.1 Emulsions

An emulsion is a significantly stable suspension of finely dispersed particles of a liquid within a second immiscible liquid [50]. The finely dispersed liquid is referred to as the dispersed phase and the liquid it is dispersed throughout is called the continuous phase. It is common for the emulsions to be referred to as either oil-in water (o/w) or water-in-oil (w/o) with the first phase stated being the dispersed phase and the second stated the continuous [51]. The Diesel fuel and water emulsions under discussion in this work are w/o. Macro-emulsions are the most common type of emulsion, an opaque liquid with particle (dispersed phase) size above 400nm. These emulsions are thermodynamically unstable and will separate out into a water rich and oil rich bulk phase [52]. The interfacial tension between the two immiscible liquids is always greater than zero [50]. The fine division of the dispersed phase greatly increases the interfacial surface area, considering 10ml of water and a droplet diameter of 0.2μm, the corresponding increase in surface area (ΔA) is of the factor of 106. With an interfacial surface tension (σ, Nm^{-1}) between the oil and the water of 52mNm-1(typical value [51]) , the work required to form the emulsion is given by

$$W = \sigma \Delta A \tag{1.3}$$

and is of the order of 2J. This work is stored in the emulsion as potential energy and is referred to as in increase in the interfacial free energy. The emulsion is therefore thermodynamically highly unstable. A surface active ingredient (surfactant) is used to stabilize this inherently unstable mixture. The surfactant must perform two functions. It must reduce the interfacial tension at the liquid-liquid interface, thus reducing the interfacial free energy and increasing its thermodynamic stability. Secondly it must reduce the coalescence of dispersed droplets by forming a barrier around the dispersed phase particles, a surfactant film.

Surfactants have a molecular structure described as amphipathic; a lipophillic group, usually a large hydrocarbon functional group in the form of a long chain; and a hydrophilic group. The hydrophilic group informs the classification of surfactant as

- Anionic- Hydrophilic group carries a negative charge
- Cationic- Hydrophilic group carries a positive charge
- Non-ionic- Hydrophilic group has no charge

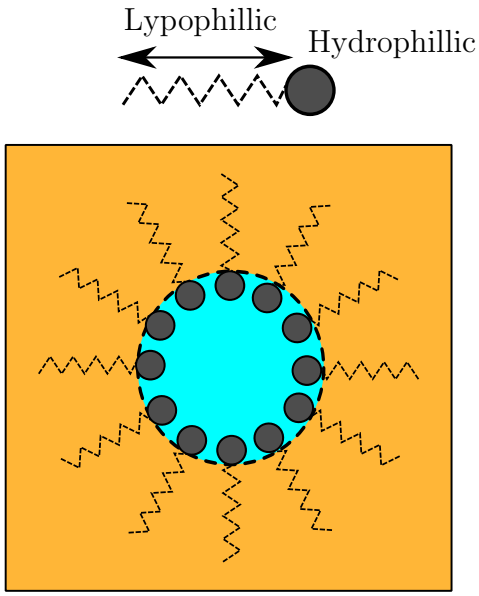

Figure 1.5: Schematic of the conceptual model of a surfactant's interaction with the dispersed and continuous phases, resulting in a stable emulsion of two immiscible liquids.

Fig.1.5 shows the lipophillic tail and hydrophilic head of a typical surfactant molecule and how they arrange themselves within the dispersed phase with their tails in the continuous oil phase when a w/o emulsion is formed. The combined structure of the surfactant causes a concentration of the surfactant at any interface and leads to a reduction in the interfacial tension [51].

Emulsion formulation is complex and the behavior of the surfactant during the emulsification process is very hard to predict just using the surfactants structure. Emulsion formulation and choice remains a highly empirical process. There are a number of rules of thumb that have developed to help narrow down the choice of surfactant considering the type of emulsion that is desired [51]. The hydrophile-lypophile balance (HLB) indicates a surfactants behavior implemented using a scale of 0 to 40, in relation to the balance between the hydrophilic component of the molecule and the lipophilic component. Surfactants with a larger hydrophobic component (least hydrophilic, larger lipophilic component) with low water solubility have a low HLB number (3-6). Conversely, those with a smaller hydrophobic component (most hydrophilic, smaller lipophilic component) with higher water solubility have a higher HLB number (8-18). As a general rule, w/o emulsions are stabilized using a low HLB surfactant and o/w emulsions use a high HLB [50].

1.2.2 Impact on Combustion and Microexplosions

The reduction in observed NO_x is believed to be a result of reduced peak flame temperature. The dispersed water droplets in the emulsion act as a *"heat sink"*. The water content of the inner phase partially absorbs the enthalpy of the combustion reaction, decreasing the burning gas temperature hence thermal NO_x generation [28, 42, 49].

There are a number mechanisms proposed that explain the observed reduction in PM when an emulsified fuel is utilized. Applying optical diagnostics to emulsified fuels (10, 20 and 30% water) in an optically accessible engine it has been observed that the ignition delay is increased [28, 53, 54]. Hence the initial premixed burn fraction is increased, this portion of the reaction will take place under well mixed conditions, approaching stoichiometric conditions which are suitable to reduce soot formation [18]. Longer liquid lengths of the fuel injection spray have been observed in optical studies where emulsified fuels have been utilized [53, 54, 55]. In the work [56] the longer liquid length is identified as droplets and ligaments and is differentiated from the *"solid"* intact liquid core. It is proposed that this increase in liquid length may reduce soot formation hence PM emissions [53, 55, 57]. With reference to the Dec conceptual model, Fig.1.4, a rich vapor fuel and air mixture is noted downstream of the liquid core (equivalence ratio 2-4 [28]). In the conceptual model this region is defined as the premixed burn region and differs from the *initial premixed burn* which occurs at the end of the ignition delay. The premixed burn region is used to define the region of the quasi-steady reaction region downstream of the liquid core of the spray. An increase in liquid core length will move this region further downstream (away from the injector nozzle) which would result in more air entrainment into the premixed region hence a leaner mixture in the jet and the products of the standing quasi-steady, premixed combustion zone would likely contain fewer soot precursors [57].

With reference to the conceptual model again, the flame lift off length may be defined as the distance from the nozzle exit to the start of the diffusion flame. This distance is known to have a significant influence on the air entrainment and hence soot formation during the quasi-steady period of flame that the model covers [28, 57]. The use of emulsified fuels has been shown to increase this distance [28, 55, 56, 57]. The liquid length and flame lift off length are most probably a result of the higher specific heat of water compared with Diesel fuel and the higher enthalpy of vaporization of water, allowing the liquid to propagate further into the combustion chamber before complete evaporation occurs [55, 58]. The work also suggests that the often observed increase in viscosity of a Diesel fuel and water emulsion may

Table 1.1: Diesel fuel and water properties

Property	Diesel fuel	Water
Boiling Temperature (°C)	(Initial) 169[67]	100
Final boiling Temperature (°C)	371.8 [43]	n/a
Boiling Range (°C)	180-230[58]	n/a
Enthalpy of vaporization (kJ/kg)	232 [43]	2440[43]
Specific Heat (kJ/kg.K)	2.2	4.18 [55]

help increase the liquid length [59]. These arguments are only really relevant to the quasi-steady period of the combustion in a CI engine that the Dec model applies to.

The microexplosion phenomenon is often used as the underlying explanation for many of the observed advantages of emulsified fuels. In the absence of bubble forming nuclei, liquids may be heated to temperatures far in excess of there boiling point to the superheat range. When the phase transformation occurs at an interface rather than in the bulk the process is known as heterogeneous nucleation [60]. Heating to the superheat limit is made possible by suppressing heterogeneous nucleation, this may be achieved by immersing the volatile liquid in another liquid [61], thus isolating from rough solid surfaces containing gas nuclei [62]. If the superheat limit is reached, boiling begins spontaneously by homogeneous nucleation within the bulk [62, 63]. Under these circumstances the evaporative fluxes, fluid accelerations and departures from thermodynamic equilibrium are orders of magnitude greater than in ordinary boiling [62].

It is this vapor explosion which has been shown to occur with fuel and water emulsion droplets. The dispersed inner phase consists of the lower volatile water (lower boiling point, see Table.1.1). The temperature in the combustion chamber during injection is in the range where the water may become heated to the superheat limit, The superheated droplets are in a thermodynamically metastable state [64, 65] until the super heat limit is reached. As the internal phase (water) approaches the superheat limit, homogeneous bubble nucleation dominates, leading to the formation of vapor bubbles within the water. The water undergoes rapid evaporation resulting in violent disintegration of the superheated liquid droplet. The water vapor explosion rips through the surrounding fuel. The resultant momentum of the explosion disperses the fine secondary droplets into the surrounding volume enhancing the fuel/air mixing in the combustion chamber [41, 46, 66].

The microexplosion phenomenon has been examined using single droplets on hotplates, suspended droplets in capillary tubes and wire (thermocouple) supported droplets[59, 64, 65, 68, 69]. The presence of microexplosion in atomized emulsion

sprays has been examined in separate experiments by a number of investigators [70].

The work [70] studied a fuel oil and water emulsion spray combustion flame using a laser light scattering technique which analyzed a polarization ratio at 90° to the illumination. Micro explosion was inferred by the increase in scattered intensity, not directly imaged. The experimentation was conducted in a furnace arrangement, the ambient pressure, density and temperature were not representative of those in a CI engine during injection. No details concerning the injector are given.

In [71] high speed (125,000 fps) backlit shadow imaging was applied to a hollow cone spray of n-dodecane and water emulsion. The chamber was filled with nitrogen at 673K, chamber walls at 823K, atmospheric pressure. The injector was operated in a continues manner. Droplets in the size range of 50μm were observed to undergo what the authors describe as "puffing", secondary atomization as the inner phase reached superheat limit.

In [47] Diesel fuel and water emulsion spray combustion is examined in a rapid compression expansion machine. High speed imaging of the natural flames luminosity of used. The authors state that small regions of varying luminosity in the tip of the spray flame are due to microexplosion (Fig.1.6).

The work [56] examines the spray and combustion of a Diesel fuel and water emulsion in a constant volume, high temperature, high pressure chamber. Backlit shadowgraph images are collected to examine spray character while flame temperature and soot concentration is measured using emission based line of sight techniques. The injector is of a similar dimension to that in a real engine, 0.14mm with a 1200 bar injection pressure. Chamber temperature was 830K with an ambient pressure of 50bar. Glowing spots were observed in the emulsion flame that were not observed in the Diesel flame which the author attributed to microexplosion.

The work [72] examined the spray combustion of Diesel fuel and water emulsion in a pre-combustion constant volume chamber. High speed (15037 fps) liquid scattering imaging and broad-band luminosity images were collected to examine spray liquid penetration and combustion. The chamber could mimic the real diesel engine environment by burning a mixture of acetylene, oxygen and nitrogen. The experiment was conducted at 800 and 1200K with an ambient gas density of 14.8kg/m^3. A realistic injector configuration was use with a nozzle orifice of 0.14mm diameter, injection pressure of 700 bar. The Diesel and water emulsion had longer liquid penetration and longer ignition delay under low ambient temperatures due to the lower volatility of the water, a result of the relatively large enthalpy of vaporization of water and higher viscosity of the water. At high ambient temperature, the physical

properties of the fuel are weakened; the spray cone angles indicated violent breakup events taking place upstream of the spray jet. Glowing spots were consistently observed under certain conditions believed to be micro-explosion (Fig.1.7).

In all four of these studies the microexplosions are not directly observed in the spray as they are observed with single droplet experiments. One study [73] doubts the existence and extent of the phenomenon in CI engine due to the range of droplet sizes in the injected spray [74]. It is apparent from the literature that the existence of the microexplosion phenomenon with Diesel fuel and water emulsions in CI engine fuel sprays is not agreed upon. with a number of works claiming their existence [47, 56, 72] and a number either ignoring them [53, 55, 57], doubting there existence [28]) or believing they are not possible [74].

Figure 1.6: Natural luminosity flame image of an Diesel fuel and water emulsion combustion in a rapid compression machine[47]. The small dark regions in the image on the left are suggested by the authors to be evidence of the microexplosion phenomenon.

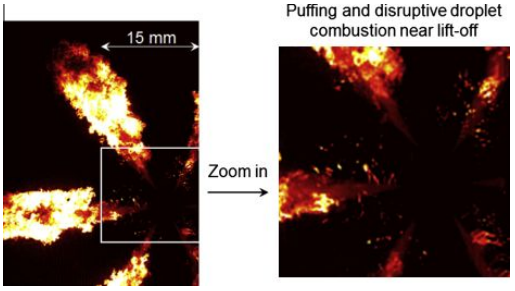

Figure 1.7: Natural luminosity flame images of a Diesel fuel and water emulsion in a content volume combustion chamber. The so called “puffing” in the flame images is suggested by the authors to be evidence of microexplosion.[72]

The observed PM reduction is also postulated to be a chemical effect due to the introduction of water into the combustion zone. During combustion, temperatures are high enough for partial dissociation of the water into hydroxyl radicals (OH) and hydrogen atoms (H) which have been shown to enhance the oxidation of soot to CO [56, 75, 76].

1.3 Scope of this study

The increased use of the CI engine fueled with Diesel fuel has been established. The strict legislation brought in, with particular attention to the EURO regime has lead to much development in the design and operation of the CI engine. The required targets are being met under ideal lab circumstance but the real world air quality,

particularly in urban environments does not seem to be improving. Recent press releases suggest the large uptake of Diesel fueled vehicles is to blame and there are calls for the use of CI engined vehicles in European urban environments to be curtailed [77]. To continue using the current fleet of vehicles and meet real world emission targets there needs to be a reduction in NO_x and PM tailpipe emissions. The use of Diesel fuel and water emulsions has shown promise to this end. A large number of studies have been conducted in engines, with some optical studies to examine the emission reduction and their mechanisms. To this date there is little data concerning the fundamental spray parameters of Diesel and water emulsion sprays with little to no data examining spray fundamentals in high pressure and density conditions of non-vaporizing sprays. Whilst the existence of the microexplosion in the spray combustion is contested, the effect of emulsification on non-vaporizing sprays has not been considered. This seems particular wise to examine considering the possible effects a multi-component /phase flow under extreme conditions such as high pressure and high ambient density may have on fundamental spray character. The emulsification effect on spray cone angle and tip penetration has not been considered for non vaporizing conditions.

Other methods to characterize the emulsion spray such as hydraulic characterization i.e mass flow rates and momentum fluxes have not been applied. This study goes some way to address these gaps in the research. The work presented here details the development of an experimental facility to examine the high pressure sprays of Diesel fuel and Diesel and water emulsions under what is considered non vaporizing conditions (ambient temperature) but at elevated ambient density. The sprays are observed optically utilizing high speed photography with a number of spray parameters, including spray cone angle and tip penetration measured. The experimental facility also includes the examination of the fuel sprays hydraulic character, such as mass flow rates, momentum flux and discharge coefficients. The study then progresses to examine combustion of the emulsions in a new piece of equipment which at this stage has been operated to examine the combustion without any spray and flame overlap. At this point the combustion study conducted and presented is incomplete but is included to demonstrate what would be a complete characterization of Diesel and water emulsion behavior in a CI engine.

2. Literature Review

Introduction

In the following section fuel spray fundamentals are introduced with their features that may be used to characterize their behavior. Characterization of fuel sprays is discussed, with variable that should be considered and methodology that should be applied in any measurement technique used. Optical techniques that are used for spray experimentation are detailed with their underlying workings , advantages and disadvantages introduced. Their is then a short review of previous findings that have applied optical spray characterization with some empirical models.

Hydraulic characterization of fuel sprays is then introduced. Fuel mass flow rates, instantaneous mass flow, and techniques using the fuel momentum flux are introduced. Various orifice coefficients that may be used to characterize the spray are the discussed with their use in previous works outlined.

2.1 Fuel Sprays

The requirement to meet stricter emissions targets along with demands for increasing engine efficiency has been established in the introduction. To meet these requirements the combustion process taking place in CI engine combustion chamber must be well understood and improved. A primary factor controlling the combustion is the mixture formation. Mixture formation is controlled by the characteristics of the injection system, the nature of the air motion in the combination chamber (swirl, turbulence) and fuel spray character. This mixture formation affects the associated ignition delay period (along with fuel properties) and the flame development. The mixture is formed by the discharge of pressurized fuel through a small, or number of small orifices, into the compressed air in the combustion chamber. This is the process known as fuel injection.

2.1.1 Spray Structure

During the pressurized fuel's journey from the injector into the chamber, the liquid jet transitions from a bulk liquid into dispersed droplets to a liquid/vapor mixture with the vapor intimately mixed with the ambient air. These atomized droplets and the vapor are the fuel spray and the process the liquid jet undergoes is called break-up. As the liquid leaves the nozzle and enters the combustion chamber an intact liquid core can be identified. This disintegrates into ligaments (blobs) with small droplets being stripped from the edge of the jet [78] in the so called churning flow region [79]. These liquid parts are like large droplets with sizes comparable to the nozzle diameter. The break-up of the liquid jet into droplets as it exits the orifice is called primary break-up. Primary break-up of the liquid jet is governed by different mechanisms which are usually characterized by: the distance from the orifice exit to the point of droplet formation on the liquid jet surface, referred to as the break-up length and; the intact liquid core length, the distance from the orifice exit to the point where the liquid jet breaks into droplets on the jet centerline[80].

The liquid core occupies a considerable fraction of the spray volume. Its density is much larger than the gas phase, with its contribution to the total mass even greater, this region is often refereed to as the dense spray [79]. Droplets that have formed in this region have a high probability of collision with other droplets which may result in droplet size change, velocity change or combination (coalescence).

Momentum is conserved and the droplets move downstream and are subjected to aerodynamic forces arising from the relative velocity between them and the surrounding gas resulting in break-up into smaller droplets. This is called secondary break-up and is characterized by the droplet size. The droplets transfer momentum to the surrounding gas, thereby causing them to decelerate. Droplets at the spray tip are subject to the strongest drag force and are decelerated more than the droplets in their wake. Droplets at the tip are replaced by new ones from behind and the tip penetration (S) increases with time from start of injection (SOI). The droplets with lower kinetic energy are pushed aside and form the outer spray region. A conical full-cone spray (spray cone angle θ) is formed that is more dilute downstream as the surrounding air is entrained into the spray. Primary break-up is the most important mechanism in fuel injection systems as it determines the size of the droplets that separate from the liquid core which then undergo secondary break-up prior to vaporization.

2.1.2 Primary Break-up

Four regimes of primary break-up: Rayleigh regime; first and second wind induced regime; and the atomization regime have been distinguished. Quantitative description of the break-up process and discretization of these regimes uses the liquid Weber number,

$$We_l = \frac{v^2 D \rho_l}{\sigma} \tag{2.1}$$

and the Reynolds number

$$Re_l = \frac{v D \rho_l}{\mu_l} \tag{2.2}$$

where v is velocity, σ is the surface tension at the liquid-gas interface (N/m) , ρ_l is the liquid density(kg/m^3), μ_l is the dynamic viscosity of the liquid (Pa.s). D is the characteristic length scale which is by convention the nozzle diameter. These two numbers are combined to eliminate the jet velocity but retain the relevant liquid properties to give the Ohnesorge number.

$$Oh = \frac{\sqrt{We_l}}{Re} = \frac{\mu_l}{\sqrt{\sigma \rho_f D}} \tag{2.3}$$

The Ohnesorge number is a ratio of the viscous forces and the surface tension forces. The break-up regimes are classified according to Oh as a function of the jet velocity, most often using Re_l [81]. Fig.2.1 shows the Ohnesorge diagram with the different break-up regimes as a function of the liquid Reynolds number with the region that is most applicable to direct inject CI engine sprays.

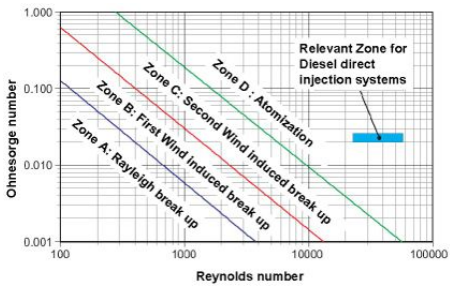

Figure 2.1: Ohnesorge diagram, Ohnesorge number as a function of the Reynolds number, with jet break up regimes [79].

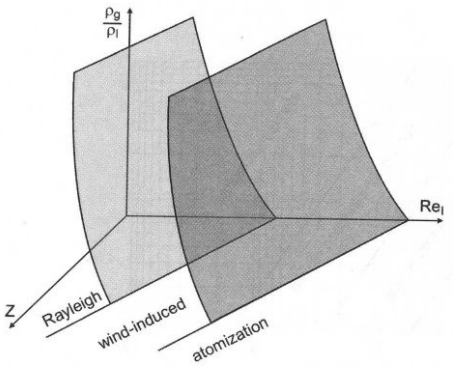

Figure 2.2: Ohnesorge diagram extended into a three-dimensional form to include the gas-to-liquid ratio ($\frac{\rho_g}{\rho_l}$).

The injection fluid properties do not fully describe the primary break-up of the spray. It has been shown that the break-up is influenced by the density of the gas

that the spray is forming in. For this reason the gaseous to liquid density ratio is included in the Ohnesorge diagram (Fig.2.1 is extended into its 3D form in Fig.2.2 [79, 80]). In order to distinguish the atomization regime, which is the regime most associated with CI engine fuel sprays, from the other primary break-up regimes already mentioned, the four main regimes are briefly introduced here. The four primary break-up regimes are

- **Rayleigh Regime** Break-up results in droplets with sizes larger than the jet diameter and is due to unstable growth of axis-symmetric surface waves caused by liquid inertia and surface tension forces. Break-up length is far (many nozzle diameters) downstream of the nozzle orifice and increases with increasing jet velocity [82].

- **First Wind Induced Regime** As jet velocity is increased, the inertia of the the gas phase becomes more important and forces due to the relative motion between the liquid jet and the ambient gas augment surface tension forces leading to droplets with sizes the order of the jet diameter. Increasing the jet velocity results in the break-up length reducing. Relevant parameter is the gas phase Weber number.

- **Second Wind Induced Regime** Jet velocity is increased further and the flow inside the nozzle becomes turbulent. Jet break-up now occurs due to unstable growth of short wavelength surface waves that are initiated by jet turbulence and amplified by aerodynamic forces due to the relative motion between the ambient gas and the liquid jet which are opposed by the liquid surface tension. Jet break-up is characterized by divergence of the jet spray after an intact or undisturbed length downstream of the nozzle orifice. The break-up process begins at the surface and gradually erodes the jet until it is completely broken up. Two break-up lengths are distinguished. The length describing the beginning of the surface break-up (intact surface length) and the length at the end of jet break-up (intact liquid core length). The unstable growth of short wavelength waves produces droplets of average size much less than the jet diameter and break-up length decrease compared with the first wind induced regime and decrease with increasing Reynolds number (jet velocity).

- **Atomization Regime** The intact surface length described in the second wind induced regime is zero, droplets are formed on the surface of the liquid jet at the nozzle orifice exit. Droplet diameter is much very much smaller than the orifice diameter. The jet forms a cone shape spray commencing at the nozzle

exit, the vertex of the spray cone is located inside the nozzle. An intact liquid core or at least a dense region consisting of large liquid fragments may still be present a number of nozzle diameters downstream of the orifice exit. It is a complex regime that is not fully understood, with the breakup process highly dependent on flow conditions inside the nozzle orifice. This is the most important regime for high pressure, CI engine fuel injection sprays [79, 82] as it provides the atomization required for rapid mixture formation. There are two main multiphase flow regions within the dense spray: liquid core and the dispersed flow region beyond the surface of the liquid core.

2.1.3 Atomization of Fuel Sprays

Modern fuel injection system for CI engines have nozzle orifice diameters in the range of 200μm [83] with injection pressures up to 200 MPa [84]. This suggests in nozzle jet velocities of up to 500ms^{-1} ($v = \sqrt{\frac{2\Delta P}{\rho_f}}$) which places the break-up firmly in the atomization regime. The mechanism for the break-up of the liquid jet in the atomization regime is not fully understood and a number of mechanisms have been postulated [82].

- **Aerodynamic Interaction** A growth of jet surface waves due to aerodynamic forces due to the very high relative velocity between the jet and surrounding gas [81]. The unstable growth of these waves due to aerodynamic forces (shear) is time dependent and cannot explain the zero surface break-up length that characterizes the atomization regime. This surface effect cannot account for the jet disintegration observed at its inner structure in the dense spray region (diffuse edge of intact liquid core).

- **Turbulence** Liquid turbulence within the nozzle itself with radial turbulent velocity components disrupting the liquid-gas interface resulting in droplet formation once the restraint imposed on the flowing liquid by the nozzle orifice walls ceases as the liquid emerges from the orifice [82].

- **Relaxation of Velocity Profile** The abrupt change in the boundary conditions as the liquid emerges from the orifice exit into the combustion chamber destabilizes the jet. In fully developed turbulent pipe flow with a large nozzle length to diameter ratio (L/D), the velocity profile may change as it exits the pipe, no longer a no-slip wall boundary condition, the outer region of the jet accelerates which may result in instabilities. The small L/D ratio of fuel injector nozzles makes this mechanism unlikely [81].

- **Cavitation** Cavitation is the the transition from liquid to vapor of a fluid due to reduction in pressure below the vapor pressure of the fluid [85]. Cavitation in fuel injector nozzles occurs due to the low pressure at the inlet to the nozzle orifice. These low local pressures are due to boundary layer separation near the nozzle inlet orifice. In this region, due to strong change in cross sectional area (reduces from A to A_{eff}, effective area) and flow direction, the boundary layer tends to separate from the the orifice wall and a structure known as the "*venacontracta*" forms. A recirculation zone appears between the "*venacontracta*" and the orifice wall (insert of Fig.2.3). A pressure depression forms due to fluid acceleration. If this static pressure in this pressure depression drops below the vapor pressure of the fluid, vapor is formed and cavitation has occurred. The fluid (liquid and gas) density can change from the liquid (ρ=880 kg/m^3) to vapor phase (ρ=1.2 kg/m^3) abruptly both temporally and spatially [86]. The cavitation number, Ca, is a dimensionless parameter used to characterize the flows sensitivity to cavitation and represents the ratio of forces suppressing cavitation versus the force promoting cavitation [87].

$$Ca = \frac{P_\infty - P_v(T_\infty)}{{}^1\!/_2 \rho_f U_\infty^2} \tag{2.4}$$

  where P_∞ is the pressure at a reference point in the flow, P_v is the vapor pressure at the reference temperature T_∞, ρ_f is the liquid fuel density and U_∞ is the velocity at the reference point.[88] As the cavitation number (Ca) of the flow decrease, nucleation will occur at a value, which is dependent on the fluid properties and experimental conditions. The value of this incipient cavitation is defined by a critical cavitation number. Vapor bubble growth is very much affected by temperature changes in the fluid and therefore Ca_{crit} is also dependent on the liquid temperature. However, values of Ca_{crit} are not common in the injector nozzle literature. A popular definition of a cavitation number for injection systems is given by

$$CN = \frac{P_{inj} - P_{amb}}{P_{amb} - P_v} \tag{2.5}$$

  where P_{inj} is the injection pressure, P_{amb} is ambient pressure and P_v is the vapor pressure.

Characterization of the primary break-up is often done using lengths: break-up length, intact core length, tip penetration (S) and; spray cone angles (θ). These may be refereed to as macroscopic characterization [84, 89], these parameters are

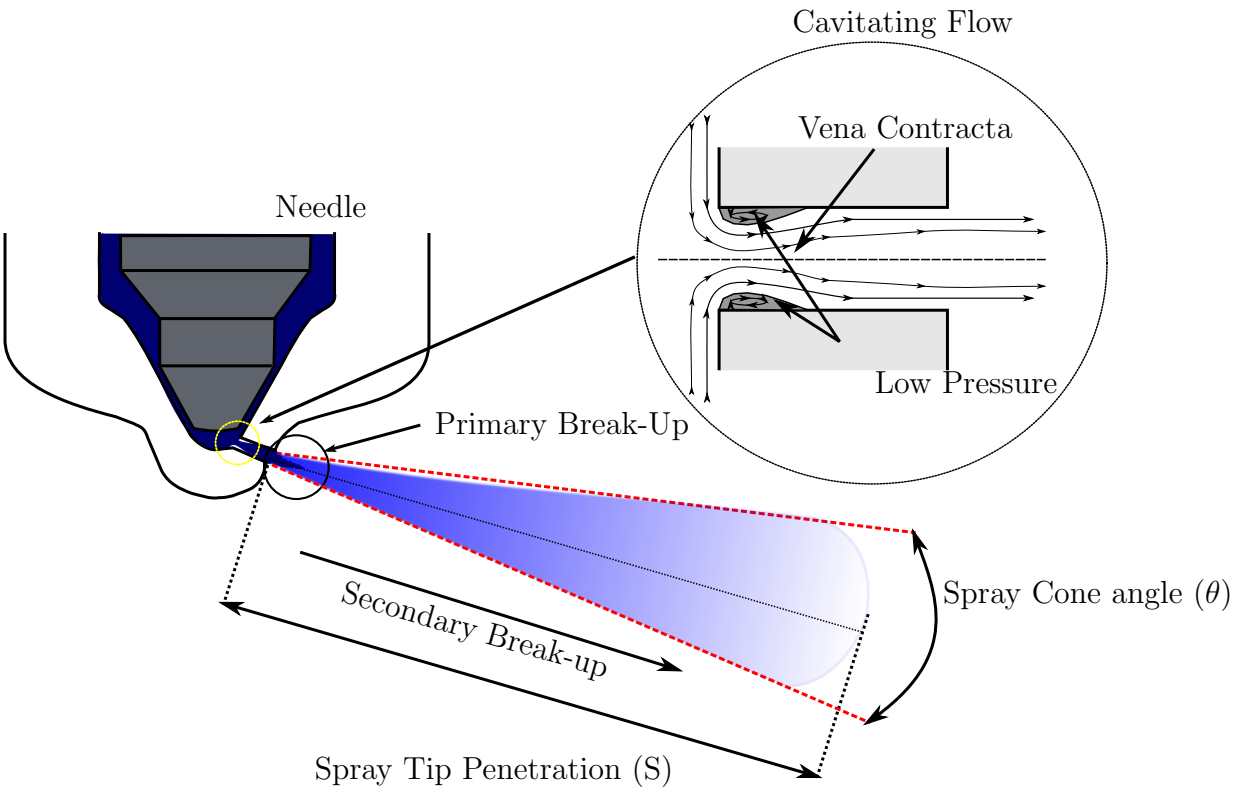

Figure 2.3: Spray break-up summary with insert showing the aviation structure in the nozzle orifice.

shown in Fig.2.3. The intact core and measurements around the dense spray are exceedingly difficult due to the density of droplets in this region, high velocities and small dimensions involved.

2.1.4 Secondary Break-up

The break-up of the droplets formed during primary break-up is caused by aerodynamic forces induced by the relative motion between the droplets and the surrounding gas phase. Unstable waves grow at the liquid/gas interface or of the whole droplet itself. Droplets are broken down into smaller droplets which are themselves subject to the aerodynamic forces. The aerodynamic forces are opposed by the liquid surface tension. Decreasing the droplet diameter results in a larger curvature at the surface which results in a larger surface tension force. The relative velocity required for further break-up (critical velocity) is larger. The gas phase Weber number is used to describe the break-up where the characteristic length scale is the droplet diameter and expresses the ratio of the aerodynamics forces the droplet is subjected to and the surface tension forces present at the liquid surface. As with primary break-up, a number of break-up regimes have been identified which are

transitioned with increasing Weber number [81]. In a CI engine, Weber number is high near the orifice exit and is where most of the break-up takes place (atomization regime), moving downstream, the velocity of the droplets reduces as momentum with the surrounding gas is exchanged and the droplets become smaller resulting in lower Weber number and transition to the different break-up modes, and a reduction in break-up. Secondary break-up is characterized by the size and velocity of the droplets and may be referred to as a microscopic characterization due to the sizes involved.

2.2 Spray Characterization

Numerous fundamental experiments and semi-empirical relations of the general behavior of spray parameters of full-cone CI engine fuel sprays such as spray cone angle (θ), spray penetration (S), break-up length and average droplet diameter as a function of the spray boundary conditions have been performed and published. Characterization of the spray behavior as a function of parameters governing the injection process is the desire in most cases, to provide adequate design information and provide suitable fundamental understanding for the construction of models used for simulation. Consideration of the injection system yields a number of parameters which would be expected to effect the spray behavior, some of these may be fuel properties or injector geometrical features that are essentially fixed or parameters that may be changed throughout the engine's operational range to best match the requirements of combustion at different operating points. The main fixed parameter is the nozzle geometry which will include: orifice diameter; nozzle conicity; surface roughness; sac/mini-sac volume; needle seating; hole angle and orientation relative to other holes and injector central axis. Parameters that may be adjusted during engine operation are the injection pressure; opening time and duration; needle opening speed and; the properties of the trapped air mass (TAM). The TAM may be modulated through turbo charging, inter-cooling, EGR and valve timing, the trapped air mass properties are also a function time (crank angle degree of the cycle) hence injection timing used is essentially a TAM variable.

This thesis deals with characterizing the sprays of Diesel fuel and Diesel fuel and water emulsions. The primary break-up of the spray has been considered with secondary break-up not considered. For this aim the spray parameters used to characterize the sprays is the spray cone angle (as a function of time and full-spray cone angle), the spray tip penetration and the spray tip velocity. In the following sections, the methodologies employed to make the measurements used for the

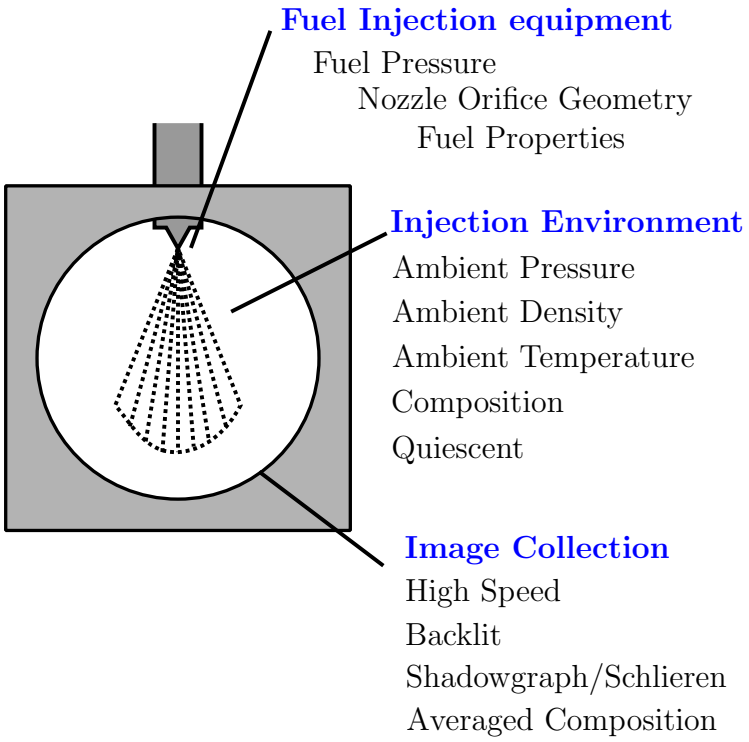

Figure 2.4: Structure of an fuel injection spray investigation experiment using optical methods. Structure includes parameters and techniques that should be considered.

characterization are introduced and then previous findings concerning the characterization parameters are given. To describe the influence of the spray on mixture formation it is necessary to characterize the spray parameters and the influence of injection parameters on these. Primary break-up (dense spray) is difficult to characterize using conventional optical measurement techniques (such as the phase Doppler technique or PIV). For this reason spray tip penetration, spray tip velocity and spray cone angle, which can be obtained using photographic techniques, are among the most frequently reported parameters in fuel-spray research [90]. Fig.2.4 shows the structure of such an experimental measurement with the variables, parameters and conditions to be considered.

2.2.1 Fuel Injection Parameters

The spray is formed by the injection equipment usually consisting of a fuel delivery system, high pressure pump, injector, nozzle with orifice and a driver of some kind. The main injection parameters considered when conducting a spray characterization measurements are the nozzle geometry, the injection pressure, injection profile and the fuel being injected. The nozzle orifice is the component of the injection system where spray is actually initiated so is obviously an important parameter to consider

when characterizing the spray. The orifice is in the form of a very short pipe, connecting the internal volume of the injector to the ambient gas. This short pipe has an inner diameter, a length, outer diameter and the corners at the entrance to the pipe have a radius. Sharp orifice inlets (low radius) lead to greater axial velocities at the inlet which results in a low static pressure that initiates cavitation [88]. Larger radius corner (less sharp) shown to reduce the spray mass distribution (cone angle) due to the reduction in the extent of cavitation [86]. Cavitation generated in the nozzle enhances the fuel atomization performance and the longer nozzle orifice length induces more fuel atomization [88]. The orifice "pipe" may be cylindrical or conic, with a convergent or divergent profile. Convergent nozzles have been shown to result in larger tip penetration than cylindrical whilst divergent nozzle orifices show a lower tip penetration. Orifice profile is characterized but the K-factor [91, 92]

$$K = \frac{D_i - D_o}{10\mu m} \tag{2.6}$$

Convergent nozzles have been shown to reduce cavitation [92, 93, 94]. Injector nozzle orifices are usually in the range of 100 to 200μm[83, 90], produced using spark erosion and hydro-ground to achieve an entry radius and surface finish roughness.

The fuel injection pressure arises due to the high pressure pump raising the pressure of the fuel while the injector needle is closed. The injector is opened by the needle lifting off its seat and allowing unrestricted access to the nozzle orifice. The fuel experiences a rapid pressure drop across the orifice. Injection pressures examined in the previous works include: [95] high injection pressures in the range 50 to 250MPa while [96] used ultra high injection pressure up to 300MPa, both using a high pressure accumulator (rail). The range of pressures used is usually smaller such as 75 to 160MPa in the work [97], up to 100MPa in [98], 30 to 180 MPa in [99] and 30 to 135MPa in [90]. All of these works utilize a common rail accumulator in between the pump and the injector in which high pressure fuel is stored. This results in near constant pressure during the injection process. Older studies often used lower pressures, utilizing jerk style pumps which increase the fuel pressure dependent on pump speed. The needle is seated using a spring, as the pressure increases the needle may snap open and an injection occurs [100, 101]. Increasing injection pressure results in an increase in the tip penetration and tip velocity while for complete atomized sprays the cone angle has been shown to be independent of injection pressure (P_{inj}) [95, 96, 97, 98, 99, 101]. The findings pertaining to injection pressure effects will be discussed in greater detail in a later section.

The different primary break-up regimes were identified with the use of the Weber

number and the Reynolds number (Eq.2.1 and 2.2). These dimensionless numbers are used to include the liquid properties and their effect on spray parameters. The liquid parameters of interest are the fuel viscosity, the fuel surface tension and the fuel density. The effect of these parameters on spray is usually done by changing the fuel that is being injected. The work [102] specifically set out to examine the influence of fuel properties on spray. Ten fuels with varying density (683 to 876 kg/m^3), viscosity (0.6-7.0 mm^2/s and surface tension (16.0 - 30.1 mN/m) were examined. Increasing fuel density and increasing viscosity was shown to reduced spray angle. As injection pressures increased, the viscosity effect on spray angle reduced, above 150MPa all fuel angles were similar independent of fuel viscosity. Temporal evolution of the tip penetration increased with increasing density, and the density effect decreased with injection pressure increase. During the very early "initial zone" of tip penetration, fuel density was shown to have no effect. Fuel viscosity increased tip penetration during the "fully developed zone" with no effect during the very early period of spray development.

Most works effect a fuel property investigation indirectly by the application of alternative fuels, such as biodiesel. Table.2.1 show some typical fuel properties employed in such tests. In the work [103] biodiesel (RME) had a slightly longer penetration and narrower cone angle with this compared to mineral Diesel fuel. In the work [104] biodiesel and Diesel fuel were compared. The tip penetrations of biodiesel were shorter than those of Diesel fuel during the earlier period (up to 1.5ms). The tip penetration of biodiesel then increased rapidly and became longer than that of Diesel fuel until the end of the injection. It is argued that as the viscosity of the biodiesel is almost twice as high as that of Diesel fuel, friction between the biodiesel and nozzle surface is increased resulting in the tip penetration of biodiesel increasing more slowly at the early stage of injection. Due to the higher density, the momentum of biodiesel is higher than that of Diesel fuel, which makes the tip penetrations of biodiesel exceed those of diesel at the later period of injection.

In the work [105] it is concluded that generally, biodiesel (rapeseed oil) was characterized by greater penetration length and smaller spray angles compared to Diesel fuel. Their results indicated that the spray tip penetrations increase in accordance with the increase in mixing ratio of the biodiesels because the biodiesels are atomized less in comparison to conventional Diesel fuel due to the high surface tension. The work [106] reported that the spray tip penetrations of biodiesel and biodiesel-blended fuels showed a similar pattern, regardless of the mixing ratio of the biodiesel. Droplet size measurements shown that the atomization performance of the biodiesel-blended fuel was inferior to that of the conventional Diesel fuel due to the high surface tension of the biodiesel fuel. The injection velocity of biodiesel was lower than that of

Diesel fuel during the beginning of the injection and became higher than it after 1 ms. The work [107] compared biodiesel and DME sprays. The spray cone angle of the biodiesel spray was wider than that of the DME spray. The work [96] compared Diesel fuel with two biodiesels from different sources, palm oil and used cooking oil (Table.2.1. With the ambient density of 15.5 kg/m^3, biodiesel gave a longer spray tip penetration than Diesel fuel at a specific time after the start of injection (about 0.3 ms), while biodiesels and Diesel fuels give similar values of spray tip penetration before about 0.3 ms. The difference of spray tip penetration among three fuels is quite small under high ambient density (30 kg/m^3). With the ambient density of 15.5 kg/m^3, spray penetration difference between palm and used oil biodiesel is decreased with increasing injection pressure. When injection pressure is increased to 300 MPa, the spray tip penetrations of all fuels is similar. Averaged spray angles for the biodiesels gave smaller spray angle.

The discussion so far has one study where the fuel properties have been altered and a number of works where biodiesel, Diesel fuel and DME spray parameters have been investigated. Whilst engine testing of emulsified fuels is widely published, fundamental spray experiments are rare. The work [56] is partially concerned with the spray parameters of Diesel fuel and water emulsions. The emulsion contained 10% (wt) water. Its viscosity was measured at 25, 40, 50 and 70° and was larger than Diesel's at all temperatures. Cone angle was determined at 42 and 112 nozzle diameters downstream of the nozzle. Only one injection pressure of 120MPa was considered. Sprays were injected into a chamber under vaporizing conditions as the temperature was 830K, pressure 5MPa. It is difficult to draw conclusions concerning fundamental spray structure as the measurement is made with combustion commencing. The tip penetrations were not seen to be different between the fuels. At the 42 diameter point, the emulsion's cone angle was very slightly larger, at the 1112 point, angle was the same for each fuel. No conclusions concerning the fundamental nature of the spray parameters under non-vaporizing conditions are made. Also included in the study is a micro-emulsion which is not included in the scope of this study. Viscosity measurements and the 42 diameters downstream angle measurement are included here in Fig.2.5 and 2.6

2.2.2 Injection environment

As the liquid break-ups, once it leaves the confines of the nozzle orifice, the surrounding gas through which it is traversing is the next parameter that will greatly effect

Table 2.1: Fuel density, viscosity and surface tension for a number of fuels that have been examined in previous experimental spray investigations.

Fuel	Density kg/m^3	Viscosity mm^{2}s^{-1}	Surface Tension N/m
Biodiesel	886.4	7.10	[104]
Diesel	835	3.933	
5%RME Diesel	831	2.38	0.023
30% RME Diesel	851	3.12	0.025
RME	879	4.47	0.028 [103]
Soybean oil	884	4.0-6.0	0.028[107]
DME	660	0.12-0.15	0.012
Diesel	830	3.36	0.0255 [96]
Palm oil biodiesel	874.4	5.53	0.262
used oil biodiesel	885.1	4.45	0.0257

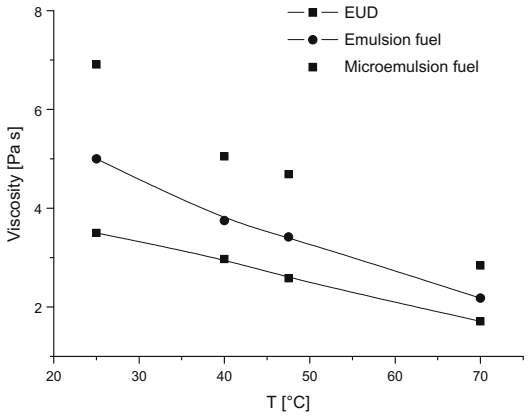

Figure 2.5: Viscosity of Diesel fuel, a Diesel fuel and water emulsion and a micro emulsion at 4 temperatures [56].

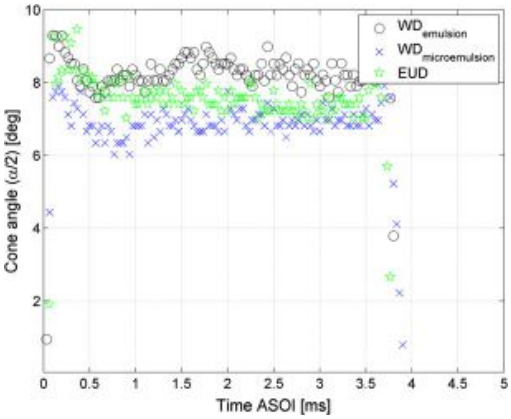

Figure 2.6: Variation of the half spray cone angle with time after SOI for a Diesel fuel, a Diesel fuel and water emulsion and a micro emulsion [56].

the spray character. Fundamental spray experiments are conducted into various atmospheres (alternative terms include gas phase, ambient, surrounding gas) with a range of properties. The main gas phase properties to consider are the temperature, density, pressure and composition. The desired outcome of the characterization dictates the gas properties and hence the equipment design. Broadly speaking sprays may be considered under ambient conditions described as:

- **Non-Vaporizing** The ambient gas is relatively cool, usually around room temperature (standard temperature). As the spray break-up commences and droplets move downstream from the nozzle orifice, vaporization of the sprays is not enhanced as would occur in real CI engine fuel sprays. These measurements are useful for fundamental understanding of sprays. Gas density and pressure

may be atmospheric or increased to that approaching the density and pressure in a real CI engine at or around TDC. May be referred to isothermal spray [108]

- **Vaporizing** Sprays enter a hot gas environment with temperatures approaching those experienced in a real CI engine round TDC. These measurements are useful for gaining insight into the spray in real world conditions. Density and pressure may be atmospheric or increased up to that in a real CI engine at or around TDC.

- **Non-Reacting Conditions** The fuel spray enters a gas phase which prohibits combustion from commencing. This is most readily achieved with the adoption of an inert gas, such as nitrogen. Conditions may be vaporizing or non-vaporing but combustion is not studied. Used where spray fundamentals in real world conditions are required.

- **Reacting Conditions** This is the characterization which most closely resembles real world CI engine conditions. Not only spray but combustion is studied, particularly ignition delay and flame lift off length. The environment is closely controlled to form a region of known temperature, density, pressure and composition.

The most basic of tests examine sprays in a chamber at standard temperature and pressure whilst the most complex and one that most closely approaches conditions in a real engine is an optical research engine. Optical research engines typically replace elements of an engine with high strength windows to allow optical access to the combustion chamber allowing spray and combustion visualization. This is usually done using transparent cylinder liners and a bow-ditch piston design. Material properties limit the range of pressures to around 2MPa, realized with a reduced compression ratio [109]. The use of optical engines introduces other problems concerning accurate description of the flow field in the chamber, difficulty to determine pressure and temperature. Their operation is usually done in skip fired mode [109] to avoid over stressing the engine. Fundamental spray research requires highly repeatability measurement conditions to fully appreciate the influence of different parameters on what is inherently a highly transient and temporal event. Alternative research engine arrangements are also used which utilize a chamber attached to the top of an engine cylinder, essentially operating the engine as a rapid compression machine, these arrangements are also susceptible to flow field effects [110, 111, 112, 113].

A constant volume chamber or cell (CVC) is considered a good compromise for fundamental CI engine spray research. It provides good optical access with a large

observation area and good control (reproducibility) over the gas phase conditions prior to injection. The desired pressure, density and temperature conditions are achieved using a number of solutions. Density and pressure have been met with the use of nitrogen supplied directly from a high pressure cylinder in a number of works [100, 114, 115, 116]. Nitrogen is also used in the works [93, 117, 118], with a low flow rate maintained through the chamber (pressures up to 6MPa) with nitrogen supplied from a cylinder and recirculated throughout the chamber using a roots compressor. The flow rate is maintained to reduce window fouling and purge the chamber of fuel spray. The fuel is removed from the nitrogen flow after leaving the chamber, gas temperature is regulated using a heat exchanger to maintain constant pressure and density conditions in the chamber. The flow rate is deemed to be too low to effect the spray dynamics.

In a number of works the nitrogen is replaced with Sulfur hexafluoride (SF_6) [108, 119, 120]. SF_6 has a higher molecular weight with a viscosity similar to air. At room temperature, SF_6 allows experiments at a density of 30 kg/m^3 (comparable to nitrogen at 30bar) with a pressure of of less than 0.5 MPa. SF_6 is an inert gas which avoids corrosion and has optical properties similar to air. As with some nitrogen flow chambers, a low flow rate (velocity of 2 m/s) of pressurized gas parallel to spray axis ensures scavenging of the fuel between injections [108, 119].

Air is also used [102] with air pressurized by a compressor at room temperature(0-3MPa), with a low flow rate used whilst the work [121] uses air straight from a cylinder. Argon has also been used as the gas phase [122] ensuring non-reacting conditions. The use of these gases, wether from a cylinder or compressed results in the pressures desired. Density is achieved with careful consideration of the filling and flow in the chamber to maintain a near constant temperature [121]. The experiments mentioned so far have been non-vaporizing where the temperature has been maintained at around 293K to 298K.

The temperature of the gas phase is heated electrically in the works [92, 122] using cartridge heaters inserted in the chamber walls with gas temperatures up to 850K stated. In the case of [92] the temperature distribution in the chamber is assisted with the use of a small fan and lined with a ceramic resin to aid insulation. An alternative electrical heating technique is outlined in the work [123], in this study, nitrogen or air is heated and pressurized external to the chamber in a 12 liter autoclave. The hot gas is admitted into the chamber via a cam driven inlet valve and exhausted through a pneumatically operated valve. An engine cycle without piston motion or flow is simulated [123]. Additional temperature and pressure increase is achieved with a small pre-injection combustion event prior to main injection. This

appears to be a novel arrangement and is shown in Fig.2.7.

The most advanced CVC in operation in a number of institutes is the pre-combustion chamber. In this arrangement the CVC is filled with a combustible gas mixture which is ignited prior to injection. In the work [124] a known mixture of CO, Air and O_2 is used while [97] and [109] use a mixture of oxygen, nitrogen, and (a mixture of) hydrogen, ethylene and/or acetylene. The mixtures in [97] and [109] are used as the fuels support flame propagation even in very lean mixtures and are easy to ignite. Variation in the composition of the mixture allows for different pre-injection pressure/temperature combinations. The presence of CO_2 in the post combustion gases in [124] renders the mixture different to that typically found in a CI engine except when a relatively high level of exhaust gas recirculation is used. Operation of the pre-combustion chamber starts with an initial, short period of heating to the peak pressure, a result of the combustion the combustible gas mixture. This is followed by cooling via heat loss to the vessel walls. Fuel is injected when the pressure and temperature reach their target values [124]. This results in a high temperature, high pressure, high density environment to examine vaporizing, reacting sprays. Heating of the chamber walls is used to avoid condensation forming on the walls and windows [89].

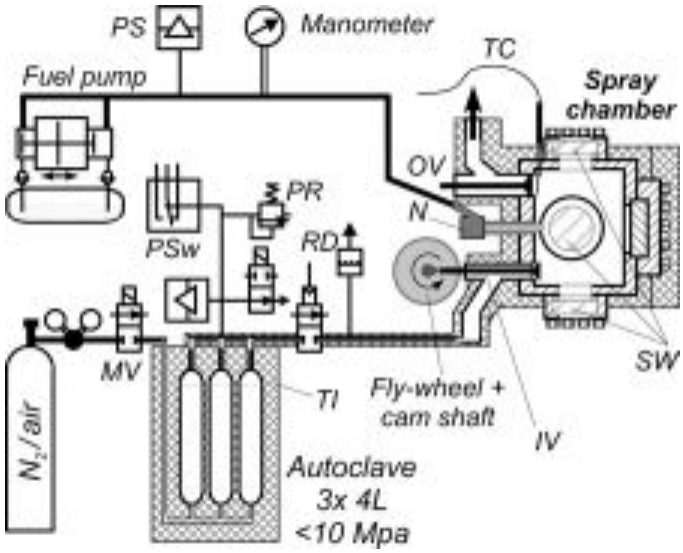

Figure 2.7: High pressure constant volume chamber schematic as used by [123]. SW: sapphire window, TI: thermal insulation, IV: inlet valve, OV: outlet valve, TC: thermocouple, PS: pressure sensor, PSw: pressure switch, MV: magnetic valve, RD: rupture disk, PR: pressure relief valve ,

2.3 Imaging Techniques

Imaging of the fuel spray may be accomplished a number of ways. The methods employed may be broken down according to the visualization technique used and the methods used to collect and store the image. When considering the characterization parameters tip penetration and spray cone angle there are, broadly speaking, two main forms of visualization employed. These themselves may use a number of optical arrangements. The first form may be thought of as a classical visualization technique [84] which uses the change in refractive index or transmittance of the region under investigation, referred to as the test section. The second form uses scattering techniques which use elastic dispersion or scattering of incident light by the spray droplets, ligaments and dense core.

2.3.1 Shadowgraphy and Schlieren (Classical)

Schlieren and shadowgraphy are two related techniques that are used to visualize the spatial variation of density in a transparent medium, which in most cases is a gas (e.g.air). The density gradients may arise due to temperature gradients, shockwaves, gas jet or liquid evaporation (not exhaustive list). The density gradient results in variations of the medium's refractive index which results in disturbance (bending) of any light ray as is passes though the medium. This results in a spatial modulation of the light intensity distribution with respect to the original intensity [125] traversing the test section. A shadowgraph is formed when this spatial modulated light is projected onto a screen (or camera imaging plane) resulting in a shadow of the refractive index field prevailing in the region of the density gradient. The most simple form of shadowgraph is called a divergent direct shadowgraph [126] and may be formed quite simply with a point light source projecting rays though the medium with a screen on the opposite side of the medium (Fig.2.8) [127].

The method may be enhanced with the use of parallel light traversing the test section and is demonstrated to have twice the sensitivity (for same test section to screen distance) compared with divergent arrangements [127]. In practice parallel light is obtained using a point source and a collimating lens or a parabolic mirror (Fig.2.9). In both divergent and parallel cases the refractive index field which is visualized is a shadow, *"a shadowgram is not an image, it is a shadow"*. The shadowgraph reveals the spatial dervative of the deflection angle ($\partial\epsilon/\partial x$ or $\partial\epsilon/\partial y$), this is the second spatial derivative or Laplacian of the refractive index ($\partial^2 n/\partial x^2$ or $\partial^2 n/\partial y^2$), and

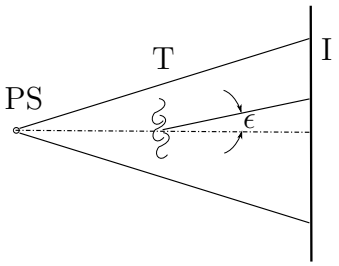

Figure 2.8: Basic single point source shadowgraph system. PS=Point source, T=Test section, ϵ=deflection angle, I= Image screen where shadow is formed.

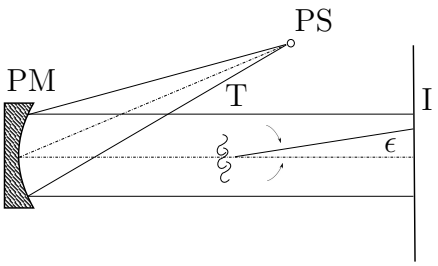

Figure 2.9: Point source parallel bean shadowgraph system utilizing a parabolic mirror to collimate the light as it passes through the test section. PS=Point source, PM=parabolic mirror, T=Test section, ϵ=deflection angle, I= Image screen where shadow is formed.

hence density [125]. This makes it ideal for sharp edged inhomogeneities such as spray boundaries and thus evaluating macroscopic spray scales, whether vaporizing or non-vaporizing, inert or reactiing [112].

The method is improved further with the adoption of the so-called "focused" shadowgraph method [127]. The"focused" shadowgraph technique differs from direct shadowgraphy in that an optical image is produced by a focusing lens or mirror interposed between the test area and the shadowgram [126]. The focusing lens or mirror brings the test field into a more-or-less sharp focus imaging plane. An advantage of focused shadowgraphy is that it allows variable magnification of the shadowgram. A number of arrangements are possible to achieve a practical "focussed" shadowgraphy system for CI engine spray characterization. Space and equipment are most likely the limiting factors. One method employed in ballistics work is the double mirror, z-type system, Fig.2.10. The point light source and the camera lens are positioned one focal length away from the mirror, aberrations in the focused shadowgraph are kept to a minimum by keeping the offset angle of the light source and the camera small and using long focal length mirrors with a large f/number. Assuming optical access to the spray is in the region of 100mm, mirror size should be comparable with f around 12. This results in focal length of around 1200mm, it is clear that the system size can get rather large.

An alternative method uses one mirror, this has the disadvantage of the light not being parallel. This may be called the single-mirror coincident systems or the single mirror double pass system, as the light will traverse the test section twice. This has been shown to increase sensitivity [127]. The light source is placed on axis at the radius of the curvature of the mirror (which is equal to two focal lengths

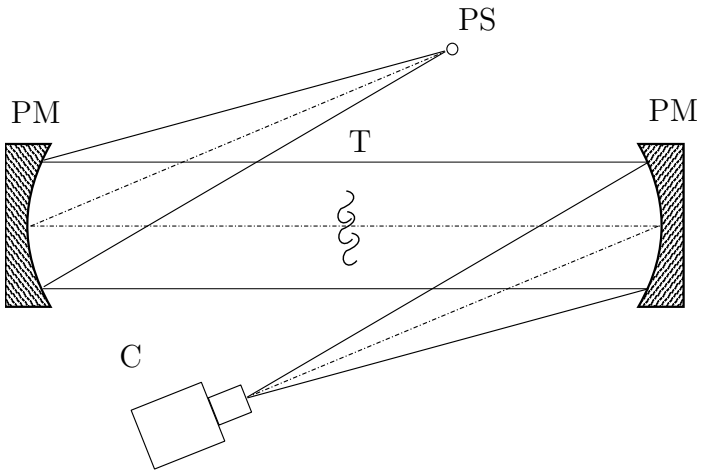

Figure 2.10: Double mirror, Z-type focussed shadowgraph system. PS=Point source, PM=parabolic mirror, T=Test section, C=camera

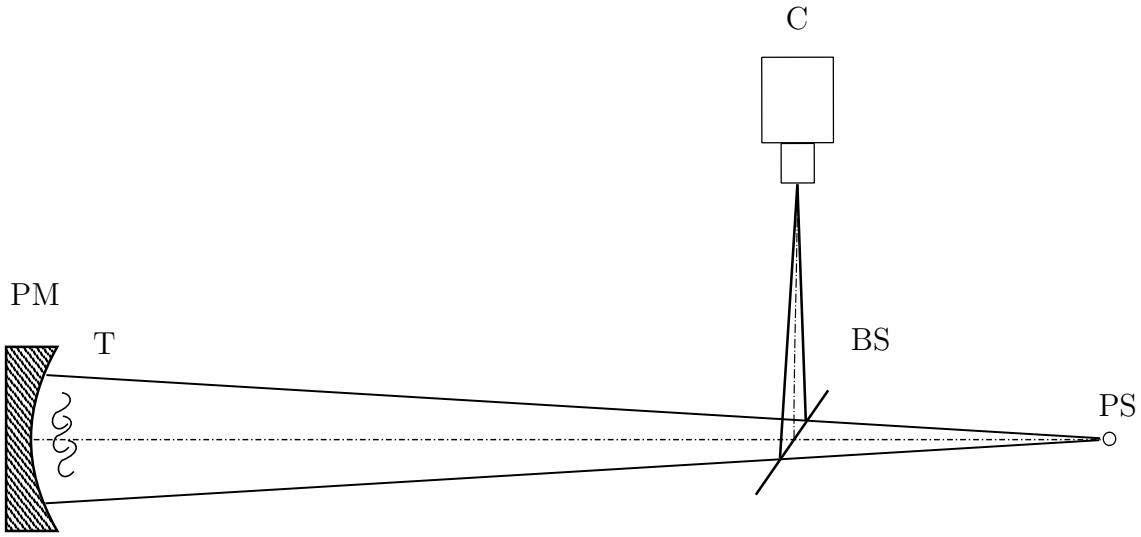

Figure 2.11: Double pass, focused mirror shadowgraph system. PS=Point source, PM=parabolic mirror, T=Test section, BS=beamsplitter, C=camera.

of the mirror) with the test section as close to the mirror as possible (Fig.2.11). Reflected light is diverted into the camera using a beam splitter, usually at 50/50 type. This methodology is mostly used where there is limited access to lenses and mirrors but has the sensitivity advantage as well as easing the optical alignment of the components.

An alternative method replaces the mirror with a collimating lens, see Fig.2.12. In the figure a knife edge has been placed at the focal length of the second lens. The addition of this "filter" changes the shadowgraph into a schlieren image. The knife edge is positioned to cut off a portion of the light that has been disturbed by the refractive index field in the test section. Fig.2.12 includes two rays that have been deflected by the density gradient in the test section. Both rays miss the focal point of the lens, the red ray brightens a point on the camera lens and the blue

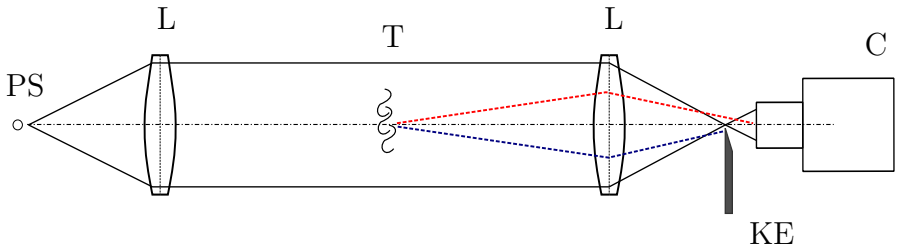

Figure 2.12: Lens focused schlieren system. PS=Point source, L=lens, T=Test section, KE=knife edge, C=camera. Red and blue lines are deflected rays, red line results in bright point in camera image plane, blue line is blocked knife edge resulting in dark point on the camera image plane.

ray is blocked by the knife edge. This differs from the shadowgraph system in that an actual image is formed, not just a shadow. The image reveals detail concerning the spatial density field present in the test section with the illuminance level in the image responding to the first spatial derivative of the refractive index (hence density) $\partial n/\partial x$ [127]. An important step in the alignment procedure is to adjust the percent cutoff by the knife-edge in order to obtain the desired sensitivity. If the cutoff is small, a large amount of light passes over to the screen and results in poor contrast of the schlieren images. If the cutoff is large, high contrast images are possible but the measurement may result in the loss of information in regions of low density gradient [125].

Both schlieren and shadowgraphy have been utilized in a various forms to examine and characterize spray parameters. The work [112] used a collimating lens, focused shadowgraph system. Point light source was in the form of a Xenon lamp attached to a fibre optic bundle with a 1mm iris. Two lens, 60mm diameter, focal length 250mm were used (f/number=4). The small beam diameter used required the apparatus to be moved when examining the early period of the spray formation when tip penetration was short. A lens type focused system is used in the work [89] with a Xe arc lamp continuous light source focused through a pinhole and collimated by a 1000mm focal length lens, the resulting beam is slightly larger than the visible window diameter. After exiting the test section the light is focused by an identical lens onto the camera lens system.

The work [56] introduces an ambiguity that is present in the literature concerning the shadowgraph technique. In this work the shadowgraph methodology is stated as being used but the light source is not a point source. Instead the light passes through a diffuser screen and is then collimated. It is unclear to what extant the light traversing the lens will be collimated due to the diffuser screen. It is a form of parallel shadowgraph but the light may not be considered parallel. The ambiguity

arises through the use of the diffuser screen. An optical diffuser is an optical element that allows light through and scatters the light through a large range of angles, resulting in a relatively uniform, highly divergent light source [128]. A common application of the shadowgraph technique uses a none-point source and an optical diffuser as used in the works [92, 93, 102, 104, 114, 129, 130]. The technique has the advantages of: avoiding non-uniform lighting of sprays; reducing the effects of beam-steering on the images [129] and; being extremely easy to set-up using low cost equipment. The optical diffuser usually take the form of a textured, ground glass plate [128]. The shadow is formed not just by a density gradient and bending of the light but also attenuation and extinction of the light passing through the spray, similar to the formation of a shadowgraph (or shadowgram) by a silhouette puppet. It is unclear how sensitive this technique is to the vapor and air mixture in the spray tip region of a spray as there are no examples in the literature where the techniques have been compared. Experience has shown that the diffused backlit sensitivity is highly dependent on illumination levels and camera lens settings. The correct terminology to use is also ambiguous as it is unclear whether the diffuse backlit technique, as it is most often called ([92, 93, 102, 104, 114, 129, 130]) forms a "true" shadowgraph. For the purpose of this study, clear distinction is drawn between the techniques, with the focused shadowgraph refereed to as shadowgraphy, forming a true shadowgraph, and the diffused backlit technique refereed to simply as backlit.

Schlieren has been applied also to CI engine sprays. In the works [131, 132, 133] a double mirror, z-type schlieren arrangement was used. In [133] the point source is a focused mercury-xenon arc lamp with 1mm aperture. Collimation is achieved with two 115mm, $f/8$ mirrors (this is thought of as being small [127]). It is unclear whether the knife edge was actually included or not, in which case the system would have been a focused shadowgraph. This highlights the ambiguity that is present in the literature concerning the two techniques. A novel method employing a plain, flat mirror mounted in the chamber behind the injector, creating a double pass system is used in the work [134]. Parabolic mirrors are used as usual outside of the chamber. The work shows that the technique is highly flexible and may be incorporated into constrained geometrical configurations.

2.3.2 Elastic scattering

Another methodology considered to characterize the spray parameters widely used is the elastic scattering of light. The spray is illuminated with a light source, a Xenon lamp or a laser which is scattered by the droplets which are much larger than the wavelength of the light. For this reason the scattering is in the Mie regime, hence the

technique when applied is refereed to as Mie scattering [118, 122, 135, 136, 137]. The light may be introduced to the spray front on [138] or from the side [122]. If a laser is used the light may be shaped by lenses to form a conic shape to provide uniform light in the test region [122] or formed into a sheet [133, 135, 137] to illuminate only a cross section of the spray. If a laser sheet is formed, illumination is always perpendicular to the camera axis. If a laser is used the technique may be referred to as laser elastic scattering (LES) [123].

The scattered light received by the detector, usually a camera, is a function of the droplet number density of the scattering medium [123]. The droplet number density decreases smoothly along the radial axis of the spray and Mie signal is very weak at the spray boundaries. The spray cone angle and the tip penetration measured are strictly related to the optical setup and the image post processing used [118]. The use of Mie scattering introduces difficulties in discriminating the border between the vaporized droplets and surrounding gas phase, particularly in high temperature and/or reacting conditions [56]. Because of its dependents on the droplet number density it does allow for qualitative measurement of the droplet density number in the spray with adequate post processing [122].

2.3.3 Recent advances

During the last decade, intense X-rays from synchrotron sources have been introduced to fuel spray research to circumvent the strong multiple scattering problem in the near-field. Hard X-rays, which have weak interaction with the liquid fuels, can pass through the optically dense materials without multiple scattering and severe absorption [139]. In addition, the phase variations of the emerging radiations from the liquid/gas interfaces inside the dense fuel jet can be recorded to understand the morphology of fuel jet, ligaments, and droplets. Based on the phase difference during the wave propagation, an X-ray phase-contrast imaging (XPCI) technique has been introduced to visualize the features inside the dense spray region [140].

2.3.4 Image Collection

For both of the optical techniques, the visualization of the spray is completed with capture of the image. This is most readily done with a digital camera either a CCD (charge coupled device) or CMOS (Complementary metal oxide semiconductor) type. There are two methods employed in the literature for the application of their use. The ensemble average, or phase averaged methodology does not take a

video of the fuel spray event, rather it takes images, utilizing a very fast shutter, at specified times after the SOI. A number of images are taken at each time step for a number of injections, allowing an average image at each time step to be produced. Examples of the time steps between each image used in previous works include 20μ [138]100μs [112] and 200μs [115]. The time step chosen clearly influences the temporal resolution of the measurement while the number of repeats chosen demonstrates the variability attached to the highly transient spray parameters being characterized.

More often in use now, with the advent of very high speed video cameras is the use of continuous image collection in the form of an image sequence (a video). When this technique is applied, the frame rate of the camera is chosen according to the required rate available for a given spatial resolution. The camera is triggered to recored along with the injection event. While the frame rate of the camera is the time interval between each measurement point, the actual time that the shutter is open may be much less and synchronized with a pulsed illumination source to freeze the fast spray in the image, reducing any blur [96, 121, 133]. Extremely high frame rates of up to 500kfps (kilo frames per second) have been observed in recent works [121] giving insight into the very early period of spray development.

2.4 Previous Works findings

In the following section a brief outline of the characterization of CI engine sprays from previous work will be presented, theoretical models, empirical models and experimental considerations will be included.

2.4.1 Spray Cone Angle

The spray cone angle or spray dispersion [97] has a great influence on the fuel distribution in the combustion chamber and hence mixing. A wider spray angle suggests a greater degree of break-up, remembering that in the atomization regime, the break-up length is zero and the angle is formed at the orifice exit. A larger angle also suggests a reduction in the tip penetration [84] which may result in under utilization of the available air [141]. The spray cone angle can be calculated from aerodynamic theory that attributes jet breakup to the aerodynamically induced growth of unstable surface waves. This theory can be derived by considering the infinitesimal surface waves on the liquid-gas interface; it predicts [80, 84].

$$tan\alpha = \frac{4\pi}{A}\left(\frac{\rho_a}{\rho_f}\right)^{1/2} f\left[\frac{\rho_f}{\rho_a}\left(\frac{Re_f}{We_f}\right)^2\right] \tag{2.7}$$

where A is an empirical constant or approximated by A=3.0+0.28(L/D). In the book [80], Eqn.2.7 is introduced as part of the construction of a two-zone CI engine model. It is accepted in the work that the spray cone angle depends on the density of the mixture in the cylinder and, is therefore a function of time (after SOI) but is assumed to be constant for the model purposes. A number of alternative CI engine models are introduced which rely on the spray cone angle or the half angle with a reliance on experimental derived constants. One such model is the well known Hiroyasu model [142] which is itself developed from a dimensional analysis in the form

$$\theta = f\left(\frac{\rho_f}{\rho_a}, \frac{d_o u_o \rho_f}{\mu_a}\right) \tag{2.8}$$

where u_o is the initial fuel jet velocity and d_o is the nozzle orifice diameter, μ_a is the viscosity of air (hence the term may not be reduced to the Reynolds number). The spray angle is assumed constant after jet break-up to droplets, Eqn.2.8 may be expressed with the velocity derived from Bernoulli ($v_B = \sqrt{2\Delta P/\rho_f}$)

$$\theta = \delta\left(\frac{\rho_f}{\rho_a}\right)^m \left(\sqrt{\frac{2\Delta P}{\rho_f}}\frac{d_o\rho_f}{\mu_a}\right)^n \tag{2.9}$$

δ, m and n are experimental constants (δ=0.00413, m=-1/4 and n=1/2) Then

$$\theta = 0.05\left(\frac{d_o^2\rho_a\Delta P}{\mu_a^2}\right)^{1/4} \tag{2.10}$$

The proposed expression is restricted in it's appropriateness due to the inclusion of only one nozzle parameter, d_o [142]. It has been shown that for the same diameter nozzle orifice, spray angles varying by a factor of two or three are possible by changes to the nozzle geometry. It is also suggested that the relationship to gas density is an important parameter but it is misguided to confuse this with gas pressure [142]. Experimentation has shown that, by changing the molecular weight of the inert ambient gas so as to keep the same pressure and temperature but with different densities, it is the density which is the important parameter. In a more complete presentation of the work Hiroyasu [98] shows the spray angle increasing with an increase in injection velocity to the point where it takes the maximum value and

then reaches an almost constant value in a compete spray region (atomization). The empirical equation for the spray angle when it reaches its constant value is expressed by (for sac hole nozzle)

$$\theta = 83.5 \left(\frac{L}{d_o}\right)^{-0.22} \left(\frac{d_o}{d_{sack}}\right)^{0.15} \left(\frac{\rho_a}{\rho_f}\right)^{0.26} \tag{2.11}$$

where d_{sack} is the sack chamber diameter of nozzle. In case of small L/d_o ratios cavitation structures do not collapse inside the orifice but enter the combustion chamber, collapse outside the nozzle and increase the spray cone angle. Large d_o/d_{sack} promotes the reduction of effective cross-sectional area at the entrance to the nozzle (vena contracta), reduces the static pressure and facilitates the inception of cavitation. The most influential parameter is the density ratio. The higher the gas density, the smaller the penetration and the more the fuel mass inside the combustion chamber is pushed aside by the new droplets. Another model presented in [80] based upon experimental work is in the form

$$tan\theta = A \left(\frac{\rho_a}{\rho_f}\right)^{0.33} \tag{2.12}$$

where A is an experimentally derived constant. In this model the spray angle is shown to be a function of the nozzle geometry and the ratio of liquid and gas densities (ρ_a/ρ_f), not the injection velocity (hence injection pressure). The breakup regime that the liquid jets are disintegrating under is not made clear, the injection pressures are 11.1MPa to 107.6MPa. The spray angle increases with an increase in the gas density (larger ρ_a/ρ_f), decreases with liquid viscosity and with the nozzle length to diameter ratio (L/d_o) for ratios greater than 10. Rounded inlet nozzles result in smaller spray angles than sharp edged inlet nozzles.

In the work [97], a review is conducted of the relationship between spray cone angle and the density ratio (ρ_a/ρ_f). The experimentation is conducted over a rather large range of ambient densities (maximum 196kg/m^3) which is much larger than most other experimental conditions. The reported dependence between the spray cone angle (refereed to as dispersion in the work) is $tan\ \theta \propto (\rho_a/\rho_f)^{0.19}$ with no significant influence from the injection pressure. An example of the data from this work is reproduced in Fig.2.13, showing the tangent of the cone angle with the density ratio. A logarithmic scale is used.

All of the findings and suggested models include a density ratio term and there is also one more thing that they have in common. The temporal development of the

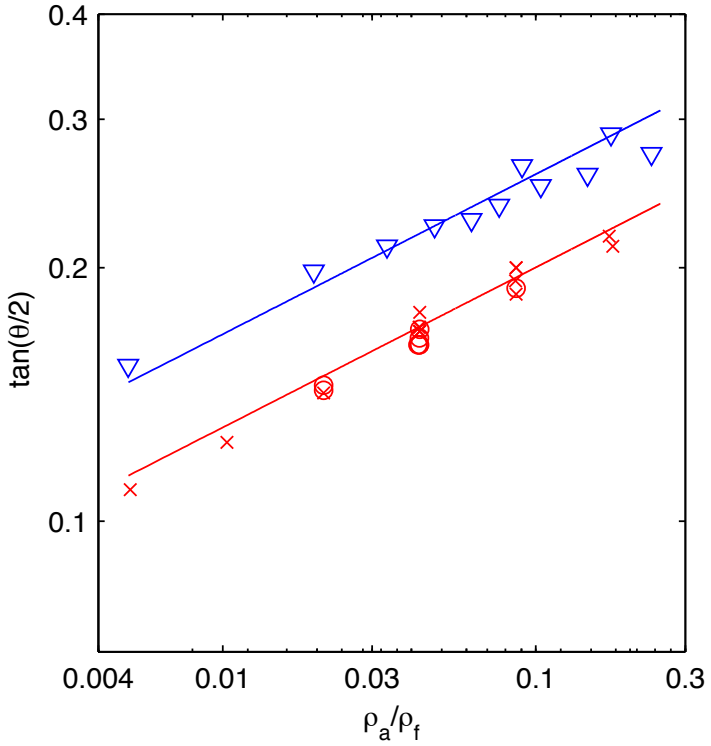

Figure 2.13: Spray cone angle with density ratio for non-evaporating sprays from [97]. The upper blue line is the power fit for the measurements with the nozzle with 340μm (triangle data points). The lower red line is the power fit for the measurements with the nozzle with 257 μm (cross data points) and with 198μm (circle data points).

full-cone spray is completely ignored. All of the measurements and the experimental fits to proposed models have been taken from the quasi-steady/constant period of spray-cone angle. Nabers and Siebers [97] recognized a transient trend with an "initial transient time" of approximately 500μs reaching θ values in the region of 20°. In previous works there are sometimes a graphical representation of the angle changing with time but there are no correlations and transition times discussed. Two works where the temporal development is graphically shown is [92] and [103] Figs.2.14 and 2.15 respectively. In the work [92], θ approached a constant value after approximately 400μs with θ of around 20°. The work [95] presents the spray cone angle vs time only after 600μs of injection after which θ was observed to become constant with a θ between 15-20°. A similar trend with comparable injection parameters is observed in [143] with a constant θ in the region of 20° reached after approximately 300μs. Ghurri et al [144] show a similar trend for Diesel fuel and bio-diesel with a decrease in θ from a maximum at SOI, however the constant value is not reached until much later at between 1000-1200μs with a θ value around 15°. Bougie et al [123] present θ for a comparable injections with a transient time around

150μs and a constant with a θ between 10-18°. Klien-Douwel et al [89] demonstrate a trend very close to the trend observed in this work with the θ value at SOI around 40° reducing to a constant approximately 30° at around 1000μs. Two pieces of work by the same authors [145, 146] show an apposing trend of θ starting with a smaller value and increasing to a constant value between 300-500μs depending on measuring technique employed.

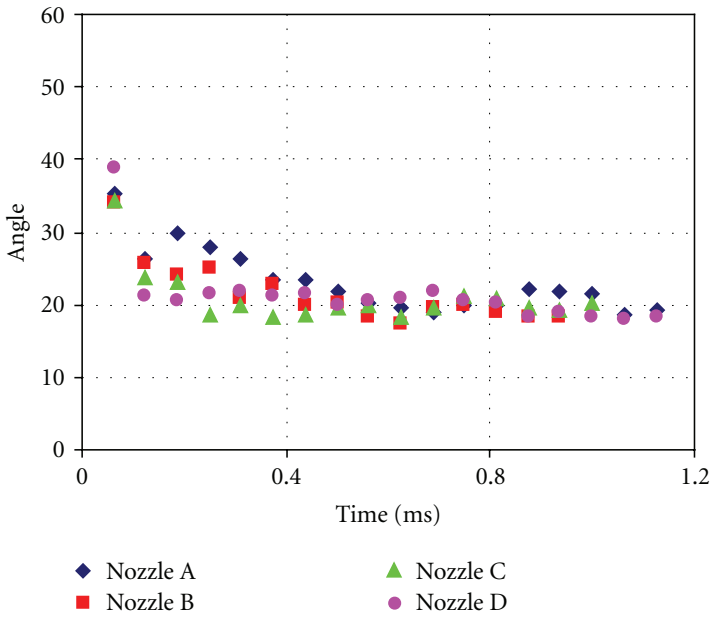

Figure 2.14: Spray cone angle variation with time of Diesel fuel sprays with four different nozzles used in the work [92].

The transient nature of the spray cone angle development is discussed in [81] with the injection divided into three phases. During the first phases, the needle opens. During this early phase, the small cross sectional flow area at the needle seat is the main throttle reducing the mass flow though the injector. Due to the low axial velocity and the strong radial velocity fluctuations (turbulence), the first spray angle near the nozzle is usually large. This effect is supported by the low momentum of the injected mass, resulting in an increasing amount of mass near the nozzle that is pushed aside by the subsequent droplets. As soon as the axial velocity increase, the resulting spray cone angle near the nozzle becomes smaller. Hence, the early spray structure depends on the speed of the needle: a very slow opening results in larger spray angles, a fast opening in smaller angles. Once the needle is fully unseated and the flow area at the needle is large than the nozzle orifices, the extent of cavitation now depends on the orifice geometry and will determine the spray angle. At the end of injection, needle closure will reuse the jet velocity, atomization breaks down,

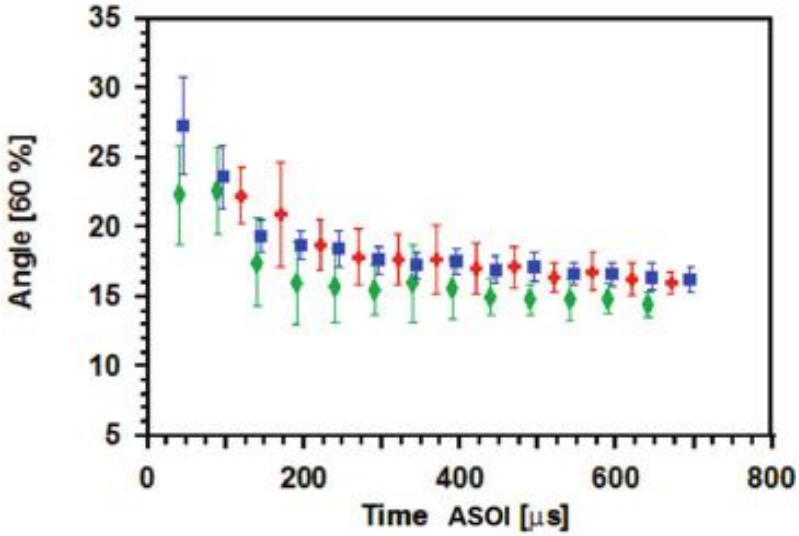

(b). Spray cone angle

Figure 2.15: Spray cone angle variation with time of Diesel fuel sprays with three different fuels, Diesel fuel, biodiesel and a blend used in [103]

droplets and ligaments form. In the work [97] this needle closure period is postulated as the cause of the small increase in spray angle at the end of injection (using a sac type injector).

The spray cone angle is most often measured at points on the spray boundary corresponding to a fixed a percentage of the tip penetration. As the injection progresses and tip penetration develops, the position where the angle is measured between also develops. There are a number of works where a near and far field measurement have been specified. In the works [146, 145] the near field measurement is taken at 60 times the diameter of the nozzle office along the spray central axis, the far field is taken at 100 times the diameter. At both measurement points, a simple tangent is made to the spray edges with their apex at the nozzle orifice. There findings were that in general, the near field angle is greater than the far field angle throughout the whole spray process. However they also found that the near and far field angles increased with increasing injection pressures, which is contrary to most other works. In the work [144], the near field was classified as 1/3 of the tip penetration and the far field 2/3 of the tip penetration. The authors note no real difference between the two measurements. For both sets of work, the angle measurement was made at two different points from the same images, there was no magnification of the near field region used compared to the far field measurement.

It should also be borne in mind that the angle measured depends on the experimental technique used. Images collected using Mie scattering record light in a small

solid angle, scattered by the liquid phase (typically observed at 90° or 180°). Shadowgraphy records the combined effects of scattering in all directions and attenuation. This may lead to Mie scattering results yielding a smaller apparent angle [89].

2.4.2 Spray Tip Penetration

The temporal development of the spray tip penetration into the combustion chamber has been examined for some time. A driving force behind this has been design considerations so as to avoid fuel impingement on chamber walls. The desire to achieve full air utilization in the chamber leads to a refusal to design for under penetration. Later the tip penetration was seen as critical in development of models to predict and simulate engine combustion and operation. Early works examining the correlations of injection parameters and tip penetration were brought together for the first time in the work [141] which drew largely on previous experimental findings integrated with theoretical jet theory. The findings in [141] suggest tip penetration dependence on injection parameters in the form:

$$S = 13.6 \left(\left(\frac{\Delta P}{\rho_g} \right)^{1/2} td \right)^{1/2} \left(\frac{530}{T_g} \right)^{1/4} \tag{2.13}$$

The most widely excepted findings and developed correlations come from the work [98] which is still used for comparison purposes in current work [92, 114, 121]. The findings are based on a large piece of experimental work with spray penetration determined from photographic recordings. Injection pressures were in the range <40MPa and ambient density 10 to 33kg/m^3. Two distinct periods of tip development are identified. An early stage of the spray development where $S \propto t$. After a short period of injection there is a transition after which $S \propto t^{1/2}$. The spray velocity during the early period is constant and spray develops a steady jet. The time where the relationship transitions is described as the breakup time which was shown to decrease with increasing injection pressure. The linear relationship in the early stage has been a staple of tip penetration models since. The proposed model is developed from a breakup length model using the following assumptions:

- The liquid jet density (ρ_f) is moving in a gas medium with a density $\rho_a \ll \rho_f$.
- The relative velocity between the liquid jet and the gas is large.
- The amplitude of the jet surface disturbance is accelerated by the pressure disturbance in the gas.

- As the amplitude of the jet increases, the jet tends to be unstable, and finally, the jet may break up into droplets.
- The breakup length (L), is calculated from the breakup time (t_{break}).

$$L \approx v t_{break} \approx \alpha \sqrt{\frac{\rho_f}{\rho_a}} d_o \tag{2.14}$$

  where α is an experimental constant and d_o is the nozzle orifice outer diameter.
- Jet velocity within the intact length is equal to the initial jet velocity.
- The spray tip velocity is proportional to $\sqrt{t}$ based on continuous jet theory

The jet velocity before any breakup is given by Bernoulli's equation in the form

$$v_B = \sqrt{\frac{2\Delta P}{\rho_f}} \tag{2.15}$$

with the inclusion of a corrective term, C_v. Though not specified in the work [142] this correction is clearly the velocity coefficient, C_v, which takes into account the loss in the velocity though an orifice [138]. The resulting expression is in the form

$$v = C_v \sqrt{\frac{2\Delta P}{\rho_f}} \tag{2.16}$$

The transient time from the start of injection to jet breakup is obtained from v and L

$$t_{break} = \frac{\alpha \rho_f d_o}{\sqrt{2 C_v^2 \rho_a \Delta P}} \tag{2.17}$$

The tip penetration is proportional to $\sqrt{t}$ after breakup to droplets, spray tip penetration can be expressed as

$$S = \beta \sqrt{t} \tag{2.18}$$

with β derived from the conditions $S{=}L$ and $t{=}t_{break}$

$$\beta = 2^{1/4} (\alpha C_v d_o)^{1/2} \left(\frac{\Delta P}{\rho_a} \right)^{1/4} \tag{2.19}$$

The values of the constant are determined using an experimental fit to the results in [98] with the values of: α= 15.8 and C_v=0.39. The result is the common Hiroyasu and Arai model that is so often used in the literature, given in the form

$$0 < t < t_{break} \quad S(t) = 0.39\sqrt{\frac{2\Delta P}{\rho_f}t} \tag{2.20}$$

$$t \geq t_{break} \quad S(t) = 2.95\left(\frac{\Delta P}{\rho_a}\right)^{\frac{1}{4}}\sqrt{d_0 t} \tag{2.21}$$

$$\text{where,} \quad t_{break} = \frac{29\rho_f d_o}{(\rho_a \Delta P)^{\frac{1}{2}}} \tag{2.22}$$

The discontinuity between the two periods has not always been excepted, though the the linear relationship during the early period has been. A short coming of the model from its inception was the reliance on only one nozzle geometric parameter (d_o) with no reference to the length to diameter ratio or inlet curvature. It was known at the time that for the same diameter, having a longer orifice length could produce a very intact jet whilst having a very short length results in a short or no intact length [142]. It is hard to approach any literature concerning the spray tip penetration and not encounter this model.

Nabers and Siebers [97] also found the early period linear relationship of tip penetration and time but the correlations at the much higher injection pressures and ambient densities used are not the same. Using a similar starting point as Hiroyasu, the authors develop a non-dimensionalized analysis that accounts for the effects of ambient gas density, fuel density and orifice parameters. Orifice parameters are included in the form of the velocity coefficient, C_v and the orifice area contraction coefficient, C_a to give $d_f = \sqrt{C_a}.d_o$. These are determined using a momentum flux measurement technique which is only briefly described in the work but is obviously of great importance and should probably have been subject to greater scrutiny. The resulting correlation/model is given in the form

$$0 < t < t_{break} \quad S(t) = C_v \sqrt{\frac{2\Delta P}{\rho_f} t} \tag{2.23}$$

$$t \geq t_{break} \quad S(t) = \sqrt{\frac{C_v \sqrt{2C_a}}{atan(\theta/2)}} \left(\frac{\Delta P}{\rho_a}\right)^{\frac{1}{4}} \sqrt{d_0 t} \tag{2.24}$$

$$\text{where,} \quad t_{break} = \frac{\sqrt{C_a/2}}{C_v atan\theta} \frac{\rho_f d_n}{(\rho_a \Delta P)^{\frac{1}{2}}} \tag{2.25}$$

where a is an experimentally fitted constant that related real measured full cone spray angles to angles in a jet model. One of the main difference between Hiroyasu and Arai [98] and Nabers and Siebers [97] is their respective descriptions of the transition times physical implications. While Hiroyasu and Arai [98] think that during the early period the spray is not fully atomized with the liquid vein not broken and the spray cone shape not developed which results it penetration with a constant velocity. Hence the transition time is the time where breakup occurs. It is unclear how this justification fits into atomization regime theory of the CI engine spray where breakup length (no intact core length) is assumed zero. Nabers and Siebers [97] described the transition time as the time where the spray is dominated by injected liquid to being dominated by entrained gas.

More recent work[93, 119] accept the the correlations of ΔP, outlet diameter,ϕ, ρ_a and time with the inclusion of the instantaneous momentum flux ($\dot{M}$ in a dimensional analysis). As with the Nabers and Siebers, momentum flux parameter (see Section.2.5) is included as it takes into account internal flow parameters such as contraction of flow cross sectional area and velocity coefficients. The model developed is based upon

$$S = k_p \left(tan\frac{\theta}{2}\right)^{-1/2} \rho_a^{-1/4} \dot{M}^{1/4} t \tag{2.26}$$

For the fully developed period of the spray (after t_{break}) where k_p is an experimentally derived constant. The initial linear portion of the spray tip development is modeled using

$$S = k_i v_{eff} t \tag{2.27}$$

The k_i term is an experimentally derived constant to take account of injector opening time. Whilst this seems to be an advance on the Hiroyasu and Nabers

method, it is essentially based on the same parametrical dimensional analysis with the addition of the momentum flux measurement for the experimental constant fitting.

The linearity of the initial stage has come into question in some recent studies, particularly with the adoption of increased temporal resolution measurement techniques. The work [89] uses a low frame rate of 4500 fps. In it the authors show that the tip penetration, determined from the first frame captured with spray present, should not be linearly back extrapolated to the origin of any plot as the velocity is not constant. They believe spray break-up has occurred before the first image is collected, which would make more sense when considering the atomization regime. Tip penetration after the early period till shows the $S \propto \sqrt{t}$ relationship.

The short comings of the linear period are also addressed in the work [121]. The authors state that the linearity of the tip penetration development in the initial stage does not make physical sense as the instant the injector opens the jet velocity must be zero. An infinitesimal period of time later a sharp rise in spray velocity must occur. The authors cite recent models which have revised the spray penetration during the early stages of injection but do not address the issue of zero velocity at time zero. The work studies the initial period of Diesel fuel sprays at injection pressure of 500 and 1000bar with ambient pressures of 1, 10 and 50 atmospheres. The work stresses the time resolved nature of the measurements and the high frames rates utilized (maximum of 500,000 fps).

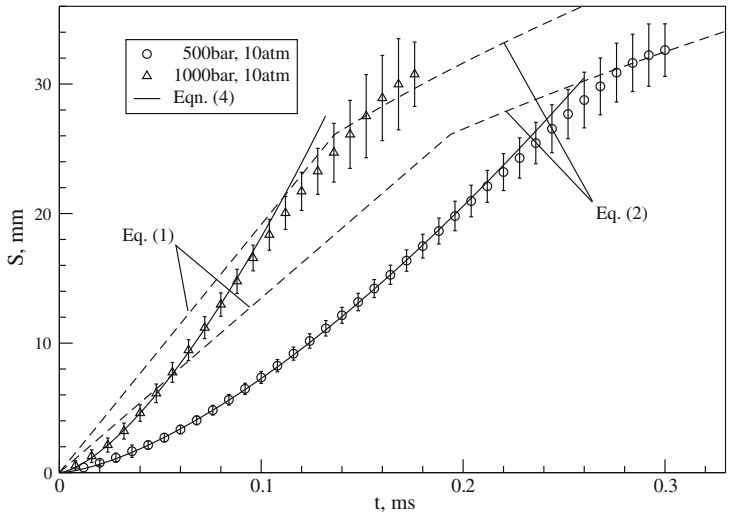

Figure 2.16: Initial Diesel fuel spray tip penetration. Collected at frame rate of 125,000fps, 500 bar inject pressure (circles), 1000 bar injection pressure (triangles with chamber pressure of 10 atmospheres. Results are compared with Hiroyasu model and model proposed by Kostas[121].

The authors results show poor agreement with the Hiroyasu model as shown in Fig2.16 where the dashed line labeled Eqn.1 is a plot of the Hiroyasu model at those conditions. A purely empirical relationship for the early stage injection is proposed of the form

$$S(t) = At^{3/2} \tag{2.28}$$

where A is an empirically fitted constant. No physical explanation is attempted to derive or explain the relationship. Upon differentiation the proposed model reduces to zero at t=0.

The work [92] builds upon the findings presented in [121]. Frame rates are much lower, at a maximum of 32,000 fps but their findings are in general agreement concerning the lack of linearity in the early injection period. An empirical relationship of injection parameters and the initial period to determine the values of A are presented in the form

$$S(t) = \left(\frac{\rho_f}{\rho_g}\right)^{0.25} \left(\frac{\rho_g^{1/3}\Delta P}{12\rho_f}\right)^{0.5} t^{3/2} \tag{2.29}$$

In the work [121] the penetration after the t_{break} is considered to be the the same as in the Hiroyasu model while [92] introduces a nozzle conicity term to take into account any cavitation effects in the form

$$S(t) = 2.95\left(\frac{\Delta P}{\rho_a}\right)^{0.25} \sqrt{(C_f)^z d_o t} for t \geq t_{break}, C_f = \frac{d_i}{d_o} \tag{2.30}$$

2.5 Hydraulic Characterization of Fuel Sprays

Some of the fundamental features of CI engine sprays have been introduced in Section.2.1. The characterization of the sprays by experimental observation has been detailed with attention paid to the so called "macroscopic" parameters, spray cone angle and tip penetration. Briefly mentioned in Section.2.4.2 is the application of dimensionless nozzle parameters: the velocity coefficient C_v and; contraction coefficient, C_a. In relation to these parameters the momentum flux parameter is introduced. The following will deal, in some detail with the theoretical rationale behind the dimensionless parameters and the momentum flux ($\dot{M}$), of a CI engine fuel spray. These will fall under the umbrella of hydraulic characterization of the spray, which will also include parameters such as the nozzle's mass flow m, the instantaneous mass flow rate $\dot{m}$ and discharge coefficient C_d.

2.5.1 Mass Flow rate and Instantaneous Mass Flow Rate

The most basic of hydraulic characterization of a fuel injector nozzle is the measurement of the fuel mass flow (m). The mass flow will state the total mass of fuel that flows through the nozzle for the duration of the injection event (t) the time that the needle is in the open position. Injection parameters will be: the pressure drop across the orifice, ΔP, which determines the flow velocity through the orifice, given by Bernoulli's theory (Eqn.2.15); the flow cross sectional area, A_{geo} where the subscript identifies the real geometrical cross section area and; the fuel density, ρ_f. The total mass flow is easily measured by injecting the fuel into a closed vessel and measuring the mass of fuel injected for a number of injections, from which the average mass of fuel for each injection is calculated. This method forms the basis of the simple tests to check injector operation in the real world, such as in an injector maintenance center. The mass flow may elucidate metering parameters and be useful for basic 1st law thermodynamic analysis but it is of limited use when considering temporal spray development.

The fuel injection rate or mass flow rate is crucial in gaining a more complete understanding of the spray and combustion process in a CI or a direct injection, gasoline, spark ignition (GDI) engine. The hydraulic behavior in terms of fuel metering accuracy and injection rate control capability is undoubtedly a key parameter in controlling the spray formation and evolution and hence combustion. With the advent of split injection protocol in CI engines, utilizing pre, main and post injections, accurate metering of extremely short injection periods is important [147].

The introduction of GDI injectors with nozzle orifice patterns designed to result in fuel sprays that interact with the moving air in different regions of the combustion chamber has lead to the requirement to have a detailed understanding of the fuel mass flow through each orifice. Not only does accurate fuel metering need to be addressed but the degree of charge stratification in the chamber may also be more accurately assessed. A number of methods are employed to measure the injection mass flow rate. An average mass flow rate m_{av} may be determined from the mass flow through the nozzle and the time duration of the injection. The instantaneous mass flow rate, $\dot{m}$, a time resolved measurement of the mass flow rate is much more useful. The two main methods used to measure $\dot{m}$ are based upon the Zeuch method and the Bosch method [115, 147, 148].

2.5.2 Bosch and Zeuch Methods

The Bosch method determines time resolved mass flow rate by measuring the pressure variation during an injection event. A pressure wave is generated by the injection of a volume of fuel into a length tubing containing a compressible fluid, usually Diesel fuel. The method is based upon the pressure velocity equation, which is valid for a single pressure wave in an instationary flow [149].

$$P = a\rho_f u \tag{2.31}$$

where P is the pressure, a is the speed of sound in the fluid, ρ_f is the liquid(fuel) density and u is the flow velocity. Combined with the continuity equation, the governing equation for the Bosch method is in the form

$$\frac{dq}{dt} = \frac{AP}{a\rho_f} \tag{2.32}$$

where q is the volume of fuel hence dq/dt is the volume flow rate and A is the cross sectional area of the tube. The apparatus consists of injector mount, pressure transducer, measuring tube, orifice, following tube and a check valve, see Fig.2.17. The injector mount positions the injector so as to allow an injection of fuel into the measuring tube and holds the pressure transducer. The injector issues an injection into the measuring tube which is filled with the compressible fluid. The pressure trace is rescaled to give instantaneous volume flow rate [150]. The length and diameter of the measuring tube depends on the size of the examined injector. It must be long enough to attenuate any noise from the reflected pressure wave at

the pressure transducer. Typical lengths of the measuring tube are in the range of 20m, with internal diameters in the range of 5mm. The adjustable orifice determines the portion of the reflected pressure wave. If the orifice is too large the majority of the pressure wave will enter the following tube creating a negative wave after reflection. In order to adjust the back pressure of the system, a variable check valve is mounted on the end of the following tube [149]. The integration of Eqn.2.32 produces q, the total injected volume. This may be checked against the measured volume that is discharged form the check valve to determine accuracy [151]. A number of commercially available systems based upon the Bosch technique have been used by researchers [102, 115, 143, 152]. With the Bosch technique it is common to see fluctuations in the measured rate due to pressure reflexes in the measuring tube[150] and its application to small "pre" injections may be difficult. The Bosch method relies and quite a large experimental set-up and one can imagine that when examining a number of fuels, changing the fluid in a 20m plus tube would be time consuming and cumbersome.

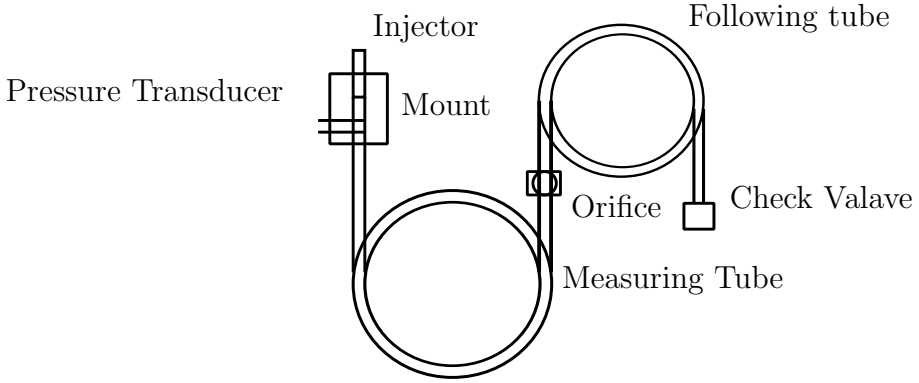

Figure 2.17: Schematic of a Bosch injection rate tube apparatus.

The Zeuch method records the pressure in a constant volume chamber during an injection event. Injection is conducted in a closed, fixed volume chamber filled with the injection fluid. The pressure in the chamber prior to injection is maintained at a constant level. During injection, a volume of fuel is injected (Δq) into the chamber resulting in a pressure rise. The pressure history in the chamber is used to determine the injection rate according to

$$\Delta P = \frac{k}{V}\Delta q \tag{2.33}$$

Where k is the bulk modulus of the fuel and V is the volume of the chamber [147]. The bulk modulus of the fuel is a function of pressure and temperature and is defined as the change in pressure due to a change in volume multiplied by the original volume. The bulk modulus is analogous to the modules of elasticity of

metals [151]. Its evaluation is critical to the measurement but is very complex due its dependents on fuel composition and is significantly effected by temperature and pressure [147].

Differentiating Eqn.2.33 results in the injection rate in the form,

$$\frac{dq}{dt} = \frac{V}{k}\frac{dP}{dt} \tag{2.34}$$

The mass flow rate may be determined using the fuel density in Eqn.2.34.

The compression in the chamber caused by the injected volume results in a change of temperature which changes the liquids bulk modules. For this reason the chamber's temperature is monitored throughout and the bulk modulus at the mean chamber temperature is used [151]. The schematic of a Zeuch chamber is shown in Fig.2.18. The solenoid relief valve is operated immediately after the injection to release the injected volume and maintain the baseline pressure in the chamber. The pressure increase in the chamber is recored using a piezo type transducer [149].

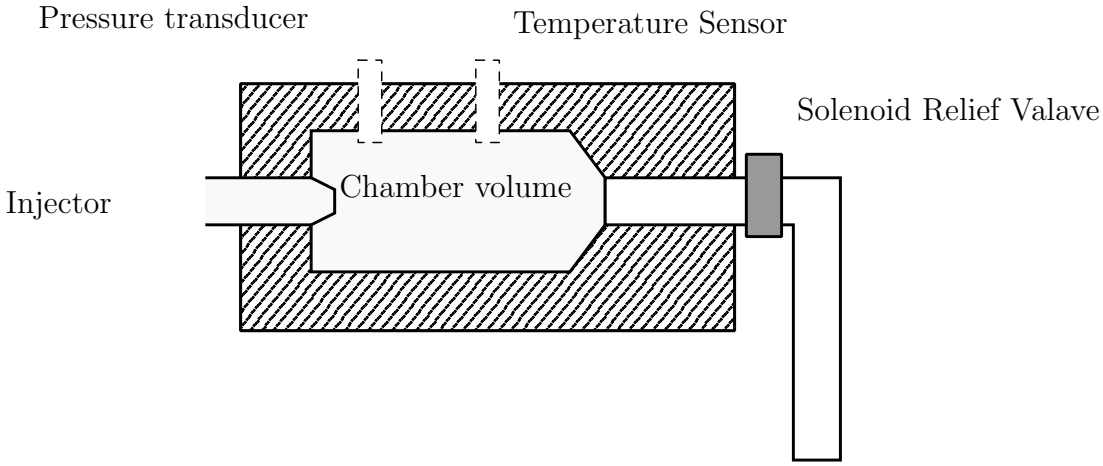

Figure 2.18: Schematic diagram of a Zeuch chamber.

The Zeuch method is more accurate but requires more complex signal processing [147] and accurate determination of the bulk modules [151]. Manufacture of the chamber must be to a high specification, as must control systems Timing of the solenoid relief valve but be accurate to maintain a high repetition rate of the measurement.

Two other methods have been proposed and tested by Marcic [153, 154]. A charge measuring method is introduced in [153] where the electrical charge created by friction of the fuel in the nozzle is deposited onto an electrode. The charge is amplified and converted to current which is scaled to give the mass flow rate. The method was compared with a Bosch tube and showed good matching [153]. The next method

[154] is similar to the Bosch and Zeuch due to its use of a pressure waves. In this work the pressure waves deform a membrane on the surface of a measuring volume. Strain gauges are used on the membrane in conjunction with a Wheatstone bridge and temperature compensation is implemented. There is no application of either these techniques in the literature. In the work [155] a mono injection qualifier was built and used. This mono injection qualifier system is based on the measurement of the displacement of a piston located in a closed chamber. During the injection event the spray impacts the piston, moving the piston downwards. Piston position is related to the volume of fuel injected, with the injection rate curve evaluated bases on the derivative of the instantaneous piston displacement [155].

2.5.3 Momentum Flux method

The final method of accurately measuring the fuel injection rate is that applied by Nabers and Siebers [97] which has been applied in some form in subsequent work [148, 150, 156, 157, 158, 159, 160]. The method relies on independently measuring the momentum flux of the fuel spray emanating from the nozzle orifice and the total mass of fuel injected during the injection event. Spray momentum flux is measured indirectly through the measurement of an impact force of the spray. This is achieved by placing a linear force transducer in front of the nozzle orifice, very close to the exit. With the transducers measuring surface normal to the spray central axis. The transducers sensing surface is a flat surface, refereed to as the target, which is orthogonal to the spray central axis. The control volume, CV, in Fig.2.19 is considered.

The spray target interaction is governed by the following momentum conservation equation

$$F = \frac{\partial}{\partial t} \int_{CV} \rho v dV + \int_{A} v^2 \rho dA \tag{2.35}$$

where v and ρ is the velocity and density in the control volume, dV is the volume differential, dA is differential area taken as a vector normal to the control surface of the control volume and F is the resultant force acting in the control volume. The first term on the right hand side is the rate of change of momentum stored in the control volume and the second term is the momentum flux through the control volume. The equation is considered along the the spray axis and simplified assuming [119, 161]:

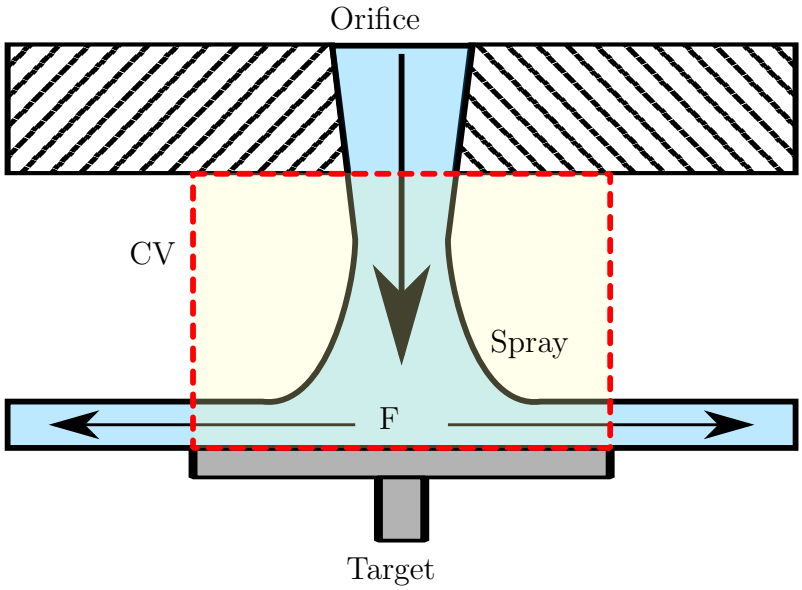

Figure 2.19: Conceptual control volume of fuel injection spray emerging from the injector nozzle and striking a target attached to a force transducer's measuring sensor.

- The liquid jet area exiting the orifice is equal to the geometrical orifice area, A_{geo}, and is considered differential area in Eqn.2.35.
- Negligible effects due to gravity
- There is negligible mass of fluid in the control volume that is accelerating which makes the first term of Eqn.2.35 zero.
- Spray deviation at the target face is orthogonal to the spray central axis so has no axial velocity component
- Negligible air entrainment, hence the density is the density of the liquid ρ_f which is constant.
- The liquid jet exiting the orifice has a uniform velocity v_{eff}, (effective velocity).

The resultant force F experienced by the transducer target is given by the second term of Eqn.2.35 with the axial velocity of the liquid jet v_{eff}.The force equates to the injected momentum flux at the orifice exit, $F = \dot{M}$. The interaction experienced by the target is now expressed in the form

$$\dot{M} = \rho_f A_{geo} v_{eff}^2 \tag{2.36}$$

From Eq.2.36, we see that the velocity of liquid jet, v_{eff} is proportional to the root of the momentum flux, $v_{eff} \propto \sqrt{\dot{M}}$. The instantaneous mass flow rate $\dot{m}$ is

given by

$$\dot{m} = \rho_f A_{geo} v_{eff} \tag{2.37}$$

It follows that the instantaneous mass flow rate is proportional to the square root of the momentum flux $\dot{m} =\propto \sqrt{\dot{M}}$. Naber and Siebers [97] suggest that the relationship between the instantaneous mass flow rate and the momentum flux can be determined by normalizing the square root of the transducers output by the area under the curve for the square root of the output. The normalization results in a profile proportional the injection velocity which when multiplied by the total mass per injection event gives the instantaneous mass flow rate. The normalization is conducted using Eqns.2.36 and 2.37 to give the mass flow rate in the form [159]

$$\dot{m} = \sqrt{\dot{M}\rho_f A_{geo}} \tag{2.38}$$

with the total mass injected during the injection event given by

$$m = \int_0^t \dot{m}.dt = \int_0^t \sqrt{\dot{M}\rho_f A_{geo}}.dt \tag{2.39}$$

to give the instantaneous mass flow rate by

$$\dot{m} = \frac{\sqrt{\dot{M}\rho_f A_{geo}}}{\int_0^t \sqrt{\dot{M}\rho_f A_{geo}}.dt} m = \frac{\sqrt{\dot{M}}}{\int_0^t \sqrt{\dot{M}}.dt} m \tag{2.40}$$

Fuel density and orifice area drop out of the normalization and the instantaneous mass flow rate may be determined using the momentum flux (the transducer output) and the total mass of fuel injected during the injection event. The total mass injected can be independently measured by collecting the injected fuel in a container and weighing the mass from a number of injections.

The work [97, 157, 159] used this methodology as outlined above with [157] taking the measurements while the injector was still installed in an optical engine with a custom in-cylinder transducer bracket. This demonstrates one of this methods advantages over the other methods reviewed here, with the measurement being able to be made in situ. The work [158, 160, 156] use a similar method but the instantaneous mass flow rate has been calculated using the fuel density and geometrical area of the orifice.

The method relies on the interaction between the liquid jet, entrained air and the transducer target within the control volume. The size of the target and the distance that the target is from the orifice exit will determine the volume of the control volume, the amount of air entrained in particular may make the removal of the first term in Eqn.2.35 unwise. The work [161, 162] paid particular attention to this and was concerned with the transient measurement of the momentum flux and the null assumption of the first term of Eqn.2.35 along with the assumption that the second term consists entirely of injected fuel with zero air entrainment. An experimental and CFD study found that for the transient, short duration injections, as is the case in real world short injection periods, a small target, close to the orifice is most suitable. Target sizes considered were 7.5, 10, 15, and 20mm with orifice to target distances of 10, 15 and 20mm The authors state that the target must be large enough to capture all the spray but not greater; at the same time it must be small to allow a good temporal fidelity, but not smaller [162].

Other target sizes and distance previously employed are: 5mm target, 4.5mm distance [150]; 10mm for both [160]; 6.35mm target, 2mm distance [159]; 5mm target (no target size stated) [119] ; 0.5, 1 and 2mm distances (no target size stated) [158] and 1 to 9.5mm distance [148]. The work [158] found very little difference in the momentum flux measured in the distance range used but examination of their figures suggest the lower value of 0.5mm may have provided the better result.

The momentum flux measurement in itself has been shown to be useful in characterizing fuel sprays, not just as a measurement to be made to determine the instantaneous mass flow rate [99, 103, 161, 162, 163, 164]. Sprays from GDI injectors may also be analyzed in terms of momentum flux, applied to the entire spray or following a local approach, by which the momentum flux distribution inside the spray structure (e.g. along a planar surface orthogonal to the spray axis) is measured [164].

2.5.4 Orifice Coefficients

The hydraulic character of a nozzle orifice under varying conditions may be described with a number of dimensionless numbers. These numbers are usually in the form of a ratio . The discharge coefficient is defined as the ratio of the actual mass flow rate through an orifice to the theoretical mass flow through the orifice, for the same fluid and same pressure drop. It may be thought of as the efficiency of the nozzle (on a mass flow basis) which characterizes the mass flux through the orifice. It is an important parameter to describe the flow through an orifice [152]. The theoretical

mass flow rate through an orifice may be determined using Bernoulli's equation between the inlet (P_1) and the outlet (P_2) to give the theoretical velocity for a given pressure drop (ΔP);

$$v_B = \sqrt{\frac{2\Delta P}{\rho_f}} \tag{2.41}$$

The theoretical velocity, v_B can be used in place of v_{eff} in Eqn.2.37,to determine the theoretical mass flow rate. The geometric area, A_{geo}, is still used [99]. The discharge coefficient is given by;

$$C_d = \frac{\dot{m}}{\dot{m}_{th}} = \frac{\dot{m}}{A_{geo}\rho_f v_B} = \frac{\dot{m}}{A_{geo}\sqrt{\rho_f 2\Delta P}} \tag{2.42}$$

The discharge coefficient may be divided into two parts. The flow velocity may be reduced from the theoretical maximum, v_B to the an effective velocity, v_{eff} due to friction, boundary layer effects and turbulence in the orifice. This reduction in velocity is accounted for by the velocity coefficient, C_v defined as the ratio of the effective velocity to the theatrical maximum;

$$C_v = \frac{v_{eff}}{v_B} \tag{2.43}$$

and applied as;

$$v_{eff} = C_v\sqrt{\frac{2\Delta P}{\rho_f}} \tag{2.44}$$

The second part of the discharge coefficient is accounted for by the area contraction coefficient, C_a. The area contraction coefficient accounts for flow area losses as a result of vapor bubbles generated by cavitation [97, 85, 94], non-uniform velocity profiles at the outlet section hole and changes in density [119]. The area contraction coefficient is most often defined as ratio of the effective area of the flow as it exits the orifice, A_{eff} to the geometric area of the nozzle orifice, A_{geo}[163, 162, 119]

$$C_a = \frac{A_{eff}}{A_{geo}} \tag{2.45}$$

In the work [85] an area coefficient is described that has two possible meanings;

the area is equal to the geometrical section and the generation of vapor has reduced the density or; the vapor density is neglected with respect to the liquid one and the area coefficient is taking into account the section which the liquid is occupying from the outlet section. The area coefficient in [85] is given as

$$C_a = \frac{A\rho}{A_{geo}\rho_f} \tag{2.46}$$

where A and ρ are not well defined but is assumed to be a real area and a real density. This is included to draw attention to the fact that the effective area and effective velocity being used here are not real values but are themselves approximations based on a simplified flow situation in the nozzle orifice that for the purpose of calculation and elucidation of the character of a highly complex flow are valid. The simplification employed is visualized in Fig.2.20 which forms the theoretical basis of the usage of A_{eff} and v_{eff}.

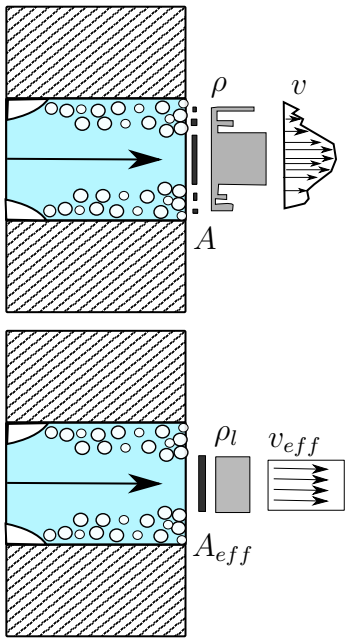

Figure 2.20: Conceptual basis of the effective flow of high reassure fuel though the injector orifice. The cross sectional area of the liquid phase of the flow is reduced from the geometrical cross sectional area of the nozzle to an effective area, A_{geo} by gas phase. The velocity profile across the cross sectional area is not constant but may be modeled as a smaller, effective velocity which is [119].

The discharge coefficient is a product of the velocity coefficient and the area contraction coefficient given by

$$C_d = C_v C_a \tag{2.47}$$

There are a number of works applying momentum flux measurements to examine C_d, C_v and C_a of nozzles. Nabers and Siebers [97] used the measurement to determine mass flow rate and the orifice coefficients for their study of Diesel fuel spray dispersion and penetration. In the work [103] the momentum flux measurement were coupled with optical work as in [97] to aid the development of empirical fits for the fuel spray tip penetration, which included the momentum of the spray for biodiesel and Diesel blends. The work [99] is similar with the momentum flux applied to gasoline in a common rail system. It is interesting that in both [99, 103] separate mass rate measurements were taken in a Bosch tube without applying the Nabers and Siebers technique, The work [161, 162, 163, 164] use a momentum flux measuring device to examine Diesel fuel sprays. In [162, 161] the method is evaluated against CFD for validation while in [163, 164] a new, localized momentum flux device is used. These works are all by the same author group and as with other studies, the mass flow rate is measured separately in a Zeuch chamber of their own design [147] to examine the orifice coefficients.

There are a number of papers that have used the momentum flux to calculate the discharge coefficient directly. This would obviously be quite advantageous as the discharge coefficient could be determined from quite a basic measurement. A number of works have applied the momentum flux, with the continuity equations [148, 156, 158] and end up with the discharge coefficient in the form

$$C_d = \left(\frac{F(t)}{2A_{geo}\Delta P} \right)^{1/2} \tag{2.48}$$

where $F(t)$ is the transducer output and ΔP is the pressure drop across the orifice. Critically, this form of the discharge coefficient is derived from the understanding that it is due only to velocity effects and is therefore equal to what has previously been defined as the velocity coefficient C_v. This is a form of the discharge coefficient that has also been observed in other work [90, 160]. This is not entirely wise when considering the degree of cavitation or other effects that may be reducing the area section of the flow as it exits the orifice.

It is cavitation that is examined using the momentum flux measurement in the work [85, 119, 138, 165]. In these studies the cavitation number is introduced (Sec.2.1.3). The cavitation number appears in the literature in a number of forms [166] but is usually based upon the pressure difference across the injector orifice [94]. A common form is that based on the work of Nurick [85, 94, 166, 167, 168] defining the cavitation number as

$$K = \frac{P_{inj} - P_v}{P_{inj} - P_{amb}} = \frac{P_{inj} - P_v}{\Delta P} \tag{2.49}$$

This form of the cavitation number differs from Eqn.2.5.

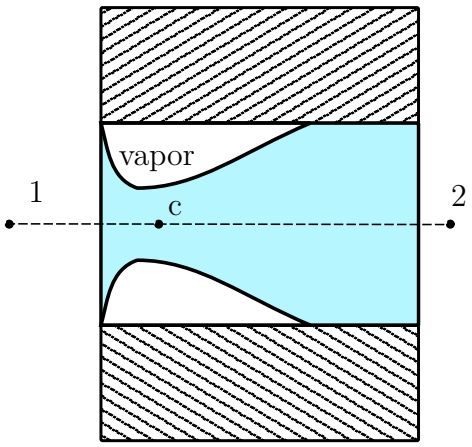

Figure 2.21: Conceptual diagram of a cavitating flow through an injector nozzle orifice. Fuel is flowing from the high pressure region in the injector at position 1 to the lower pressure region outside of the nozzle at position 2. The cavitating flow results in a constriction of the flow at position C[169].

At the onset of cavitation the discharge coefficient decreases. In previous works the vapor pressure has been omitted due to its extremely small size compared with the other pressures [119]. This is demonstrated in [94, 119] where the vapor pressure is 0.08MPa. A cavitating flow through an orifice will reduce the area cross section, Fig2.21, reducing the discharge coefficient. To simplify any analysis the vapor region is teated as a fixed, slip boundary which occupies a fixed fraction of the orifice section. This is most likely to occur at the throat, near the inlet to the orifice as this is where the liquid undergoes its largest direction and hence velocity change as it enters the orifice. This has been seen to be a good approximation in [138]. The area of the liquid flow at this contraction is termed A_c. A dimensionless parameter to denote the contraction at that point, the contraction coefficient C_c is given

$$A_c = C_c A_{geo} \tag{2.50}$$

It is assumed there is no radial velocity, the liquid density is constant and there is no mass transfer between the phases [169], the mass flow rate through the constriction, $\dot{m}_f$ is given by;

$$\dot{m}_f = \rho_f A_c v_c \tag{2.51}$$

where v_c is the velocity through the constriction. Applying Bernoulli's through the constriction between point 1 and c, since the cross section of the orifice at point c has both liquid and vapor phases, we assume that the pressure at point c is equal to the vapor pressure, P_v;

$$P_1 = P_v + {}^1\!/_2 \rho_f v_c^2 \tag{2.52}$$

combining Eqns.2.50, 2.51 and 2.52 the mass flow rate through the nozzle;

$$\dot{m}_f = A_{geo} C_c \sqrt{2\rho_f (P_1 - P_v)} \tag{2.53}$$

The mass flow rate of the cavitating flow in Eqn.2.53 is independent of the downstream pressure so the flow may be considered to be choked [169] and the term mass flow choked may be applied [138]. The discharge coefficient of the cavitating orifice is given by

$$C_d = C_c \sqrt{\frac{P_1 - P_v}{P_1 - P_2}} \tag{2.54}$$

so the discharge coefficient becomes proportional to the square root of the cavitation parameter and is expressed as

$$C_d = C_c \sqrt{K} \tag{2.55}$$

K increases as injection pressure decreases or back pressure increases; with an increase in K there is a moment where the cavitation will disappear and the discharge coefficient will become constant, this is termed K_{crit}. For values above K_{crit} the flow will be pure liquid phase and will be dependent on the Reynolds number [85]. The plot of the measured discharge coefficient using the momentum flux and the square root of the cavitation number is used to examine the cavitation of a nozzle and identify the injection pressure or fluid conditions where cavitation initiates [94, 119, 156, 170]. Fig.2.22 shows an idealized scheme of such a plot with the K_{crit} identified while Fig.2.23 shows an example plot from a previous experiment [85].

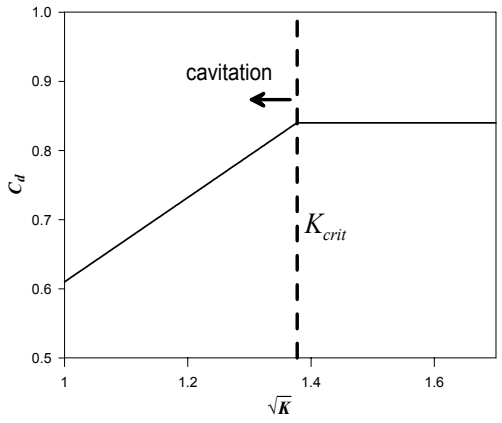

Figure 2.22: Idealize plot of the nozzle discharge coefficient variation with the square root of the cavitation number K. K_{crit} shows the cavitation number where the nozzle has started to cavitate as the injection pressure has been increased. At lower pressures the flow though the nozzle is pure liquid, once the cavitation injection pressure has been reached, the flow is a mixture of liquid and vapor phase with any further increases in injection pressure leading to further reductions in the nozzle discharge coefficient[85].

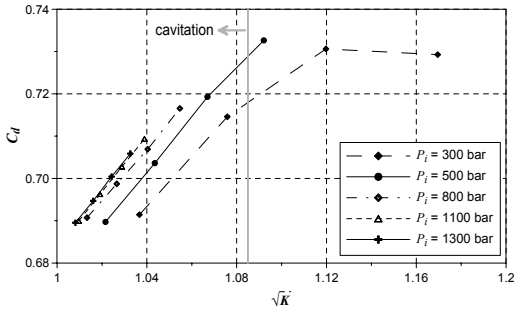

Figure 2.23: Experimental data used to produce a real plot of discharge coefficient with the square root of the cavitation number. The range of cavitation numbers has been achieved through adjustment of the injection pressure and the back pressure of the chamber into which the injection was taking place.The critical cavitation number may be identified for the once condition in the plot with circles and the broken line [85].

2.6 Summary

Fuel injection sprays as they exist in a CI engine have been introduced. Fundamentals of their structure and formation have been examined with how the spray may be characterized. Spray cone angle and spray tip penetration have been identified as are measurements that have been made optically and have proved useful in characterizing sprays of Diesel fuel and some alternative fuels. The optical techniques employed have been considered. The findings of previous works have been discussed with some empirical models presented. From the extensive review of the literature, there is very little evidence of optical spray measurements of this sort being conducted with Diesel fuel and water emulsions. The impact of emulsification on fuel spray cone angle and spray tip penetration has rarely been considered.

The alternative methodology of fuel spray characterization using hydraulic features including mass flow and fuel spray momentum have been introduced. A number of methodologies used to determine mass flow rate have been introduced. The

momentum flux principle has been introduced and discussed with reference to previous examples of it's use in the literature. The application of the method to examine the nozzle discharge coefficient and cavitation has been examined. There are no example in the literature of such a characterization method being applied to diesel and water emulsions.

3. Experimental Methods

Introduction

In the following section, all experimental methods are introduced. The collection of data required the design and construction of a number pieces of equipment which have been brought together to form a compete injection characterization rig. The details of their design and construction are outlined. All spray optical characterization experiments in this study have been conducted using an in-house designed and constructed high pressure chamber with optical access. Fuel injection has been achieved with the use of a novel fuel injection system, utilizing a range of original manufacture and research equipment. Optical measurements have been made using high speed video photography coupled with an in-house designed and constructed schlieren/shadowgraph system. The illumination source and control has been designed and optimized to the spray studies performed in this work.

All hydraulic optical characterization experiments in this study have been conducted using a custom designed and constructed momentum flux device installed into the high pressure chamber. The fuel injection used the same system as the optical measurements.

Data acquisition and experimental control has been achieved with a custom LabView program tailored to each experiment. Data processing has been accomplished with a combination of Matlab code coupled with Microsoft Excel. Diesel and water emulsions examined have been produced according to a protocol developed during testing and subjected to a number of tests prior to any spray studies were conducted. Once constructed the experimental equipment has been commissioned and optimized through a stringent and extensive optimization procedure to ensure high precision of data retrieved.

Additional, preliminary combustion studies of a diesel fuel and water emulsion have also been conducted in an in house designed and constructed optical combustion

chamber. This utilized a modified version of the injection system and a specialized data acquisition system.

3.1 High Pressure Chamber design

The high pressure chamber in which the fuel sprays were initiated and observed has been designed and constructed at QMUL. The chamber consists of a main cylindrical section which was formed from a cast cylindrical section of 304 stainless steel with two flanges at each end. The casting was machined to form a cylindrical section 131mm in length, internal diameter 138mm, flange outer diameter 210mm and wall thickness of 16mm. Three orthogonal holes were machined into the mid-section of this part with a diameter of 63mm to form the optical access. These dimensions were calculated as sufficient to observe the main portion of the spray under investigation assuming that at full extension, the spray would be a maximum of 90mm long. A compromise was made so that the maximum observable length of spray was in the region of 60mm. The internal dimensions ensured that there would be no spray/wall interaction. At this stage basic calculations were conducted based upon cylindrical pressure vessels with flat ends, to ensure that the target pressure of 40bar was within safety limits of the chamber.

Sapphire windows of 82mm diameter and 10mm thickness were used to provide the optical access into the chamber. These windows sat in saddles which were welded into position on the outer surface of the section aligned with the optical access holes. The windows were clamped into position with an outer ring which were secured using twelve 6mm high tensile bolts. The design of the clamps and saddle were such that different thickness windows could be secured in place as there were a set of quartz alternatives available with a 25mm thickness.

Particular care and attention was given to ensuring that the injector would be suitably positioned in the chamber that would make maximum use of the optical access that was available, ensuring that the spray would extend across the diameter of the window.

The optical diagnostics chosen were a schlieren/shadowgraph system and a diffused backlit system. For both systems it was necessary for the spray to emerge into the chamber central volume with optical access either side of the spray, hence the need for the two of the windows to be opposite each other. The third window was added should the chamber later be used for any laser sheet or Mie scattering tests. The injector was a seven hole, piezo actuated Siemens mini-sac type.Details of the

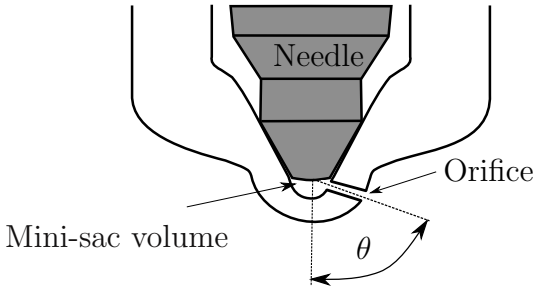

Figure 3.1: Schematic cut away diagram of a mini-sac type fuel injector. θ is the spray central axis referenced from the injector body central axis.

injector are in Table.3.1.

Table 3.1: Injector details

Injector	Siemens Piezo Lynx
Injection pressure range	25-160MPa
Number of holes	7
Cone angle	152°
Hole diameter	120μm
Type	Mini-sac

The nozzle holes were known to form an angle in the range of 152° but this angle is not symmetrical around the central axis of the injector nozzle, precise details of the hole angles relative the central axis were unknown. Due to the arrangement of the nozzle holes, it was necessary to block all but one hole to allow single spray examination. To complete the design of the chamber and ensure the injector would be in the correct position, accurate details of the nozzle hole angles were required so as to use the best hole for placement in the chamber and to ensure any injector clamping system held the injector in the correct position relative to the windows. The required geometrical knowledge of the injector and the basic form of the mini-sac nozzle is shown in Fig.3.1.

3.1.1 Injector Geometry

The injector nozzle hole geometry was determined using a silicone molding technique similar to that developed by Macian et al [171]. The technique has been used extensively in previous studies [92, 119, 152, 170]. Polyvinylsiloxane, a dental impression material was utilized to make molds of the internal geometry of the nozzle. The silicone consists of two pastes, a base and a catalyst, which are stored separately in two tubes which fit into a caulking gun. The pastes are mixed in a central tube

which attaches to the two tubes and is pumped into the geometry which the mold is being taken from. The two pastes, once mixed, cure to form a highly elastic, high tear strength dimensionally stable silicone rubber. Before curing the two pastes have excellent flow properties and will easily flow, under small amounts of pressure into the hole of the injector nozzle.

The silicone was introduced into the internal geometry of the injector using a small aluminum tube which was machined so as to accept the end of the caulking mixing tube at one end and to fit into the central hole of the nozzle (which would usually hold the needle) at the other. The aluminum tube was sealed into the nozzle with a small amount of PTFE tape. On curing the aluminum tube allowed extraction of the mold without any breakage of the mold. For the purpose of the molding, an old injector nozzle was used which was soaked in toluene for a number of days, cleaned with compressed air and dried in an oven to ensure the internal geometry was clean. Fig.3.2 shows the nozzle, aluminum applicator/extractor and an example mold while Fig.3.3 shows an example of the molding extractor in use.

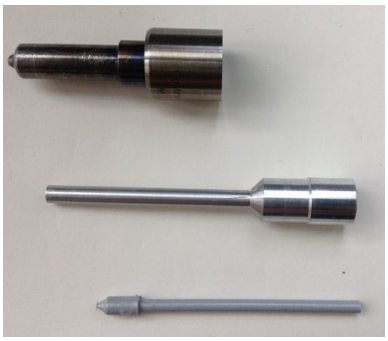

Figure 3.2: Photograph of the injector nozzle tip (top), the aluminum tube used to fill and extinct the silicone from the nozzle (middle) and an example silicone mold (bottom).

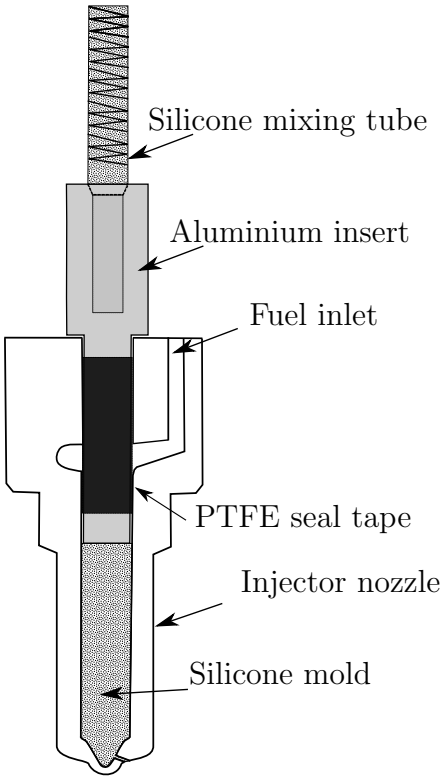

Figure 3.3: Schematic cut away diagram of the molding technique.

Once the mold had been extracted it was photographed using a scanning electron microscope (SEM). For this purpose the sample was required to be electrically conductive This was achieved by depositing a gold coating on the silicone mold. This gold coating does not interfere with any measurements as its thickness is of the order of 0.01μm. The mold was then photographed in the SEM and these photographs were used to determine angles and diameters of the nozzle hole geometry.

The hole which formed the largest angle with the central axis of the injector was chosen as the hole to be left unblocked. This would result in a spray traversing across the diameter of the optical access ports. The holes to be blocked were laser welded using a jewelers welding rig with the holes blocked up from the outside to avoid any alteration to the internal geometry of the min-sac and needle seat. The modified nozzle complete with welds is shown in Fig.3.4.

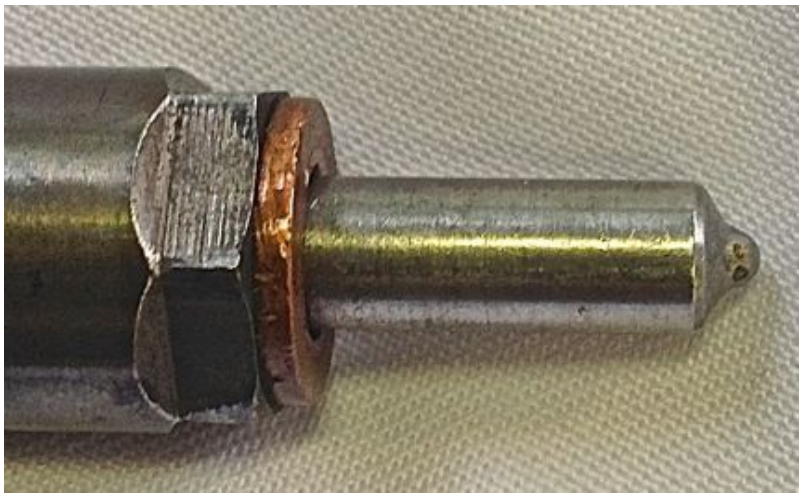

Figure 3.4: Photgraph of the modifies injector nozzle. The holes that have been welded are visible on the tip as small back dots.

Once the nozzle had been welded, the silicone molds were taken again to provide a check that the internal geometry of the injector has not been altered. Precise measurements of the hole were then take. Fig.3.5 shows the SEM photographs obtained complete with measurements made using the image software, ImageJ.

3.1.2 Injector positioning

Once the injector geometry was known, the method to be used to position the injector into the chamber could be designed and produced. As the chamber was intended to be used at ambient temperatures only, no cooling system was required which greatly simplified the design. The clamping system was designed so as to allow

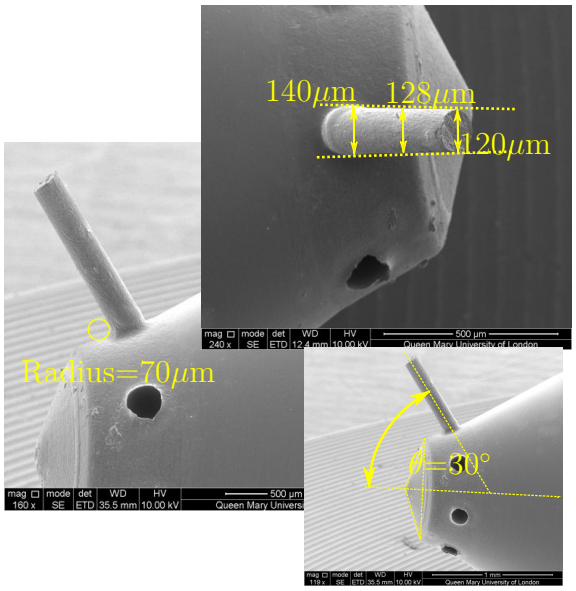

Figure 3.5: SEM images of the silicone mold of the injector nozzle after all but one hole had been welded. The welded holes are visible as black circles. The yellow text shows the sizes and angles as determined using ImageJ.

injector rotation in the chamber. This was required as to achieve alignment with the camera image plane and to allow the spray to be positioned in a different orientation for subsequent momentum experiments in the chamber. Of critical importance at this time was the positioning of the injector at the correct depth into the chamber so as to ensure that the spray traversed across the optical port diameter. The injector clamping system was produced out of carbon steel and secured the injector in position in the chamber end plates, also made of carbon steel. Fig.3.6 shows a CAD drawing with the position of the spray from the single hole relative to the optical window and the expected spray profile across the window diameter.

The centre window port/saddle was blanked off using a stainless steel blank and was used as the base of the chamber. An optical bread board was used to secure the chamber at this base and allowed the optical system to be accurately aligned around the chamber. The injector was aligned in the chamber so as to ensure the centre of the spray axis was parallel with the camera image plane. This was achieved using the camera positioned along the central axis of the chamber with the bottom removed and a software grid overlaid on the image. A high degree of illumination was use at this point to allow the unblocked hole to be imaged, injector rotated into position and then clamped down firmly.

A positioning hole was drilled in the clamping system that allowed the injector to repositioned should dismantling be necessary. Full C.A.D drawings of the chamber are presented in App.A along with a stress analysis, conducted using Autodesk

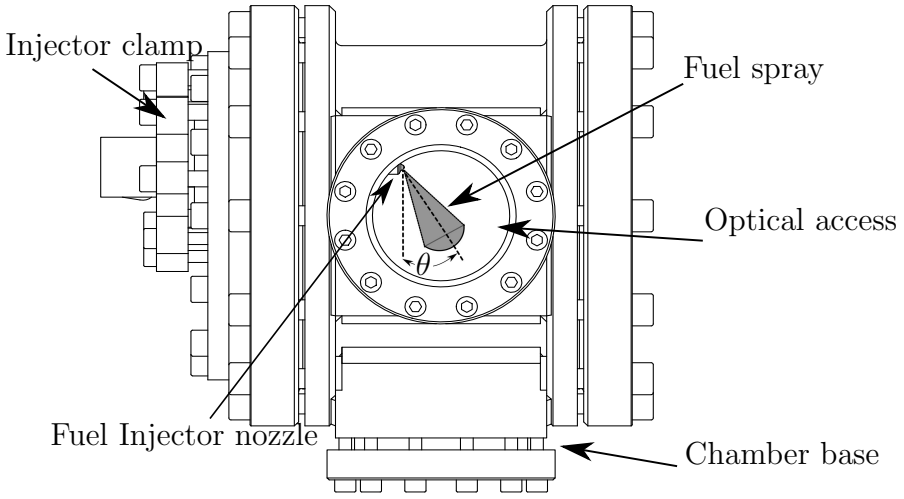

Figure 3.6: Side view CAD drawing of the chamber with the injector secured in place in the chamber using the clamp. The spray central axis, determined using the silicone mold has been used to show that the fuel spray will traverse across the window diameter.

Inventor (2013) (Fig.A.10). The chamber was found to have a safety factor of 3.04 at 40bar pressure (ambient temperature).

3.1.3 Injection System

Fuel injection was by means of a high pressure common rail system. The injector was connected to the original manufacturer common rail to the connections that during unmodified use would be the rail fuel inlet. The rail has four injector ports, two of which were blanked with the remaining two used as the high pressure inlet from the fuel pump. The rail was fitted with a piezo force transducer. For all conditions in this study, the common rail pressure measured by the pressure transducer fitted in the rail was taken to be the injection pressure. The high pressure pump was a double ended hydraulic type (Sprague P4333), driven by compressed air capable of supplying fuel to the rail at up to 200MPa . The outlet pressure was controlled via the compressed air inlet pressure, once this was set at the regulator, no adjustment or control was required to maintain the outlet pressure.

The injector was controlled by the Hartridge HK853 driver which was triggered from a TTL signal controlled from a custom LabView program. The high pressure fuel outlet from the rail which connects to the injector was positioned in-line with the rail along the central axis of the chamber and injector so as to allow rotation of the injector in its mounting. The common rail was mounted to the optical bread board via a support strut which resulted in a strong and rigid high pressure fuel

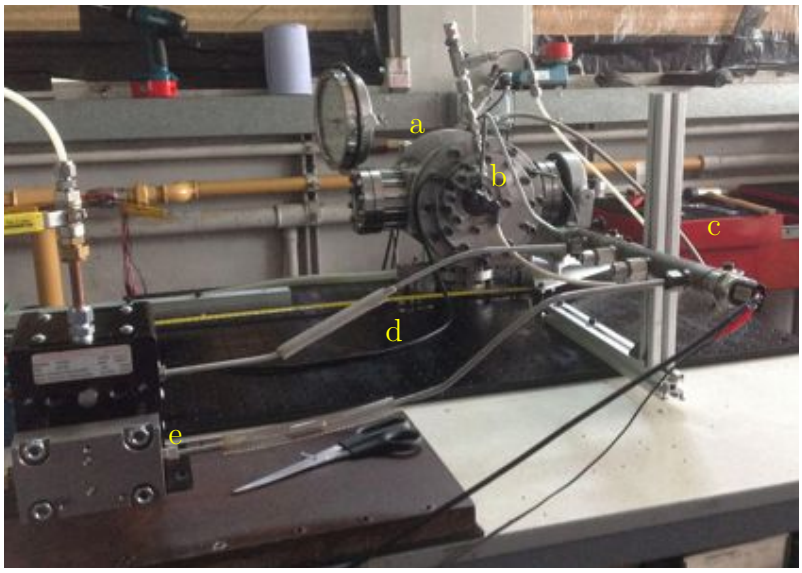

Figure 3.7: The high pressure injection equipment coupled to the injector mounted in the high pressure chamber. a.) High Pressure Chamber. b.) Fuel Injector. c.) Common Rail. d.) High Pressure fuel lines. e.) High Pressure pump.

delivery system being established. The high pressure pump was seated on a heavy steel plater on a rubber mat. This went some way to insulate the chamber from any pump vibrations. The nature of the pump operation results in a lower cycle frequency which further helped to reduced vibration in the system.

3.2 Optical Arrangement

3.2.1 Schlieren/Shadowgraph System

The first sets of data were collected utilizing focused shadowgraph images. The system was originally designed to operate in schlieren mode as well as shadowgraph mode with the addition of a knife-edge in front of the camera lens. All data in this study was collected with the shadowgraph system hence the knife edge was not included. The system was of the double pass single mirror type. The mirror was a spherical, concave 101mm (4 inch) diameter with focal length of 1219mm (48 inches) ($f/12$) mounted into a positioning mechanism. The mirror was placed as close as possible to the back window of the chamber.

The point light source was placed a distance of two focal lengths from the centre of the mirror. The light source is discussed in detail in Sec.3.3. An aluminum square section, 25mm by 25mm was used as an optical rail for positioning the light source.

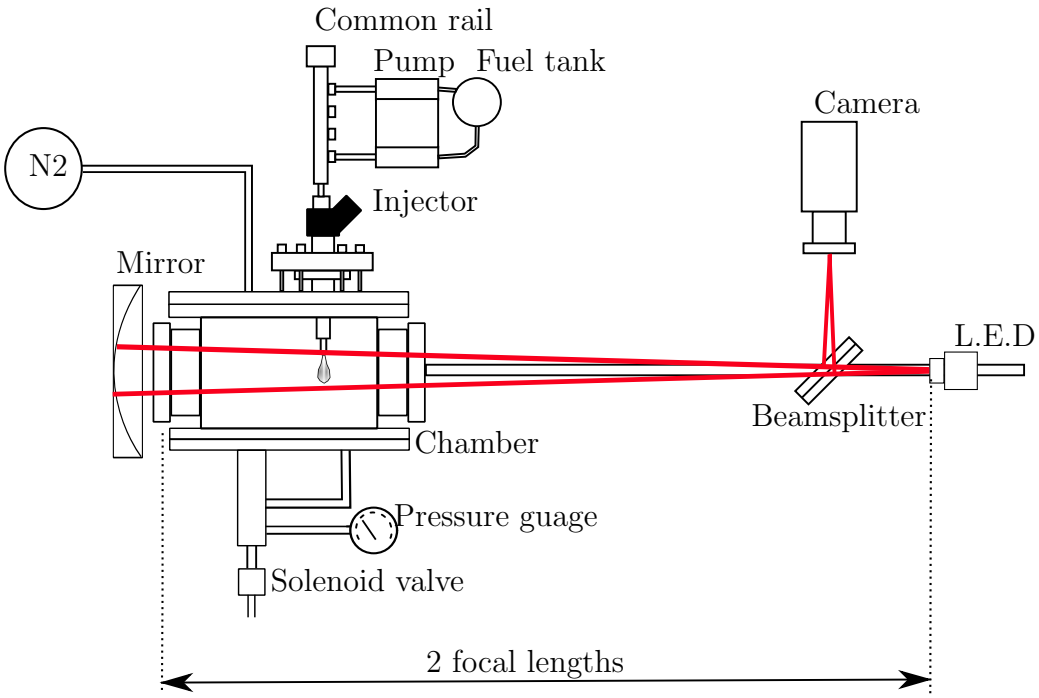

Figure 3.8: Schematic of the focused shadowgraph system used with the high pressure chamber.

The aluminum section was attached to the optical bread board at the chamber end and attached to a work bench at the light source end. Alignment of the rail was achieved with the aid of a laser alignment tool. The diverging beam of the point source passes through the chamber test region, fills the mirror and returns along the coincident path, forming a source image upon the light source itself. The test region was directly in front of the mirror where the path of the light from the point source was diverging, as well as in the converging light path as it was reflected from the mirror. Ideally each point in the test region was traversed twice by the same ray, which acquires the deflection angle (ϵ) once on each pass. Since ϵ was small and the distance between the test section and the mirror was short, this actually does work in practice, yielding the advantage of twice the sensitivity of a single pass system. Operation of the light source in a low current, continuous mode was utilized to fine adjust the system. The mirror mechanism allowed fine tuning of the mirror position until the reflected light source image was observed to enter the pin hole forming the point source.

The light returning from the mirror was diverted into the camera lens by a 50/50 beamsplitter (Edmund Optics) which was mounted onto the optical rail at a distance of 2133m (84 inches) from the mirror. The converging light was reflected 90° by the beamsplitter and focuses at a distance of 300mm (12 inches) from the beam splitter. The camera was positioned with the lens at a distance of approximately

51mm (2 inches) from this focal point with the central axis of the camera 90° to the optical rail. The camera was mounted onto an adjustable mounting which allowed fine tuning motion to be achieved in a vertical and a horizontal plane. After some experimentation with the arrangement, the ideal lens was found to be an Olympus 200mm lens with aperture set to $f/11$. The camera used was a Phantom v7.11 coupled with its proprietary software. To capture the full length of the sprays as they traverse across the optical region, the camera was operated with a resolution of 256 by 256 (pixels). Maximum frame rate at this resolution was 30,075 frames per second. Due to the experimentation being conducted under non-vaporizing conditions and no combustion present, the addition of the knife edge to form schlieren images was found to be unnecessary and resulted in a less intense image due to the removal of much of the light entering the camera. This was a particular concern due to the loss of light from reflection off the chamber windows, which were traversed four times by the light, and loss at the beamsplitter which was traversed by the light twice. A schematic of the system is shown in Fig3.8.

3.2.2 Backlit Diffuse system

The second set of data were collected using a backlit illumination system. This system was developed for a number of reasons.

- There was a desire to test the LED system at a higher frame rate.
- There was a desire to examine the sprays using a higher magnification.
- There was a desire to examine the sprays during the very initial, near field region of the spray.

The backlit system utilized the same light source as the shadowgraph system (see Section.3.3) but was positioned on the other side of the chamber, secured to the optical bread board with the pin hole removed to form an extended light source. A sheet of ground Bauxite glass was placed between the light source and the chamber window to act as an optical diffuser. The camera was positioned with its central axis coincident with the the central axis of the light source passing through the chamber test region. Fine tuning of the camera's position was achieved with the same mounting used in the shadowgraph system which was attached to the optical bread board. A schematic of the system is shown in Fig.3.9.

The camera was attached to the 200mm lens. The illumination source provided a near homogenous illumination region that extended to a distance of approximately

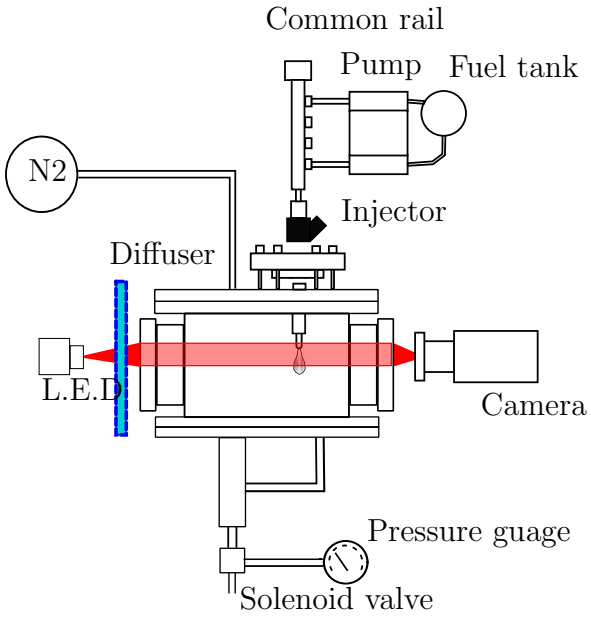

Figure 3.9: Schematic of the diffused backlit system used with the high pressure chamber.

15mm from the nozzle orifice. The aperture of the lens was set to $f/8$. This setting was found to result in spray shadows with well defined edges. This size of the measurement region was found to reduce due to window fouling by previously injected fuel during spray experiments. The fouling formed in the lower portion of the optical region, away from the nozzle. The maximum length of spray from the nozzle orifice that could be imaged with any degree of repeatability throughout an experimental condition was 10mm. This effectively limits the measurement to this region, hence the camera resolution could be reduced to 128 by 128 (pixels) which allowed the camera to be operated at 88,888 frames per second. The backlit image collected was similar to that of the shadowgraph system in that the spray image was actually a shadow. However, a distinction is drawn between the two images by the fact that the shadowgraph system uses a concave spherical mirror to collimate the light (to a certain degree). The backlit system useed an extended source with highly divergent rays and the image formed is not considered a true shadowgraph/shadowgram. Due to the short penetration from the nozzle which was observed and the proximity of the observation region to the nozzle this measurement is termed a near field measurement.

3.3 L.E.D illumination system

In order to achieve suitable images at the frame rate desired a high intensity light source was required. This is because of the short exposure time required, at 30,000

fps, maximum exposure time is approximately 30μs. This length of exposure was still too long to freeze the spray to produce sprays with very well defined edges and tips. Exposure times in the region of 1 to 10μs were found to be ideal for this purpose. To achieve such high intensity at such short exposure times, most continuous sources may be rejected. Non-continuous, pulsed light sources offer the benefit of reducing the total exposure time during each frame. With very short duration light emission pulses the exposure time was effectively independent of the shutter time of the camera, as long as its duration was longer than that of the pulse and timed such that the sensor was exposed for the entire pulse duration. Light sources that have been used previously in pulsed form are spark gap/arc lamps, usually xenon flash lamps; pulsed lasers and light emitting diodes (LED) [172]. In deciding what kind of system to use for this study, system cost and availability were very important. A cost comparison was conducted by [172] that shown the L.E.D option to be approximately a third of the price of a comparable xenon system and one ninth of the cost of a laser diode system. Other considerations concerning the use of laser system were the extensive time and cost penalties of laboratory safety feature installation. Although lasers have high intensity, short pulse duration emissions, they are highly coherent with a very narrow wavelength range which causes speckle artifacts in any collected images. Xenon lamps do not require such safety measures but are noted for the large amounts of heat generated during use. It was decided to make use of a pulsed overdriven LED system based upon the work in [172, 173, 174, 175, 176, 177].

3.3.1 Design Considerations

The basic idea of the LED system was to utilize a high power LED and operate it in a pulsed mode of very short duration pulses with a current much larger than the LED has been designed to operate at. The use of LEDs in this manner offer a number of advantages (as discussed in the works [173, 174, 175, 176, 177].

- Much lower cost compared to pulsed laser system and lower than a high intensity discharge (HID) system.
- No safety issues
- Incoherent, wider range emission removes speckle effects.
- Stable pulse to pulse intensity
- Overdriven, short pulse operation results in considerable increase in light emission

- Very short, almost instantaneous rise time in response to current pulse

The camera used in the experiment here was a Phantom 7.3. When considering which LED to use, the response of the camera was taken into account.. Fig3.10 shows the camera response curve, supplied by Vision Research [178] for the camera. The solid black line shows the response in amperes of current produced per watt of light falling on the sensor. The broken lines show the quantum efficiency(QE) of the sensor. The solid red and green lines are the emission wavelengths of a red and green LED that were under consideration for use. Both green and red LEDs are of the CBT-40 range (Luminous Phatlight, [179]). The camera exhibits a similar response for the two LED wavelengths (red approximately 0.15 A/W, green approximately 0.128 A/W), with both on the 30% QE line. The illumination source for the schlieren/shadowgraph system must be in the form of a point source hence the direction of the light emitted from the surface of the LED was also considered. The Luminus Phatlight range of LEDs, originally developed for projector use and used in previous works [172, 173, 174, 176, 177] was ideally suited because of its high power and its flat emitting surface, hence the light is emitted in a smaller radiance pattern than from a traditional dome shaped emitting surface.

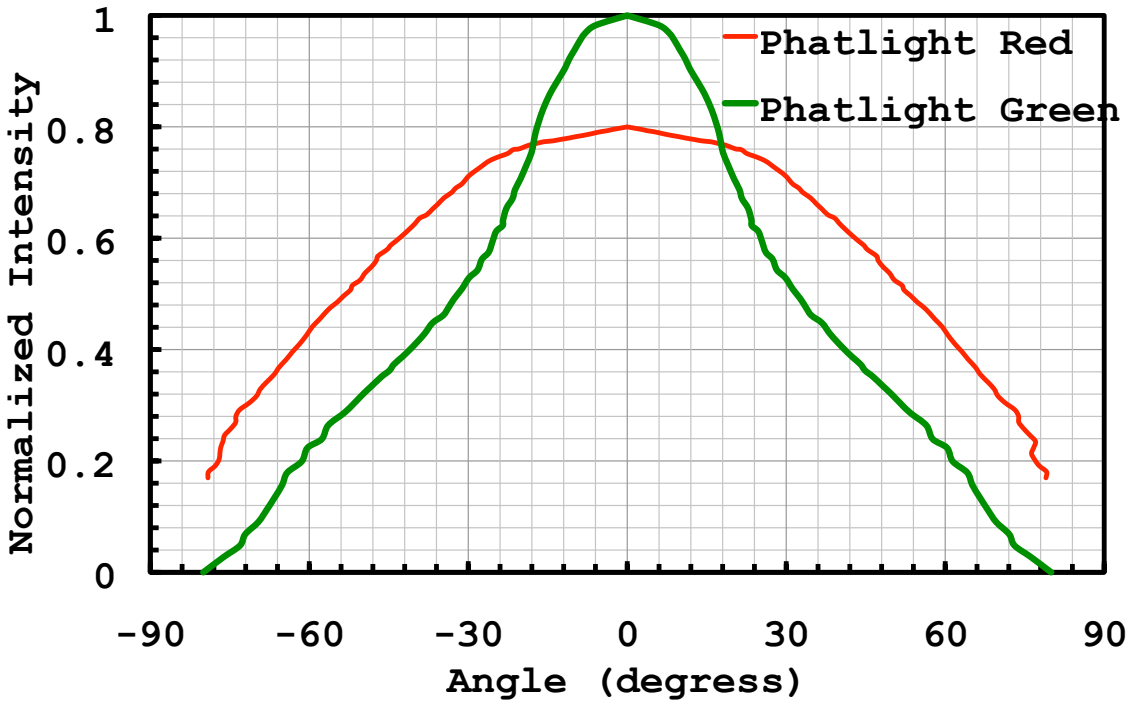

Figure 3.11: Angular emission of CBT-40 Luminus Phlatlight LEDs (from [179]. Intensity of the emission has been normalized to the green LED.

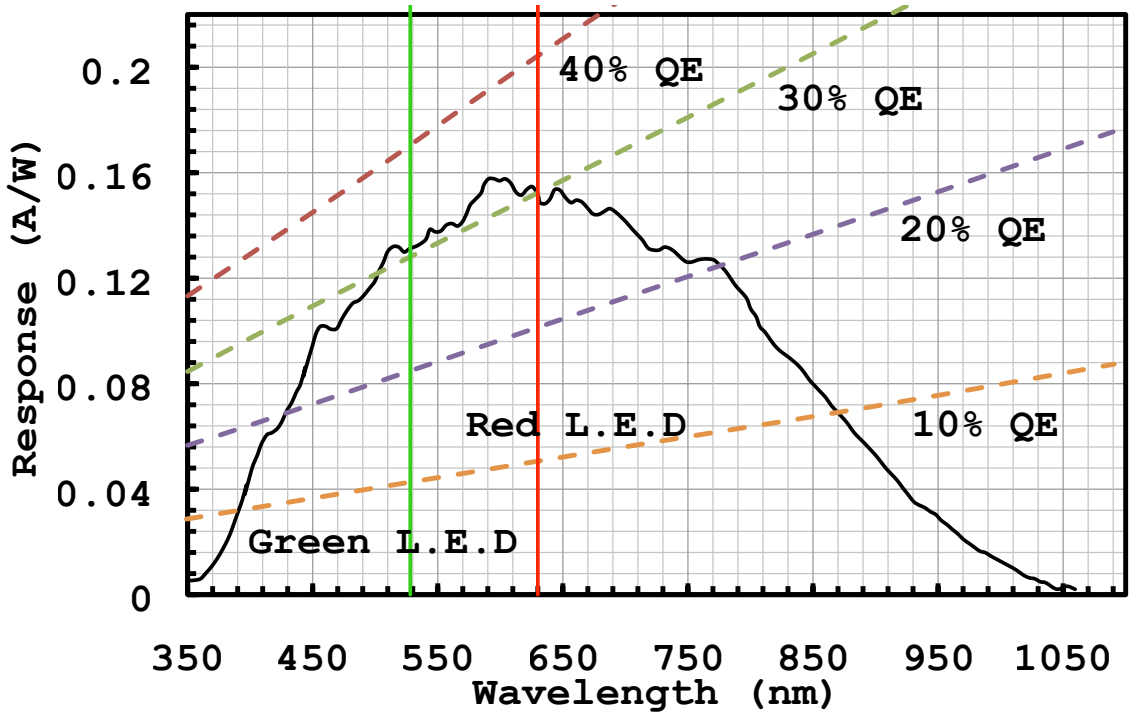

Figure 3.10: Camera sensor response to the wavelength of light impinging on it sensor surface in amps/watt. Broken lines show the quantum efficiency of the camera with wavelength. The solid green and red line show the wavelength of the two CBT-40 Luminous Phatlight LEDs considered for use

.

The specifications state a radiometric flux of 1.9W (9.8A pulsed operation) for the green LED while the red provides about one fifth more with 2.3W. The red LED emits its light across a wider angle, its emission pattern was more divergent compared with the green. Fig.3.11 shows the emission divergence for the two LEDs (normalized) [179]. Along the central axis, the red LED emits approximately 20% less light compared with the green, for a small aperture schlieren/shadowgraph configuration the two LEDs would provide almost the same amount of light. The green LED was chosen considering that the radiance pattern suggested a higher degree of collimation from the point source and the advise in previous work [177].

The high current, short duration pulse of the LED was achieved with the design and construction of a drive circuit. Signal generation for the timing of the drive circuit was handled by a LabView program on the data acquisition PC. Details of the circuit are shown in App.B along with the mounting system used to provide the point light source.

3.4 System Completion

The high pressure chamber was completed with the construction of the injector clamping system which consisted of a recessed seat into which the injector was inserted. Sealing was achieved with a copper washer, the same as was used when the injector was installed into an engine. The chamber sealing at the windows, top and bottom plate and clamping system was done with gaskets constructed from a graphite material (Klinger-TopGraph 2000). This material was chosen as it was hoped that in the future the chamber could be used at higher temperature and there were also concerns about the durability of standard nitrile seals when exposed to bio-diesel. Chamber construction was completed with the addition of a safety release valve, set to open at 35bar. Chamber pressure was monitored using a pressure transducer (Omegadyne) inserted into the chamber bases, connected to the data acquisition. The ambient temperature in the chamber was measured with a K-type thermocouple placed very near to the injector tip through the chamber top plate. Chamber charging was handled by a precision gas regulator attached to a nitrogen cylinder. All injections were conducted in this inert nitrogen atmosphere. Gas handling was by a high pressure flexible line on the entrance and solid stainless line on the exit. The exit line consisted of a needle valve for flow rate control, a liquid trap and a coil in an ice bucket before venting into the atmosphere.

During testing window fouling was a major issue. In previous works [102, 103, 119] this had been addressed by having a constant flow of nitrogen at very low flow rate

through the chamber. The flow rates used were considered too low and of a low enough velocity not to interfere with spray development. This was attempted but the shadowgraph system was very sensitive to any density gradient in the chamber and the flow was generally visible. This would add complexity to any image post processing so was best avoided. At the very low flow rates that were acceptable in terms of the images collected, the window fouling issue was not resolved. There were also concerns about the high level of gas consumption that this would entail. For preliminary testing the needle valve on the chamber gas exit line was used to control gas flow rate. The issue was resolved with the installation of a high pressure solenoid valve (Alcon, Pmax 60bar). The solenoid valve was placed upstream of the needle valve and was operated via a relay by the LabView control software. Once an injection was complete, the solenoid valve was opened for a short period, in the region of 2-3 seconds to allow the fuel spray cloud to be purged from the chamber. This method was found to work well to avoid window fouling during the data collection.

All triggers were handled by a custom LabView program. Camera trigger and injection trigger coincided utilizing the same TTL output. Solenoid time of opening and duration were controlled relative to the end of injection. The camera recording and settings were handled by its own dedicated computer. The LED TTL control was handled by the LabView on a dedicated output, with the period and the pulse controllable to match that of the camera frame rate and exposure time. Fine tuning of camera and LED syncing was possible by inducing a small delay in the camera from the trigger to account for any discrepancies between the LabView clock and the camera clock and any lag induced in the system. Chamber pressure, rail pressure and chamber temperature were recorded using the LabView. The complete shadowgraph system is shown in Fig.3.12

3.5 Momentum Flux Measurement Device

A momentum flux measurement device was designed to meet the requirements outlined by the theory introduced in Section.2.5.3. The initial portion of the design was reliant on the injection system and the conditions that the experiments would be collected at. The fuel injection system used was the same as that used in the previous experiments, detailed in Section.3.1.3. All injections took place in the high pressure chamber as detailed in Section.3.1. The spray emerging from the nozzle orifice was required to impact onto a surface orthogonal to the the spray central

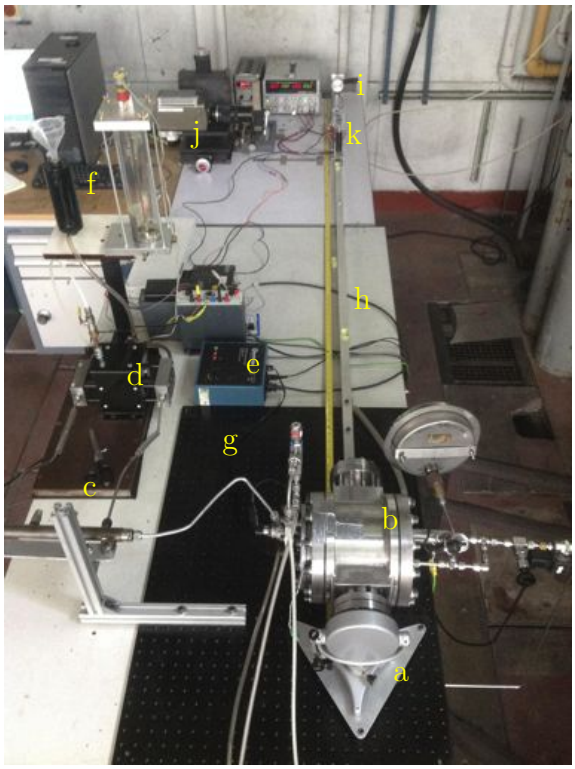

Figure 3.12: A photograph of the optical system in shadowgraph configuration. Component labels are in Table.3.2

Table 3.2: Components of the shadowgraphy system in Fig3.12

Key	Component
a	Spherical Schlieren mirror
b	Chamber
c	Common Rail
d	High Pressure Pump
e	Injector driver
f	Fuel tanks
g	Optical bread-board
h	Optical rail
i	LED
j	Camera
k	Beamsplitter

axis. The central axis relative to the nozzle body central axis was well defined due to the silicone mold measurements taken, detailed in Section.3.1.1.

A piezoelectric force transducer/sensor was required to measure the spray impact force. Previous studies have utilized a range of force or pressure transducers. The transducer was to have a range of at least 0 to 10 N. The short time scale of the measurement required a devise with a rise time of the order of several microseconds ($<10\mu$s). The short time scale and the oscillatory nature of the measurement required a device with a high natural frequency of at least 50kHz [157]. The transducer sensing face which is impacted by the high pressure fuel jet needed to be resistant to physical and chemical erosion. The Kistler model 9215 force transducer was chosen for this study and has been used in previous work including [157, 159, 161, 162, 163, 164]. The force transducer is a pre-loaded, piezoelectric force transducer used for measuring quasi-static and dynamic forces from -20 to 200N (tension and compression) with the ability to measure loads as small as 1mN and a natural frequency in excess of 50kHz. The transducer design consists of the sensor body with on outer thread for mounting. The face of the transducer consists of a 2mm threaded bore to accept a screw. It is this screw which introduced the force into the transducer's sensing component. In original form this screw's head is

dome shape. This screw was replaced with a a stainless steel screw with the head machined to a smooth surface, 4mm in diameter. This screw was the spray target and is referred to as the target from here. Full transducer details are included in Appendix.C.

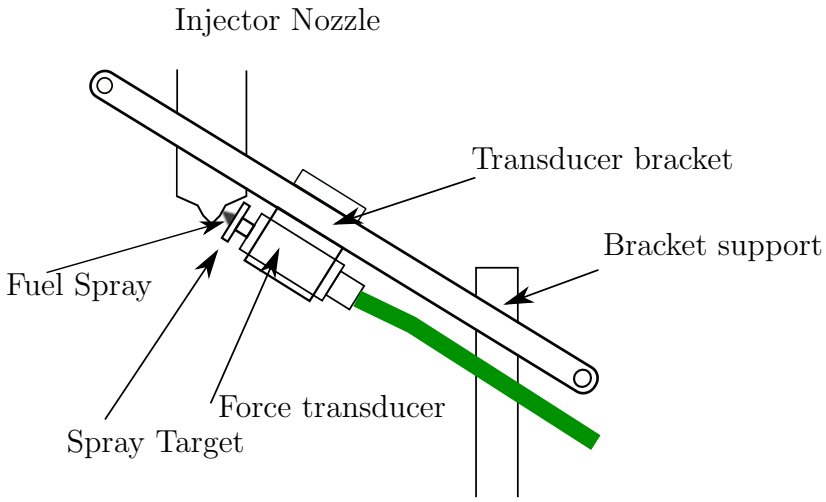

Figure 3.13: Schematic diagram of the force transducer fitted with the target presented to an emerging spray.

The transducer target was positioned in front of the nozzle orifice by an aluminum bracket attached to a supporting bar which in turn was attached to the base of the high pressure chamber. A schematic of the transducer in the bracket with a fuel spray emanating from the nozzle and striking the target is shown in Fig.3.13. To align the injector into the correct position, the injector sat in a lower position in the high pressure chamber compared with the position used in the optical measurements. This meant that the spray was not optically accessible during here measurements. Fig.3.14 is a cut-away CAD drawing showing the transducer presented to the nozzle orifice. Fig.3.15 is included to show the transducer bracket in the high pressure chamber. Here the chamber bottom plate is removed to allow access into the chamber.

The bracket design allowed the transducer target distance from the nozzle to be adjusted. For all tests here the distance was kept to a minimum. Due to nozzle geometry this was found to be 0.5mm. The distance was measured using a feeler gauge which was used to position the target at this distance. The alignment of the transducer was accomplished using the high speed camera and the 200mm lens set-up with the chamber bottom plate removed, as in Fig.3.15. The grid overlay option was used (camera software option) with high illumination in the chamber to align the nozzle orifice with the transducer target. Once fixed in position the transducer and bracket were not moved in any way during the data collection period. Good

alignment was desired and strived for but small deviations in the angle away from perfect alignment are inevitable. This error will be small as the measured force is proportional to $\cos(\Delta\theta)$ where θ is the deviation away from perfect alignment, for small angles, $\cos\theta$ is approximately 1.

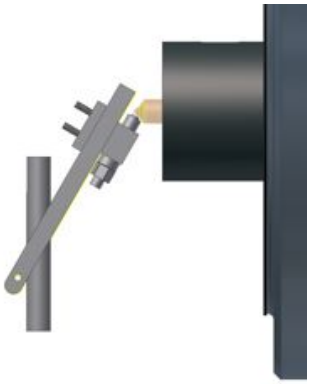

Figure 3.14: CAD drawing of the bracket holding the force transducer as it was in the high pressure chamber.

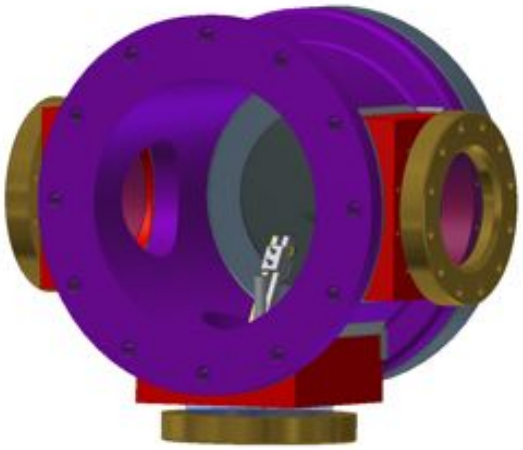

Figure 3.15: CAD diagram of the force transducer held the bracket, in position in the high pressure chamber. Chamber bottom plate removed.

The signal from the transducer was amplified by a Kistler 5007 charge amplifier. The voltage output signal from the charge amplifier was acquired at a frequency of 100kHz by a 6024E DAQ card (National Instruments). The injection trigger was handled by the custom LabView program which also handled the data acquisition. The data recorded consisted of a voltage the voltage signal which was linearly proportional to the force exerted on the target by the spray. Data recording started with the injection TTL trigger which was sent to the Hartrigde driver (introduced in Section.3.1.3). Injection duration for all test was set to 0.5ms (TTL onetime of 0.5ms). A total of 10 injections were conducted with a rest period of 1 second between each injection. The data recorded would then be saved and another set of injections could be conducted. In total, 100 injections for each condition were conducted. Post processing of the voltage signal was handled using Matlab. Various filters were experimented with. Those built into Matlab along with an FFT filter but these were found to be unnecessary when the mean signal of the 100 injections was used.

Prior to installation in the chamber the force transducer was calibrated with known masses in the range 50 to 300g (approximately 0.5 to 3N). To achieve this the transducer was vertically mounted onto a work bench with the target in place.

A hinged sheet of aluminum was the placed over this to support the weights as they were applied to the transducer target. A total of 10 readings for each weight were used to construct a calibration line to check linearity over the range. The gradient of this line was then used as the calibration constant to extract force from the voltage signal recorded by LabView.

3.6 Combustion Observations

Some preliminary combustion experimentation has been conducted in an in-house designed and constructed optically accessible combustion chamber (OACC). Fuel injection has been achieved using a modified version of the system previously employed. Combustion imaging was made using high speed video photography. Images were collected in the broadband visible portion of the spectrum with no filtering or intensification applied. The natural luminosity of combustion was used to examine combustion using a semi-quantitative metric, the spatially integrated natural luminosity (SINL). The fuel spray was not imaged and no illumination source was used. Data acquisition and experimental control has been achieved with a custom LabView program coupled to a custom engine control unit (ECU) tailored to this experiment. the Diesle fuel combustion has been observed along with one Diesel and water emulsion. Diesel and water emulsions examined have been produced according to a protocol developed during testing and subjected to a number of tests prior to any spray studies were conducted.

3.6.1 Optically Accessible Combustion Chamber

The combustion chamber in which fuel combustion was visualized has been designed and constructed at QMUL. The chamber consists of a solid cylindrical section of 304 stainless steel with an internal chamber machined into it. The cylindrical section is 100mm in length with a diameter of 90mm. The combustion chamber and injector were fitted along the central axis of the section. One end of the section was used for the combustion volume, with a cylindrical combustion chamber 40mm in diameter and 21mm in length machined the end. The other end of the section has a seat machined to accept the injector with a hole the width of the nozzle, allowing just the very tip of the injector nozzle to be introduced into the combustion chamber. The combustion volume portion of the section was sealed with a sapphire window, 60mm in diameter, 15mm thick, held in place with a clamp secured with 12, 6mm high tensile bolts. Gas sealing was ensured by a combination of copper rings between

Table 3.3: Specifications of the 4 cylinder Ford used with the optical combustion chamber.

Engine	Ford in-line OHV 4 cylinder Direct Injection diesel
Bore	93.67mm
Stroke	90.54mm
Con rod length	153.6mm
Engine cylinder capacity	623.9×10^{-6} m^3
Clearance Volume (with flat top piston)	13.78×10^{-6} m^3
Compression ratio	16.1:1

the clamp and the window along with graphite gaskets.

The combustion chamber is designed to fit onto the top of one cylinder of a four cylinder, four-stoke OHV DI diesel engine (Table. 3.3 for details). The combustion volume has been moved from the region above the piston in the cylinder and externalized in the cylindrical combustion chamber. The cylindrical combustion chamber is attached to the top of the engine cylinder which is at the opposite end of the engine from the crank shaft output, cylinder number 1. The original piston in the cylinder was replaced with a flat topped piston which reduces the clearance volume with in the cylinder at TDC to almost zero (ignoring wall clearances). The cylinder clearance volume is transferred into the external cylindrical combustion chamber via a connecting tube which is installed through the cylinders original injector port. The connecting tube introduces the hot compressed air into the external combustion chamber during compression. The tube is secured to the cylinder by two, 10mm high tensile bolts using the fittings in the cylinder head that originally housed the injector clamp. The other end of the tube is threaded and screws in at the center of the base of the external chamber. A schematic of the chamber fitted to the engine cylinder is shown in Fig.3.16.

The internal volume of the external chamber corresponds to that of the volume of the original cylinder clearance volume. With reference to Fig.3.16 it can be seen that the connecting passage enters the combustion volume in the center of the lower surface, this means there is no tangential flow around the inside of the chamber during compression. For this purpose, a hollow ring is placed inside the combustion chamber which the compressed air travels around and enters the chamber through three angled holes. These holes introduce an element of swirl into the combustion volume during the compression stroke. During this piece of work there has not been an attempt to quantify the degree of swirl via measurement but an estimate of the swirl ratio based upon the mean piston speed and the chamber circumference yields

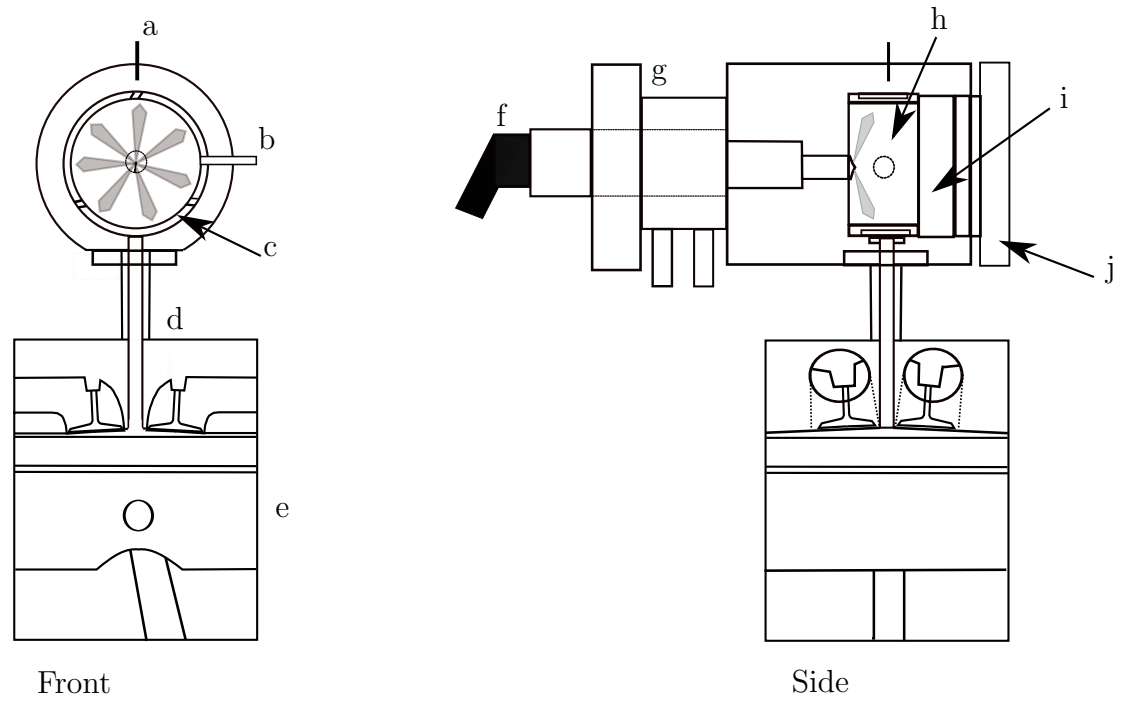

Figure 3.16: Schematic diagram of the OACC attached to the top of cylinder number 1 of the four stoke DI engine. a.)Thermocouple. b.) Pressure transducer. c.) Swirl ring. d.) Connecting tube. e.) Engine cylinder. f.) Injector. g.) Cooling jacket. h.) Combustion region. i.) Window. j.) Window clamp.

a swirl number of 1.45. It was found during testing that the swirl ring was required to ensure combustion. A number of swirl rings were tried with different volumes resulting in a change of the compression ratio. This was done as an attempt to counter any losses that may be incurred due to externalizing the combustion chamber, such as pumping and increased heat losses, similar to those that would be experienced in an older, indirect injection engine deign. For the purpose of this study the compression ratio has been fixed at 16.7, a slight increase from the engines original. With the window clamp in place, an optical region 40mm in diameter was visible. The chamber design provides a compression ignition zone which is optically accessible, readily set-up and controlled and operated under conditions similar to those of a running engine. Like all other diagnostic strategies, such as shock tubes and optical engines, it inevitably creates conditions which differ somewhat from target but in this case provides a convenient means of comparing fuels under repeatable conditions [67, 180, 181].

The chamber is fitted with a pressure transducer (Kistler 6123) monitoring the pressure inside the combustion volume coupled to a charge amplifier (Kistler 5007). The transducer's face sits flush with the internal wall of the combustion volume. A k-type thermocouple is positioned with it's tip mid way between the inner and outer

Table 3.4: Optical accessible combustion chamber specifications.

Chamber Part	Volume
Combustion Volume	27.70×10^{-6} m^3
Swirl ring	11.10×10^{-6} m^3
Graphite gasket	0.63×10^{-6} m^3
Connecting Tube	6.40×10^{-6} m^3
Total Volume at TDC	37.41×10^{-6} m^3
Compression Ratio	16.68

surface of the wall surrounding the combustion volume to measure the chamber wall temperature. The air intake system for the engine is modified so as to separate the air entering the external chamber and that entering the remaining three cylinders. The air feeding the three cylinders flows through the standard intake system with access to the cylinder number one blocked with an aluminum plate. The intake to the external chamber enters through an orifice plate fitted to a large damping chamber. On entering the cylinder intake system, air is heated by an in-line electrical air heater installed between the damping chamber and the intake to cylinder number 1. Preliminary testing identified the target air temperature as 120°C which was found to result in guaranteed combustion in the external chamber. The air heater was controlled by a PID controller. The pressure drop across the orifice plate is measured using a digital manometer to determine the air flow rate into cylinder number 1.

The engine is run on standard pump Diesel fuel, using the three remaining unmodified cylinders to establish the speed at which the external chamber was motored. For all cases the engine was operated at 1000rpm with no load applied. There were no attempts made at this time to increase the operational speed of the engine or to apply any load. Prior to experimentation the operating protocol of the chamber was developed. For this end, the chamber was completed with the installation of the injector, complete with a copper gasket for gas sealing and clamped into position by three, 6mm high tensile bolts. For this period of the testing, no injections were conducted. The chamber is completed with the addition of an insulation wrap of foil back mineral wool to reduce thermal losses from the chamber outer surface.

The chamber was operated (motored) continuously for approximately 50 minutes with the chamber wall temperature from the thermocouple recorded every 3 seconds. Chamber pressure was recorded for 10 (what would be combustion) cycles every 10°C increase in wall temperature.

The temperature record is depicted in Fig.3.17. It was found over a number of

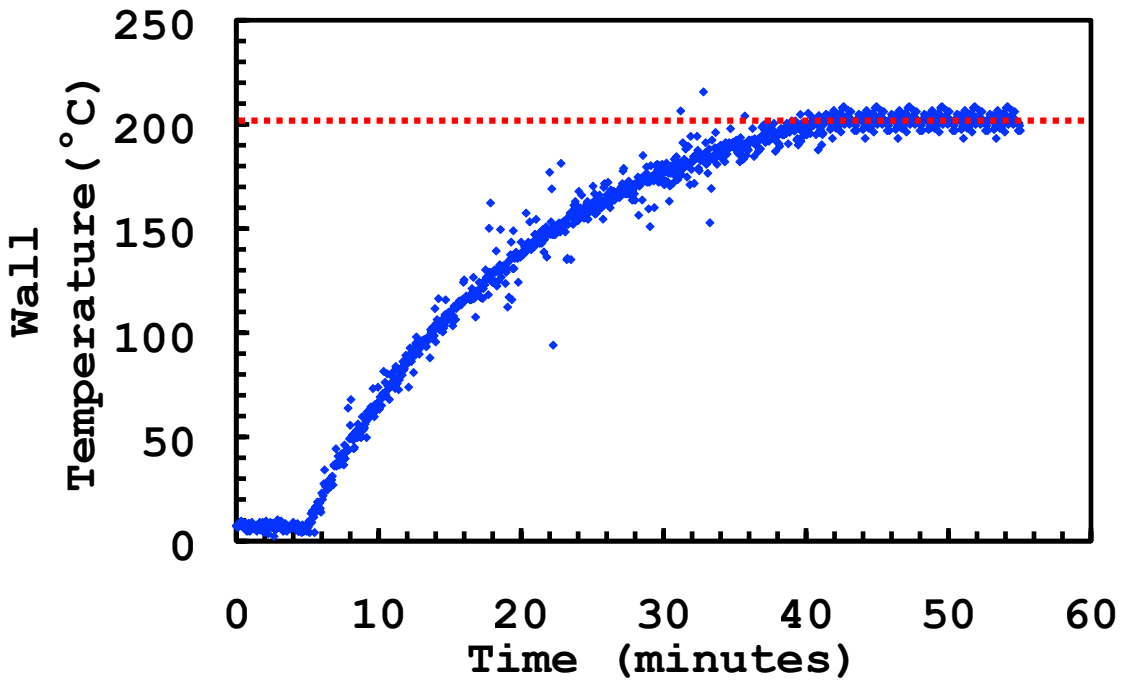

Figure 3.17: Variation of the temperature measured by the thermocouple installed into the chamber wall with time during motored operation at 1000rpm. t=0 corresponds to the starting of the engine.

repeats of this process that the chamber wall temperature tended towards 200°C. All subsequent experimentation has been conducted with the chamber wall temperature at 200°C. Chamber volume was determined using Eqn.3.1

$$\frac{V}{V_c} = 1 + \frac{1}{2}(r_c - 1)[R + 1 - cos\theta - (R^2 - sin^2\theta)^{1/2}] \tag{3.1}$$

where V= cylinder volume+external chamber volume at that instance; V_c is the clearance volume; r_c is the compression ratio, including the external chamber volume; R is the ratio of connecting rod to crank radius and; θ is the crank position (in radians) [18]. The pressure collected from the chamber and the volume determined using the shaft encoder signal and Eqn.3.1 were used to produce a LogP-LogV chart of the type shown in Fig3.18. Considering the compression and expansion process to be polytropic according to the polytropic relationship $PV^n = constant$ where n is the polytropic index, the slope of the line during compression and expansion of Fig3.18 was used to determine n as an indicator as the potential losses incurred due to the external chamber. This process had been conducted at different chamber wall temperatures as well as at 200°C. The polytropic index of compression increased from a value of 1.07 with chamber wall at 40°C to 1.31 after approximately 45 minutes of motoring with the chamber wall at 200°C. This is quite a good result considering isentropic compression would have a index value of 1.34 (specific

teat ratio). This methodology is similar to that employed in previous work with the external combustion chamber [182]. This helped inform the operational protocol of start up, run time and potential losses from the chamber. All experimental data was collected after a warm up time of approximately 45 minutes with injection in the chamber taking place when the thermocouple temperature was 200°C.

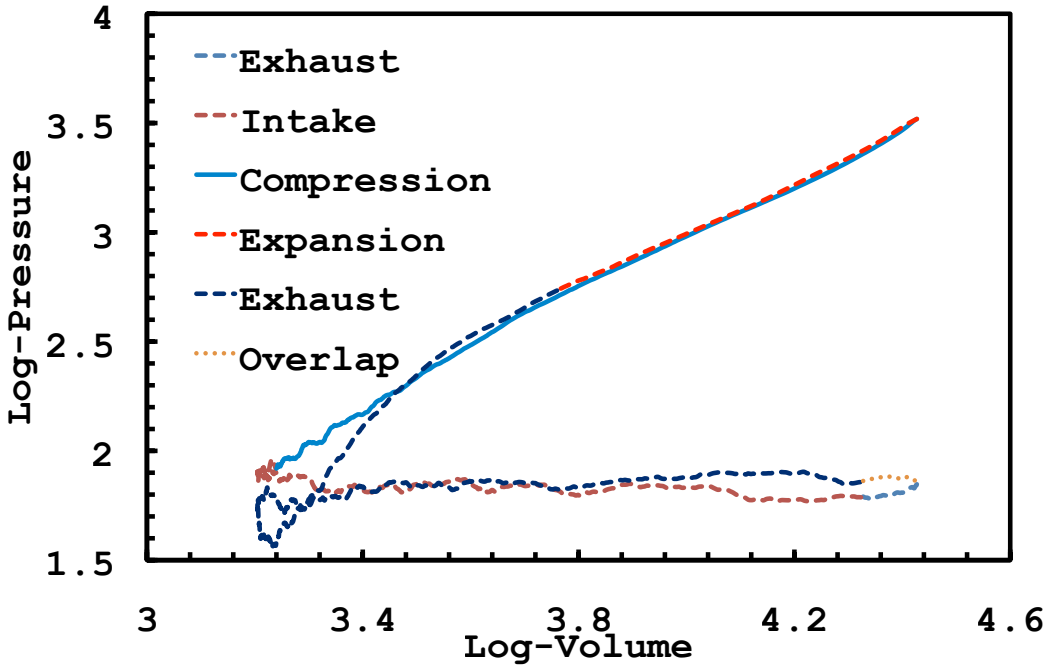

Figure 3.18: Log-of-cylinder pressure versus log-of-total volume (engine cylinder+ OACC) doing motored operation at 1000rpm with the thermocouple temperature reading 200°C.

3.6.2 Injection system

Fuel injection was by means of the high pressure common rail system previously employed with some modifications to the fittings so the common rail and pump configuration could be installed near the engine. The injector used was of the same type used in the previous experiments, detailed in Table.3.1 but with no modifications made to the holes. All seven holes were left unblocked. Injection timing and duration were controlled by a custom ECU (Measurement Computing USB4303) connected to a dedicated injector driver (Hartridge HK853). The ECU was fed engine input timings from a shaft encoder attached to the engine output shaft. The shaft was also fitted with a TDC sensor. Compression TDC was identified by applying a threshold to the chamber pressure output. A custom built LabView program controled the ECU as well as recording chamber and rail pressures. The injection

timing was controlled on a CAD basis, in terms of position in the cycle and duration.

An injection delay arising from the driver was measured optically at a high frame rate of 20000 fps with the spray illuminated using a custom LED illumination system. The injection signal sent to the driver was identified using an LED connected to the ECU which was positioned in the corner of the frame. The number of frames between the LED illuminating and the first appearance of spray was used to determine the time difference between the two events. Delay for all fuels tested was measured to be 300μs (1.8 Cad at 1000rpm).

During operation of the injector it was discovered that when the chamber wall temperature was at 200°C, the injector started to fail after a around 20 minutes with the fuel return volume increasing to around 100ml every 15minutes. This resulted in an inability for the rail pressure to be maintained at target pressure. The operational temperature of the injector is 90°C. A spare injector was adapted to house a k-type thermocouple in the nozzle to determine the temperature of the injector when the external chamber was at operational temperature. The injector was found to be drastically over heating. A cooling jacket was made which allowed the flow of water around the injector body between the injector clamp and the rear of the external chamber. It was necessary to conduct some testing to check that the cooling jacket was cooling the injector but not having a detrimental effect on the chamber wall temperature. The temperature recorded by the injector and chamber thermocouple, with and without cooling applied is shown inFig.3.19. The cooling was effective at maintaining the injector at a near content temperature of around 10°C while having no effect on the chamber wall temperature. Observations were made and the rail pressure was found to change by no more than 2% during injection when cooling was applied. For all conditions an injection pressure, as measured by the transducer fitted into the common rail was 50MPa.

3.6.3 Optical measurement

Natural luminosity images were collected using a high speed video camera. The injection spray was not illuminated during combustion tests. The start of injection was determined using the same LED connected to the ECU as used to determine delay. A Phantom V 4.3m digital camera equipped with a high speed CMOS sensor was used. The recording speed used for this study was 8146 frames/s which corresponds to 0.73 crank angle per frame and a derived error of 123μs. The image resolution was 256 x 256 pixels. A Nikon 60mm f.2.8 lens was mounted on the

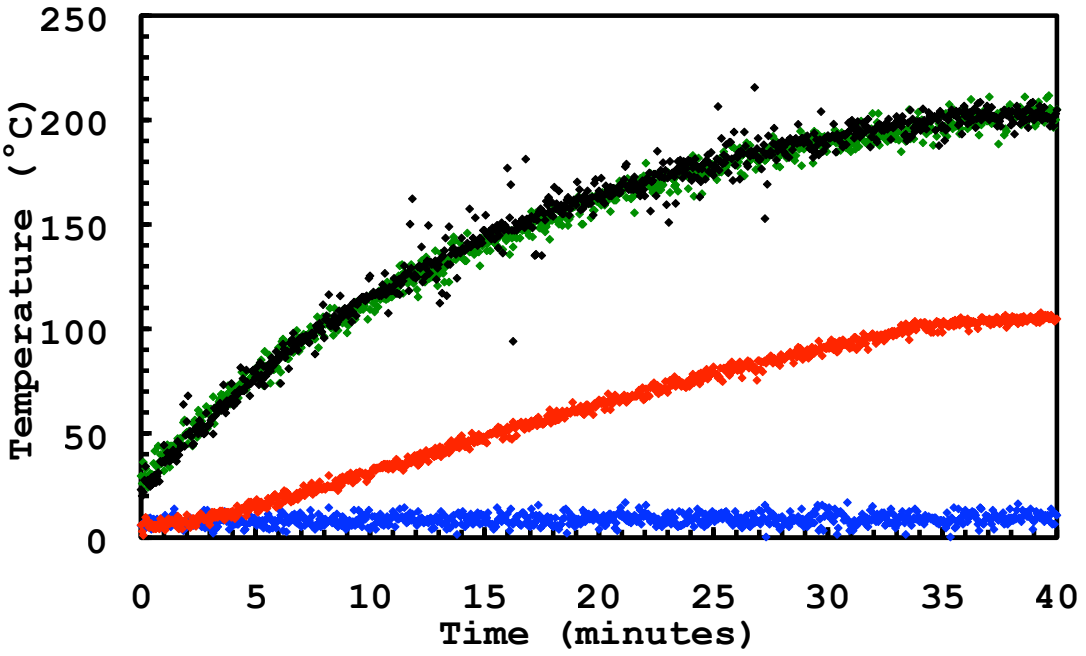

Figure 3.19: Variation of the temperature measured by the thermocouples installed in the OACC wall and the adapted injector nozzle, with time during motored operation at 1000rpm. t=0 corresponds to the starting of the engine. The green data series is the chamber thermocouple when no cooling was applied, the red data series is the injector thermocouple when no cooling was applied. The black data series is the chamber thermocouple when cooling was applied, the blue data series is the injector thermocouple when cooling was applied.

camera. No filtering or intensification was applied so broadband emission spectrum was visible. Pixel saturation was avoided by setting the lens to $f/11$. The camera was mounted to a custom stand which secured the camera in position in front of the external chamber and was insulated from the vibration of the engine. The camera was controlled by Phantom software running on a separate laptop computer. The camera trigger was connected to the same ECU output as the injector driver. For all recordings a number of frames prior to the trigger were recorded and saved with the post trigger images so as to capture the first frame when the spray indicating LED was illuminated. Fig.3.20 shows the complete system including the external chamber and the camera.

3.7 Fuels tested

Three fuels have been tested during the element of the study: a base fuel of pure Diesel fuel (D) and two emulsified fuels, Diesel fuel with 10% water and 20% water

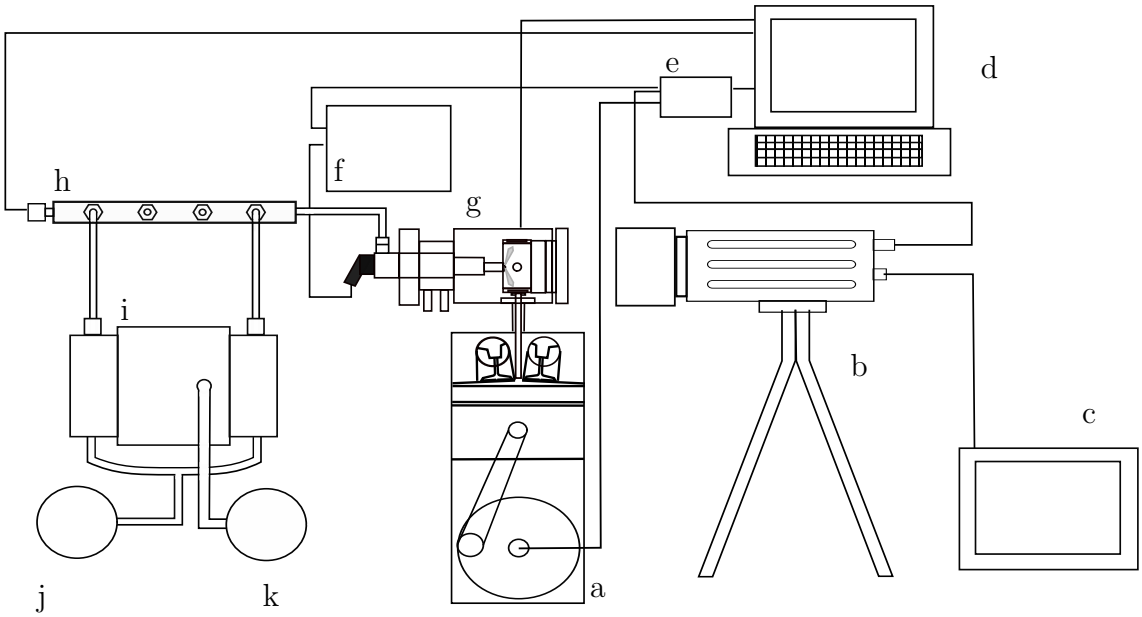

Figure 3.20: Schematic diagram of the entire optical combustion system. a.) Engine crankshaft fitted with an opticalshaft encoder. b.) Camera. c.)Camera's control and recording computer. d.) Data acquisition computer. e.)ECU. g.) OACC. f.) Hartridge injector driver. h.) Common rail. i.) High pressure pump. k.)Air supply for pump. j.)Fuel tank.

(D10 and D20 respectively). Details of the base Diesel fuel are shown in Table. 3.5.

Table 3.5: Diesel fuel details

Property	Diesel
Chemical formula	$C_nH_{1.8n}$
Density(kg/m^3)	827-840(quoted) 814 (measured)
Kinematic viscosity(mm^2/s)	2.9
Cetane number	52
Lower heating value(MJ/kg)	42.5
Initial boiling point(°C)	169

3.7.1 Emulsion production

The two emulsified fuels were made using a base (pump) Diesel fuel with the addition of 10% and 20% of water. Production was accomplished as follows. Approximately 500ml of the base fuel was weighed to determine the mass percentage of water to be added. The emulsions were stabilized with the addition of an appropriate surfactant. For both emulsions 1% by total mass of surfactant was used. The various components of the emulsions were homogenized using ultrasound. The choice of

suitable surfactant used for the Diesel fuel and water emulsions was made using the hydrophilic-lipophilic balance (HLB) methodology along with results of previous studies [44, 48, 58, 183, 184]. The two surfactants used were Span 80, a non-ionic lipophilic surfactant with a HLB of 4.3 and Tween 80, a non-ionic hydrophilic surfactant with a HLB of 15. Small volumes of emulsions were made with varying HLB (from 4.3 to 15) using the HLB addition method, (mixing the two surfactants together in varying relative quantities) with the final HLB given by Eqn. 3.2 where HLB_i is the HLB of emulsifier i multiplied by n_i, its mass percentage.

$$HLB_{mix} = \sum_i HLB_i \times n_i \tag{3.2}$$

Samples were drawn from these test emulsions into 10ml graduated flasks and left for a 5 day period to access stability. It was found that the surfactant mixture resulting in a HLB of approximately 6.4 (80% Span 80 and 20% Tween 80) resulted in the most stable emulsion. It has been seen in studies elsewhere [183, 185] that the use of mixture a of Span 80 and Tween 80 leads to better result compared with the use of a single surfactant with equivalent value of HLB. This method is termed using a co-surfactant.

Once the required components had been weighed the emulsion was constructed. The surfactant mixture was first dissolved in the Diesel fuel and then the water was added. The mixture was then subjected to 5000J of ultrasonic mixing using an ultrasound generator (Sonics, Vibra-cell 750W, 20kHz) and an ultrasonic probe (Model CV33). The probe was inserted so that its end was at mid-depth in the mixture. Due to the heating effect that arises when a liquid is subjected to ultrasonic waves of this nature, the mixtures where kept cool during the process using an iced water bath. The ultrasonic method of mixing has been used elsewhere [46, 186, 187, 188] and has been shown to result in: smaller mean droplet size; a larger number of water droplets that are distributed more uniformly in the continuous phase; lower separating rates of the water droplets from the emulsion when compared with emulsions prepared by a more conventional mechanical homogenizer [46]. Ultrasonic emulsification is therefore recognized as a fast, efficient technique for producing tiny and uniformly-sized droplets.

For each emulsion, approximately 300ml were produced at a time. From this, a 10ml sample was drawn into a graduated cylinders to monitor the emulsion stability over a period of time. Both emulsions were very stable stable over a two week period with no visible separation or layers forming in the cylinders.

3.7.2 Fuel characterization

Each fuel used in the experimentation was characterized by density and viscosity. Fuel density was measured using a 10ml measuring cylinder and a set of scales (Ohaus Adventurer AV114). The measurement was made in the characterization lab at QMUL which is a temperature controlled environment. The fuel samples to be used for the measurement were stored in the lab overnight along with the measuring cylinders and scales. This was done so all the samples were at the same temperature. Emulsified fuels were stirred before samples were drawn to ensure dispersion of the water droplets throughout the sample. Each measurement was repeated 10 times with the same measuring cylinder.

The fuel viscosities were determined using a TA Instruments AR 2000 rheometer. A 40mm Peltier plate was utilized for the measurement with a stepped shear rate applied. Shear rate was automatically adjusted by the rheometer from 10 to 1000s^{-1}. The Peltier plate maintained the sample at 20°C during measurement.

3.7.3 Mass of Injection

To complete the hydraulic characterization, the total mass of injected fuel (m) must be known. This was achieved by injecting the fuel into a glass bottle with an adapted lid that allowed the injector nozzle to fit through, with an O-ring sealing the nozzle to stop any injected fuel escaping. The injection system was changed slightly in that the injector was removed from the chamber and clamped in position with the nozzle sealed into the bottle. After 500 injections, 0.5ms duration, the bottle was weighted using a Ohaus Adventurer AV114 scale. The mean mass of fuel per injection was then determined. This process was repeated 5 times for each condition. To assess the quality of the measurement, the range of the 5 measurements (max-min) has been determined along with the ratio of the range to the mean (range/mean). Results are shown in Table.3.6. The ambient pressure into which these injections took place was atmospheric. The effect that the higher ambient pressure (20 and 30 bar) when the injections take place in the high pressure chamber, will have on the mass of fuel injected per injection has been assumed to be negligible. The mass injected for the Diesel and water emulsions is presented in the results section.

Table 3.6: Mass of Diesel fuel collected for 500 injections, 0.5ms duration, at 500, 700 and 1000 bar, back pressure is one atmosphere (1bar). Mass per shot is mass of fuel injected for one individual injection. Each case has been repeated 5 times. The range of the measurements made is including along with ratio of the range to the mean value

Injection Pressure	Mass Collected(g)	Mass/shot(g)	Range (max-min)	Fractional variation (range/mean)
500 bar	1.1771	0.002354		
	1.1761	0.002352		
	1.1808	0.002362		
	1.1738	0.002348		
	1.1763	0.002353		
mean		**0.002353**	1.4×10^{-5}	0.005
700bar	1.3366	0.002673		
	1.3385	0.002677		
	1.3236	0.002647		
	1.3275	0.002655		
	1.3295	0.002659		
mean		**0.002662**	3.0×10^{-5}	0.01
1000bar	1.3694	0.002739		
	1.3881	0.002776		
	1.3753	0.002751		
	1.3879	0.002776		
	1.3600	0.002720		
mean		**0.002752**	5.6×10^{-5}	0.02

3.7.4 Injection mass calibration

Injection timing in the OACC was controlled in a different manner. The injection timing and hence the mass injected is a function of the engine's shaft encoder signal. For each fuel tested a calibration curve was constructed which describes the injected mass as a function of the number of shaft encoder pulses. With the engine running as normal at 1000rpm to provide the shaft encoder signals, the injector is secured with its tip sealed into a special capture container. An injection pressure of 500 bar was maintained. The injection duration was established by selecting the number of shaft encoder signals the injection would last for. Using a calibration chart supplied by the injector manufacture, it was known that at an injection pressure of 500bar, 8mg of fuel is injected for a duration of 410μs. The shaft encoder emitted 5000 signals per revolution. At 1000rpm each shaft encoder signal equates to approximately 12μs hence for an 8mg injection quantity 34 shaft encoder signals were used. This was used as the value to test around to build the calibration chart. The calibration was conducted with the engine running to provide shaft encoder signals rather than a separate timing circuit so the variation in engine rotational speed would be the

same as in experimentation. This was done in an attempt to average out any small differences in actual duration of injection that may be encountered due to rotational speed variation. For each duration used to build the calibration curve, one thousand injections were carried out, repeated three time for each duration. The total mass of the injections was determined by weighing the container before and after the test, which allows for a direct calculation of the fuel mass per injection. A linear fit is applied to the calibration data which is then used to determine the required number of shaft encoder pulses for the desired injection mass. All cases used 8mg injection per stoke. The calibration chart produced is shown in Fig.3.21. To maintain an injection mass of 8mg for each fuel, the Diesel fuel was injected for 35 pulses and the D10 was injected for 33 pulses.

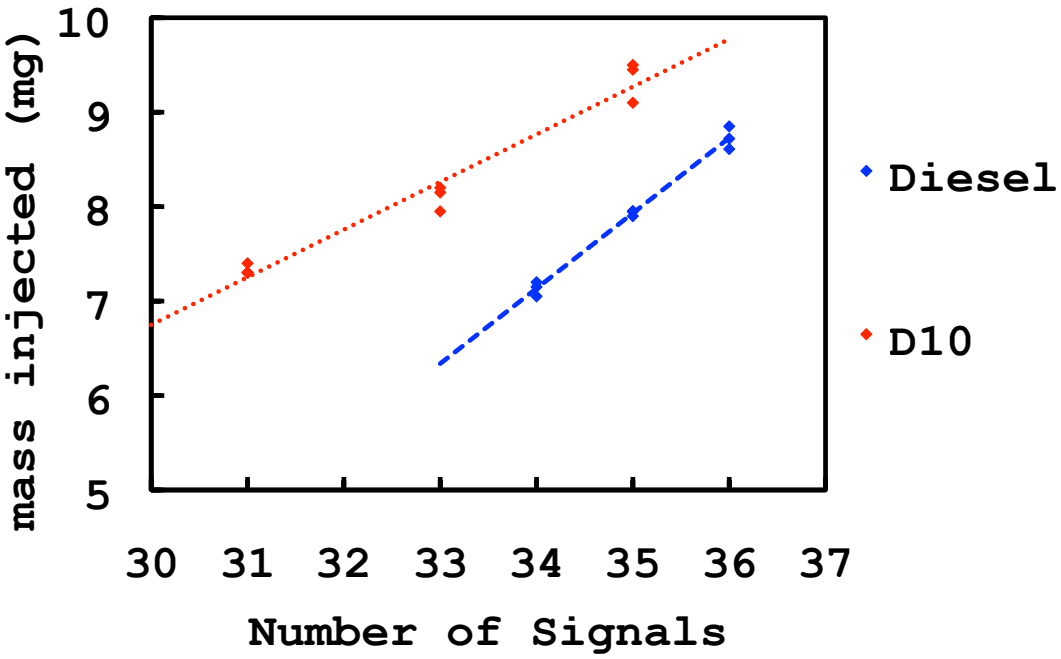

Figure 3.21: Injection mass calibration chart for Diesel fuel and D10, constructed by varying the duration of the injection, in shaft encoder signals, with the engine at motoring the chamber at 1000rpm. Injection pressure was 500bar.

Table 3.7 shows the energy content injected into the cylinder per combustion stroke for the two fuels tested. The emulsion's energy content is derived knowing that 10% of the fuel mass has been displaced by the addition of water.

Table 3.7: Energy content of 8mg of the Diesel fuel and the D10 fuel.

Fuel	Energy content per stroke (kJ)
Diesel	0.340
Diesel fuel and water emulsion	0.306

3.8 Analysis Techniques

3.8.1 Spray Image Processing

The image sequences collected were used to determine the spray cone angle variation with time and the spray tip penetration variation with time. The videos collected consisted of a sequence of images (frames), with each frame from a subsequent time step (dependent on the frame rate). Each image contained a background, consisting of the chamber windows and empty volume, and if present, a shadow formed by the spray. The initial action of the post processing was to remove the background. This was achieved by using a number of frames from the beginning of the sequence when no spray was present. An average image was produced from these frames, to form an average background image. This average image was subtracted from each image in the sequence and is called background subtraction. This removes features such as the edge of the window, any speckles that were present on the mirror surface, window fouling from previous injections and the injector nozzle. The resultant image was of a homogenous black background behind the spray. For the shadowgraph images, the first 15 frames were used while for the backlit, the first 25 frames were used to produce the average background image. The first frame with spray was detected by measuring the average pixel value in the background subtracted images. Once the spray started, the average pixel value in these images always rises steeply and identifies the frame when spray first appears.

Processing could then be applied to the frames with spray shadow imaged. The portion of the image which was spray must be identified and segmented from the background. The spray angle (θ) and tip penetration (S) may then be directly measured from the segmented spray image. Both of these parameters vary with time so needed to be measured by a repeatable method for each frame. The method needed to process a large number of individual images so had to be automated. This automated process had to be able to handle changes in the light intensity, window fouling and very small changes in alignment of optical components. All image processing has been conducted in Matlab.

The end of injection was very difficult to define due to the persistence of the spray formation in the chamber after the injection had finished. It was possible to manually identity the end of injection if required but this was not acceptable for each image sequence. A cut-off frame number was chosen as the point where processing stopped, this may not have been the frame where the injection event actually ended. For the shadowgraph image sequences, this cutoff was chosen as frame 55 (18295

μs after trigger) while for the backlit image sequences the cut-off was frame 160 (1800μs after trigger).

A number of methods have been used to remove the spray from the background of the image with most techniques resulting in a binary image where the spray was all white and the background was all black (or vise versa). The binary image will usually be in the form where a pixel value of 1 was white and 0 was black. Images collected by the camera are usually of a gray-scale where the pixel value represents the brightness of the pixel. The pixel values are often an 8-bit integer with a range of possible values 0 to 255, 0 black and 255 white, with any value between a shade of grey. This was the type of image that was collected during this study. The ambiguity is introduced when attempting to create the binary image from the grey scale. Can one pixel value be chosen to state with certainty that any pixel with a value greater than this was background (assuming image is of shadow type with background lighter than the spray shadow region). This is described as thresholding the image.

A technique often employed is to produce a cumulative intensity histogram of the grey-scale pixel values. Two peaks will be present in such a histogram, a peak at the high values for background (brighter) and a peak in the lower values for spray (dark shadow region). A value midway between these peaks is often chosen as the threshold value and applied to all images in that sequence [92, 97, 96, 104, 115, 131, 144, 145, 189].

If a light scattering technique is being used to illuminate the spray, rather than a shadow image being formed, these values are obviously in reverse, with the brighter portion of the image consisting of the spray. This may be refined further by running an algorithm that checks for connectivity between pixels of this value to try and remove any erroneous edges [190]. Other methods use edge detection algorithms which examine the the statistics of pixel values within the image [95, 114, 121, 132, 145]. An example of these is the log-likelihood ratio test that has been developed and used extensively by [99, 103, 119]; Sobel operators used by [121, 132, 145] and; the Otsu's method [165, 191].

The Otsu method has been applied here, implemented using the built in Matlab function *graythresh*. The Otsu method was chosen for a number of reasons; built in function means stable bug free code which operates efficiently; the method is not reliant on user defined inputs; and it has been shown to be suitable for spray edge detection. The Otsu method is detailed in [191, 192] and assumes that the image contains two classes of pixels foreground pixels and background pixel. It then calculates the optimum threshold separating the two classes so that their combined

spread (intra-class variance) is minimal.

Once the spray has been separated from the image background the tip penetration and angle can be measured. The tip penetration is usually measured first as in most circumstance the angle measurement will be made at some proportion of the tip length. The tip penetration of the spray is most often defined as the position along the spray central axis, downstream of the nozzle, where the last pixel which may be described as belonging to spray occurs [92, 95, 115, 144, 145]. Alternatively the spray is projected onto the axis and a fixed fraction of the maximum projected signal intensity yields the position of the spray tip [89]. The definition of the spray tip penetration used in this study is the last spray signal along the spray central axis downstream from the nozzle. Most often the technique will use a spray central axis based upon the nozzle hole geometry [56, 123, 144, 145, 193] which must be known *apriori*. This method also assumes a symmetrical spray around this central axis.

The desire in this study was to develop a measurement technique that relied as little as possible on assumptions and defined values with all measurements being made from the image available. The spray central axis was not used as an input variable but measured from the image itself. This was achieved using built in Matlab functions which apply a bounding box around the binary spray region, with its edges defined by the extremities of the binary region. The upper left corner of this bound box is the spray origin. The center of mass of the spray region (centroid) was computed and a line was plotted from the origin, through this centroid, to form the spray central axis. The last spray signal along this line is taken as the tip penetration and a pixel value of this position was determined using pythagorus.

There are a number of techniques applied when measuring the cone angle. The edges of the spray may be used to construct lines (or tangents) fitted though the upstream portion of the spray edge which meet to form an apex at the nozzle, the angle between these lines is then determined. The lines do not usually extend the full length of the spray but some proportion of the tip penetration. The proportion of the spray tip penetration used varies between studies with [104, 144] using 1/3, [92, 107] using 1/2, [99, 117, 119, 194] using 60%, [131] using 20mm, [96] using 40mm and[132, 145, 146] using 60 and 100 orifice diameters. In these works the methodology used to construct the lines/tangents from the edges is not described. An alternative method introduced in the work [97] and also utilized in [123, 130, 189] is proposed. The angle corresponds to that of a triangle whose area is equal to the projected area of the upstream half of the spray. The angle θ is given by

$$\theta = 2tan^{-1}\left(\frac{A}{(S/2)^2}\right) \tag{3.3}$$

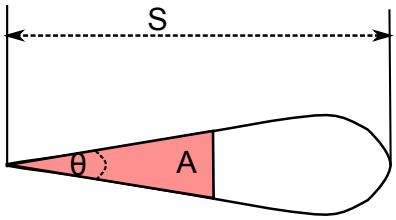

Figure 3.22: Spray cone angle calculated using the triangle technique. The projected area of a triangle A, with a length a fixed percentage of the penetration S is used to determine the angle using Eqn.3.3.

where A is the projected area of the upstream half of the spray, $S/2$ is half of the tip penetration. This technique is referred to as the triangle technique from here. Fig.3.22 shows a graphical representation of the technique.

Both techniques, line fitting and the triangle technique were considered in this study. For the line fitting technique, the spray edge was defined from the binary image by moving across the image, in the x direction and identifying the pixel positions of the first and last white pixel in each row. These positions were then used to construct a vector to which a least square fit line was fitted using the $polyfit$ function in Matlab. The fit created a second order polynomial for the fit. This was applied to the upper and lower edges of the spray, so two fitted lines were constructed. The polynomial was fitted up to the length of the edge that corresponded to 50% of the tip penetration. The angle between these two fitted lines was then calculated using the difference between vectors technique. The technique was sensitive to the order of the polynomial chosen for the $polyfit$ function and to any anomalous features that may have occurred on the spray edge from time to time. The choice of using the edge up to 50% of the tip penetration was made in an effort to make the measurement along the portion of the spray edge that was reasonably steady and avoid the unsteady downstream portion of the spray edge.

Fig.3.23 is an example calculation of the tip penetration and spray angle using the line fitting technique. The steps of the calculation process are numbered

1. Raw image as collected using the shadowgraph system. image is from the later stages of the injection where the spray is well developed.

2. Complement image, image is reversed for the calculation.

3. First 15 frames containing no spray have been averaged and subtracted from all frames.

4. Otsu method applied to make binary image.

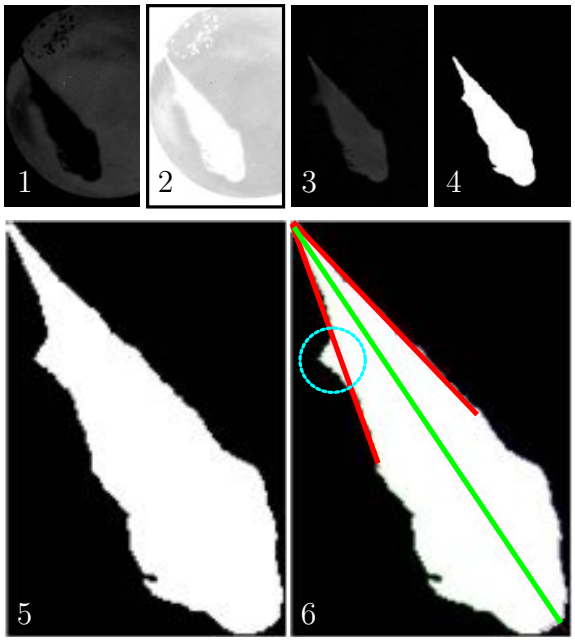

Figure 3.23: An example set of shadowgraph images of a Diesel spray used to measure the spray cone angle using the line fitting technique. 1.)Raw image. 2.) Complement image. 3.) Background subtracted. 4.) Binary image. 5.) Bounding box applied. 6.) Line fitted to edge.

5. Image bounding box applied, image is cropped to the size defined by the spray, makes calculation of the origin of the spray straightforward and the centroid of the spray for the central axis is defined.

6. Edge detected and contour plotted. Edge contour used to produce the fitted line (red) which extends to 50% of the tip penetration (green). The angle was determined treating these lines as vectors and calculating the difference between them.

The blue circle in image 6 of Fig.3.23 shows an edge anomaly which will have had an effect on the polynomial fitting used to construct the line.

To apply the triangle technique, the stages were very similar up to the point where the tip penetration is determined. Once this was known, a line perpendicular to the central axis line was plotted across the spray at 50% the total length (blue line in image 5, Fig.3.24). This perpendicular created an image mask which left the projected area upstream. The tip penetration was used along with this area and Eq.3.3 to determine the cone angle. In this sense the calculation is very different as the edges are never plotted against the spray edges and the calculation inherently averages out any edge anomalies that may be present. The lines plotted in Fig.3.24 have been added using the angle determined using the triangle technique.

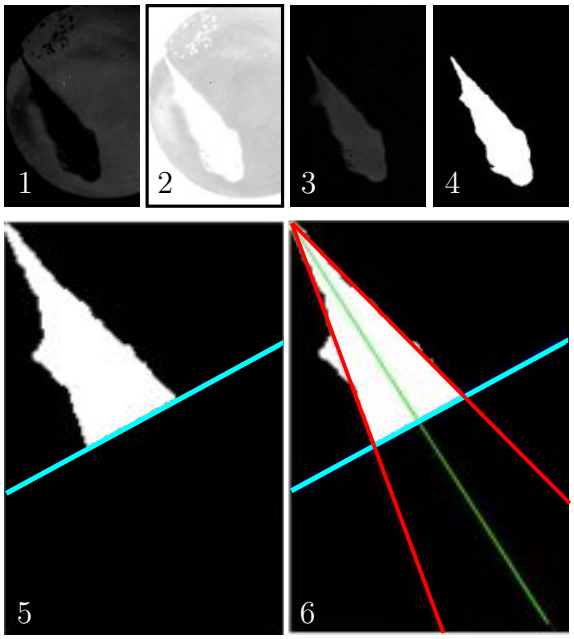

Figure 3.24: An example set of shadowgraph images of a Diesel spray used to measure the spray cone angle using the triangle technique. 1.)Raw image. 2.) Complement image. 3.) Background subtracted. 4.) Binary image. 5.) Bounding box applied and downstream half masked. 6.) Angle determined, lines added to edges.

An assessment was made of the two measurement techniques to make a decision on which technique should be applied. A D10 fuel spray, injection pressure 500bar, chamber pressure 30bar, was used as a test condition to collect an example set of shadowgraph image sequences. The image sequences for 30 injections were collected then line fitting technique and the triangle technique were applied to the image sequences. Fig.3.25 shows the temporal evolution of the spray cone angle determined using the line fitting technique for the 30 injections. The distribution histograms are produced from the 30 angles taken at three different times to demonstrate that the measured angles were normally distributed around the mean. The histograms have been normalized. The red line is a plot one standard deviation (σ) away from the mean (not shown), the blue line is a plot two standard deviations (2σ) from the mean.

Fig.3.26 shows the temporal evolution of the spray cone angle as determined using the triangle technique for the 30 injections. Distribution histograms are included and standard deviations from the mean are plotted as before. Based on the evidence of these two figure, the measured angle is of a similar magnitude during the injection period but the distribution of the angle as determined using the triangle technique is smaller and there are no data points that lie outside of the band formed by the 2σ curves. This assessment informed the decision to proceed and apply the triangle technique to all angle measurements.

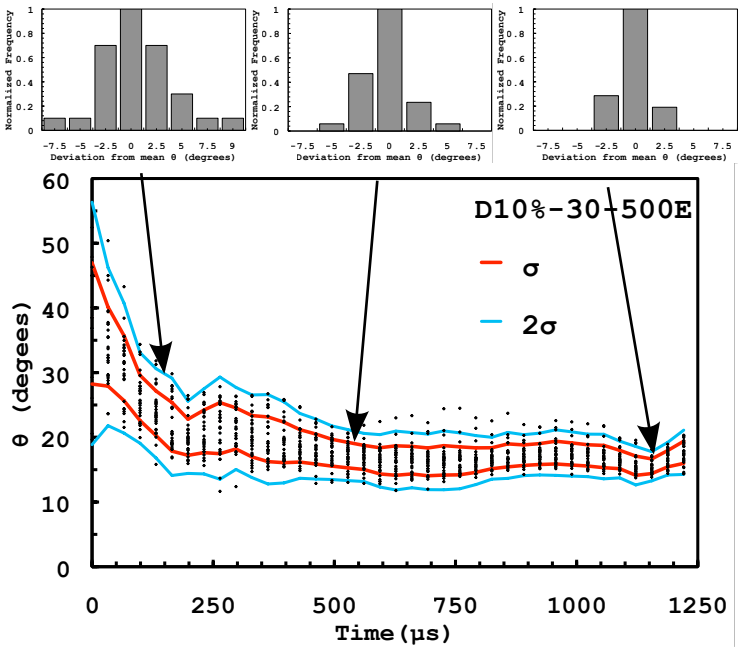

Figure 3.25: Temporal evolution of the spray cone angle for D10 fuel spray, P_{inj}=500bar, P_{amb}=30bar. Determined using the line fitting technique. The red line is plotted one standard deviation from the mean, the blue line is two standard deviation from the mean. The distribution histograms show the normalized distribution around the mean of the spray cone angles at t=130, 560 and 1155 μs after SOI (left to right).

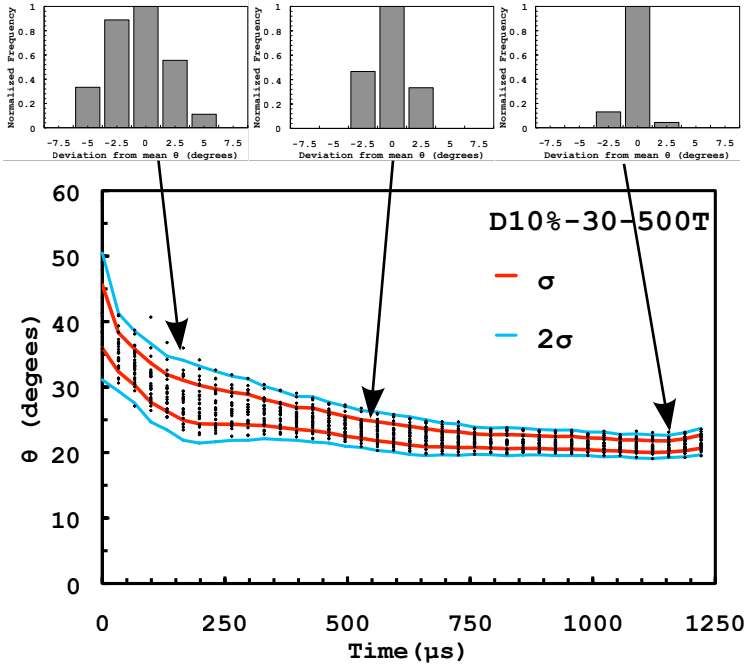

Figure 3.26: Temporal evolution of the spray cone angle for D10 fuel spray, P_{inj}=500bar, P_{amb}=30bar. Determined using the triangle technique. The red line is plotted one standard deviation from the mean, the blue line is two standard deviation from the mean. The distribution histograms show the normalized distribution around the mean of the spray cone angles at t=130, 560 and 1155 μs after SOI (left to right).

3.8.2 Momentum Flux Data Processing

All data was processed in Matlab. The first step was to remove any part of the data stream with was collected while no injection was taking place. The signal from the transducer was noted to drift slightly during the data collection, this was dealt with in part by reseting the charge amplifier between sets of 10. The data was further processed to compensate for this small drift from zero. The recorded voltage signal was scaled to give the force using a the calibration constant. The mean of the 100 injections was calculated and the standard deviation of the 100 injections determined. The instantaneous mass flow rate was determined using the scaled momentum values and the total mass injected using Eqn.2.40. For this purpose, the scaled momentum from each injection was used, not the mean. Hence for each condition, 100 instantaneous mass flow rates were determined and the mean of these then calculated. This was done in attempt to reduce the progression of experimental error and to allow the standard deviation of the calculated mass flow rates to be determined. The discharge coefficients, momentum coefficients, momentum efficiency and velocities of the sprays were then determined (Eqns.2.42, 4.9,4.11 and 4.7).

3.8.3 Combustion image analysis (SINL)

Natural flame emission collection is an extremely simple diagnostic to set up, not requiring any special filtering or intensification and allows for the relative comparison between cases when using an unfiltered lens as long as camera settings stay the same for each case [195]. The natural luminosity (NL) comes from chemiluminescence and soot incandescence radiation. In hydrocarbon flames, chemiluminescence was typically seen in the visible and near ultraviolet from the OH, CH, and C2 radicals [196]. Standard camera lens and CMOS sensors impedes ultraviolet observation thus OH chemiluminescence observation. CH chemiluminescence throughout the combustion process was weak compared with the radiation from soot [112]. The radiation emission was therefore dominated by incandescence from hot soot within the combustion chamber [197]. The soot thermal radiation has broadband emission spectrum and is referred to as soot luminosity. The intensity observed was the result of the combination of two effects: soot concentration and soot temperature. A flame would have the same NL intensity as another one presenting lower soot concentration but higher soot temperature [112, 198, 199]. It has been shown that spatially integrated NL (SINL) varies linearly with the soot emissions in diesel engine exhaust for several fuels and over a range of charge gas temperatures [194]. When

using the optical system described here, the luminosity was not exclusively from soot as the CMOS will inevitably recorded some low intensity chemiluminescence, the term natural luminosity (NL) is therefore used instead of soot luminosity. Imaging of the natural flame luminosity through the use of an optical engine has been a technique that has been used in a number of previous studies [112, 194, 195, 196, 197, 199, 200].

Integration of pixel value over the entire image gives the value of the SINL. The optical configuration for all cases was maintained to be the same which allows a fair comparison of the SINL for each different case. Eqn. 3.4 gives the SINL. A Matlab code was used that processed the images to get the SINL and acquire an average for 40 combustion cycles for each condition.

$$SINL = \frac{\sum_i \sum_j I_{i,j}}{N} \tag{3.4}$$

where $I_{i,j}$ is the flame intensity at pixel position (i, j) and N is the total pixel number [200].

3.9 Experimental Procedure

3.9.1 High Pressure Chamber Optical Data Collection Procedure

All experiments were conducted according to a developed protocol after considerable testing of the chamber to ascertain its ideal operating conditions. The different experimental conditions are summarized in Table.3.8 along with the nomenclature/legend used for each condition. Each condition nomenclature/legend follows the form; Fuel-Chamber Pressure-Injection Pressure i.e. D-20-500 refers to Diesel fuel injected into a ambient pressure of 20bar at a pressure of 500bar.

The chamber was charged to the desired pressure using the nitrogen gas. During charging the temperature in the chamber increased by approximately 6°C. After around 5 minutes the internal temperature of the nitrogen as indicated by the thermocouple reached an equilibrium with the ambient temperature in the lab of 20°C. For the two ambient pressures considered, 20 and 30 bar, once this equilibrium temperature had been reached, equate to ambient densities of ρ_a=22.6 kg/m^3 and ρ_a=34.5 kg/m^3 respectively. When the injections took place and the solenoid

Table 3.8: Summary of the experimental conditions with the naming scheme used.

Fuel	Ambient Pressure	Injection Pressure	Legend
Diesel(D)	20	500	D-20-500
		700	D-20-700
		1000	D-20-1000
Diesel+10% water(D10)	20	500	D10-20-500
		700	D10-20-700
		1000	D10-20-1000
Diesel+20% water(D20)	20	500	D20-20-500
		700	D20-20-700
		1000	D20-20-1000
Diesel(D)	30	500	D-30-500
		700	D-30-700
		1000	D-30-1000
Diesel+10% water(D10)	30	500	D10-30-500
		700	D10-30-700
		1000	D10-30-1000
Diesel+20% water(D20)	30	500	D20-30-500
		700	D20-30-700
		1000	D20-30-1000

valve was in operation, recharging of the chamber and subsequent equilibrium were reached within 2 minutes, hence the injection rate was conducted at a maximum of one every 2 minutes. For the shadowgraph images, injection duration was set at 0.5ms. Camera frame rate was set at 30,075 frames per second (fps) with a frame interval of 33.25μs. Exposure time was set at 31μs. The LED period was 33.25μs to match that of the camera, with the pulse width (period when LED was on) in this period set to 3μs. Hence the effective exposure time of each image was 3μs. After some experimentation, it was found that a frame delay of 10μs was needed to sync the camera and LED. Keeping the camera exposure longer than the LED flash duration aided in this syncing. At the end of injection the solenoid valve was opened for 2 seconds to purge the chamber. The camera was run in gated memory mode, no images pre-trigger were kept and post trigger 100 images were stored. It was found that after approximately 15 injections the windows would start to foul and would need cleaning. This effectively reduced the repetition of each condition to 15 injections. For the backlit collected image sequences, injection duration was maintained at 0.5ms. Camera frame rate was increased to 88,888 fps with a frame interval of 11.254μs. Exposure time was set to 9.25μs. The LED period was 11.25μs to match that of the camera, with the pulse width (on time) in this period set to 2μs. No frame delay was used to sync the camera and the LED. 100 images post trigger were stored. The same process of purging, charging and waiting for equilibrium were used as previously stated. The window fouling was not as much of a

problem as before because much of the fouling occurred in a region which was out of the cameras field of view. It was found that approximately 30 to 40 injections could be conducted before the windows needed cleaning. Repetition for each condition was around 30 injections.

When the fuel being examined was changed, the entire injection system was stripped down and drained. The common rail, any piping and the fuel tank were cleaned with compressed air. The injector was not removed from the chamber during this cleaning. When the new fuel to be tested was charged into the injection system, the injector was operated at 700 bar injection pressure with long injection duration (3ms) with a cap and tube attached to the nozzle. This was continued until the fuel that was primed in the system was present in the injected fuel and in the injector return with no trace of the previous fuel. This usually took around 1 minute of continuous injections. The fuel tank for the Diesel fuel and water emulsions was fitted with a stirring device to avoid any droplet separation/settling during the experiment.

3.9.2 High Pressure Chamber Hydraulic Data Collection Procedure

The experimental conditions examined were the same as those outlined in Section.3.9.1. As window fouling was not an issue to contend with the requirement to purge the chamber was removed between injections. The injection period (TTL duration) was kept the same as the optical experiments but the rest period between injections was reduced to 0.5 seconds. After 10 injections the chamber was purged for 2 seconds using the solenoid valve (Section.3.9) and the collected data saved to disk. This process was repeated 10 times for each condition, so a total of 100 injections for each condition were conducted. After each set of 10 injections it was necessary to reset the transducer charge amplifier. The fuel injection system was cleaned according to the process outlined in Section.3.9 between fuel changes.

3.9.3 Optically Accessible Combustion Chamber Data Collection Procedure

For each test case a defined procedure was followed. The engine was run on standard Diesel fuel and operated the OACC under motored conditions until the chamber wall temperature measured by the thermocouple reached 200°C. During this warm up period the air heater was also on. The LabView software was then used to initialize

injection into the external chamber. For all cases presented in this study an injection timing of −10CAD ATDC, injection mass of 8mg per injection and injection pressure was maintained at 500bar. For each case 40 injections took place. Due to restrictions in the DAQ and memory allocation available to the camera image grabber, all 40 injections recorded by the camera are not consecutive. The external chamber was operated continuously throughout the data collection period. All data presented is the arithmetic mean of these 40 injections. In the current configuration, operating at these conditions, window fouling was not found to be a problem.

3.10 Injection delay and Duration

The injection delay observed with the OACC has been dealt with in Sec.3.6.2. During operation of the high pressure chamber, for optical and hydraulic characterization tests, an injection delay was observed. The injection delay consists of two distinct parts. There was a portion of the delay which arises from the various electronics used which apply the current and voltage to the piezo stack in the injector. After user initiation of the injection via the LabView user interface a TTL signal was sent to the Hartridge driver. The piezo actuator was charged by a current spike of 5-9A and a voltage of approximately 140V. The driver consists of a number of power amplifiers and capacitors to achieve these currents and voltage. A portion of the electronic injection delay was due to the driver. The piezo actuator in the injector has a charge time of approximately 150μs [201] and accounts for the other portion of the electronic injection delay. The second portion of the delay arises due to the hydraulic action of a mushroom valve and the needle inside the injector. This may be referred to hydraulic delay. The injection delay, measured from the shadowgraph system image sequences, the backlit image sequence and the momentum flux measurements are shown in Fig.3.27. For the optical measurements, the delay was determined from the number of image frames present before spray was visible. For the momentum flux measurements, the delay was determined from the period recorded when there was no force measured by the transducer after the TTL triggered the recording of the voltage signal.

The portion of the delay which was hydraulic is not known but for each injection pressure it was not the same. As the injection pressure was increased, the injection delay increases. The increase in injection pressure will have no influence on the electronic delay as the pressure was controlled via a separate air circuit. Hence the increase in injection delay observed with increasing injection pressure was only

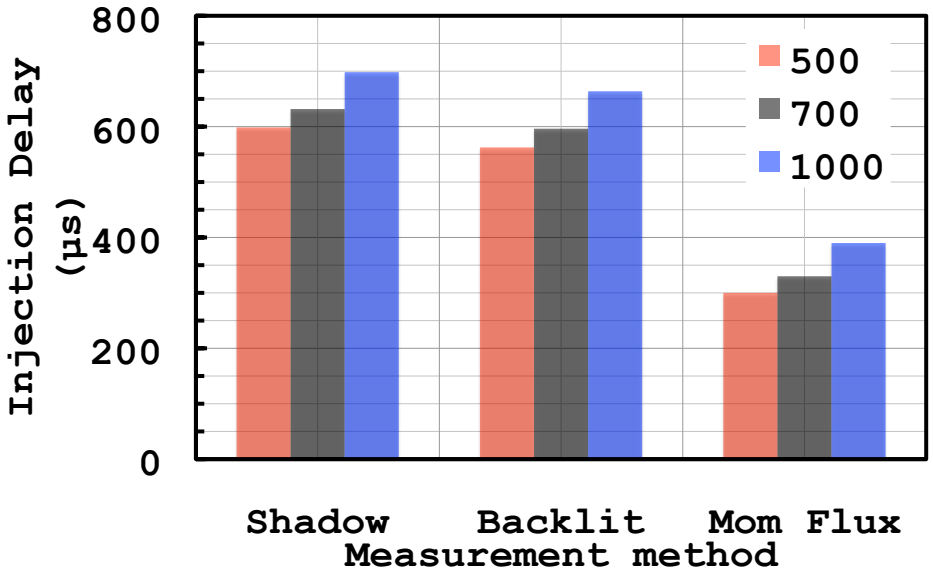

Figure 3.27: The injection delay (in μs). The time after the TTL signal had been initiated and sent to the injector driver and the injection started. Delay determined using the image sequences collected using the shadowgraph system (shadow), the backlit system (backlit) and the force transducer measuring the momentum flux (mom flux) The delay for injections of 500, 700 and 1000bar are shown.

hydraulic. This portion of the delay has remained the same irrespective of the measuring technique, i.e the increase in delay with increasing injection pressure was the same for the optical and momentum flux measurements. For the data sets collected optically the injection delay was around 300μs longer than the delay from the momentum flux data. Although the end of injection was not well defined optically, the duration of the optically measured injections also increased by approximately 300μs compared with the momentum flux experiments.

The only difference in the experimental system and conditions between the optical sets of data and the momentum flux data was the inclusion of a camera in the system. During momentum flux measurements the camera was not available so was not plugged into the data acquisition circuit. During optical characterization tests, the charge amplifier and transducer were not unplugged from the system. The addition of the camera has lead to a increase in the injection delay. This is explained as follows: The TTL signal connection for the injector driver was the same connection that was used for the camera trigger. For all experiments in this study, the TTL signal was high (on) for 0.5ms. With the camera included and the TTL connection

made, the injector driver has not operated as expected. It is understood that the additional electrical connection has lead to another earth connection. Considering the rapid charge times required of the driver circuit, any charge leakage due to the addition of signal cabling may have a relatively large (i.e 300μs) effect. This seems the most likely cause as the TTL signal from the LabView program was recorded and was not effected by the addition of the camera trigger cable. The injector driver used was a cheaper model that was not 100% ideal for laboratory work of this nature and was determined to be the factor that introduced this fault. Overall the discrepancy has no effect on the injection event in terms of spray character or momentum profile but does have an effect on the post processing and any analysis comparing the optical data and the momentum data sets.

4. Results and Discussion

Introduction

In the following sections the results collected are presented. The optically determined spray characteristics for Diesel fuel, D10 and D20 are presented first. These have been collected from sprays in the high pressure chamber. Image collection was achieved with the shadowgraph and the backlit systems.

The hydraulically determined spray characteristics for Diesel fuel, D10 and D20 are presented next. These have been collected in the high pressure chamber. Spray momentum flux was recorded using the momentum device. Results presented include: spray momentum flux; total mass injected; instantaneous mass flow rate; injection velocity; nozzle discharge coefficient; momentum coefficient and; momentum efficiency.

The preliminary findings of a combustion characterization experiment with Diesel fuel and D10 in the OACC are presented last. High speed imaging collection has been used to collect natural luminosity images which have been used to determine the SINL. Chamber pressure is also presented. The ignition delays and SINL in relationship to soot are discussed.

4.1 Spray Cone angle and Tip Penetration

In the following section the spray angle(θ) results for Diesel fuel (D) injections, determined using the triangle technique are presented. The spray shadowgraph images collected for Diesel sprays are presented, complete with post processing.The same image sequences for D10 and D20 are presented in App.D and App.E. The calculated angles are then presented. The spray angle has been calculated at a tip penetration of 50% (S/2) and referred to as θ_S.

Following this the spray angles determined using the backlit, near-field images are presented and referred to as θ_B. For this calculation the angle is calculated at 70% of the tip penetration. The two angles (θ_S and θ_B) are then presented together for comparison of the measuring technique applied. The tip penetrations, determined as part of the triangle technique for both shadowgraph and backlit image sequences are then presented (S_S and S_B respectively). These results are then discussed and any correlations, trends and observations made.

4.1.1 Shadowgraph Spray Angle

Fig.4.1-4.11 shows an example set of Diesel fuel spray images collected using the shadowgraph system complete with the image processing stages used to determine the θ_S. Fig.4.1-4.8 are the first image collected in which spray was present progressing though the collected images sequentially until Fig.4.8, these are included to show the spray during its earlier transient period. Fig.4.9, 4.10 and 4.11 are the images collected at time $t = 399, 731.50$ and 1064μs respectively and are included to show the spray as it is approaching it's quasi-steady, quasi-constant θ period. The same image sequences for D10 and D20 are presented in App.D and App.E.

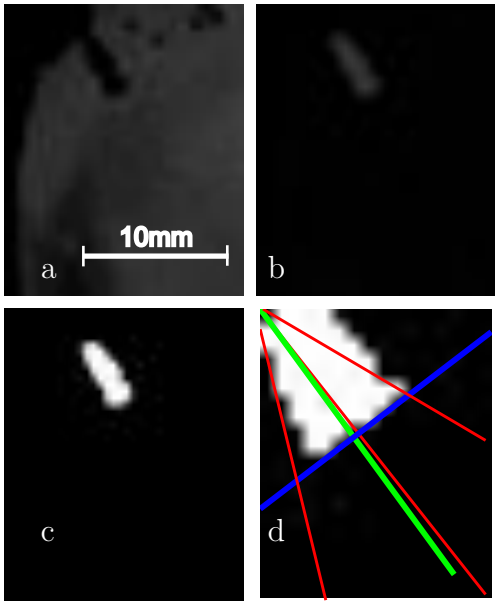

Figure 4.1: Shadowgraph Diesel spray image at the SOI $t = 0\mu$s (first frame containing spray). (a)Raw image, (b)Complement image, (c)Black and white image, (d)Cropped, processed measurement image.

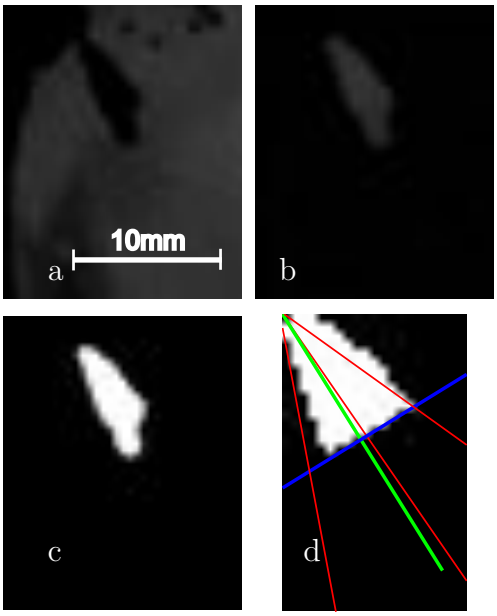

Figure 4.2: Shadowgraph Diesel spray image at $t = 33.25\mu$s (second frame containing spray). (a)Raw image, (b)Complement image, (c)Black and white image, (d)Cropped, processed measurement image.

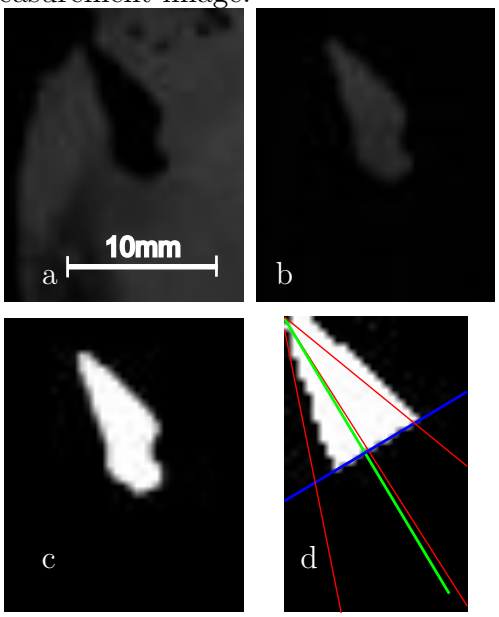

Figure 4.3: Shadowgraph Diesel spray image at $t = 66.50\mu$s (third frame containing spray). (a)Raw image, (b)Complement image, (c)Black and white image, (d)Cropped, processed measurement image.

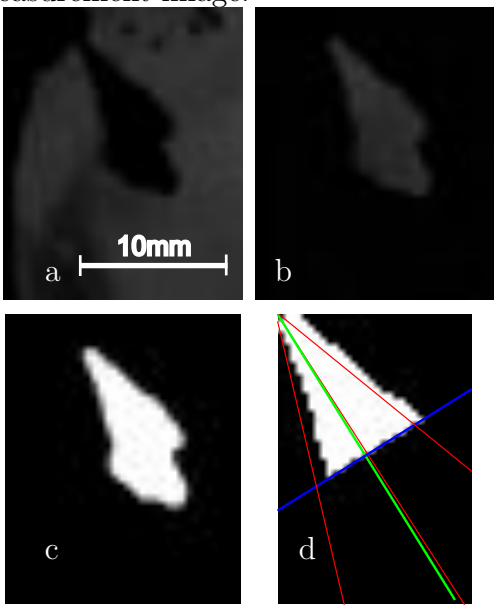

Figure 4.4: Shadowgraph Diesel spray image at $t = 99.75\mu$s (fourth frame containing spray). (a)Raw image, (b)Complement image, (c)Black and white image, (d)Cropped, processed measurement image

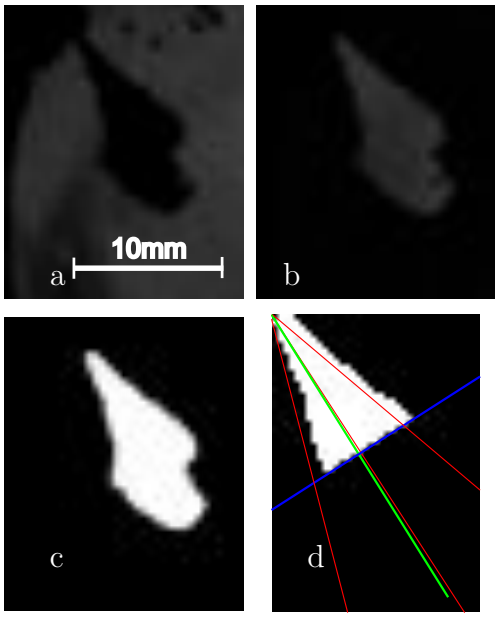

Figure 4.5: Shadowgraph Diesel spray image at $t = 133\mu$s (fifth frame containing spray). (a)Raw image, (b)Complement image, (c)Black and white image, (d)Cropped, processed measurement image

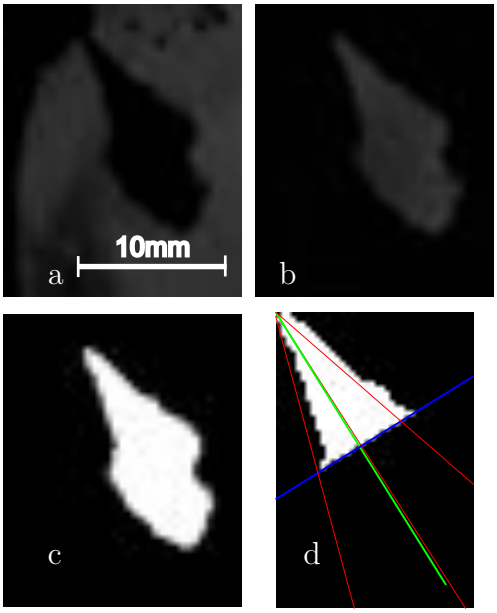

Figure 4.6: Shadowgraph Diesel spray image at $t = 166.25\mu$s (sixth frame containing spray). (a)Raw image, (b)Complement image, (c)Black and white image, (d)Cropped, processed measurement image

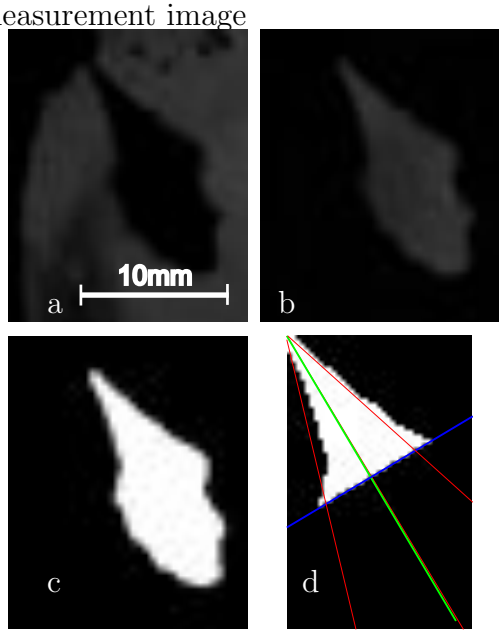

Figure 4.7: Shadowgraph Diesel spray image at $t = 199.50\mu$s (seventh frame containing spray). (a)Raw image, (b)Complement image, (c)Black and white image, (d)Cropped, processed measurement image

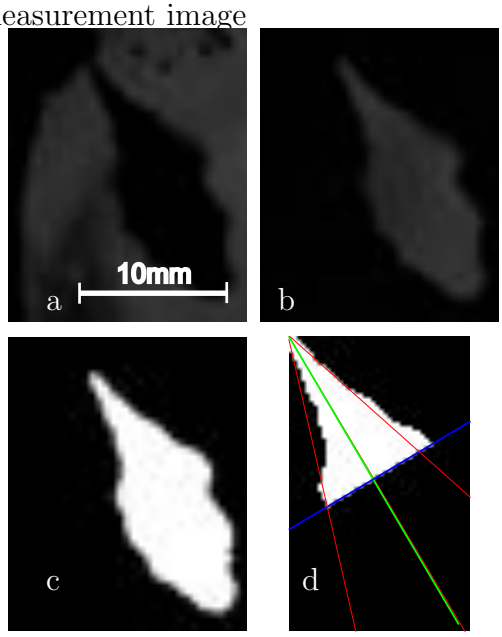

Figure 4.8: Shadowgraph Diesel spray image at $t = 232.75\mu$s (eighth frame containing spray). (a)Raw image, (b)Complement image, (c)Black and white image, (d)Cropped, processed measurement image

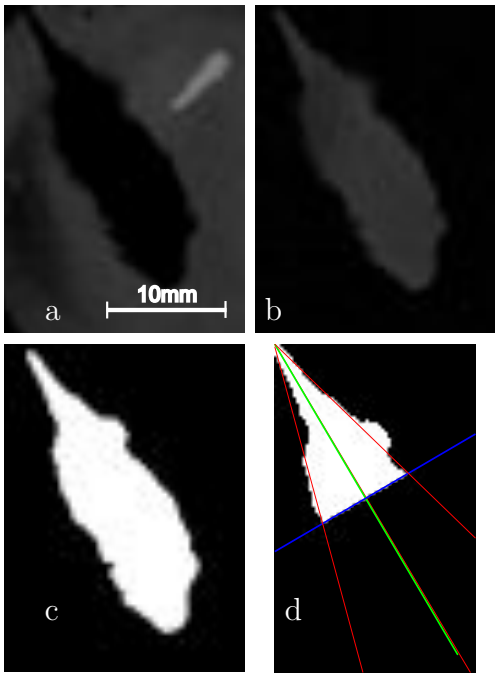

Figure 4.9: Shadowgraph Diesel spray image at $t = 399\mu$s (thirteenth containing spray). (a)Raw image, (b)Complement image, (c)Black and white image, (d)Cropped, processed measurement image

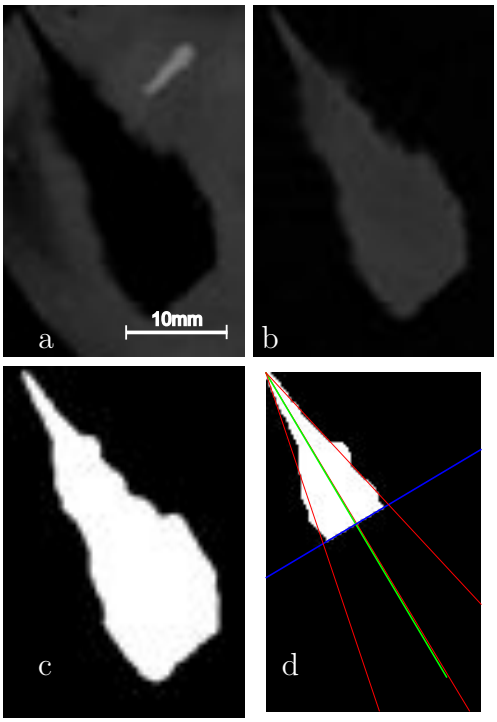

Figure 4.10: Shadowgraph Diesel spray image at $t = 731.50\mu$s (twenty third frame containing spray). (a)Raw image, (b)Complement image, (c)Black and white image, (d)Cropped, processed measurement image

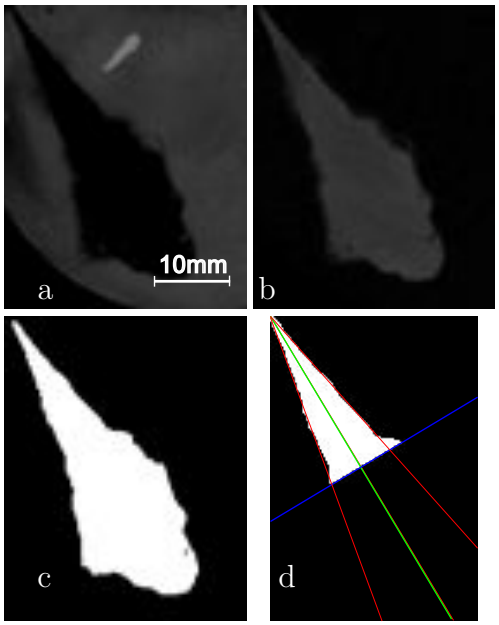

Figure 4.11: Shadowgraph Diesel spray image at $t = 1064\mu$s (thirty third frame containing spray). (a)Raw image, (b)Complement image, (c)Black and white image, (d)Cropped, processed measurement image

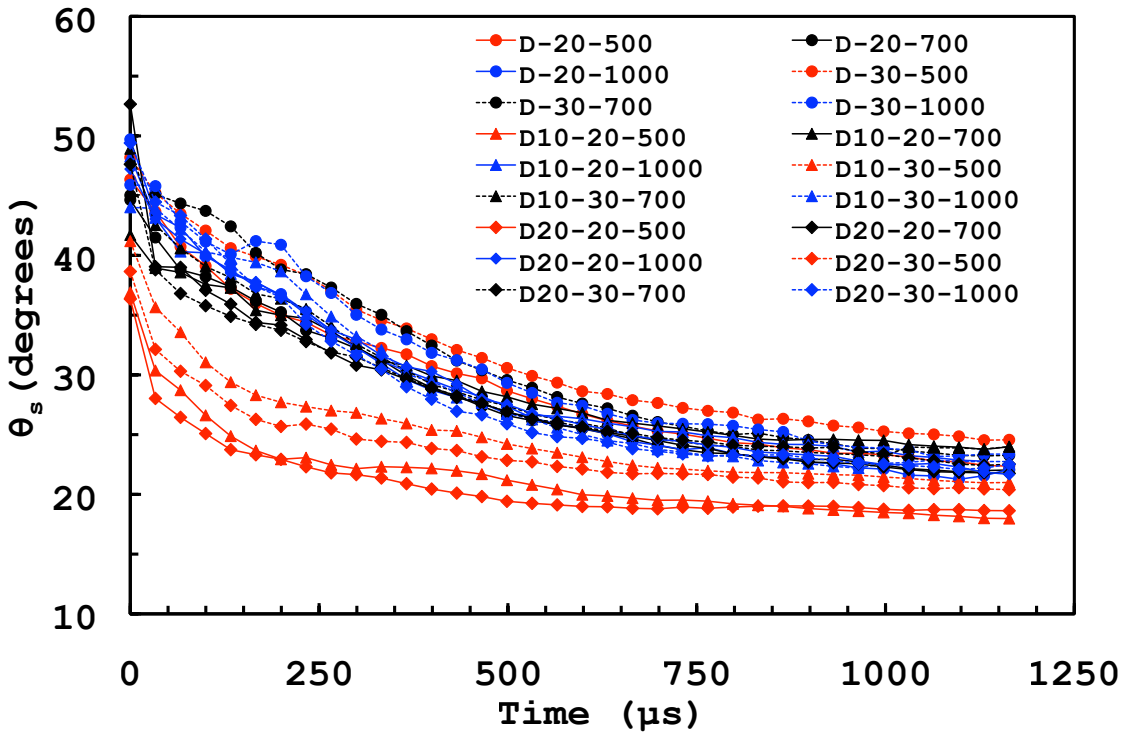

Figure 4.12: Fuel injection spray angle variation with time for all conditions with Diesel fuel (circle), D10 (triangle) and D20 (diamond). ρ_a = 22.6 kg/m^3 (P_{amb}= 20bar) shown with solid lines. ρ_a=34.5 kg/m^3 (P_{amb}= 30bar) shown with broken line. All injections at 500 bar are shown with a red line, 700 bar with a black line and 1000 bar with a blue line. Determined using the shadowgraph image sequences.

Fig.4.12 shows temporal evolution of θ_S for Diesel fuel, D10 and D20 at all conditions tested. The interval between each time step is 33.25μs. The plot has been constructed with the injection delay period removed so that the plot only includes the period that spray occurred for. The time at which spray started, which equates to the first frame in which spray was evident has been set a $t = 0$ for each condition. This allows a fair comparison between the actual spray structure evolution with time ignoring the hydraulic injection delay. The end of injection (EOI) was not well defined in the θ_S calculation and a cut off of frame number 55 (t = 1829μs after SOI) was used for all cases.

For all conditions the θ_S shows a similar trend. As injection starts, θ_S has a value between 36° and 52°. As the injection continues, θ_S decreases and appears to approach (quasi) constant values between 18° and 24° after approximately 1000μs. Cares is needed when making any inferences during the early period (t = 0 to t = 750μs) from the measurement of θ_S as it is during this period that the spread of the measured θ_S for each condition is large. This is demonstrated by the size

of the standard deviation (σ).Fig.4.13 shows that for all conditions, the standard deviation of the measured θ_S (for the 15 injection events used to determine the mean) reduces during the injection period which coincides with the period in which the spray may be considered to become quasi-steady. The standard deviation of the θ_S is an indicator of the highly transient unsteady nature of the early stages of the spray.

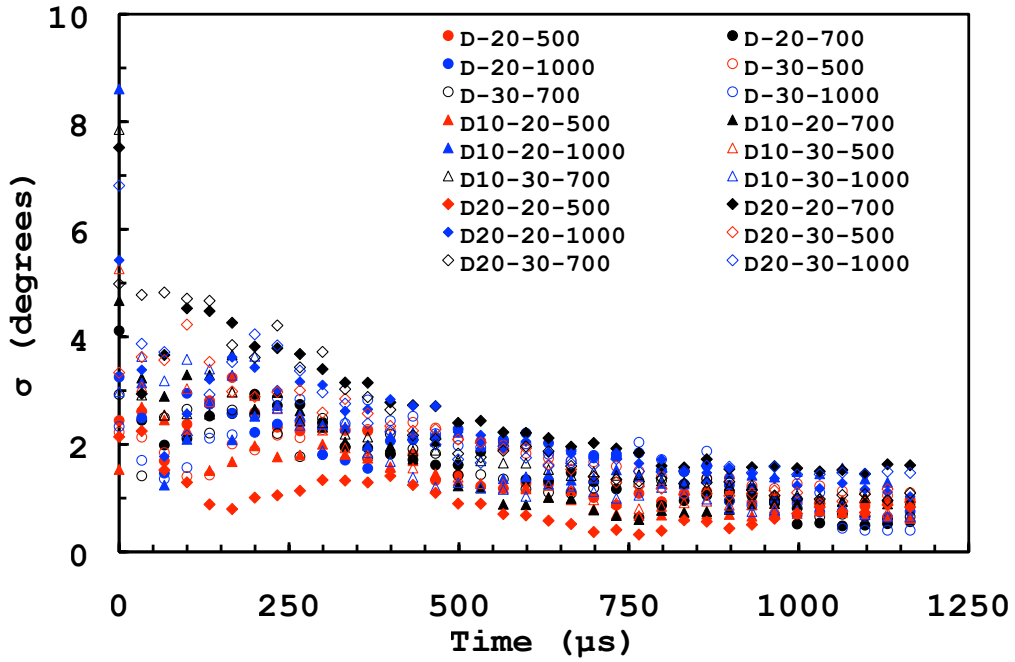

Figure 4.13: Temporal evolution of the standard deviation of the measured θ_S's for the 15 injection events used to calculate the mean θ_S for all conditions with Diesel fuel (circle), D10 (triangle) and D20 (diamond). ρ_a = 22.6 kg/m^3 (P_{amb}= 20bar) shown with solid symbols. ρ_a=34.5 kg/m^3 (P_{amb}= 30bar) shown with empty symbols. All injections at 500 bar are shown with in red, 700 bar in black and 1000 bar in blue. Determined using the shadowgraph image sequences.

Table.4.1 shows some spray cone angles (from period of constant value) and the time after SOI when the angle was observed to become constant (transition time) that have been presented in previous works. Table.4.1 shows that the θ trend and values observed here are comparable with previous work but also highlights the variability of the measured values of θ. Taskiran and Ergeneman [92] observed that there is often little discussion of the variation of θ with time reported in the literature. Empirical models, such as those of Nabers and Siebers [97] and Hiroyasu and Arai [98] are developed using the quasi-steady, quasi-constant angle period of the sprays (fully developed zone) [102]. Considering that the time involved for the spray to reach its quasi-steady, quasi-constant angle was of the same order as a typical ignition delay period in a CI engine, any influence on mixing, global and

Table 4.1: Spray cone angles and transient times observed in previous studies

Previous Study	θ°	Transition time (μs)
[97]	20	500
[92]	20	400
[95]	15-20	600
[143]	20	300
[144]	15	1000-1200
[123]	10-18	150
[89]	30	1000
[145, 146]	-	300
Here	21-27	1000

localized equivalence ratios is of interest.

It is evident in Fig.4.12 that there are a number of injections that have a significantly smaller θ_S. These are for the D10 and D20 fuel spays at P_{inj}=500 bar, for both the ambient densities considered. This observation is examined in Fig.4.14 and Fig.4.15. These figures show the same data presented Fig.4.12 but displayed in two plots, separated by the ambient density into which the injection took place; 22.6 kg/m^3 (P_{amb}=20bar) and 34.5 kg/m^3 (P_{amb}=30bar) respectively. Both figures include error bars with a size of one standard deviation (σ) from the mean.

Fig.4.14 and Fig.4.15 both show that varying the injection pressure has little effect on the the measured θ_S of neat Diesel fuel injection sprays. This is in accordance with previous works [95, 96, 97, 98, 99, 101] which have found the spray angle for complete atomized sprays to be independent of injection conditions (P_{inj}) and only dependent on the gas density. For the emulsified fuel, D10 and D20, with a P_{inj}=500 bar, there is a distinct reduction in the measured θ_S compared to the same injections at P_{inj}=700 and 1000 bar. Both D10 and D20 sprays have a very similar spray angle at P_{inj}=500 bar for ρ_a=22.6 kg/m^3. As P_{inj} is increased to 700 and 1000 bar with ρ_a=22.6 kg/m^3, the spray angles for the D10 and D20 injections essentially become the same as the spray angles of the neat Diesel fuel injections at these conditions. The measured spray angles at this ambient density also exhibit a smaller standard deviation when compared to the measured angles at the ambient density of 34.5 kg/m^3. The error bars of the D10 and D20, P_{inj}=500 bar ,injections overlap with each other but not at all with the other error bars. This shows a statistically significant results.

The difference between the D10, D20 and the neat Diesel fuel spray angle at P_{inj}=500 bar are not so pronounced at the higher ambient density. This is evidenced

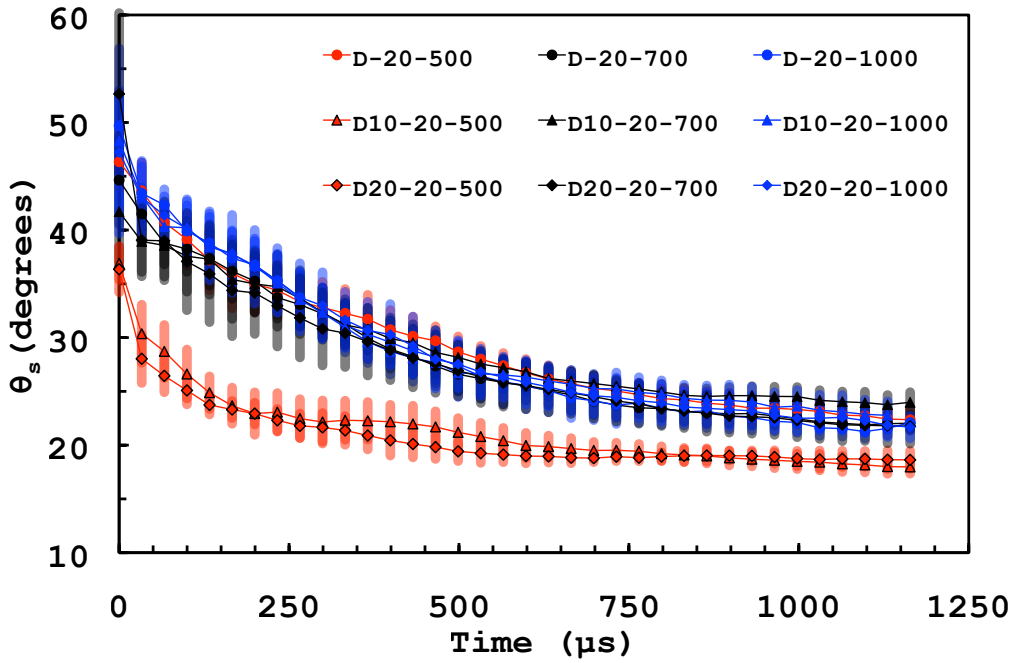

Figure 4.14: Fuel injection spray angle variation with time with Diesel fuel (circle), D10 (triangle) and D20 (diamond) and ambient tags density $\rho_a = 22.6$ kg/m^3 P_{amb}= 20bar. All injections at 500 bar are shown in red , 700 bar in black and 1000 bar in blue line. Determined using the shadowgraph image sequences. Error bars are the size of one standard deviation for the 15 injections used to calculate the mean

by the larger standard deviation of the angles at the higher density, with considerable overlap of the error bars. At the higher ambient density, the spray angle of the D10 and D20 at P_{inj}=500 bar is smaller than the angle for the 700 and 1000 bar injections during the early period of the injection. As the injection progresses, the θ_S of D10 and D20 at 700 and 1000 bar start to approach the same angle as the neat Diesel sprays. By the EOI at the higher ambient density, the D10 and D20 P_{inj}=500 bar injection spray angles are still smaller but the variation has been reduced. It is evident that the emulsification process is having an impact on the fuel spray angle at the injection pressure of 500 bar. The difference between the two emulsions is small at this injection pressure. The emulsification process appears to have reduced the spray angle when compared with the neat Diesel sprays (at P_{inj}=500 bar) by between 3 to 4.5° approximately.

Fig.4.12 shows that for all injection pressures, an increase in ρ_a leads to an increase in the spray cone angle of the neat Diesel fuel sprays but not for the emulsified fuels. This is shown a little more clearly in Fig.4.16 which shows the average, quasi-steady spray angle (θ_{Sav}) from the arithmetic mean of the final 5 θ_S values (time after SOI=1097μs to 1230μs) for each condition. This value is used as representative of the spray cone angle for each condition. In Fig.4.16 the measured θ_{Sav} for the

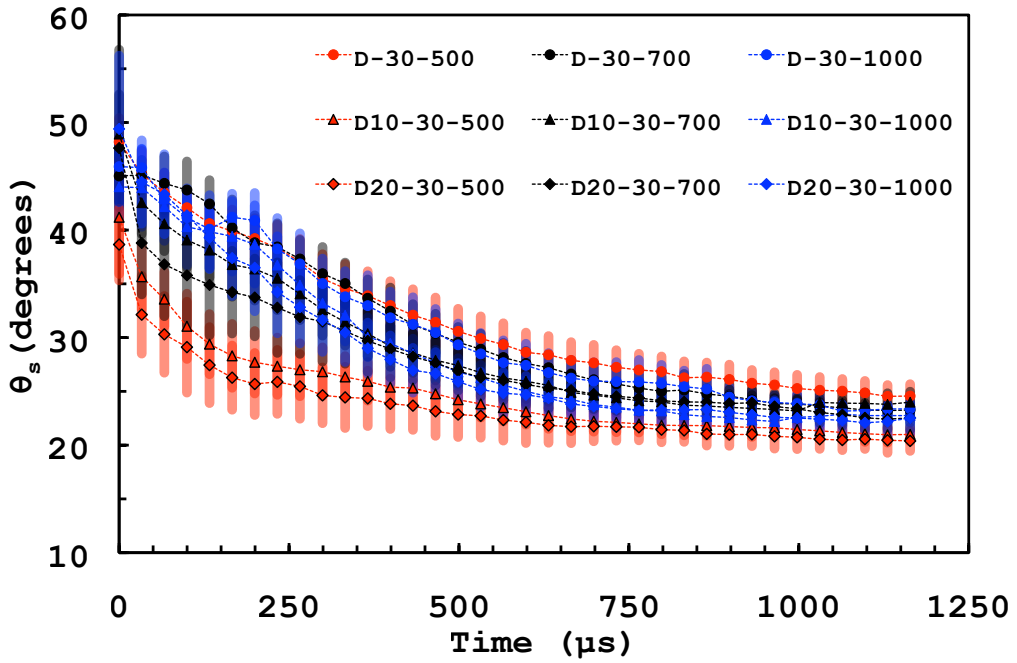

Figure 4.15: Fuel injection spray angle variation with time with Diesel fuel (circle), D10 (triangle) and D20 (diamond) and ambient tags density $\rho_a = 34.5$ kg/m^3 P_{amb}= 30bar. All injections at 500 bar are shown in red , 700 bar in black and 1000 bar in blue line. Determined using the shadowgraph image sequences. Error bars are the size of one standard deviation for the 15 injections used to calculate the mean.

neat Diesel fuel are of a similar value for each injection pressure at the same ambient density. As the ambient density is increased, θ_{Sav} has shown a small increase as well. For the D10, the θ_{Sav} of the 500 bar injection at each ambient density is much lower than for the 700 and 1000 bar injections, as has been discussed previously. Also, the small increase in the θ_{Sav} with the increase in ambient density is not observed for the 700 and 1000 bar injections. This trend is repeated for the D20 fuel sprays. The increase in θ_{Sav} that would be expected with the increase in ambient density is observed with the emulsified fuels at 500 bar injection.

As has been shown in Sec.2.4.1, the spray angle is shown to be a function of the ratio of the ambient (gas) density and fuel (liquid) density (ρ_a/ρ_f). Comparing with previous work, the range of density ratios in this study is limited, with only two chamber pressures being used, 20 and 30bar; resulting in two ambient densities of (ρ_a) of ρ_a=22.6 kg/m^3 and ρ_a=34.5 kg/m^3 respectively. The emulsification process has resulted in a variation of the fuel density as well. The fuel densities have been measured in the process outlined in Sec.3.7.2 with values of 814, 829 and 876 kg/m^3 for D, D10 and D20 respectively. The density ratio range is 0.026-0.042 and is lower than that of a modern, turbo-charged common rail CI engine. Acknowledging the

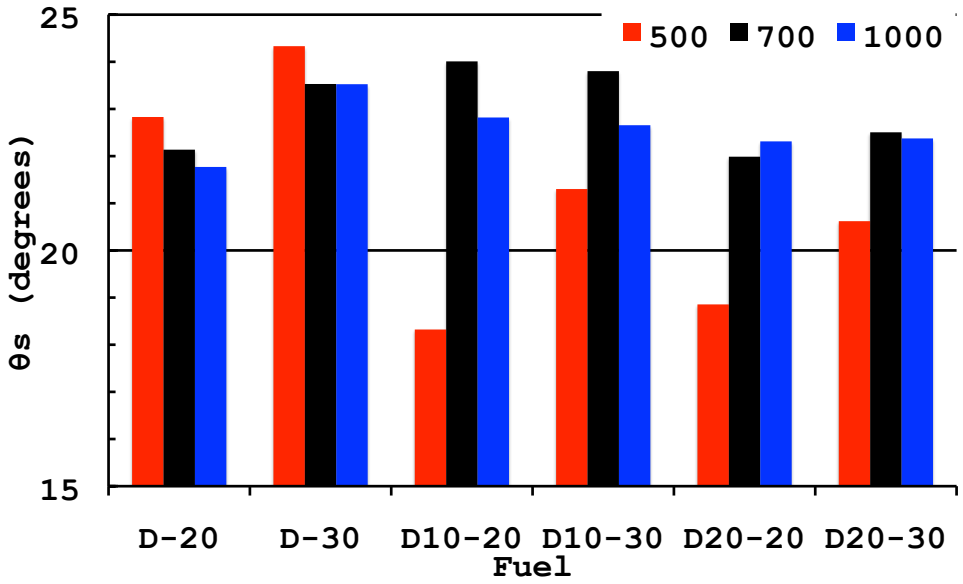

Figure 4.16: Representative spray cone angle value taken from the quasi-steady, near constant period at the EOI for Diesel fuel, D10, D20 at each condition.All 500 bar injections iare in red, 700 bar in black and 1000 in blue.-20 are injections are with ρ_a = 22.6 kg/m^3 P_{amb}= 20bar, -30 are injections with ρ_a = 34.5 kg/m^3 P_{amb}= 30bar.

limited range of data available, an attempt has been made to present the spray cone angle variation with density ratio in a similar manner as has been presented in Sec.2.4.1. Figs.4.17, .4.18 and .4.19 show the variation of the average, quasi-steady spray angle (θ_{Sav}) with the density ratio ρ_a/ρ_f for Diesel fuel, D10 and D20 sprays respectively. The plots for each fuel have been separated to aid clarity.

For each of the Figs.4.17, 4.18 and 4.19, the red broken line is fitted to the 500 bar injection, the black broken line to the 700 bar injections and the blue broken line to the 1000 bar injections. The exponent of the density ratio (a where $\theta \propto (\rho_a/\rho_f)^a$) for each injection pressure and fuel has been determined using logarithms. For the neat Diesel fuel sprays, Fig.4.17, each injection pressure shows a similar trend with the dependence on the density ratio for each pressure very similar $(\rho_a/\rho_f)^{0.14-0.18}$. These values are in accordance with previous findings for Diesel fuel sprays. The injection pressure has had little, to no effect and the increase in density ratio results in an increase of the spray cone angle. For the two emulsified fuels, D10 and D20, Figs.4.18 and 4.19, the 500 bar injections have a much smaller spray angle at the lower density than for the 700 and 1000 bar injections. The spray angle of the 500 bar injections do increase with the increasing density ratio, with a= 0.35 and 0.21 (D10 and D20 respectively). The angle for the 500 bar injections for both emulsified fuels is smaller than it's neat Diesel counterpart.

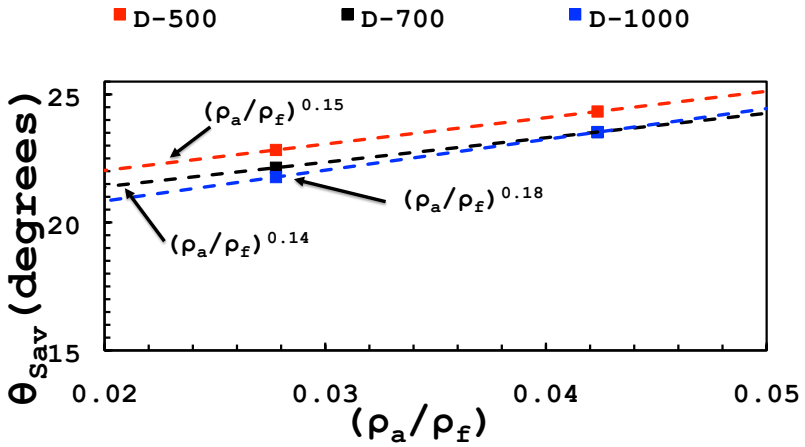

Figure 4.17: Variation of the θ_{Sav} of Diesel fuel spray with ρ_a/ρ_f. P_{inj}= 500(red), 700(black) and 1000 bar(blue). Trend line has been fitted to the points for each injection pressure with the exponent shown.

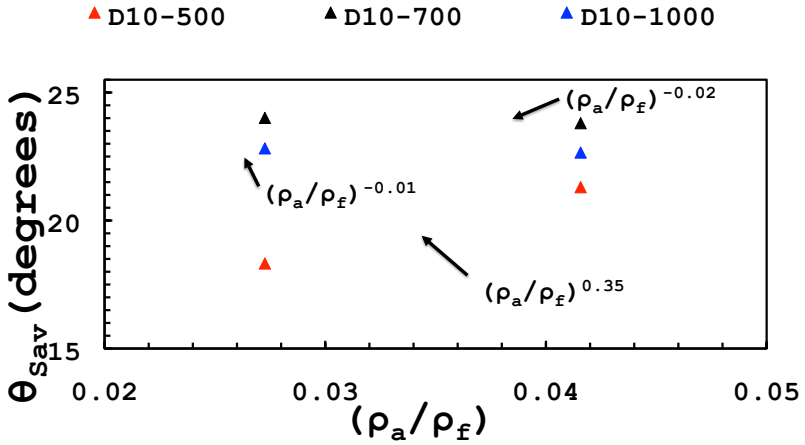

Figure 4.18: Variation of the θ_{Sav} of D10 fuel spray with ρ_a/ρ_f. P_{inj}= 500(red), 700(black) and 1000 bar(blue). Linear trend line has been fitted to the points for each injection pressure with the exponent shown.

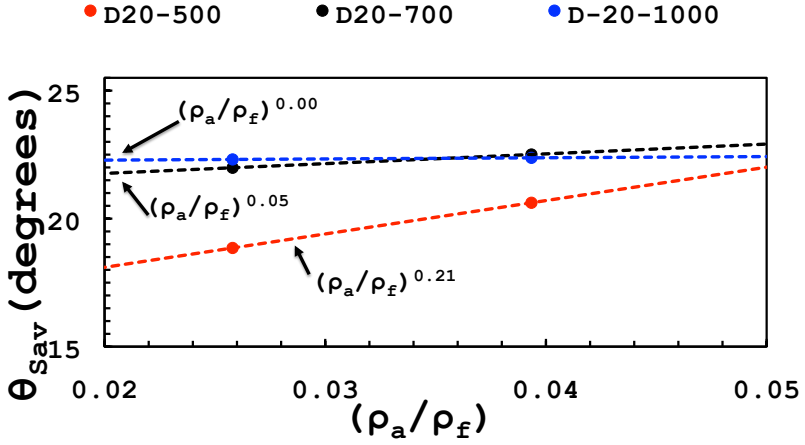

Figure 4.19: Variation of the θ_{Sav} of D20 fuel spray with ρ_a/ρ_f. P_{inj}= 500(red), 700(black) and 1000 bar(blue). Linear trend line has been fitted to the points for each injection pressure with the exponent shown.

The increase in spray angle with density ratio is not observed for the two emulsified fuels at the injection pressures of 700 and 1000 bar. This is demonstrated by the small value of a for these conditions; -0.02 (700 bar, D10 injections) to 0.05 (700 bar, D20 injections). Figs.4.18 and 4.19 support the statement that the emulsified fuels, at 700 and 1000 bar injection pressure, show no change in the spray angle with changing ambient density.

The values of a have been determined using two data points. The findings are not being overstated or stated outside of the measurement range of the experimentation conducted here, the limitations of the findings are accepted. The values determined for the neat Diesel fuel are reasonable when compared with previous findings so it is fair to say that the values should also be realistic for the emulsified fuels. The value of a determined is being used as an indicator of any effects the emulsification may have had and not as a fundamental finding of the sprays. The value a for the D10 and D20 at 500 bar suggests that at P_{inj}=500 bar, the emulsification results in the ambient density increase having a larger effect on the spray cone angle compared with neat Diesel but the actual value of the spray angle is reduced relative the neat Diesel sprays at these conditioned. The emulsification has suppressed the effect of the ambient density increase for the 700 and 1000bar injection pressures.

4.1.1.1 Summary

- Sequences of consecutive images of Diesel fuel, D10 and D20 injection sprays were collected using the shadowgraph system at a frame rate of 33,000fps.
- Image sequences were used to determine the spray cone angle for fuel sprays at injection pressures of 500, 700 and 1000 bar, into two ambient densities of 22.6 kg/m^3 and 34.5 kg/m^3 of nitrogen (20 bar and 30 bar ambient pressure respectively). For each injection condition, a total of 15 injections were used to determine the mean spray angle.
- Matlab image processing was applied to determine the angle from the image sequences.
- For all conditions the measured angle started at between 36 to 52 degrees. As the injections progressed, the angle gradually decreased until around 1000μs after the SOI where the angle appeared to approach a quasi-steady value of between 18 and 24 degrees for all conditions.
- The standard deviation of the mean, from the 15 injections used, reduced in value as the injections progressed, suggesting the spray forms a more stable

less transient angle as the injections progressed.

- The final portion of the measurement was used to extract quasi-steady values of the spray angle for each condition for comparison purposes.
- The injection pressure had no discernible influence on the spray angle for the Diesel fuel sprays. For D10 and D20 the spray angles with a 500 bar injection pressure were considerably smaller than the spray angles for the 700 and 1000 bar injections.
- An increase in the ambient density resulted in a larger spray angle for the Diesel fuel sprays. For the D10 and D20 sprays, the increase in ambient density resulted in an increase in the spray angle for the 500 bar injections but not for the 700 and 1000 bar injections.
- With an injection pressure of 500 bar, both emulsions had a smaller spray angle than Diesel fuel at the same conditions.

4.1.2 Backlit Spray Angle

Due to experimental restrictions, a full data set was not collected. The only emulsion that was tested using the backlit system was the 10% water emulsion, D10. Also, due to an experimental data collection error, the full time scale of injection was not collected for the D10-20-500 condition. The wrong frame number was applied and the final half of the injection period was not captured and recorded by the camera. This test condition was unable to be repeated to fill in the missing data.

During the early period of the spray, in the images collected, the visible part of the spray is very short and it's shape is not consistent with the classical, conical shaped spray model. This makes the angle measurement difficult to state. Fig.4.20 shows a set of example images taken from the first frame ($t = 0$) when spray first appeared for a fuel injection spray of Diesel fuel (P_{amb}= 20bar, P_{inj}= 500bar). The set shows: the raw image as collected by the camera(a); a complement (negative image) (b); an Otsu threshold, black and white image (c); a bounding box cropped image with the derived spray axis, tip penetration, axis perpendicular and derived spray angle (d). Fig.4.21 shows the same set of images taken from the next frame in the image sequence recorded by the camera.

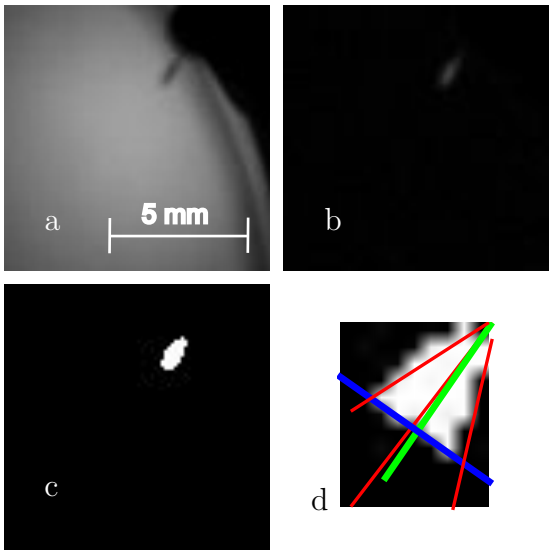

Figure 4.20: Backlit Diesel fuel spray image at the SOI $t = 0\mu$s (first frame containing spray). (a)Raw image, (b)Complement image, (c)Black and white image, (d)Cropped, processed measurement image.

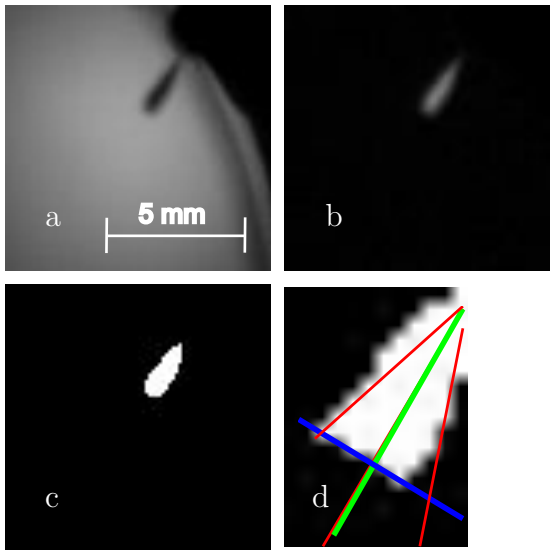

Figure 4.21: Backlit Diesel fuel spray image $t = 11.25\mu$s (second frame containing spray) after the SOI. (a)Raw image, (b)Complement image, (c)Black and white image, (d)Cropped, processed measurement image.

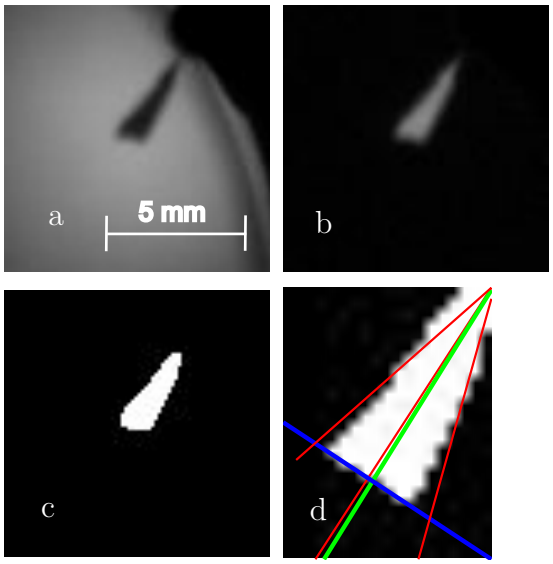

Figure 4.22: Backlit Diesel fuel spray image $t = 22.50\mu$s (third frame containing spray) after the SOI. (a)Raw image, (b)Complement image, (c)Black and white image, (d)Cropped, processed measurement image.

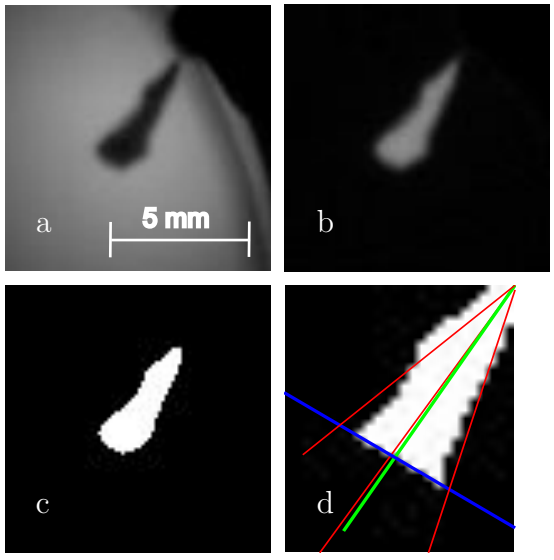

Figure 4.23: Backlit Diesel fuel spray image $t = 33.75\mu$s (fourth frame containing spray) after the SOI. (a)Raw image, (b)Complement image, (c)Black and white image, (d)Cropped, processed measurement image.

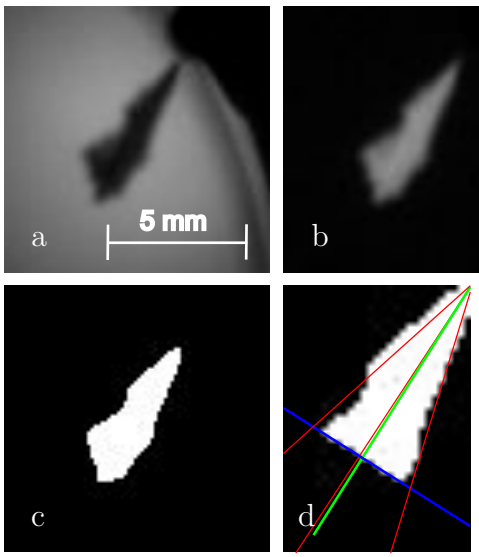

Figure 4.24: Backlit Diesel fuel spray image $t = 45\mu$s (fifth frame containing spray) after the SOI. (a)Raw image, (b)Complement image, (c)Black and white image, (d)Cropped, processed measurement image.

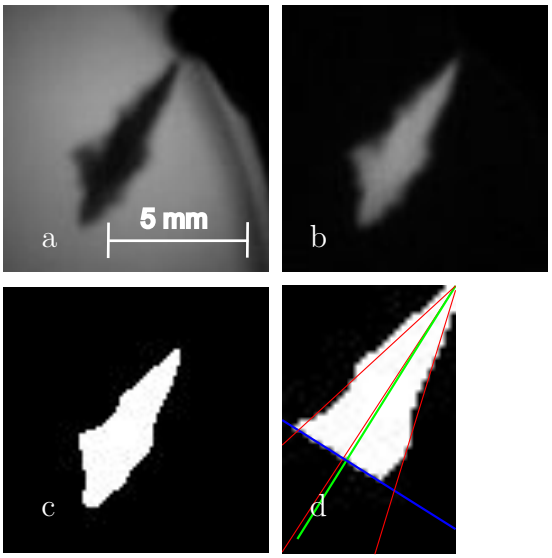

Figure 4.25: Backlit Diesel fuel spray image $t = 56.25\mu$s (sixth frame containing spray) after the SOI. (a)Raw image, (b)Complement image, (c)Black and white image, (d)Cropped, processed measurement image.

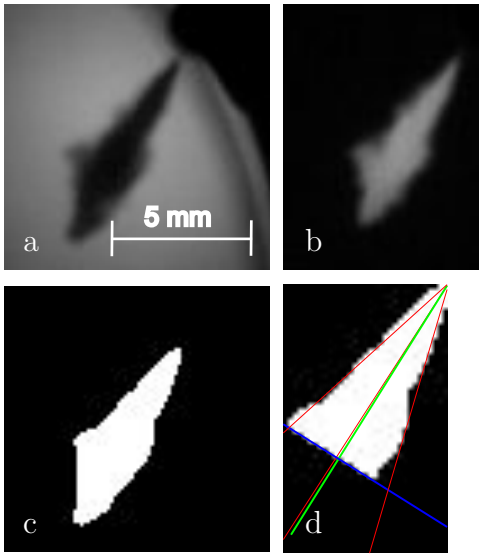

Figure 4.26: Backlit Diesel fuel spray image $t = 67.50\mu$s (seventh frame containing spray) after the SOI. (a)Raw image, (b)Complement image, (c)Black and white image, (d)Cropped, processed measurement image.

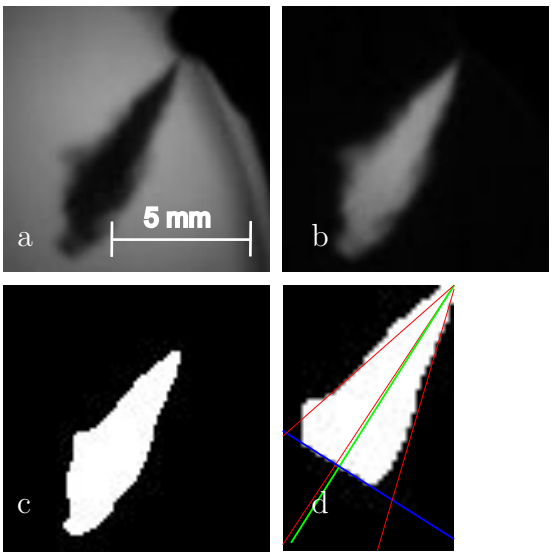

Figure 4.27: Backlit Diesel fuel spray image $t = 78.75\mu$s (eighth frame containing spray) after the SOI. (a)Raw image, (b)Complement image, (c)Black and white image, (d)Cropped, processed measurement image.

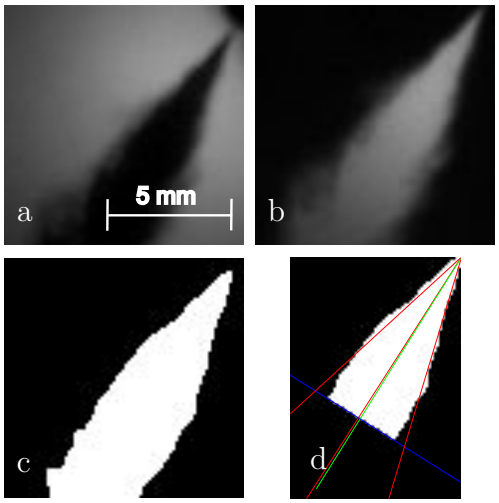

Figure 4.28: Backlit Diesel fuel spray image $t = 258.75\mu$s (twenty third frame containing spray) after the SOI. (a)Raw image, (b)Complement image, (c)Black and white image, (d)Cropped, processed measurement image.

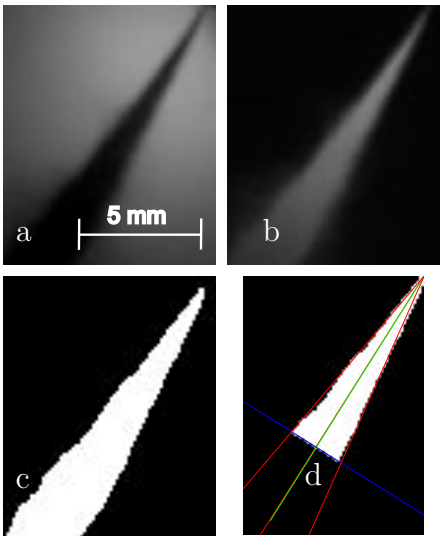

Figure 4.29: Backlit Diesel fuel spray image $t = 742.50\mu$s (sixty sixth frame containing spray) after the SOI. (a)Raw image, (b)Complement image, (c)Black and white image, (d)Cropped, processed measurement image.

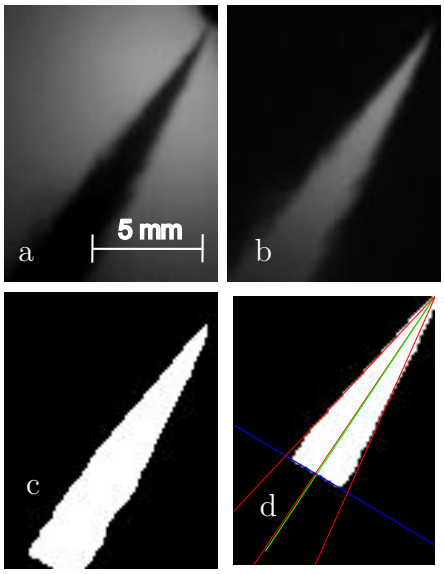

Figure 4.30: Backlit Diesel fuel spray image $t = 1001.25\mu$s (eighty ninth frame containing spray) after the SOI. (a)Raw image, (b)Complement image, (c)Black and white image, (d)Cropped, processed measurement image.

Figs.4.20 and 4.21 show that the initial spray shape recorded is not the classical, conical shape, but there is still something resembling a spray angle at the nozzle attached portion of the spray. Fig.4.22 shows the third frame from the sequence. It is evident here that the spray is starting to take the conical spray shape. The determined spray angle in Fig.4.22 is approaching the dispersion angle as usually defined in works such as [97, 92, 101]. The spray angle in these early frames (the first few data points on the curves in Fig.4.31) rapidly decreases during the first 50μs of the spray evolution. Figs.4.23 to 4.27 show the images from the same spray for frame numbers four to eight. Fig.4.25 is the sixth frame of the sequence and corresponds to the period of the θ_B temporal evolution curve in Fig.4.31 where the initial decrease in θ_B value stops at approximately 50 to 60μs. The same image sequences for the D10 fuel is presented in App.F.

Fig.4.31 shows temporal evolution of θ_B for Diesel fuel and D10 sprays at all conditions tested. As with the θ_S figures in the previous section, the delay period of the injection is not includeed in the plots. For all conditions, the temporal development of the fuel spray angles are of a similar pattern. At the very start of the injection, θ_B is between approximately 39° to 50°. This rapidly decreases during the very early period of the spray temporal evolution. For all cases, the initial reduction in the spray angle is very rapid, up to approximately 40-50μs after SOI. The rapid initial decrease in the θ_B value is followed by a very small increase and then a short period of near constant θ_B up to approximately 250μs after the SOI. The plotted curves take on a "dip" shape during the first 250μs Once this period of spray temporal evolution is complete, at around $t = 300\mu$s the spray angle shows a very gradual reduction in size as the spray evolves. The spray angle size reaches a minimum value at around $t = 800\mu$s.

Unlike the shadowgraph results it is not possible to discern a period of the injection where the transient spray angle is approaching a quasi-steady value. The EOI as measured by the camera is not well defined in the angle calculation process, it is hard to define accurately the exact time of the EOI but some inferences from the data here may be made. The injection duration for the 1000bar injections appears shorter on any plots due to the larger hydraulic injection delay at the SOI but the frame number used for the EOI is the same for all cases. The Diesel fuel spray angles, after reaching a minimum value at around $t = 800\mu$s after SOI, show an increase in size, with a very rapid increase just before the EOI. This trend is not observed with the D10 sprays, which, once a minimum value is reached at around $t = 800\mu$s after SOI have a near constant spray angle value until the EOI.

This final increase in θ_B for the Diesel sprays was thought to be due to the closing

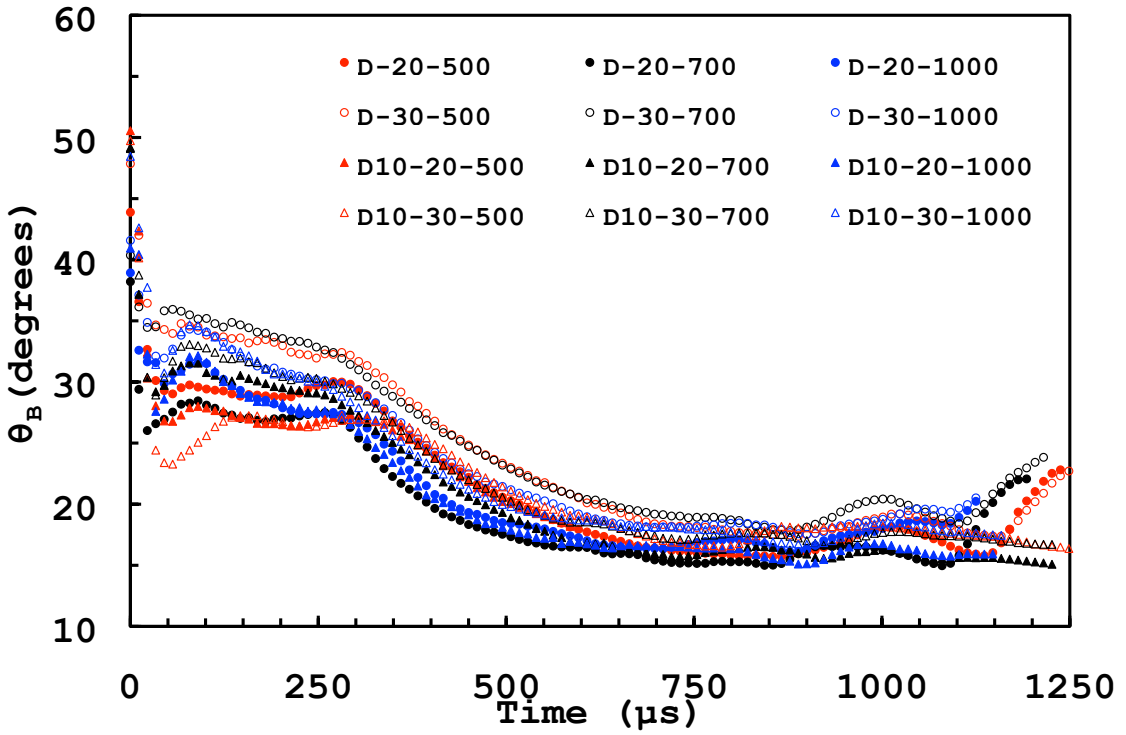

Figure 4.31: Fuel injection spray angle variation with time for all conditions with Diesel fuel (circles) and D10 (triangles) sprays ρ_a = 22.6 kg/m^3 (P_{amb}= 20bar) shown with solid symbols. ρ_a=34.5 kg/m^3 (P_{amb}= 30bar) shown with empty symbols. Determined using the near field, backlit image sequences.

of the needle. A review of the literature has shown very little analysis in terms of spray angle development with time and whilst those that acknowledge the initial transient θ_B decrease after SOI, the EOI is not really discussed. Nabers and Seibers [97] state that they sometimes observed a small increase in the spray angle at the EOI, they decided that this is mostly associated with the needle closing processes. A similar postulation is made by Wang et al [143] in another study where an increase in the spray angle is realized at the EOI. It is unclear how the needle closing mechanism would lead to an increase in θ_B but it must be result of the aerodynamic interaction between the ambient environment and the fluid changing as this is where the spray dispersion angle is formed. If the increase in θ_B at the EOI was due to needle closure, the same would be expected for the D10 sprays as well. The fact that it is not suggests that the increase in spray angle at EOI is a function of the fuel properties as well as any needle closure effects.

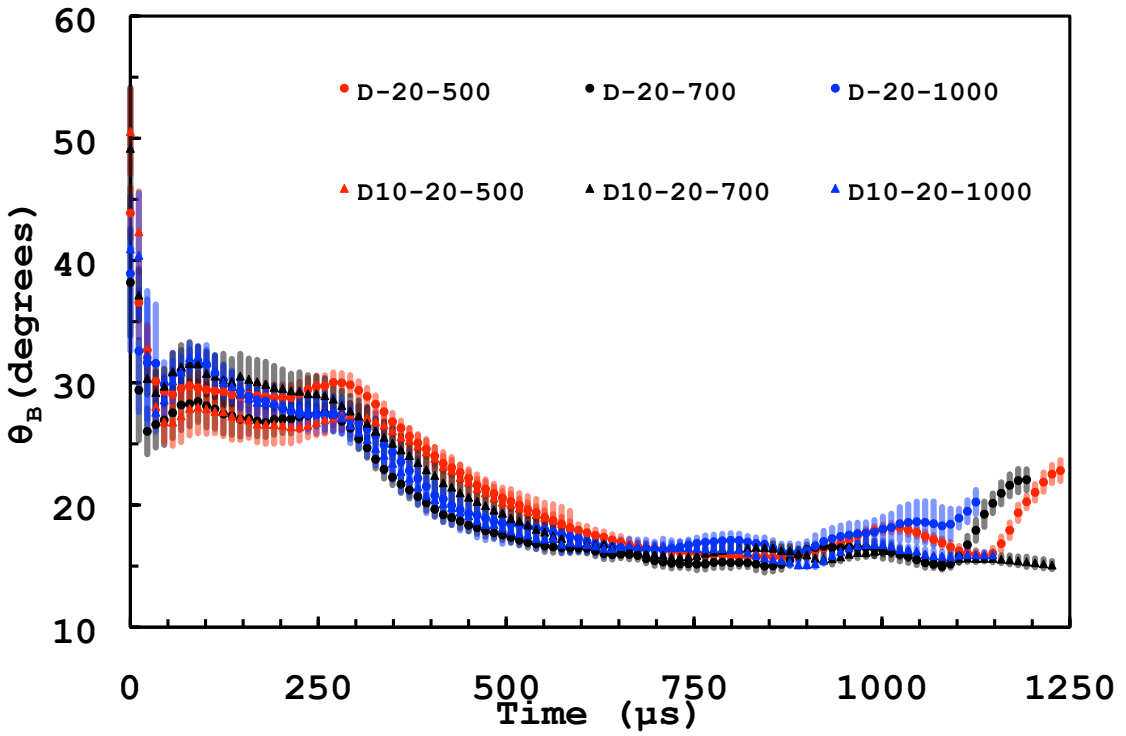

Figure 4.32: Fuel injection spray angle variation with time for Diesel fuel (circles) and D10 fuel sprays (triangles), P_{inj}= 500 (red), 700 (black) and 1000bar (blue). ρ_a=22.6 kg/m^3 (P_{amb}= 20bar). Determined using the near field, backlit image sequences. Error bars are the size of one standard deviation.

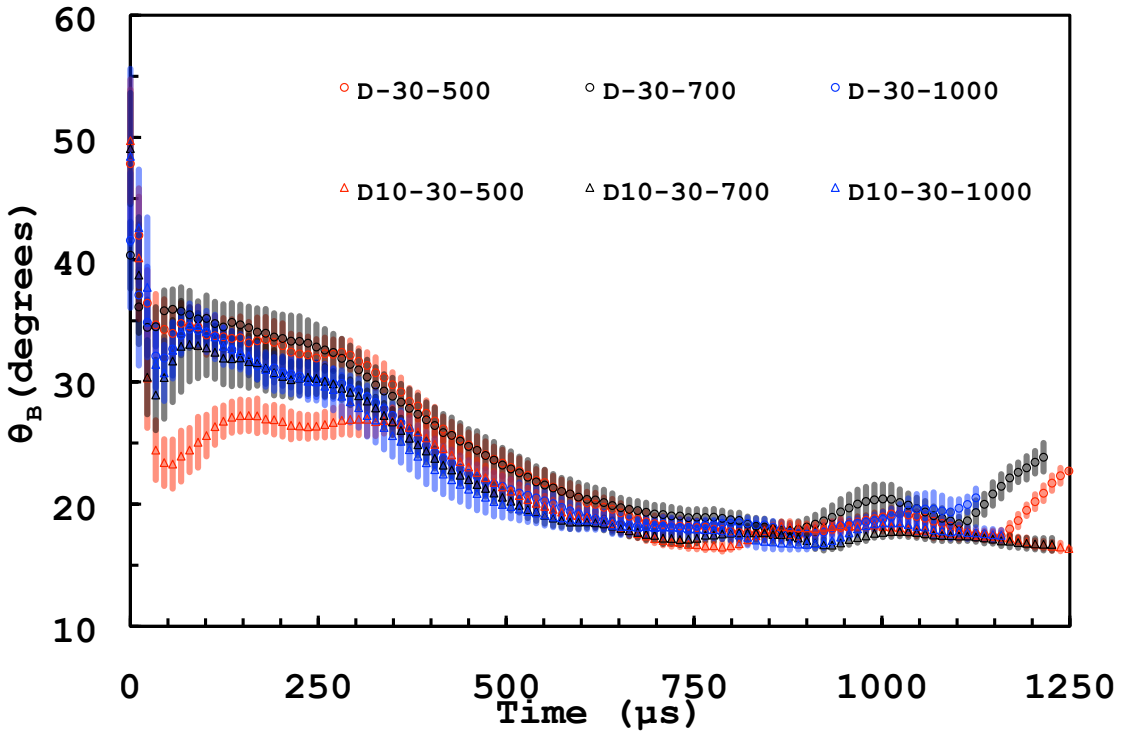

Figure 4.33: Fuel injection spray angle variation with time for Diesel fuel (circles) and D10 fuel sprays (triangles), P_{inj}= 500 (red), 700 (black) and 1000bar (blue).ρ_a=34.5 kg/m^3 (P_{amb}= 30bar) . Determined using the near field, backlit image sequences. Error bars are the size of one standard deviation.

Figs.4.32 and 4.33 show the backlit obtained temporal evolution of the spray angle for Diesel fuel and D10 sprays into an ambient density of 22.6 kg/m^3 and 34.5 kg/m^3 respectively. The plots include error bars, the size of one standard deviation from the mean for the 30 injections used to calculate the mean θ_B. The plots have been separated in this manner to show the general trends that the injection pressure has had no discernible influence on the the measured spray angle for the two fuels. The error bars are included here to demonstrate that the small variation of the mean values presented is not statistically significant and that is is not possible to really state any difference in θ_B for the different injection pressures.

The effect of the ambient density on the backlit measured spray angle is not so clear. The Diesel fuel spray angles are larger for the injections that have taken place into the higher ambient density. This is true during the injection period up to around $t = 800\mu$s. After this period, when the spray angle starts to increase in size, the angle measured with both ambient densities approaches each other in value. Plots of the Diesel fuel spray angle temporal evolution for the individual injection pressures are shown in App.G, complete with error bars. For the D10 sprays, the ambient density does not seem to have had any discernible effect on the backlit determined spray angle for any of the injection pressures. The D10-20-500 data set is incomplete, but for the period of injection that was collected, this is supported. Plots of the D10 fuel spray angle temporal evolution for the individual injection pressures are shown in App.H, complete with error bars.

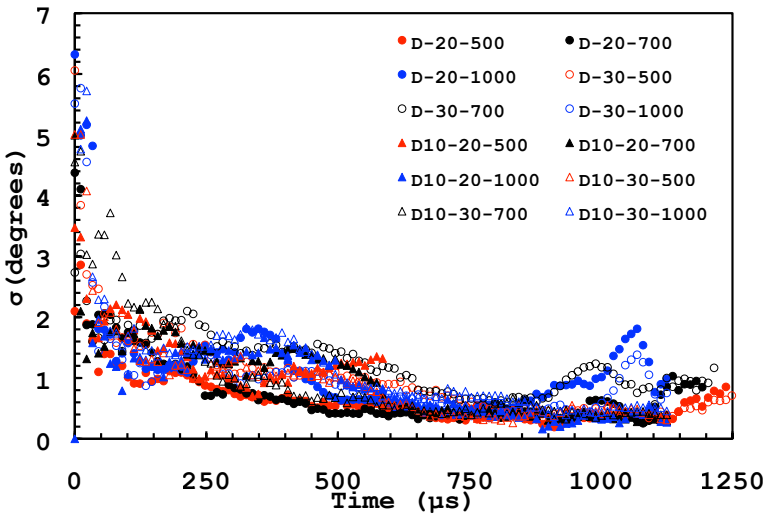

Figure 4.34: The standard deviation (with time) of the calculated θ_B's for the 30 injection events used to calculate the mean θ_B.

As with the shadowgraph results, a plot of the standard deviation of the measurement for each condition is included. The repeatability of the data is deemed to be high due to: the low standard deviation of the measurement, demonstrated

in Fig.4.34, which shows the temporal evolution of the standard deviation and; in the size of the error bars in Figs.4.32 and 4.33. Fig.4.34 shows that as the injection progresses, the standard deviation of the 30 measurements used to determine the mean value reduces to around 1° for all conditions. The reduction in the standard deviation with time also shows that the spray evolves into a spray with a less transient nature. The trend is similar to that observed with the shadowgraph results, however the backlit standard deviation values start off much larger and drop rapidly with a much smaller decrease throughout the injection period. The value seems to reach a minima at approximately 800μs after which, for some conditions there is a relatively large increase in σ. This coincides with the minimum noticed in the value for θ_B.

4.1.2.1 Summary

- Sequences of consecutive images of Diesel fuel and D10 injection sprays were collected using the backlit system at a frame rate of 88,888fps.
- Image sequences were used to determine the spray cone angle for fuel sprays at an injection pressure of 500, 700 and 1000 bar, into two ambient densities of 22.6 kg/m^3 and 34.5 kg/m^3 of an inert nitrogen atmosphere (20 bar and 30 bar ambient pressure respectively). For each condition, a total of 30 injections were used to determine the mean angle.
- An experimental collection error reduced the number of frames for the D10-20-500 condition being collected.
- Matlab image processing was applied to determine the angle from image sequences.
- The spray angle for all conditions started with a value of 39 and 50 degrees. This was followed by a very rapid decrease in size. After this very rapid decrease in value, for the period up to approximately 250μs after the SOI, the spray angle for all condition did not vary by a large amount.
- 250μs after the SOI, the spray cone angle for all conditions underwent a gradual decrease in value up to approximately 800μs after the SOI, after which the angle increased in size slightly.
- Unlike the shadowgraph obtained measurements, there is no period of quasi-steady spray angle to extract an average angle value from for comparison purposes.

- The change in injection pressure had no discernible effect on the spray cone angles determined.
- There was no clear trend on the spray angle in terms of a direct effect of the emulsification.
- The increase in the ambient density into which the spray took place resulted in an increase in the spray angle for Diesel fuel sprays but not for the D10 sprays.
- An increase in the measured spray angle was observed with the Diesel sprays at the EOI which was not present for the D10 fuel sprays.

4.1.3 Comparison of θ between Shadowgraph and Backlit collected images

So far the fuel spray angles determined from the collected image sequences using the shadowgraph and the backlit systems have been introduced and presented separately. In this section a short comparison between the determined θ_S and θ_B is made. It has been shown that for both techniques the transient nature of θ is captured and the same trends for the influence of injection pressure and ambient density have been observed, however, there are some very large differences between the transient θ_S and θ_B values.

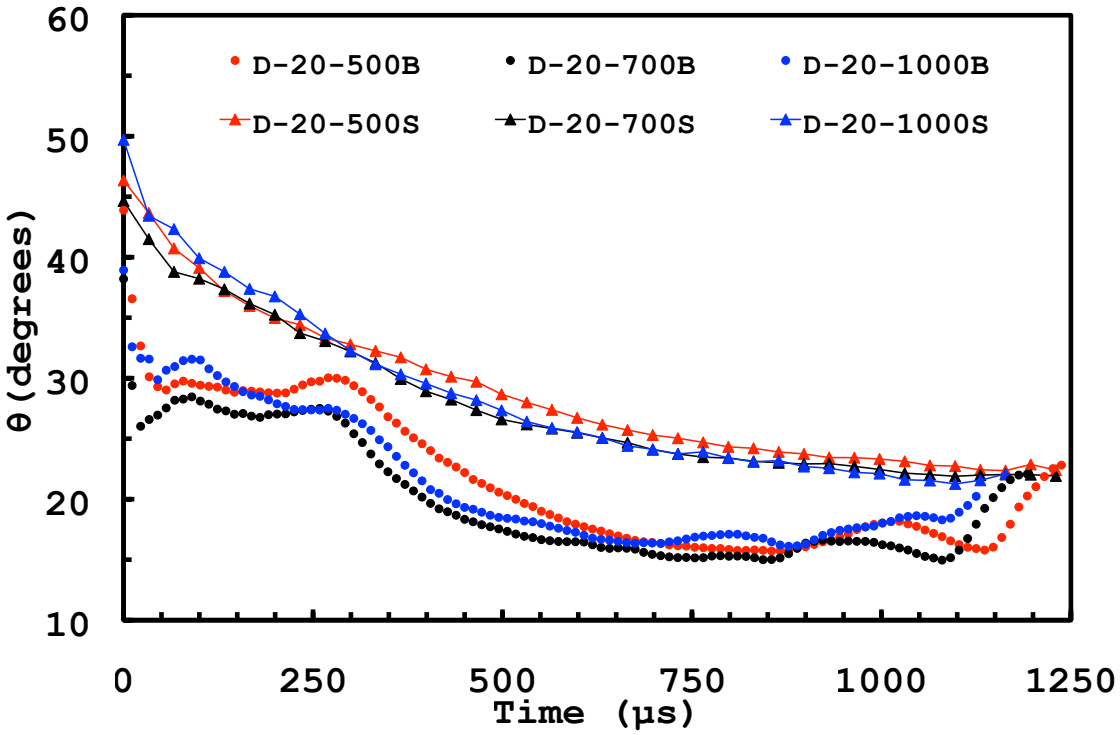

Figure 4.35: Fuel injection spray angle variation with time after SOI for Diesel fuel for P_{inj}= 500, 700 and 1000bar. ρ_a=22.6 kg/m^3 (P_{amb}= 20bar) . The circles are the θ_B and the triangles θ_S.

Fig.4.35 shows the temporal evolution of the fuel spray angle determined using both the backlit and shadowgraph image sequences for Diesel fuel injections (P_{inj}= 500, 700 and 1000bar) into an ambient density of 22.6 kg/m^3 (P_{amb}= 20bar). As the θ measurement technique applied is dependent on the tip penetration at each time step, the first measurement of θ for each technique similar in some cases. As the spray period progresses, θ_S is determined using an increasing tip penetration and an increasing projected spray area for the angle calculation. The maximum

tip penetration (S_S) determined using the shadowgraph technique is approximately 40mm (dependent on window fouling in some cases). With the angle measurement using 50% of S_S, this equates to a spray region up to 20mm in length being used to determine θ_S. The maximum tip penetration measured for the backlit near field measurements (S_B) is approximately 10mm. With the spray angle measurement using 70% S_B, this equates to a spray region up to 7mm from the nozzle being used to determine θ_B. The measurement is in essence taking an idealized average angle utilizing the projected area of the spray image. Maximum S_B is reached between 135 to 225μs after the SOI. The angle measurement is then essentially calculated using a constant value of S_B, any variation in θ_B is not a a result of spray dispersion increasing with increasing distance from the nozzle but a genuine change in the spray angle in that region alone. As the injection progresses the increased frame rate of the backlit image sequence results in higher temporal resolution for θ_B. The θ_B rapidly drops away from the θ_S value after the first few frames used to determine the angle. Throughout the injection period the θ_B value remains below the θ_S until the very end of the injection where θ_B increases and approaches the θ_S at that point. This demonstrates the much narrower angle of the spray that is present in the near nozzle region throughput the spray period. It also demonstrates the highly transient nature of the near field spay angle that is often missed when the region of the spray examined in larger.

During the experimental data collection phase it was found that the shadowgraph images were extremely sensitive to any window fouling and the smallest changes in the gas density within the chamber. One method that was examined to try and deter window condensing and fouling was to heat the chamber walls using electrical heating tape. This only marginally worked in terms of preventing window fouling and introduced an image collection issue due to the chamber walls setting up convection currents in the chamber which were detected by the shadowgraph system. The heating tape idea was abandoned as the convection currents in the chamber would have greatly complicated the spray image post processing. This did help highlight the sensitivity of the shadowgraph system to any density gradient. It is assumed that any region where fuel is present, whether in the form of a liquid core, dispersed atomized droplets or a mixture of air and evaporated fuel, the shadowgraph image would have a boundary which was easily thresholded using the Otsu method as applied in the image post processing (Sec.3.8.1).

The backlit system was not as sensitive to gas density or regions of finely atomized spray, which is one of the reasons why a larger number of samples could be collected for each condition (30 image sequences as apposed to 15 for the shadow-

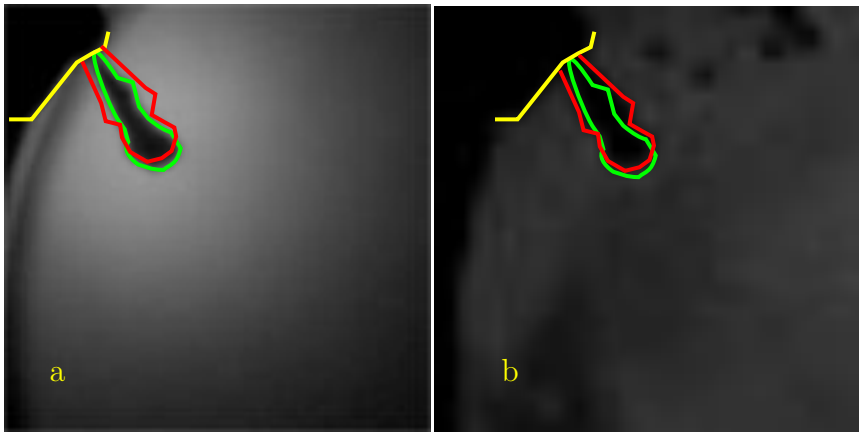

Figure 4.36: Sample Diesel spray images from the shadowgraph and backlit image sequences scaled and combined. Image (a.) is backlit derived image with the spray edge defined by the green border. Image (b.) is the shadowgraph derived image with the spray edge defined by the red border. Both images are from approximately the same time after SOI (11.25μs) and have been scaled using the injector, bordered in yellow.

graph) as window fouling was not as much of an issue when compared with the shadowgraph system. The backlit technique was also extremely sensitive to camera and lens settings: exposure time; flash time; aperture and lens focal settings. The backlit technique will not capture all spray regions, particularly some of the finely atomized and dispersed droplets, some of the liquid vapor/air mixture regions and the gas phase boundary of the spray. This explains why when backlighting or Mie scattering has been applied in previous works in the literature there is much effort and discussion concerning the thresholding technique used in the post processing of the images.

The optical attenuation of the spray is reduced at the spray edges. This is supported by examining the optical attenuation at the periphery of the spray. The attenuation describes the reduction in intensity of light as it traverses a medium, in this case a finely dispersed number of droplets (the spray). The attenuation coefficient or extinction coefficient μ_e (unit length^{-1}) is an optical property, which if a monodisperse cloud of droplets is illuminated with a single wavelength can be estimated as

$$\mu_e = \sigma_e.N \tag{4.1}$$

where N is the droplet number density and σ_e is the extinction cross section [202]. The extinction cross section is a product of the absorption and scattering cross sections. If a particle is an absorbing material and the particle size is larger than the light wavelength (520nm for green LED used here) the extinction cross section

may be approximated as

$$\sigma_e \approx 2\sigma_g \approx \frac{\pi d_d^2}{2} \tag{4.2}$$

where σ_g is the geometrical cross section of the droplet, d_d is the geometric diameter of the droplet [203]. Phase Doppler anemometry (PDA) of Diesel fuel sprays has been conducted for a number of years and yields data concerning spray droplet size, number density and droplet velocity. Using PDA data from previous works it is possible to make an estimate of the attenuation at the spray periphery. Mean droplet diameter was found to be in the range 12 μm (spray axis centerline) to 8 μm (spray periphery) in [204], similar values are reported in [205]. In the work [206] values of 3 μm to 6 μm are reported. Droplet number density is in the region of 10^{12} (m^{-3}) [113], with [207] stating a range 10^6 (cm^{-3}) (spray axis centerline) to 10^3 (cm^{-3}) (spray periphery). Using this data along with Eqn.4.37 and 4.2 the attenuation at the spray periphery is demonstrated to be reduced when compared with that at the spray central axis with approximate values of 5.7 m^{-1} (periphery) to 226 m^{-1} (spray central axis). This is clearly an approximation, however recent work [202] based around structured illumination of Diesel fuel sprays has paid close attention to determining the local attenuation coefficient as a verification of experimental procedure. Spray simulation using CFD code has been conducted in conjunction with a Lorenz-Mie software package. An example result is shown in Fig.4.37 and supports the assumption of attenuation at the spray periphery being reduced.

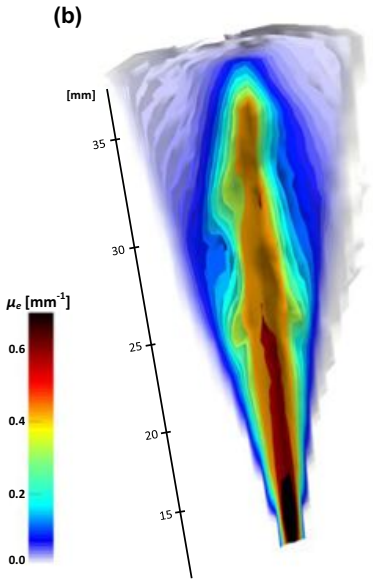

Figure 4.37: 3D iso-surfaces of the extinction coefficient in Diesel spray [202].

The shadowgraph system detected this periphery region of the spray. The backlit system was insensitive to this region of the spray. This helps explain why the

measured angle throughout the injection period for the backlit image sequences θ_B, is smaller when compared with the shadowgraph derived angles, θ_S. When thresholding is applied to this region of the backlit spray images, it is difficult to quantify how much, if any spray edge is being missed. The backlit system is much more likely to be imaging the dense liquid core and the extended boundary around this region rather than the entire spray region. Fig.4.36 shows a spray backlit (a) and a shadowgraph (b) image for a Diesel spray from approximately the same time after SOI. The yellow outline shows the injector nozzle, the green outline is the backlit spray edge and the yellow outline the shadowgraph spray edge. The images have been post processed manually to scale correctly (aspect ratio locked) using image software Inkscape. The images support the argument that the shadowgraph images contain regions of spray boundary which the backlit system was insensitive to.

4.1.4 Shadowgraph Tip Penetration

In the following sections the spray tip penetration is presented for each fuel at the three injection pressures and the two ambient densities considered. The shadowgraph results are presented first and comparison to previous findings and models is made. The backlit results are then presented with a brief discussion of the tip velocity determined from the tip penetration evolution.

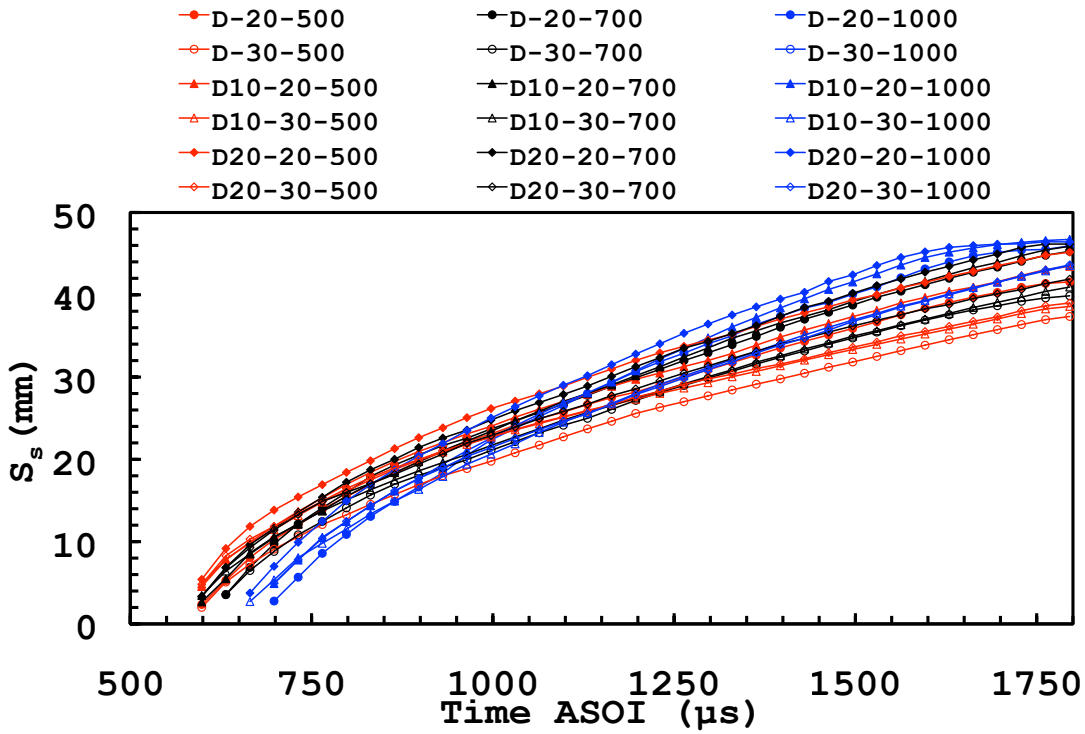

Figure 4.38: Fuel injection spray tip penetration variation with time after SOI for all conditions with Diesel fuel, D10 and D20. ρ_a = 22.6 kg/m^3 (P_{amb}= 20bar) shown with solid symbols. ρ_a=34.5 kg/m^3 (P_{amb}= 30bar) shown with empty symbols. Determined using the shadowgraph image sequences. No correction or removal of the injection delay period has been applied

Fig.4.38 shows the temporal evolution of the spray tip penetration for Diesel fuel, D10 and D20 fuel sprays at all conditions tested. The mean value determined from 15 injections is shown. The delay period has not been removed and no linear correction has been applied to align the origin of each curve. The injection delay period was comprised of an electronic portion (Section.3.10) and a hydraulic portion. The electronic portion was constant for all conditions. The hydraulic portion increaseeds with increasing injection pressure. This is a consequence of the design of the injector's control volume and unbalanced control valve.

Fig.4.39 shows the temporal evolution of the spray tip penetration for Diesel fuel,

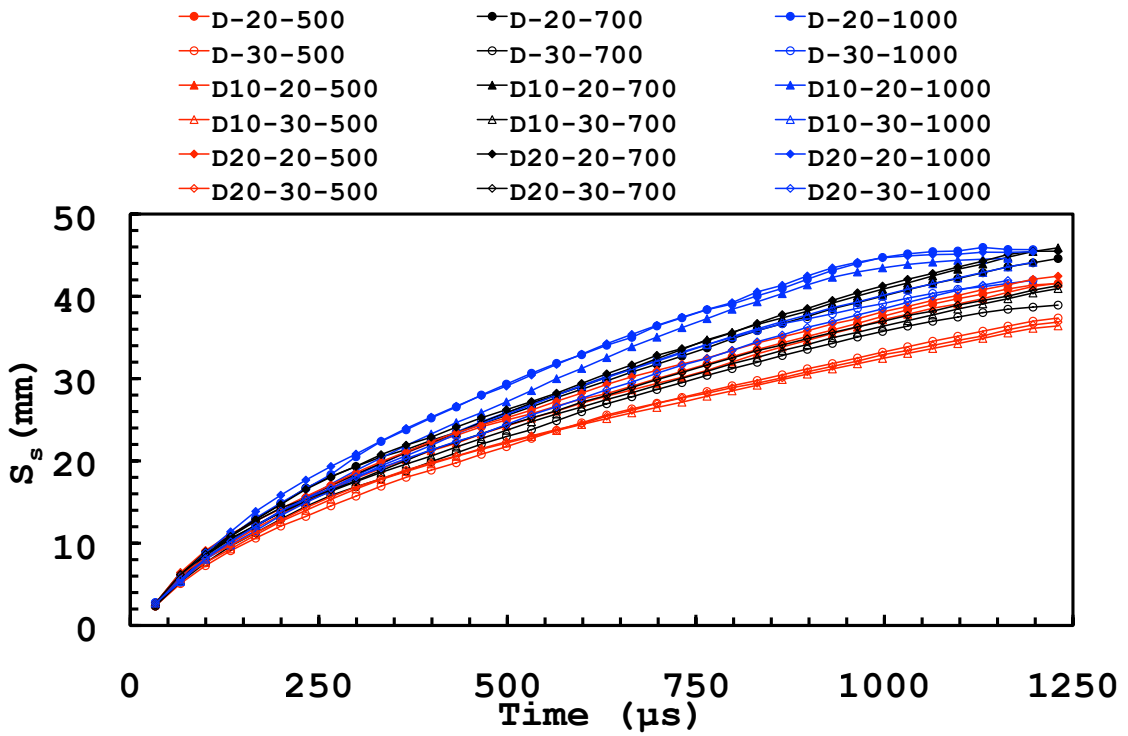

Figure 4.39: Fuel injection spray tip penetration variation with time after SOI for all conditions with Diesel fuel, D10 and D20. ρ_a = 22.6 kg/m^3 (P_{amb}= 20bar) shown with solid symbols. ρ_a=34.5 kg/m^3 (P_{amb}= 30bar) shown with empty symbols. Determined using the shadowgraph image sequences.

D10 and D20 fuel spray at all conditions tested, the mean value determined from 15 injections is shown. The delay period has been removed and a linear correction has been applied to align the origin for all conditions. The first appearance of spray has not been set at $t = 0$ as this would lead to a physically impossible situation where the spray tip has started to penetrate the ambient environment before the injection had started. The first tip penetration measurement is taken as occurring at $t = 33.25\mu s$ with each tip measurement made at $33.25\mu s$ intervals (frame rate of the camera). The tip penetration has not been back extrapolated to 0mm at $t = 0$ as this relies on the assumption of the initial rate of penetration (velocity) during this very early period of the spray evolution being linear with time. The measured spray tip for each condition has been corrected according to the first tip measurement made so the first measurement for each condition is the same. This is due to the varying injection delay encountered for different pressures and fuels and the temporal resolution of the measurement only being as high as the frame rate used ($33.25\mu s$).

As has been noted in previous works [102, 114, 93, 121], increasing the injection pressure leads to an increase of the temporal evolution of the spray tip penetration while an increase in ambient density leads to a reduction in the temporal evolution

of the spray tip penetration. An increase in P_{inj} results in an increase in the spray momentum and an increase in ρ_{amb} results in an increase in aerodynamic drag on the emerging spray.

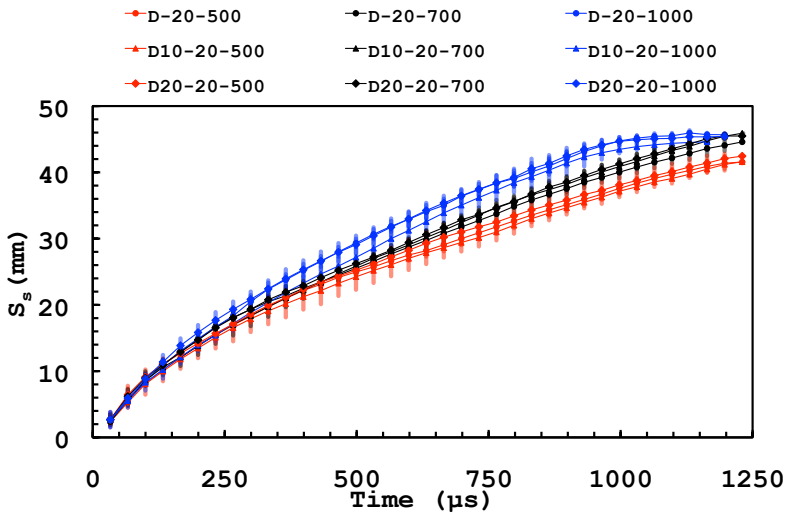

Figure 4.40: Fuel injection spray tip penetration variation with time after SOI for Diesel fuel, D10 and D20. P_{inj}= 500,700 and 1000bar. ρ_a=22.6 kg/m^3 (P_{amb}= 20bar). Error bars of one standard deviation. Determined using the shadowgraph image sequences.

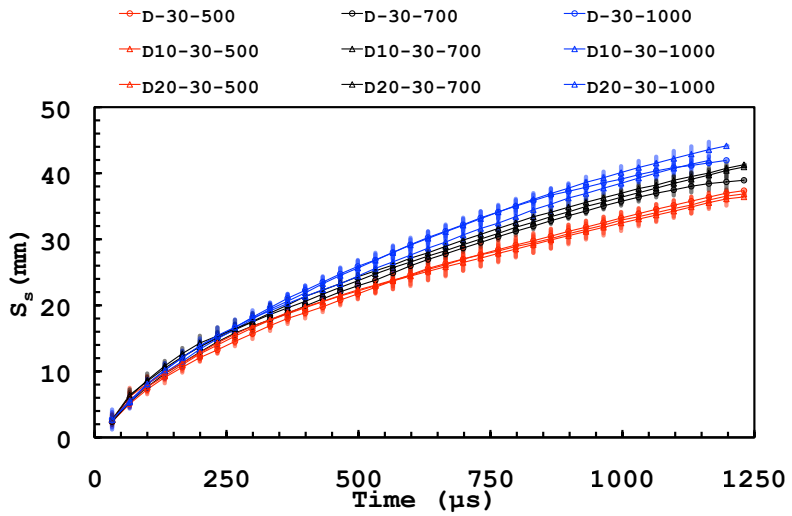

Figure 4.41: Fuel injection spray tip penetration variation with time after SOI for Diesel fuel, D10 and D20. P_{inj}= 500, 700 and 1000bar. ρ_a=34.5 kg/m^3 (P_{amb}= 30bar). Error bars of one standard deviation. Determined using the shadowgraph image sequences.

Figs.4.40 and 4.41 show the same results with the data separated out according to the ambient density (22.6 kg/m^3 and 34.5 kg/m^3 respectively) into which the

sprays emerged. Both figures include error bars the size of one standard deviation (σ) from the mean for the 15 injections used to calculate the mean S_S. These figures are included to show the good repeatability between each injection event and the statistical significant of the mean S_S determined.Figs.4.40 and 4.41 demonstrate that the emulsification of the Diesel fuel with water seems to have had little to no effect on the temporal evolution of the spray tip penetration when compared with the neat Diesel spray results.

The results have been examined and correlated with previous, semi-empirical or wholly empirical spray penetration models which have been developed for scaling the propagation characteristics for a variety of fuels, injection pressures, ambient conditions and nozzle types. The most widely discussed of these is the Hiroyasu and Arai model [98] (Sec.2.4.2) which has had a major influence on the subsequent methods of data analysis and correlation. An example of the methodology of the tip penetration analysis influenced by the Hiroyasu and Arai model is to examine the temporal tip penetration using a log plot. Experimental data points are plotted on a logarithmic plot as in Fig.4.42 and 4.43 and have been used to create average trend lines.

As described by Hiroyasu and Arai [98] and in subsequent works [97, 93, 119, 90] the plots describe two distinct periods of spray tip temporal evolution. The slope of the initial period of the curve is usually described as being equal to 1. The slope of the initial period of the curve in Figs.4.42 and 4.43 is 1.12 and 1.03 respectively which is in reasonable agreement. During this period the spray penetration is nearly linear with time, $S \propto t$, and is thought to be dominated by the propagation of the liquid core into the surrounding atmosphere [123]. The tip velocity is thought to be determined by the fuel injection velocity because the momentum exchanged between the spray and the surrounding ambient atmosphere is not yet significant [89]. Following this initial period after a short time the slope changes and is most often approximated to a value of 0.5 ($S \propto t^{0.5}$). The slope of the curve in this second period in Figs.4.42 and 4.43 is 0.6. This transition is often described as the spray break-up time and is defined as the time where the fuel spray starts to exchange momentum with the surrounding atmosphere and the tip velocity is reduced, this may be referred to as aerodynamic drag in some cases. It is also suggested this transition time is the instance when spray mixture changes from being dominated by injected liquid to being dominated by entrained gas [97, 119]. The vertical broken line in Figs.4.42 and 4.43 shows the average transition time for ρ_a=22.6 kg/m^3 ρ_a=34.5 kg/m^3 conditions. As the ambient density is increased the transition time after the SOI becomes shorter. Due to the relatively few data

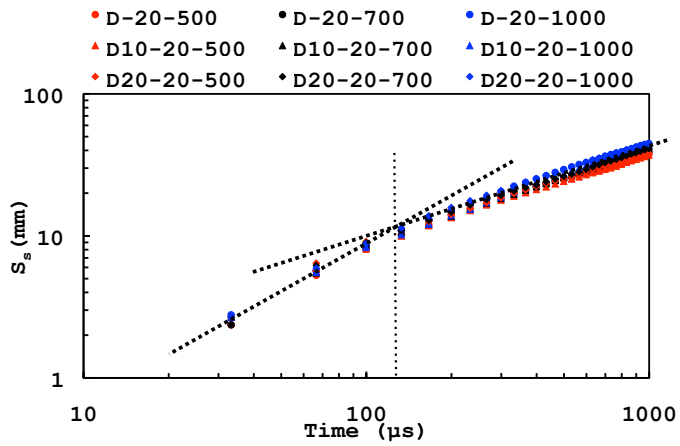

Figure 4.42: Log-penetration with log-time plot for Diesel fuel, D10 and D20 spray tip penetration. P_{inj}= 500,700 and 1000bar. ρ_a=22.6 kg/m^3 (P_{amb}= 20bar). Determined using the shadowgraph image sequences. Linear trend line fitted to the two portions of the tip penetration with intersection at break-up time.

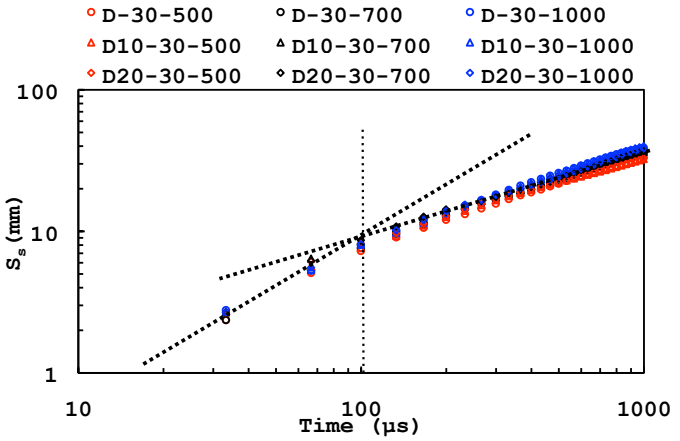

Figure 4.43: Log-penetration with log-time plot for Diesel fuel, D10 and D20 spray tip penetration. P_{inj}= 500,700 and 1000bar. ρ_a=34.5 kg/m^3 (P_{amb}= 30bar). Determined using the shadowgraph image sequences. Linear trend line fitted to the two portions of the tip penetration with intersection at break-up time.

points that have been collected during this early period, it is difficult to construct an adequate trend line for gradient extraction. Care is needed when drawing too many conclusions and values for this transition time. It is accepted that the increase in the ambient density will lead to a reduction in the break-up time (as has been demonstrated here), due to increasing aerodynamic drag and momentum exchange

with an increase in density of the ambient gas.

Adherence to this linear relationship during the pre-break-up period is clearly a physical impossibility. In the very instance of needle opening the fuel will be accelerating from $0ms^{-1}$ to an injection velocity observed here of approximately 70-$100ms^{-1}$, the velocity in this early near field region clearly cannot be linear. The few data points available at this period make any extrapolation back to the origin susceptible to misinterpretation and should be avoided, as exemplified in the work [89]. The model suggested by Kostas [121] (Sec.2.4.2, Eqn.4.3) is developed from an experiment conducted at a much higher temporal resolution than most other work and specifically investigate the early period of spray evolution

$$S(t) = At^{3/2} \tag{4.3}$$

with values of A determined from an experimental data fit. The Kostas findings appear to be more physically realistic. Upon differentiating, the spray tip velocity, U, is proportional to $t^{0.5}$, which is not ill defined as t approaches zero [121]. This fit has been further modified by Taskiran and Ergeneman [92] (Sec.2.4.2, Eqn.4.4) in an attempt to relate experimental conditions to the determination of Kostas's A values.

$$S(t) = \left(\frac{\rho_f}{\rho_a}\right)^{0.25} \left(\frac{\rho_f^{1/3}\Delta P}{12\rho_f}\right)^{0.5} t^{3/2} \tag{4.4}$$

Figs.4.44, 4.45 and 4.46 show the temporal evolution of the spray tip penetration for Diesel fuel at injection pressures of 500, 700 and 1000 bar respectively, ambient density is ρ_a=22.6 kg/m^3 and compares them to the models and data fits mentioned so far.

It is evident that the Hiroyasu model overestimates in all cases compared to the measured S_S with an earlier transition time. At the lower injection pressure, the Kostas fit underestimates but as injection pressure increases it overestimates the tip penetration. A similar trend is observed with the Taskiran fit which uses a modified Hiroyasu model for the period after beak-up. It is this portion of the model which most closely matches the measured S_S in the later stages of the injection. It is interesting that this modified Hiroyasu used by Taskiran is the first time that the nozzle geometry, in terms of conicity, is taken into account.Even with this, the measured data is a long way from that predicted in the various models, however, the difference between the models themselves shows the variability that is present in

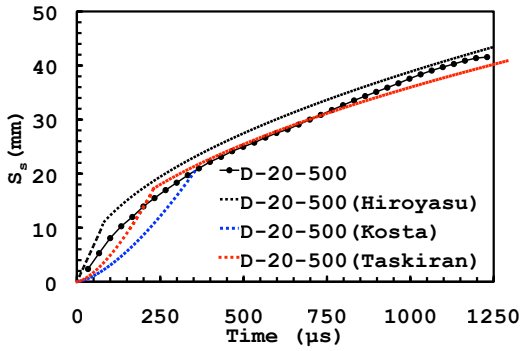

Figure 4.44: Fuel injection spray tip penetration variation with time after SOI for Diesel fuel. P_{inj}= 500. ρ_a=22.6 kg/m^3. Experimental in black, Hiyoyasu model (broken black), Kosta model (blue) and Taskiran model (red) for same condition.

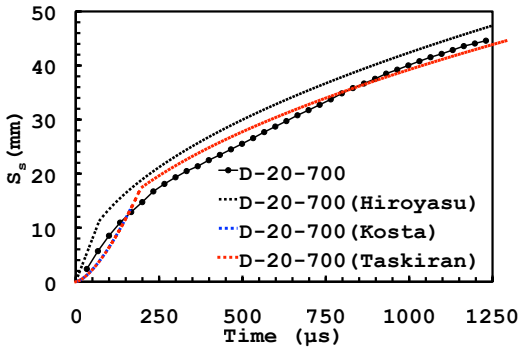

Figure 4.45: Fuel injection spray tip penetration variation with time after SOI for Diesel fuel. P_{inj}= 700. ρ_a=22.6 kg/m^3. Experimental in black, Hiyoyasu model (broken black), Kosta model (blue) and Taskiran model (red) for same condition

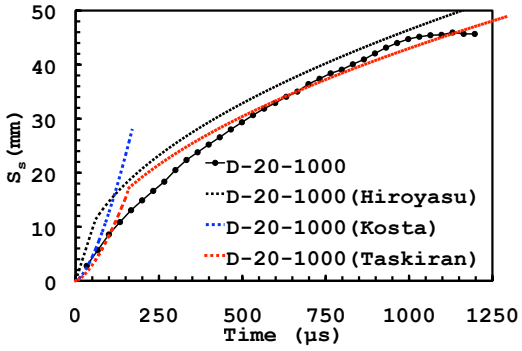

Figure 4.46: Fuel injection spray tip penetration variation with time after SOI for Diesel fuel. P_{inj}= 1000. ρ_a=22.6 kg/m^3. Experimental in black, Hiyoyasu model (broken black), Kosta model (blue) and Taskiran model (red) for same condition

the literature concerning the temporal evolution of spray tip, both experimentally collected and modeled/data fitted.

4.1.4.1 Summary

- Sequences of consecutive images of Diesel fuel, D10 and D20 injection sprays were collected using the shadowgraph system at a frame rate of 33,000fps.
- Image sequences were used to determine the temporal evolution of the spray

tip penetration for fuel sprays at an injection pressure of 500, 700 and 1000 bar into two ambient densities of 22.6 kg/m^3 and 34.5 kg/m^3 of an inert nitrogen atmosphere.

- Matlab image processing was applied to determine the spray tip penetration from image sequences.
- The penetration was not back extrapolated to 0 mm at t=0.
- Increasing the injection pressure resulted in an increase in the temporal evolution of the tip penetration.
- Increasing ambient density results in a decrease in the temporal evolution of the tip penetration.
- There was no discernible difference between the Diesel fuel, D10 and D20 fuel spray tip penetration for corresponding conditions.
- The measurements made at the temporal resolution applied support previous models, suggesting a linear dependence with time during the initial period, S$\propto t$, with a transition time after the SOI when the dependence changes to S$\propto t^{0.5}$.
- Previous models either under or overestimate tip penetration when compared with the experimental measurements made by the author.

4.1.5 Backlit Tip Penetration

Fig.4.47 shows the temporal evolution of the fuel injection spray tip at all conditions tested for Diesel fuel and D10 determined from the image sequences collected using the backlit system. The mean value determined from 30 injections is shown. The backlit technique was much less sensitive to window fouling than the shadowgraph technique, this allowed a greater number of injections for each condition to be observed but the measurement range of the tip penetration reduced during the experiments. It was observed that 10mm represents the maximum tip length that could be calculated from the image sequences for all data. As with the shadowgraph results, the injection delay period was removed.

The first data point (t=11.25 μs) for the determined S_B are very similar for all conditions with the maximum and minimum value separated by 0.6mm (approximately 40% of the maximum value). As the injections progressed, the spray penetration

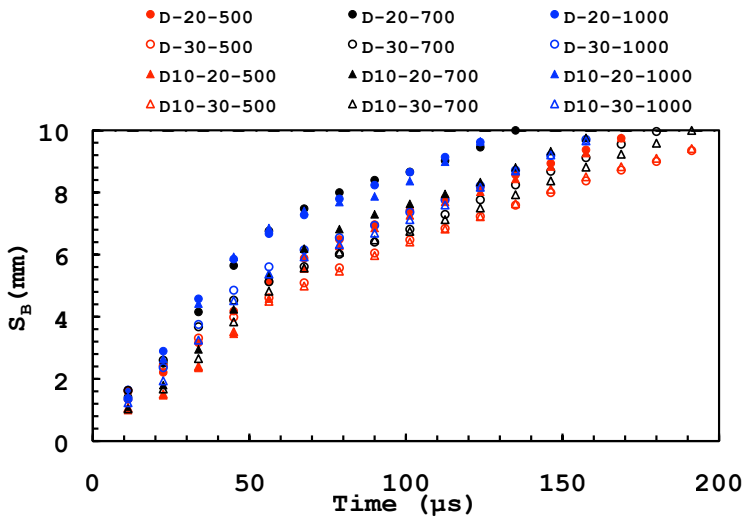

Figure 4.47: Fuel injection spray tip penetration variation with time after SOI for Diesel fuel (circles) and D10 (triangles). P_{inj}= 500,700 and 1000bar ρ_a = 22.6 kg/m^3 (P_{amb}= 20bar) shown with solid symbols. ρ_a=34.5 kg/m^3 (P_{amb}= 30bar) shown with empty symbols. Determined using the backlit image sequences.

for the Diesel fuel injections at P_{inj}=700 and 1000bar, ambient density ρ_a = 22.6 kg/m^3 are very similar throughout, it is hard to say there is any difference. The reason for this is unclear and does not fit with accepted trends. Apart from this case, the general trend is that the increase in injection pressure has resulted in an increase in the tip penetration and the increase in the ambient density has resulted in a decrease in the spray tip penetration.

The Diesel fuel and D10 tip penetrations for the 500 and 1000 bar into the ambient density of ρ_a = 22.6 kg/m^3 are almost the same after approximately 60μs. For the injections into the higher ambient density, ρ_a=34.5 kg/m^3, the Diesel fuel and D10 spray penetrations at each pressure are approximately the same after 60μs. The emulsification has had no effect on the spray tip penetration after 60μs from the SOI. Figs.4.48 and 4.49 show the same data, separated out by the ambient density. These figures show that an increase in ambient density seemed to reduce the effect an increase in injection pressure had on the tip penetration. The figures also help illustrate the change in the gradient of the curve, at approximately 60μs. This was also observed with the shadowgraph results but a little later after the SOI.

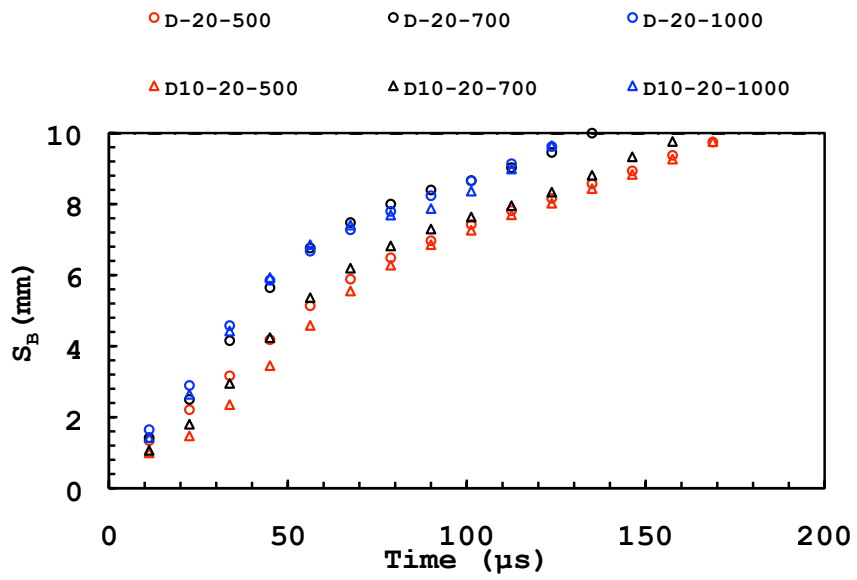

Figure 4.48: Fuel injection spray tip penetration variation with time after SOI for Diesel fuel (circles) and D10 (triangles). P_{inj}= 500,700 and 1000bar ρ_a = 22.6 kg/m^3 (P_{amb}= 20bar). Determined using the backlit image sequences.

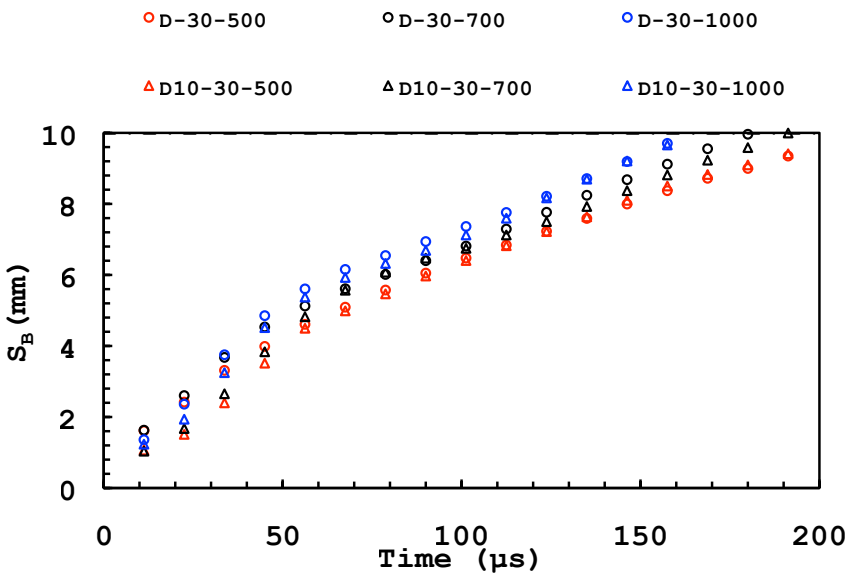

Figure 4.49: Fuel injection spray tip penetration variation with time after SOI for Diesel fuel (circles) and D10 (triangles). P_{inj}= 500,700 and 1000bar ρ_a=34.5 kg/m^3 (P_{amb}= 30bar). Determined using the backlit image sequences

As discussed previously, the early period of injection is often modeled and discussed as a linear relationship between the tip penetration and the time after SOI. The results presented in Figs.4.48 and 4.49 have not been back extrapolated to

0mm at $t = 0$ as this would rely on this assumption. This linear assumption in the very early period of the injection is examined in Fig.4.50. Here the tip penetration variation with time for all injections into an ambient density of ρ_a=22.6 kg/m^3 are separated out and plotted for the very early period of the spray. Trend lines have been fitted to these data points. The higher temporal resolution of the backlit data has allowed the very early stages of the spray evolution to be collected. The camera frame rate difference between the techniques means that for the backlit image sequence, approximately 3 images for each shadowgraph images are collected. The plot has been enlarged so as to concentrate on the initial period of the injection. A linear dependence is not an unreasonable assumption to be made for this period according to the trend lines which intercept very close to the plot origin. If the development of the tip penetration during this early period is linear with time, this implies a constant velocity during this period, with the so called break up time identified by a rapid change in velocity of the spray tip.

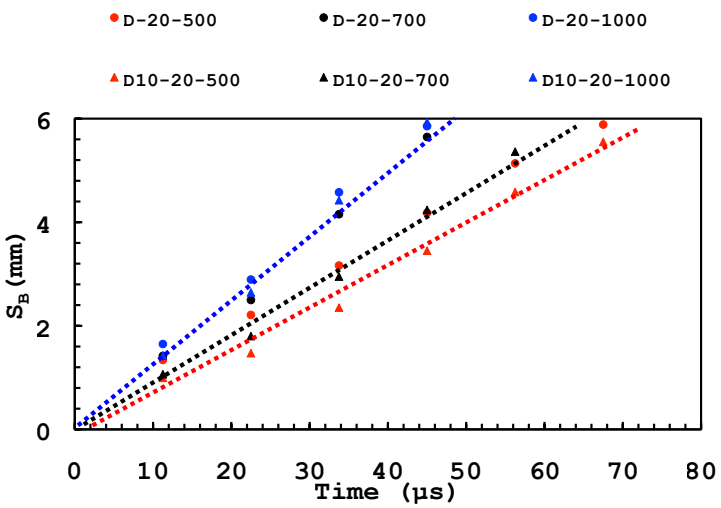

Figure 4.50: Fuel injection spray tip penetration variation with time after SOI for Diesel fuel (circles) and D10 (triangles). P_{inj}= 500,700 and 1000bar ρ_a = 22.6 kg/m^3 (P_{amb}= 20bar) shown with solid symbols. Determined using the backlit image sequences. Only the very early period of spray, up to a maximum of 70μs after the SOI is included in the plot, linear trend lines have neem fitted to these data points, ignoring the data collected after the period included in the plot.

If this is indeed a spray break-up phenomenon and is a transition to a period where the spray exchanges a substantial quantity of momentum with the surrounding gas then one would expect that this will result in a considerable reduction in the spray tip velocity. Spray tip velocity for this section of the results is referred to as U_B from here. It is worth noting here for clarity sake that the U_B at this point is a different parameter to the fuel injection velocity, v_B which is defined by the pressure drop across the nozzle orifice along with nozzle features (C_d, A_{eff} etc.) and is an upper

limit on the maximum spray velocity possible. Figs.4.51 and 4.52 show the spray tip penetration rate, U_B for all conditions determined using numerical differentiation of the spray penetration with time, for the ambient densities ρ_a=22.6 and ρ_a=34.5 kg/m^3 respectively. As this is essentially an average velocity in the time interval (11.25μs) the plot has been constructed using the mid point of each time interval as the position on the abscissa.

As the needle lifts and the orifice opens, the spray tip is accelerated, from 0 ms^{-1}, extremely rapidly though the nozzle and exits the orifice where it enters the dense ambient gas. This physically real situation is counter to the argument that the initial spray tip evolution is linear with time and suggests that linear trend line fitting, as has been conducted in Fig.4.50 and is often carried out in previous works, is unwise. This linear trend fitting is most likely a consequence of the lower temporal resolution of any measurement.

It is worth noting that the peak spray velocities measured here are considerably lower than that predicted by the inviscid flow theory, using the pressure drop across the nozzle and a conservative discharge coefficient of 0.8. As the needle lifts and the nozzle opens, the discharge coefficient will vary from zero up to approximately 0.8 for the first 50-100μs, as the effective orifice cross sectional area increases until it reaches its maximum value. The tip acceleration could also be a consequence of the reduced aerodynamic drag experienced by portions of the spray directly behind the tip which replace the spray tip as it moves aside due to interaction with the ambient atmosphere.

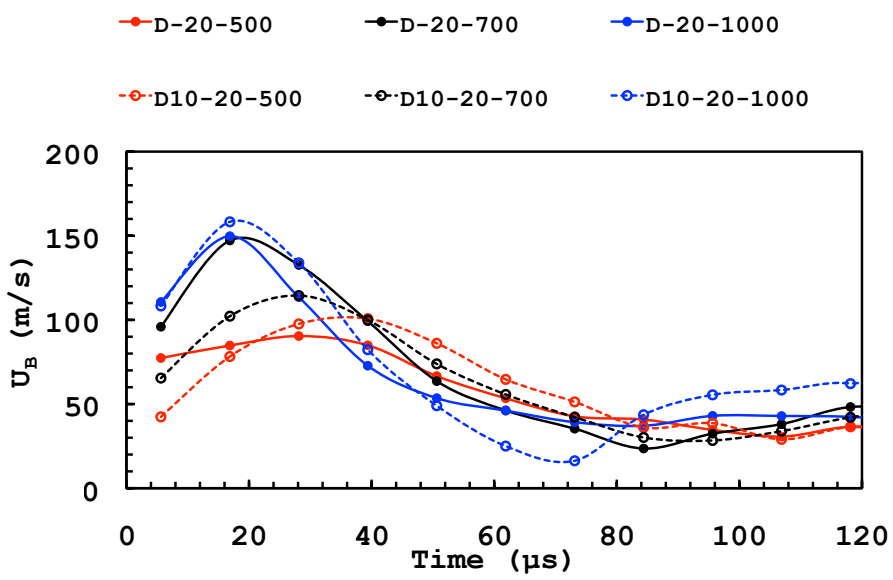

Figure 4.51: Fuel injection spray tip velocity variation with time after SOI for Diesel fuel (solid) and D10 (empty). P_{inj}= 500 (red), 700 (black) and 1000bar (blue) ρ_a = 22.6 kg/m^3 (P_{amb}= 20bar). Determined using the backlit image sequences.

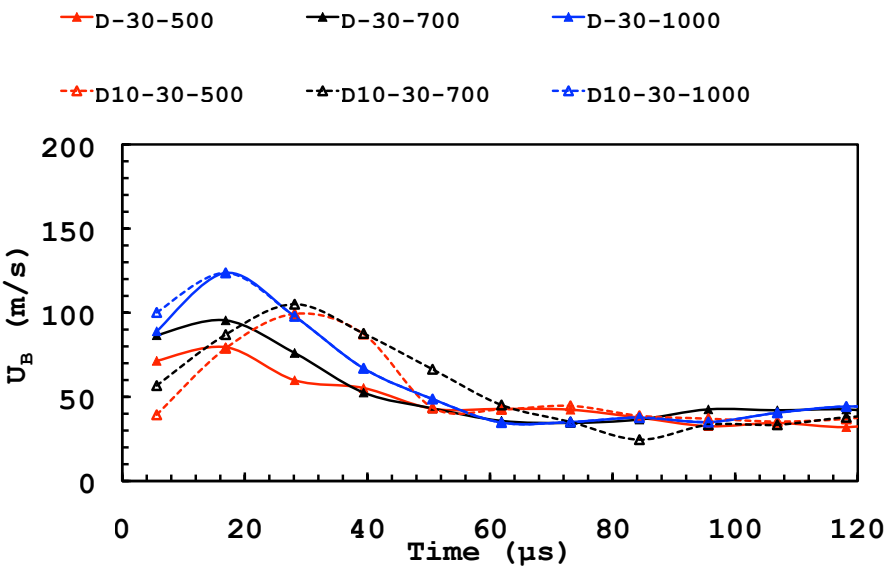

Figure 4.52: Fuel injection spray tip velocity variation with time after SOI for Diesel fuel (solid) and D10 (empty). P_{inj}= 500 (red), 700 (black) and 1000bar (blue) ρ_a=34.5 kg/m^3 (P_{amb}= 30bar). Determined using the backlit image sequences.

Examination of Figs.4.51 and 4.52 shows that for the Diesel fuel injections into ρ_a = 22.6kg/m^3, as the injection pressure is increased, maximum tip velocity, U_{Bmax}, increases in size, but the P_{inj}=700 and 1000 bar values are very close to the point

where they may be considered the same. The time after SOI when U_{Bmax} occurs decreases with increasing injection pressure, however, for the P_{inj}=700 and 1000 bar, U_{Bmax} occurs almost at the same time. This is a consequence of the spray tip penetration of the Diesel fuel injection at 700 bar, ρ_a = 22.6 kg/m^3, being almost the same as that of the 1000 bar injection. As previously stated, the reason for this is unclear and is counter to previously observed trends.

For both of the fuels, the 1000 bar injections exhibited the largest peak tip velocity. They also exhibited the largest decrease in tip velocity, with the tip velocity dropping to the lowest or near the lowest value. This is strongly exhibited for the D10-20-1000 injection, which experienced a rapid tip deceleration from the largest peak velocity to the lowest minimum velocity at approximately 70 μs ASOI. The effect is strongest for the 1000 bar injections into the 20 bar atmosphere but it was present for the injections into the 30 bar atmosphere as well. This demonstrates that the 1000 bar injections resulted in the highest peak tip velocity as the tip emerged from the nozzle and underwent a rapid momentum exchange with the surrounding gas and rapidly decelerated.

As the chamber density was increased to ρ_a=34.5 kg/m^3), U_{Bmax} was reduced for both fuels at all injection pressures. At this ambient density, the Diesel fuel sprays show a clear trend of U_{Bmax} increasing with injection pressure increase but the time where U_{Bmax} occurred stayed almost the same for each injection pressure. For the D10 fuel, at both ambient densities, the time after SOI when U_{Bmax} occured decreased with increasing injection pressure. This is more apparent in Figs.4.53 and 4.54 where the velocity data has been normalized by the corresponding peak tip velocity. The time of the U_{Bmax} for the Diesel fuel spray tips is independent of injection pressure and ambient density, apart from at the lower injection pressure of 500 bar, where the time of the peak velocity occurred later for the lower ambient density. This indicates that the emulsification process had an effect on the very early period of the spray development during these tests though a clear trend is unclear. It appears that at the 500 bar injection pressure, the ambient density had a greater effect on the time of U_{Bmax} for both the Diesel and D10 sprays. As the injection pressure was increased to 700 bar, the time when U_{Bmax} occurred for the Diesel sprays became independent of the ambient density and increasing injection pressure. This is not the case for the D10 sprays, as the injection pressure was increased to the 700 bar, the time when U_{Bmax} occurred became independent of the ambient density but not the injection pressure, as when the injection pressure was increased to 1000 bar, the time of U_{Bmax} reduced again. This also demonstrates the need for high temporal resolution measurements to be made of the very early period and that linear fitting in this period should be avoided.

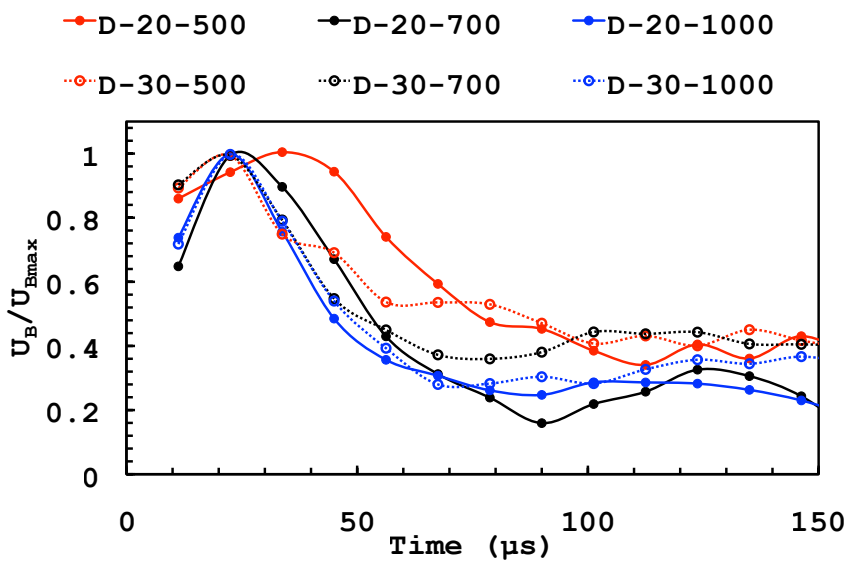

Figure 4.53: Fuel injection spray tip velocity, normalized to maximum velocity for each condition, variation with time after SOI for Diesel fuel. P_{inj}= 500 (red), 700 (black) and 1000bar (blue) ρ_a = 22.6 kg/m^3 (P_{amb}= 20bar) shown with solid symbols. ρ_a=34.5 kg/m^3 (P_{amb}= 30bar) shown with empty symbols. Determined using the backlit image sequences.

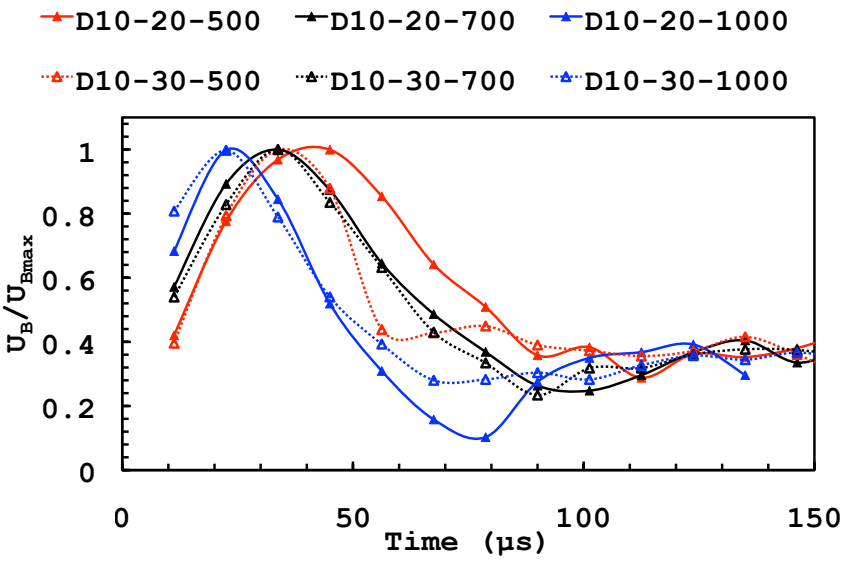

Figure 4.54: Fuel injection spray tip velocity, normalized to maximum velocity for each condition, variation with time after SOI for D10 fuel. P_{inj}= 500 (red), 700 (black) and 1000bar (blue) ρ_a = 22.6 kg/m^3 (P_{amb}= 20bar) shown with solid symbols. ρ_a=34.5 kg/m^3 (P_{amb}= 30bar) shown with empty symbols. Determined using the backlit image sequences..

4.1.5.1 Summary

- Sequences of consecutive images of Diesel fuel, and D10 injection sprays were collected using the backlit system at a frame rate of 88,888fps.
- Image sequences were used to determine the temporal evolution of the spray tip penetration for fuel sprays at an injection pressure of 500, 700 and 1000 bar into two ambient densities of 22.6 kg/m^3 and 34.5 kg/m^3 of an inert nitrogen atmosphere.
- Matlab image processing was applied to determine the spray tip penetration from the image sequences.
- The spray tip penetration was back extrapolated to 0 mm at t=0.
- Increasing the injection pressure resulted in an increase in the temporal evolution of the spray tip penetration. Injections of Diesel fuel, at 700 bar, ambient density 22.6 kg/m^3 did not fit with this trend, it is unclear why.
- Increasing the ambient density resulted in a decrease in the temporal evolution of the tip penetration.
- The higher temporal resolution of the backlit measurements, when compared with the shadowgraph derived measurements, allowed the spray tip velocity to be examined during the early period of the spray development.
- The time after SOI when peak velocity U_{Bmax} was reached was examined. The time was independent of pressure and ambient density for the Diesel sprays, apart from the 500 bar injection, ambient density 22.6 kg/m^3. The time of U_{Bmax} for the D10 was not independent of the ambient density.

4.2 Hydraulic characterization of Diesel fuel, D10 and D20 Non-vaporizing sprays

In the following section the spray momentum fluxes ($\dot{M}$) for Diesel fuel, D10 and D20 injections are presented. Spray momentum flux has been measured using the force transducer, fitted with a target, installed in the high pressure chamber. Results are shown as the time resolved, mean momentum flux from 100 consecutive injections. The injection pressures applied, P_{inj}, are 500, 700 and 1000 bar. The nitrogen pressure in the chamber (P_{amb}) into which the injections took place was 20 to 30 bar. As the pressure was increased, the temperature was allowed to reach equilibrium with the ambient temperature in the lab (20°C) which equates to an ambient density, ρ_a of 22.6 kg/m^3 and 34.5 kg/m^3. The position of the transducer target was not moved at all during the data collection and was set at a distance of 0.5mm from the nozzle orifice face. The transient nature of the momentum flux is discussed with peak values extracted and used as representative values for each condition. The total mass per injection is then introduced and this is used along with the momentum flux to determine the instantaneous mass flow rate of the injection. Fuel densities and viscosities are presented and a number of dimensionless nozzle parameters are examined for each condition, with the effects of injection pressure, ambient density and emulsification presented.

4.2.1 Spray Momentum Flux

The transient variation of the momentum flux over the entire injection period for Diesel fuel, D10 and D20 injection sprays for all conditions are shown in Fig.4.55. For all cases here the curve shows the arithmetic mean $\dot{M}$ of 100 injections. No signal smoothing has been applied. A sampling rate of 100kHz has been used (sample made every 10μs). In this plot no correction to remove any injection delay has been applied (Sec.3.10).

The portion of the delay that has been termed "electronic delay" was assumed to be constant for all conditions so may be ignored from here on. No adjustment was made to the injection TTL during experimentation. The variation in delay, shown by the start of momentum flux (t when $\dot{M}$ >0) was entirely from the "hydraulic delay". As the injection pressure is increased from 500 to 700 and 1000 bar, the hydraulic injection delay increases from 290 to 320 to 390μs respectively. The end of injection was much harder to qualify as the measured momentum flux does not

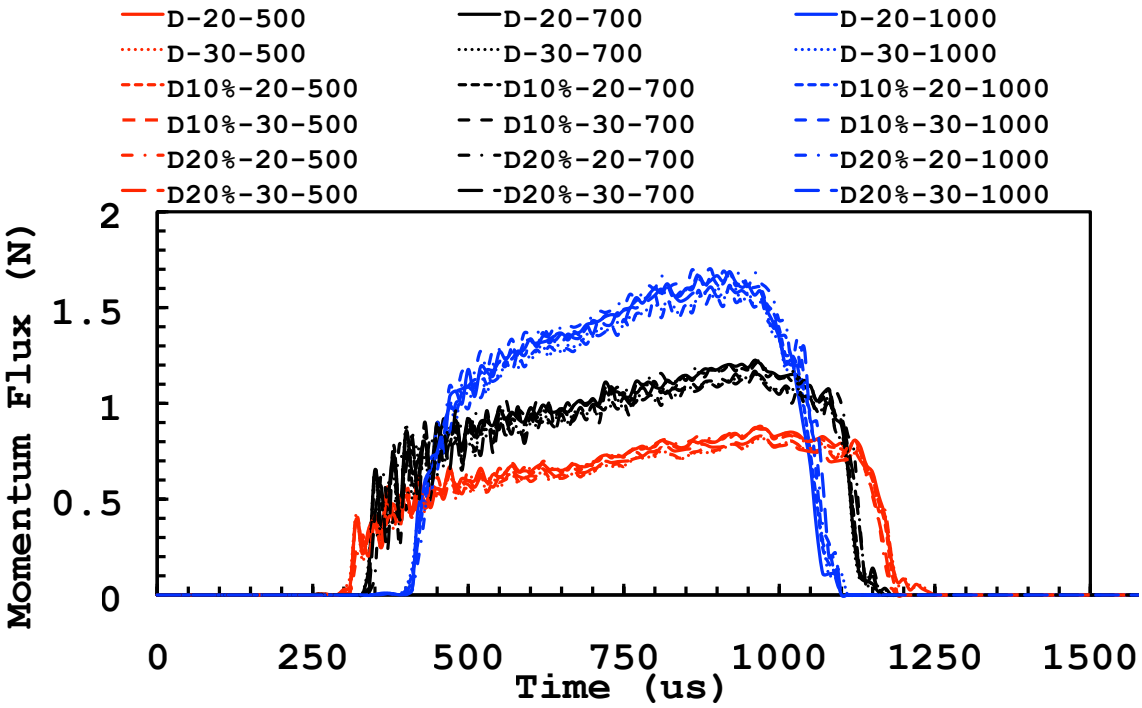

Figure 4.55: Fuel spray momentum flux variation with time, after the start of data recording (with no injection delay removed) for Diesel fuel, D10 and D20. P_{inj}= 500 (red), 700 (black) and 1000bar (blue) ρ_a = 22.6 kg/m^3 (P_{amb}= 20bar). ρ_a=34.5 kg/m^3 (P_{amb}= 30bar)

drop to zero in the same manner as it increased from zero at the SOI. This EOI feature is believed to due to;

- Transducer response to vibration of the target face after the spray force has been removed.
- A small amount of signal drift during the measurement, this had been noted during testing and was most probably a combination of charge amplifier drift and temperature drift for the transducer itself. As described in the experimental section, temperature drift was not considered critical to the design due to the nature of the target fixing into the transducer but it is reasonable to assume a small amount would be present.
- The flow field of the ambient gas in this region, very close to the nozzle, after the spray has ceased is not well understood and may lead to pressure variations in the this region.

An approximation from the plot is made as to the time of EOI, as measured by momentum flux. As the injection pressure is increased, the EOI occurs earlier, with EOI at approximately 1190, 1130 and 1090 μs (P_{inj}= 500, 700 and 1000 bar respectively). The hydraulic delay is mirrored at the EOI, leading to a decrease in

the actual duration of injection with increasing injection pressure. The injection duration used here is quite short, with a TTL signal of 0.5ms sent to the injector driver. The effective duration of the actual injection event is 910, 810 and 700μs for P_{inj}= 500, 700 and 1000 bar respectively. Emulsification has had no influence on the injection delay and duration.

The exact feature of the injector which was causing the delay and duration effects is unknown. The injector needle lifts when the pressure in the mini-sac is greater than the closing pressure when it snaps up, opening the orifice. Increasing the pressure may lead to a longer time for the closing pressure to reduce to this level. This has not been noted or discussed in previous studies. It may be an effect of having all but one of the holes laser welded closed and the dismantling of the injector to make modifications.

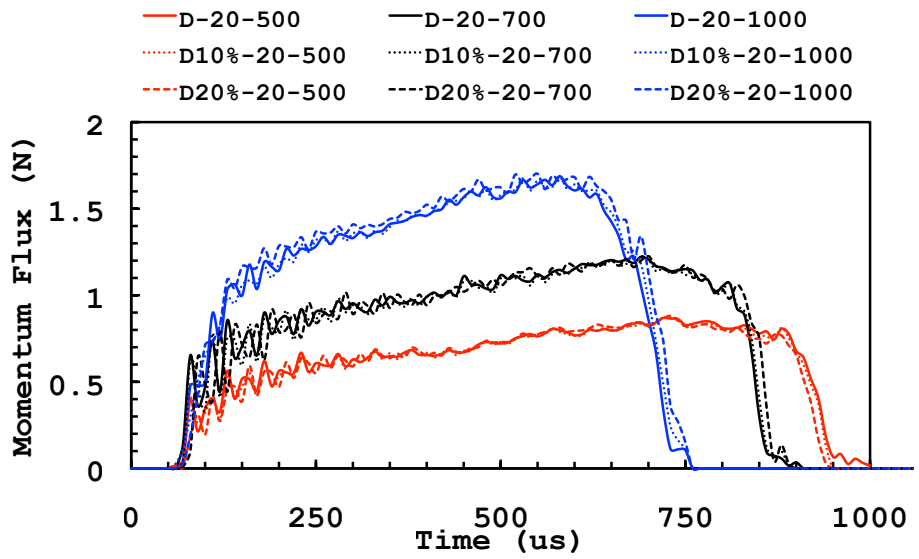

Figure 4.56: Fuel spray momentum flux variation with time after SOI for Diesel fuel, D10 and D20. P_{inj}= 500 (red), 700 (black) and 1000bar (blue) ρ_a = 22.6 kg/m^3 (P_{amb}= 20bar).

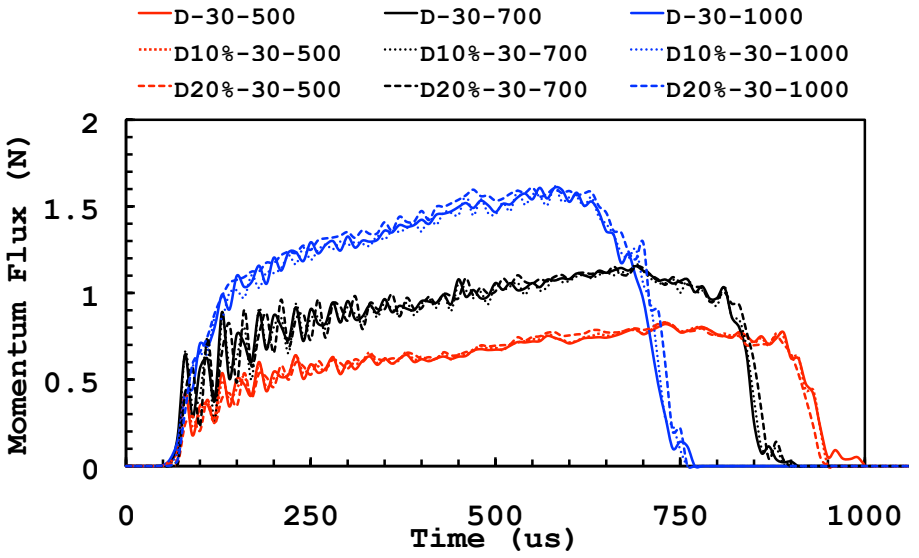

Figure 4.57: Fuel spray momentum flux variation with time after SOI for Diesel fuel, D10 and D20. P_{inj}= 500 (red), 700 (black) and 1000bar (blue) ρ_a=34.5 kg/m^3 (P_{amb}= 30bar)

Figs.4.56 and 4.57 show the transient variation of the momentum flux over the entire injection period for Diesel fuel, D10 and D20 injection sprays into the ambient density of ρ_a of 22.6 kg/m^3 and 34.5 kg/m^3 respectively. The initial non-zero momentum flux is used to align the SOI for each condition so as to allow a comparison between the cases with the hydraulic delay removed. The SOI of injection for each

case has been aligned at $t = 50\mu s$. For all conditions the initial increase in $\dot{M}$ is extremely rapid as the spray exits the injector nozzle and strikes the transducer target. The $\dot{M}$ increases at a higher rate during this initial period with a higher injection pressure applied. Throughout the injection period a higher injection pressure results in a larger $\dot{M}$. During the first 50μs of the injection there is considerable overlap of the momentum flux curves and it is difficult to clearly state any injection pressure or ambient density effects. After approximately 100μs the slope of the curve for all cases reduces and the variation of the momentum flux appears almost linear with time until peak momentum flux is reached. It is at around 100μs after SOI that the momentum flux of the injections into the ambient density of 22.6 kg/m^3 increase in size relative to the 34.5 kg/m^3 curves. There is not a large difference and for the P_{inj}= 500 and 700 bar there is overlapping of the curves, with the 700 bar injections only really showing a defined and consistent difference after 500μs.

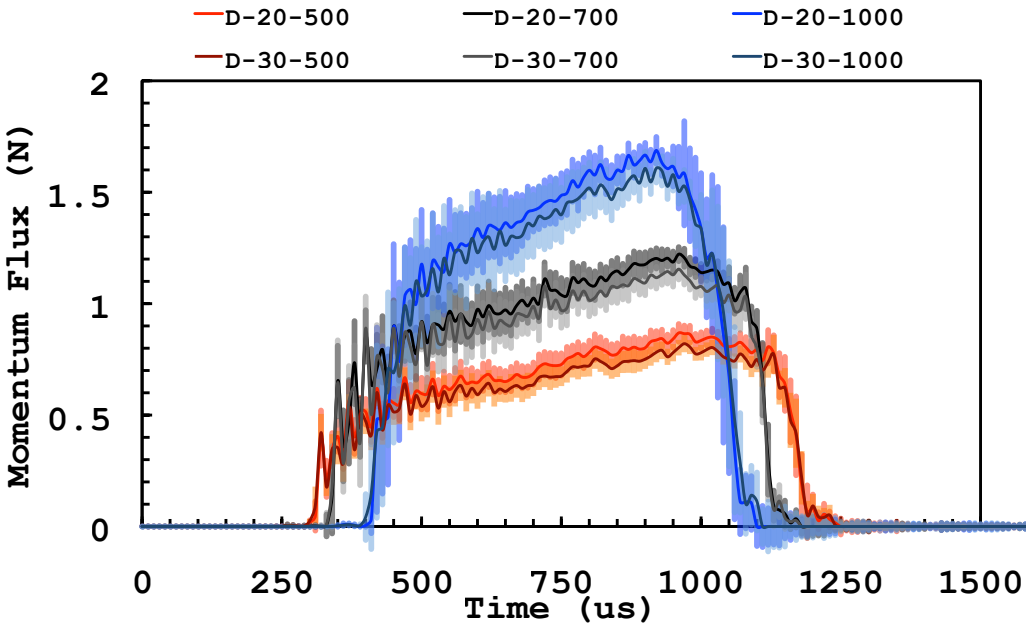

Figure 4.58: Fuel spray momentum flux variation with time, after the start of data recording (with no injection delay removed) for Diesel fuel. P_{inj}= 500 (red/orange), 700 (black/grey) and 1000bar (blue/light blue) ρ_a = 22.6 kg/m^3 (P_{amb}= 20bar) and . ρ_a=34.5 kg/m^3 (P_{amb}= 30bar). Error bars are the size of one standard deviation of the momentum flux for the 100 injections.

Fig.4.58 shows transient $\dot{M}$ for each condition, Diesel fuel only, complete with error bars the size of one standard deviation and is included as an example to show the repeatability and statistically significance of any small difference observed between the $\dot{M}$ at each condition. The standard deviation has been determined from the raw, unprocessed data, taking the $\dot{M}$ from each time step. At the time of peak $\dot{M}$, for each injection pressure, the $\dot{M}$ for the injections into ρ_a34.5 kg/m^3 is below the value of the lower standard deviation error bar for the ρ_a of 22.6 kg/m^3

injections.

The mean $\dot{M}$ signal shown in the figures so far show a large variation during the initial period of the injection period. This must be due to rapid transients in the spray structure which may be termed as hydraulic noise. When the curves for the same injection pressures are compared (with hydraulic delay removed, Figs.4.56 and 4.57) there is reasonably good alignment between this hydraulic noise which suggests this noise is repeatable and a feature of the nozzle and transducer target interaction at these injection conditions (P_{inj}, ρ_a, fuel type, injector energizing time). The natural frequency of the force transducer was 50,000 kHz. Examination of the momentum flux profiles shows the frequency of the oscillations to be in this range, hence the oscillations in the profile observed during the entire injection period were most likely a result of the natural frequency of the transducer.

The injection period was short and it could be an issue that the momentum flux did not reach a maximum value in this time and that the needle opening and closing were having a large effect on any analysis. During experimentation there was an example data set collected when the optical system was in place with the camera installed. As discussed in Sec.3.10 this resulted in a longer injection duration, as was observed during the optical experiments, even though the TTL injection signal was for the same duration.

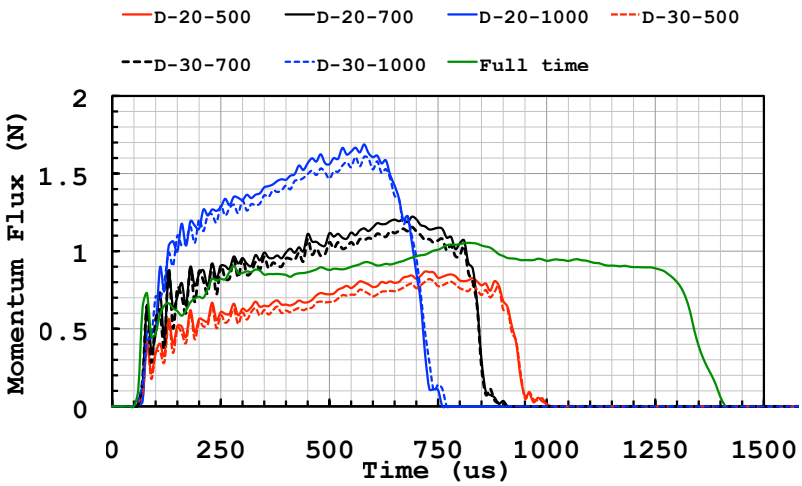

Figure 4.59: Fuel spray momentum flux variation with time for Diesel fuel. P_{inj}= 500 (red), 700 (black) and 1000bar (blue) ρ_a = 22.6 kg/m^3 (P_{amb}= 20 bar) solid line and . ρ_a=34.5 kg/m^3 (P_{amb}= 30 bar) broken line. Green line shows a sample collected with injection duration extended due the inclusion of the camera in the system, as discussed in Sec.3.10. Injection pressure of this sample was approximately 600bar, ambient density was atmospheric and is denoted as full-time.

Fig.4.59 shows transient momentum flux for Diesel fuel along with the transient

moment flux collected for a Diesel fuel injection with an extended duration due to the camera being plugged into the DAQ system. The injection pressure for this injection was approximately 600 bar, with the injection taking place into atmospheric conditions with the chamber open, hence the measured momentum flux does not match with any other data presented here. The overall trend was the same and the peak value of the momentum flux can be seen to occur at around the same time as the peak for the 500 bar injections. This figure is used to make the assumption that the peak momentum flux measured in the hydraulic experiments is a genuine peak and the momentum flux would not have increased had the injection period lasted for a longer time.

To extract a representative, mean value of momentum flux from the momentum flux profile, the 10 maximum values were used. The mean of these 10 maximum values was then used as the representative value of momentum flux for each condition. Fig.4.60 shows the 10 maximum values for each condition (grey) with the mean value determined (black). Remembering that the momentum flux profiles are themselves made from the mean momentum flux of 100 injections, the 10 maximum values are therefore the mean maximums of 100 injections. This was taken into account in Fig.4.60 which includes error bars for the 10 maximum values. These error bars are the size of the standard deviation of the mean (standard error) of the 100 injections used to generate the mean values which was used to determine the representative value for each condition.

This mean peak value is used to construct Fig.4.61. The linear relationship between the injection pressure applied and the measured momentum flux is demonstrated, as is expected from theory (Sec.2.5, Eqn.2.36). The upper, blue broken line on the plot is a linear trend line fitted to the points collected for injections into an ambient density of 22.6 kg/m^3. The lower, broken black line is trend line fitted to the points collected for injections into an ambient density of 34.5 kg/m^3. The pressure drop across the nozzle for the different ambient densities is different as the ambient density was changed by changing the pressure in the chamber. The theory introduced in the Sec.2.5 and discussed in previous work [158, 102] suggests that the momentum flux measured in this way would have no dependents on the density of the atmosphere into which the injection is taking place. If this was the case, and the momentum flux was only dependent on the pressure drop across the nozzle it would be expected that all points would lie on the same line.

Although the effect is small, the high number of samples collected suggests that this difference is statistically significant, which has been partially addressed with the

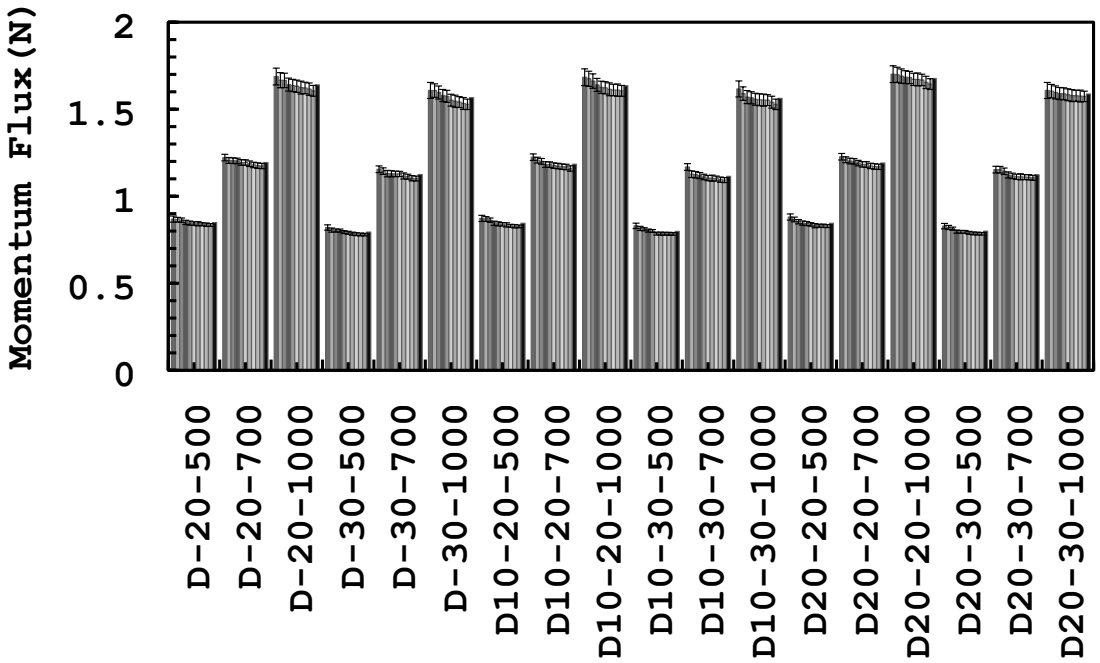

Figure 4.60: Bar chart of the 10 maximum values of the momentum flux recorded for each condition (grey) with the mean maximum value of the 10 maximums (black) which is used as the representative value of the momentum flux for each condition. Error bars on top of each bar are the size of the standard deviation of the mean (standard error) of the momentum flux value of the 100 injections.

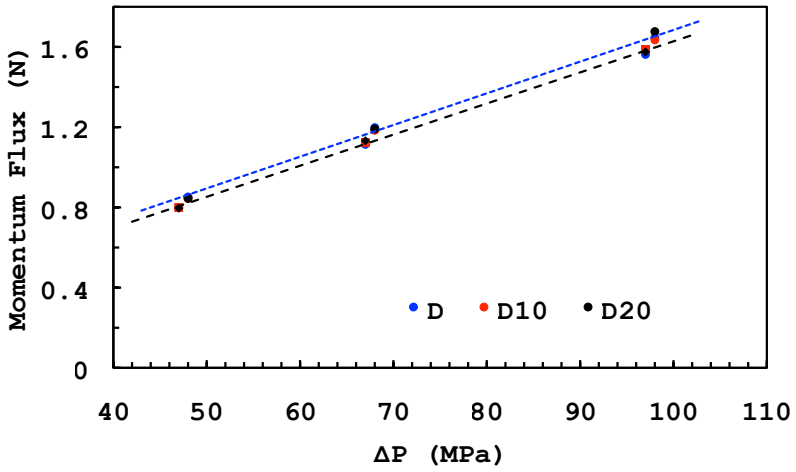

Figure 4.61: Average peak value of the momentum flux for Diesel fuel (blue), D10 (red) and D20 (black) with the pressure drop across the injector nozzle (ΔP). The blue broken line is fitted to the injections with ρ_a = 22.6 kg/m^3 (P_{amb}= 20bar). The black broken line is fitted to the injections with ρ_a=34.5 kg/m^3 (P_{amb}= 30bar).

examination of the standard deviation of the momentum flux measurements, with the Diesel fuel example shown in Fig.4.58. This is a surprise considering that the momentum flux was measured 0.5mm from the nozzle exit. It was not expected that the ambient density would have any effect on the momentum flux at this distance

from the nozzle as the spray is expected to mainly consist of liquid core at this range, which would have had little interaction with the ambient gas. The results here suggest that the liquid core or the spray is experiencing momentum exchange with the surrounding gas even at this distance from the nozzle. For each condition, the emulsification as had little, to no effect in the average peak momentum flux.

4.2.2 Total mass injected

The total mass of fuel injected at each injection pressure for each fuel has been determined according to the procedure outlined in Sec.3.7.3. The masses collected for Diesel fuel along with all repeats and relative standard error have already been introduced in full in Table.3.6. Table 4.2 shows the average mass of fuel injected for each fuel at each pressure, determined from the 5 batches of 500 injections. The ratio of the range to the mean is included to demonstrate the high repeatability between the 5 cases. As has been shown, the spray momentum flux has a dependence on the ambient density of the injection environment. It would be sensible to assume that the ambient density has an effect on the mass injected which, considering all masses were obtained at atmospheric conditions is not considered here.

Table 4.2: Mass of fuel injected per injection event for each fuel considered.

Fuel	Injection Pressure	Mass/injection(g)	Range/mean
D	500 bar	0.002353	0.005
	700 bar	0.002662	0.01
	1000 bar	0.002752	0.02
D10%	500 bar	0.002255	0.02
	700 bar	0.002492	0.01
	1000 bar	0.002630	0.03
D20%	500 bar	0.002275	0.01
	700 bar	0.002519	0.02
	1000 bar	0.002652	0.05

The data from Table.4.2 has been plotted and shown in Fig.4.62. The mass of Diesel fuel injected for each condition is larger than both emulsions for each injection pressure. The two emulsions show a very similar injected mass. The difference between the Diesel fuel and emulsions is almost the same at each injection pressure

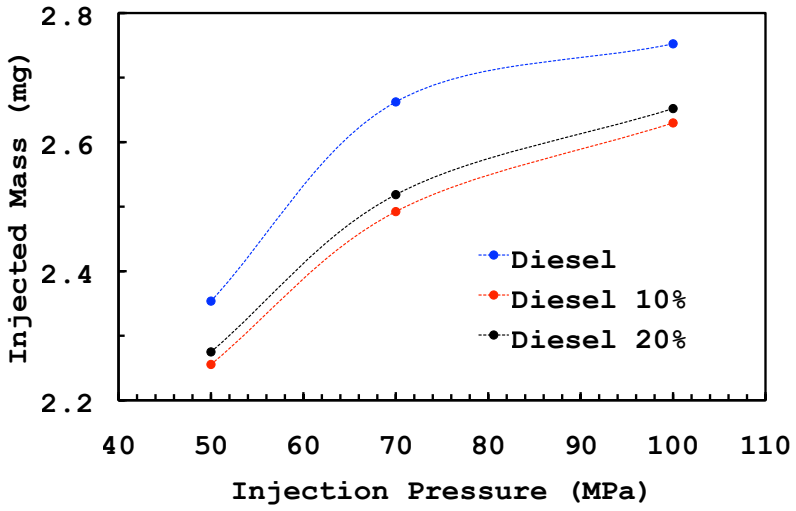

Figure 4.62: Total mass of fuel injected for the Diesel (blue), D10 (red) and D20 (black) fuels at P_{inj}= 500, 700 and 1000bar (50, 70 and 100MPa).

4.2.3 Fuel Densities and Viscosity

The density and viscosity for each fuel has also been determined and are presented in Table.4.3. The density has been measured according to the procedure detailed in Sec.3.7.2. The viscosity was determined using the rheometer according the the method detailed in Sec.3.7.2. For all cases the viscosity was observed to reach a constant when the shear rate was between 400 and 1000s^{-1}. The mean value presented is the determined from taking the mean value of this constant period. The measurement was repeated three times and these 3 mean values were used to obtain a mean viscosity of the fuels, stated in Pascal.seconds.

Table 4.3: Fuel density and viscosity

Fuel	Density (kg/m^3)	Viscosity (Pa.s)
Diesel	814	0.00588
Diese 10/% water	829	0.00669
Diesel 20/% water	876	0.00678

The emulsification of the fuel resulted in a small increase in the fuel density. This is expected due to the addition water which has a high density than the neat Diesel. The measured density has been compared to the density obtained from the model of an ideal mixture. The ideal mixture may be defined according to two different model mixtures. One relies on the assumption that the volume of the solution is proportional to the mass and uses the mass fraction of each substance and their densities.

$$\rho_n = \sum (x_i \rho_i)_n \tag{4.5}$$

where x_i is the mass fraction. The second method assumes the volumes are additive and may be more appropriate for immiscible liquid such as water and Diesel fuel.

$$1/\rho_n = \sum (x_i/\rho_i)_n \tag{4.6}$$

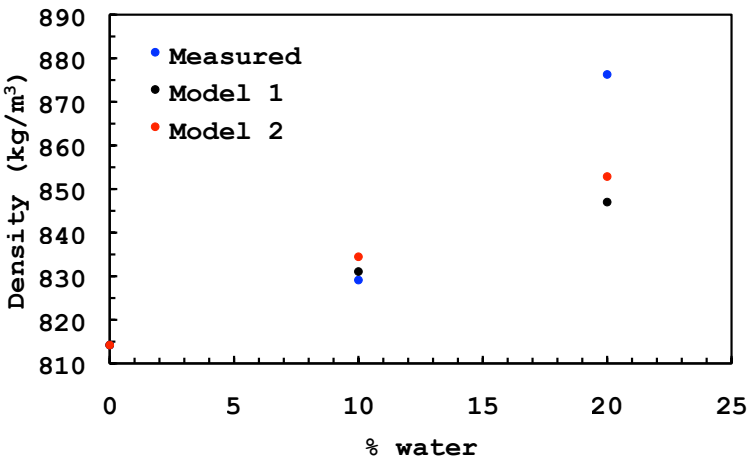

Figure 4.63: Density of the fuels with percentage of water added. Density determined from measurement in blue, density calculated using Eqn.4.5 in black. Density calculated using Eqn.4.6 in red.

The results of the measured and the two predictive models are shown in Fig. refDensity. The measured density for the D10 fuel is similar to the two predictive models. The measured density for the D20 fuel is much larger than is predicted by the two mixing models. This suggests that for the emulsified fuel, as the water content increases, the surfactant is acting to reduce the volume that the water takes up in a simple mixture. The emulsification process is not a simple mixing process and results in a complex mixture of dispersed droplets with a range of sizes and surface areas. It is evident that as the water is added, the dispersed phase becomes much larger and the droplets may be able to compact more closely together leading to an increase in the density away from a simple linear mixing model.

The small increase in density of the emulsified fuels would be expected to lead to an increase in the injected mass, considering the injected mass is given by $A_{geo}\sqrt{\rho_f 2\Delta P}$. This is not what was observed (Fig.4.62). The emulsification process has resulted in a increase in the measured viscosity compared to neat Diesel. This increase in viscosity must be countering the increase in fuel density to reduce the mass of fuel that is injected during the needle opening time.

4.2.4 Instantaneous Mass Flow Rate

The development of the momentum flux measurement was in part done to address the need to measure the instantaneous mass flow rate ($\dot{m}$) of a fuel injection event. Using Eq.2.40, the mean measured momentum flux and the independently measured total mass of injected fuel the instantaneous mass flow rate for each condition has been determined. There is no alternative technique applied here to validate findings against. The integral of the square root of the momentum flux (see Eq.2.40) is defined by the area below the momentum flux curve and has been calculated numerically using the trapezium technique in Matlab. An example of the instantaneous mass flow rate profiles is shown in Fig.4.64. This example includes profiles for each fuel at each injection pressure with an ambient density of 22.6 kg/m^3.

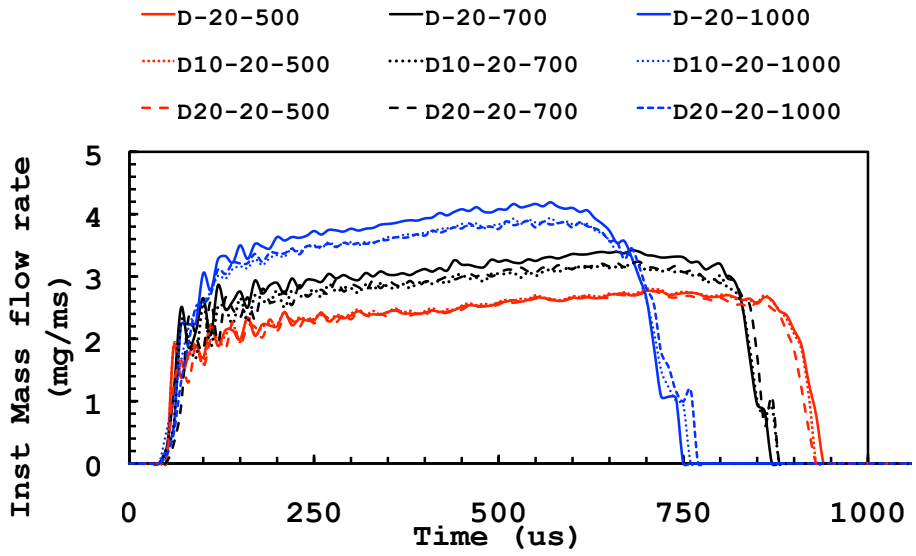

Figure 4.64: Instantaneous mass flow rate profile for Diesel fuel(solid line), D10 (fine broken line) and D20 (course broken line). P_{inj}= 500 (red), 700 (black) and 1000bar (blue) ρ_a = 22.6 kg/m^3 (P_{amb}= 20bar).

The momentum flux profiles and the instantaneous mass flow rate profiles are essentially the same shape with scaling between the two proportional to the spray velocity. Both profiles may be used in the modeling process to elucidate temporal evolution of fuel concentration in the combustion chamber and may also be used in the development of injector profile shaping for improved combustion characteristics. The total mass injected is different for each fuel, which leads to a change in the instantaneous mass flow for the emulsified fuels when compared with the Diesel fuel sprays. The 10 largest values of the instantaneous mass flow rate for each condition have been used to produce a mean peak value in a similar manner as was done for the momentum flux mean peak values in Figs.4.60 and 4.61.

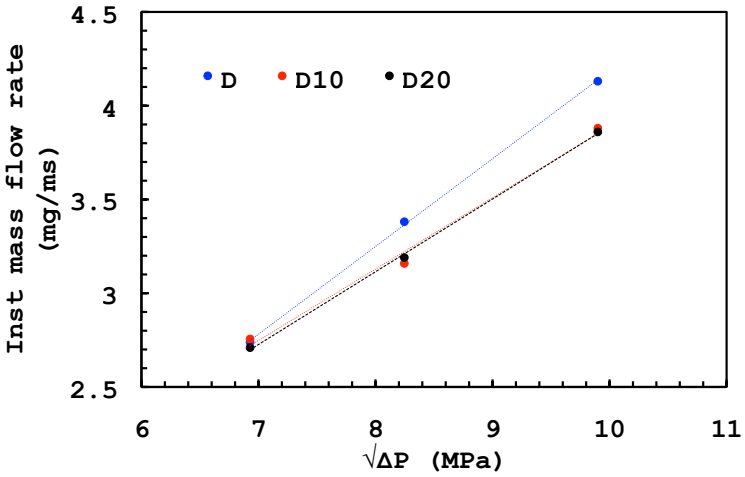

Figure 4.65: Mean peak value of the instantaneous mass flow rate for Diesle fuel (blue), D10 (red) and D20 (black) with the square root of the pressure drop across the injector nozzle ($\sqrt{\Delta P}$). $\rho_a = 22.6$ kg/m^3 (P_{amb}= 20bar).

This mean peak value is used as a representative value of ($\dot{m}$) for each condition and has been used to produce Fig.4.65. The linear dependence of the mass flow rate with the square root of the pressure drop across the nozzle is demonstrated. The two emulsified fuels have a near identical peak $\dot{m}$ at each injection pressure. As the injection pressure is increased the difference between the neat Diesel and the emulsified fuels gets larger. The $\dot{m}$ mean peak value is almost identical at 500 bar injection pressure for each fuel. At the1000 bar injection pressure there is a difference in $\dot{m}$ of approximately 0.3 mg/ms. The difference is small but this reflects the short time scale and mass scales that are involved in the measurement of these injection events. The difference in the instantaneous mass flow rates between the Diesel fuel and the emulsified fuels is to be expected when the difference in the total mass injected is examined in Fig.4.62. The technique may be considered successful at producing an instantaneous mass profile that may be used as an input into multidimensional engine models. The observed reduction in the instantaneous mass flow rates for the emulsified fuels compared with the neat Diesel fuel may be more closely examined considering nozzle non-dimensional characteristics such as the discharge coefficient.

4.2.5 Discharge Coefficient

The transient discharge coefficient has been determined using Eq.2.42 with: the instantaneous mass flow rate; the geometrical cross sectional area (A_{geo}) of the nozzle orifice, determined using the silicone mold of the nozzle (Sec.3.1.1); the fuel density and; the injection pressure. From this transient discharge coefficient profile,

a representative value was obtained from taking the mean value of the 10 largest values, a mean peak value, as used for the momentum flux and the instantaneous mass flow rate. This representative discharge coefficient value for each condition has been used to produce Fig.4.66.

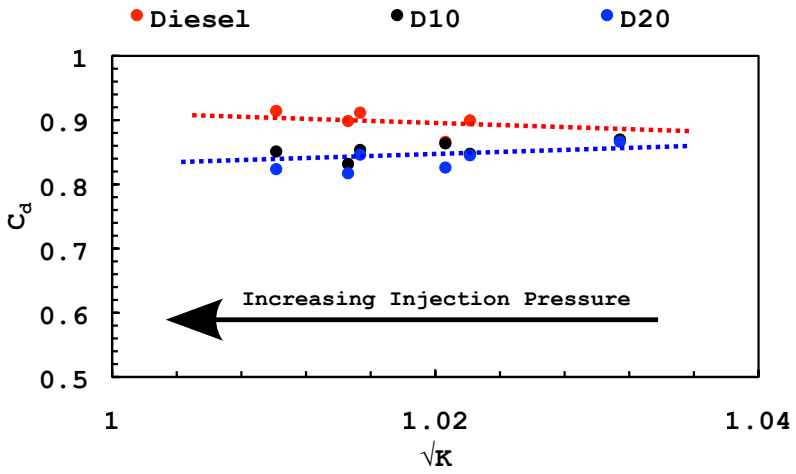

Figure 4.66: Nozzle discharge coefficient with the square root of the cavitation number (Eqn2.49) for Diesel fuel (red), D10 (black) and D20 (blue). Trend line has been fitted separately to Diesel fuel (red) and the emulsions (blue).

Fig.4.66 shows the representative mean peak value of the discharge coefficient for each condition with the square root of the cavitation number (K, see Sec.2.5.4, Eqn2.49). An increase in injection pressure results in a decrease in the cavitation number hence the arrow included in Fig.4.66 is in the direction of increasing injection pressure. The emulsification has lead to a reduction in the nozzle discharge coefficient compared with the neat Diesel conditions. It is evident that the discharge coefficient is not really changing with the change in injection pressure (hence $\sqrt{K}$) and there is no evidence that the nozzle is experiencing geometric cavitation for any conditions or that K_{crit} has been observed. The K-factor of the nozzle (Sec.2.2.1, Eqn.2.6) was determined using the measurements made in the SEM of the silicone mold of the nozzle geometry, shown in Table 4.4. The inlet radius was also measured in the SEM was determined to be approximately 70μm.

Table 4.4: Injector nozzle diameters and K-factor

D_{inlet} μm	D_{outlet} μm	K factor (μm)
140	120	2

The K-factor and the inlet radius has effectively suppressed the formation of geometric cavitation in the nozzle at the conditions considered here. It is observed that the discharge coefficient varied little with the change in K for all fuels. The

emulsification process, though reducing the discharge coefficient, did not induce any geometric cavitation at the injection conditions considered. At the injection pressure of 1000 bar (the lower $\sqrt{K}$) the difference in discharge coefficient between the Diesel fuel and the emulsions was significant. The range of K values examined in this study was limited when compared with other work which use this analysis [119, 85] so the conditions when geometric cavitation may have started cannot be assessed. Theory states that under these non-cavitating conditions, the flow is dependent on the Reynolds number [85]. To examine the Reynolds number, the flow mean velocity was required along with the fluid density and viscosity. The characteristic length scale applied is the nozzle mean diameter, determined from the measurements in Table.4.4 to be 130μm. The mean injection velocity was calculated using the mean peak momentum flux value and the mean peak instantaneous mass flow rate value in the form

$$V_{eff,mean} = \frac{\dot{M}_{mean}}{\dot{m}_{mean}} \tag{4.7}$$

and was used to produced Fig.4.67.

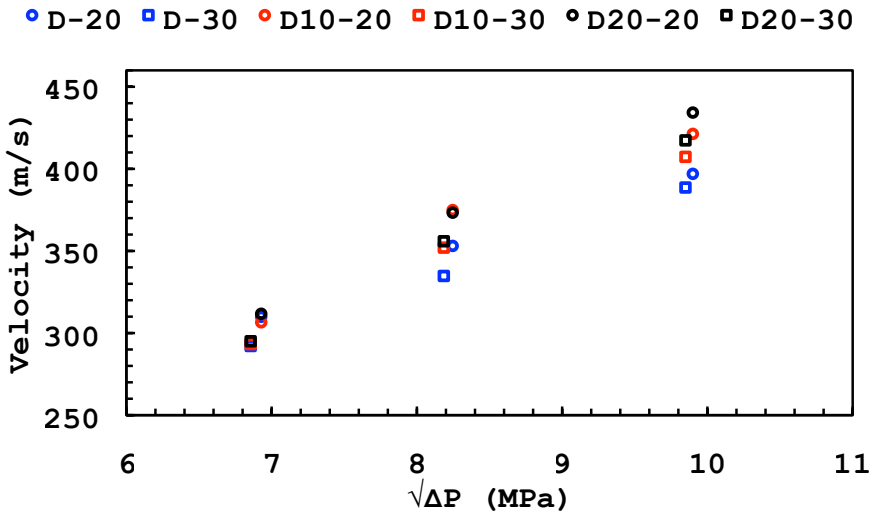

Figure 4.67: Mean peak value of the injection velocity for Diesel fuel (blue), D10 (red) and D20 (black) with the square root of the pressure drop across the injector nozzle ($\sqrt{\Delta P}$). ρ_a = 22.6 kg/m^3 (P_{amb}= 20bar) shown with empty circles. ρ_a=34.5 kg/m^3 (P_{amb}= 30bar) shown with empty squares.

The momentum flux measured was almost the same at each condition for each fuel. The mass flow rate for the emulsions was reduced compared with the neat Diesel. For the momentum to have been unchanged the velocity of the emulsions must have increased. This is reflected in Fig 4.67 which shows that as the injection pressure was

increased, the mean injection velocity of the emulsions increased compared with the neat Diesel fuel. For each condition, the injection velocity with the ambient density of 22.6 kg/m^3 was higher than when the ambient density was 34.5 kg/m^3. According to the Reynolds number equation, Eqn.4.8, the higher velocity and larger density of the emulsified fuels will lead to an increase in the Reynolds number, whilst the increase in viscosity of the emulsions will results in a reduction in the Reynolds number.

$$Re_l = \frac{vD\rho_l}{\mu_l} \tag{4.8}$$

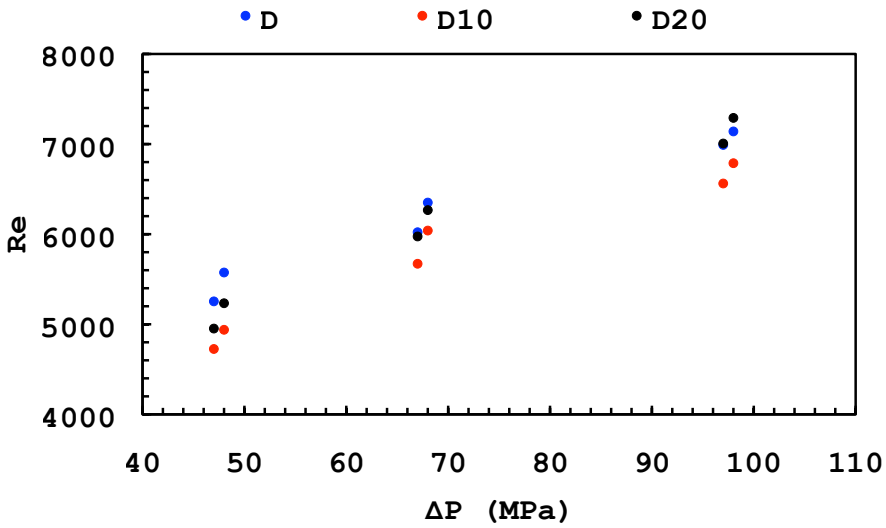

Figure 4.68: Mean Reynolds number for Diesel fuel (blue), D10 (red) and D20 (black) with pressure drop across the injector nozzle ($\sqrt{\Delta P}$).

Fig.4.68 shows the Reynolds number with the change in injection pressure for each fuel. Considering the large scale over which the Reynolds number is measured, the difference between the fuels is negligible. This suggests that, although there is no cavitation, it is not the Reynolds number of the flow in the nozzle which is reducing the discharge coefficient for the emulsified fuels. It is worth noting that the Reynolds numbers calculated for Fig.4.68 are a lot lower than those in previous works. This is believed to be due to the quite high viscosity measured here when compare with values of dynamic viscosity in the range of 0.002 Pa.s [119, 208] which is often used.

So far cavitation has been discussed in terms of geometric cavitation which occurs in the nozzle passage connecting the injector sac volume to the ambient atmosphere. The presence of vortex cavitation structures inside the sac volume of fuel injector nozzles has been observed and is termed string cavitation [209]. String cavitation has

been observed in optically accessible fuel injector nozzles [210, 211] and is thought to form as a result of the intense flow vorticity inside the injector sac volume, resulting in a low pressure region at the centre of the vortical flow. The cavitation strings appear as strings of vapor which usually connect the flow between adjacent nozzle orifices [211]. The incidence of string cavitation in the nozzle sac volume may explain the reduced discharge coefficient observed here considering the absence of geometric cavitation demonstrated in Fig.4.66. The increased flow velocity observed with the emulsified fuels may have resulted in a more intense vortical flow in the sac volume, increasing string cavitation, resulting in the reduced discharge coefficient for the emulsified fuels.

The injection velocities determined here are very different from the spray tip velocities determined using the backlit image sequences (Figs.4.51 and 4.52). The peak spray tip velocities calculated are in the range of 170ms^{-1} while the peak injection velocities are in the range 440ms^{-1}. The peak spray tip velocities occurred very shortly after the SOI, after which time the tip decelerates. The peak injection velocities occur when the momentum flux is at its greatest which is near the EOI. The two velocities are different variables. The spray tip velocity shows the spray's acceleration from stationary as the injector opens and it's interaction with the surrounding gas, as aerodynamic forces start to act and it exchanges momentum. The region of liquid/vapor at the front of the spray is pushed aside, forming its cone shape, with spray from behind this replacing it as the spray front traverses the test section. The injection velocity shows that as the injector opens, fuel starts to flow through the nozzle, there is a period where the flow is establishing itself, its velocity, hence its momentum is increasing. When the flow is well established, the momentum reaches a peak value, which is when the flow velocity is at its peak value and this really represents the velocity of the flow though the nozzle and the first 0.5mm of the surrounding gas.

4.2.6 Momentum Coefficient

The discharge coefficient may not be the best dimensionless number to help elucidate the nature of the flow in the nozzle under these conditions. Whilst the discharge coefficient may be important from a fuel metering point of view, the momentum of the spray represents the energy available to the spray as it mixes and exchanges momentum with the surrounding gas. Two new coefficients are introduced based upon the momentum. One of these, the so called "momentum coefficient" [119], C_M, is analogous to the discharge coefficient, defined as the measured momentum divided by the theoretical momentum of the spray, given by

$$C_{Mmean} = \frac{\dot{M}_{mean}}{A_{geo}\rho_f v_{eff}^2} = \frac{\dot{M}_{mean}}{2A_{geo}\Delta P} \tag{4.9}$$

The representative mean peak values of the momentum flux determined in Sec.4.2.1 are used to determine the momentum coefficient. The change in the C_{Mmean} with the pressure drop (ΔP) across the nozzle is shown in Fig.4.69. The theoretical momentum flux of the spray increases with increasing ΔP, the results shown in Fig.4.61 agree with this statement, but it is only after the momentum coefficient is determined that it is clear that, in terms of momentum, the nozzle is not performing as would be expected with increasing injection pressure. For all fuels, the increase in the ambient density in the chamber has resulted in a reduction in the momentum coefficient. The emulsification has had no discernible effect on the momentum coefficient, with each fuel, at each injection condition having a very similar, almost identical momentum coefficient.

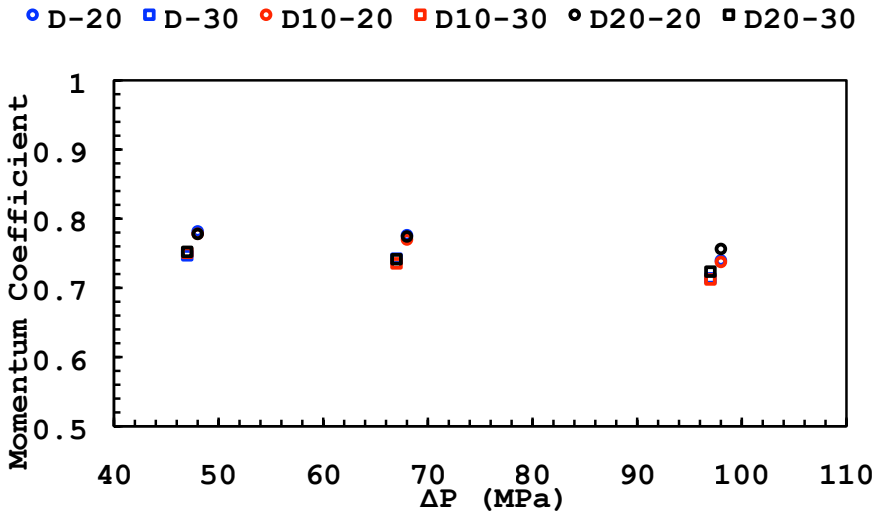

Figure 4.69: Momentum coefficient (Eqn.4.9 of sprays for Diesel due (blue), D10 (red) and D20 (black) with the pressure drop across the injector nozzle ($\sqrt{\Delta P}$). ρ_a = 22.6 kg/m^3 (P_{amb}= 20bar) shown with empty circles. ρ_a=34.5 kg/m^3 (P_{amb}= 30bar) shown with empty squares.

A new method of characterizing the spray is suggested which may elucidate some nozzle and spray features using the hydraulic measurements taken here. The momentum coefficient has been calculated using the theoretical momentum flux for each condition given by $2A_{geo}\Delta P$. The geometric area of the nozzle orifice is being utilized again which has been seen to introduce errors. The instantaneous mass flow rate has been determined using a form of normalized momentum flux measurement and the total mass injected. Any change in the cross sectional area of the fluid flow

through the nozzle away from A_{geo} has been accounted for in this measurement. It would seem suitable then to use the calculated mass flow rate with

$$\dot{M} = \dot{m} v_B \tag{4.10}$$

where v_B is a theoretical velocity from Bernoulli's equation in the form

$$\eta_m = \frac{\dot{M}}{\dot{m}.\sqrt{\frac{2\Delta P}{\rho_f}}} \tag{4.11}$$

to give the momentum efficiency.

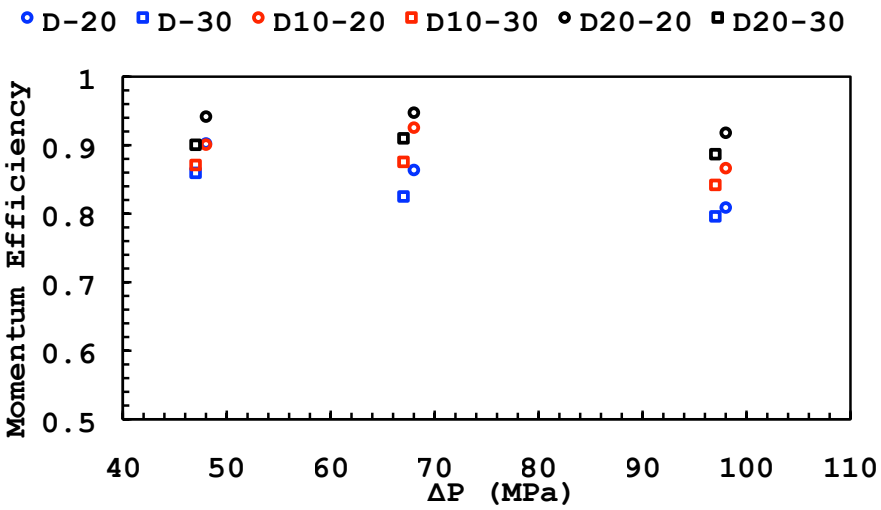

Figure 4.70: Momentum efficiency (Eqn.4.11 of sprays for Diesel due (blue), D10 (red) and D20 (black) with the pressure drop across the injector nozzle ($\sqrt{\Delta P}$). ρ_a = 22.6 kg/m^3 (P_{amb}= 20bar) shown with empty circles. ρ_a=34.5 kg/m^3 (P_{amb}= 30bar) shown with empty squares.

The momentum efficiency for the nozzle for each fuel is shown in Fig.4.70. The neat Diesel fuel sprays show a near linear decrease of the momentum efficiency with increasing injection pressure which is greater than the decrease for emulsified fuels. For each fuel at each injection pressure the higher chamber density leads to a reduction in the momentum efficiency. The D20 fuel spray have the highest momentum efficiency at each condition, followed by the D10 with the Diesel fuel exhibiting a lower efficiency at each condition. The emulsification process has been shown to lead to an increase in the injection velocity compared with an equivalent Diesel fuel spray. This is counter the increase in viscosity that arises due to the emulsification process, which may have been expected to reduce flow velocity.

The complex nature of the multi-component flow is not readily explained with the measurements here. It is apparent that the high viscosity, which would be expected to reduce flow velocity is not the only mechanism working on the emulsified fluid as it is injected. It is unclear what happens to the emulsion's density and viscosity as it is subjected to the high pressures of injection. The large pressure drop, coupled with the drastic variation in flow direction as the fuel flows through the injector may result in a "splitting" of the emulsion or the formation of a lower viscosity region in the nozzle through which the fuel may flow with a higher velocity.

4.2.7 Momentum Flux and Spray Cone Angle

The momentum flux and spray cone angle determined using the backlit system have been combined together for Diesel fuel sprays, P_{inj}= 500 in Fig.4.71. Trend lines have been fitted to the momentum flux data (solid blue lines). They show a period of rapid increase in the momentum flux up to around 150μs after SOI, after which the gradient of the line reduces with the increase in momentum flux more gradual with time. This period appears to be linear. Due to the noise in data around this transitional period it is difficult to say with a high degree of accuracy when this transition occurs. It could be that this second, more gradual linear period commences at or around the time that the transition, as highlighted by the red broken line, in spray cone angle was observed. During this transition, the spray cone angle starts to decrease in value. Due to the different durations of injections used for the momentum flux and the spray angle measurements, it is not possible to correlate the peak momentum flux and spray angle value at that time.

4.2.8 Summary and Conclusion

The momentum flux of Diesel fuel sprays; Diesel and 10%water emulsion and Diesel and 20% water have been measured using a force transducer placed at a very close distance (0.5mm) from the nozzle orifice exit. The sprays were carried out with injection pressures 500, 700 and 1000 bar. The sprays were carried out in a higher pressure chamber filled with nitrogen with two back pressure 20 and 30 bar, resulting in ambient densities of 22.6 kg/m^3 and 34.5 kg/m^3. Spray duration was short at 500μs but it has been demonstrated that in this time the spray reached a reasonable representative momentum flux value for each condition and it may be assumed that the effects of needle opening and closure are not an influence during the period where the mean peak value occurred. The 10 largest readings have been used to

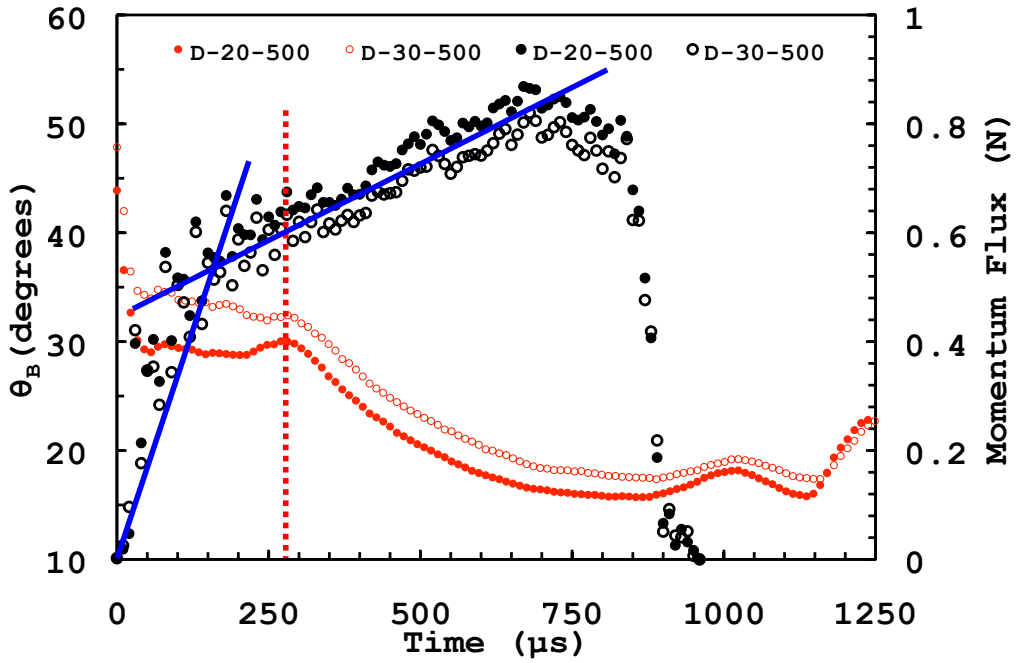

Figure 4.71: Fuel injection spray angle variation with time for Diesel fuel (red circles) (determined using backlit image sequence) with fuel spray momentum flux variation with time for Diesel fuel (black circles). P_{inj}= 500. ρ_a=22.6 kg/m^3 (P_{amb}= 20bar) Blue solid trend lines fitted to the momentum flux data, red broken line shows a time when the spray angle appears to change to a period of gradual decreasing value.

produce a mean peak value that is a single value from the transient region which is representative of the momentum flux for each condition.

- Increasing the injection pressure resulted in an extended hydraulic delay and an earlier injector closing time.
- An increase in the measured momentum flux was observed with increasing ΔP in a linear form.
- Increasing the ambient density in the chamber resulted in a decrease in the measured momentum flux, greater than would be expected due to the back pressure change that accompanied the ambient density change. The spray had not emerged very far into the chamber (0.5 mm) before the ambient density influenced the spray.
- The emulsified fuels had a very similar, almost identical momentum flux to the the neat Diesel fuel. The emulsification did not have any effect on the injection delay period or the injection closing time.
- Fuel density and viscosity were measured. The emulsions had a larger density than the neat Diesel fuel and a higher viscosity.

- The total mass of fuel injected during an injection event for each fuel at the three injection pressures considered was measured. The larger density of the emulsions was reflected in the total mass injected, with the total mass of fuel injected for the emulsified fuels less than for neat Diesel fuel at each injection pressure.

- Instantaneous mass flow rate was determined using a normalized form of the momentum flux measurement and the independently measured total mass injected during the entire injection event. Instantaneous mass flow shown a linear increase with $\sqrt{\Delta P}$.

- The nozzle discharge coefficient was determined and examined along with the cavitation number. The emulsions tended to have a lower discharge coefficient. There was no evidence that the nozzle was geometrically cavitating for any of the fuels at the conditions tested. It is believed the nozzle design effectively suppressed geometric cavitation.

- Injection velocity was calculated using the mean peak momentum values and the mean peak mass flow values. The emulsified fuels tended to have a high injection velocity than the neat Diesel fuel sprays. The velocity, along with density and viscosity was used to determine the Reynolds number for each case. The Reynolds number has shown little variation between the fuels at each condition. It is concluded that there is another mechanism resulting in the lower discharge coefficient and high injection velocities observed with the emulsified fuels.

- The momentum coefficient was determined for the sprays and is analogous to the discharge coefficient. The emulsification had little to no effect on the momentum coefficient. It is evident that the increase in the ambient density reduced the momentum coefficient for each case.

- The momentum efficiency was introduced, which used the instantaneous mass measurement and the theoretical velocity of the spray. The emulsified fuels had a larger momentum efficiency, a result of their high injection velocity compared with the neat Diesel fuel.

4.3 Combustion Results

In the following section, the results from the optically accessible combustion chamber are presented. The results show the combustion pressures, an example set of natural luminosity (NL) images and the spatially integrated natural luminosity (SINL) for Diesel fuel and D10 fuel only. The mass of fuel injected was kept the same for each fuel, resulting in a small reduction in the energy content injected for the D10 compared with the neat Diesel. The ignition delay, determined from the pressure differential and the luminosity images is presented and discussed. The implications of the NL and SINL in terms of sooting nature of the fuels is discussed.

4.3.1 Pressure

Fig.4.72 shows the arithmetic mean pressure history for the two fuels determined by taking the average of the 40 combustion events. Due to the nature of the external

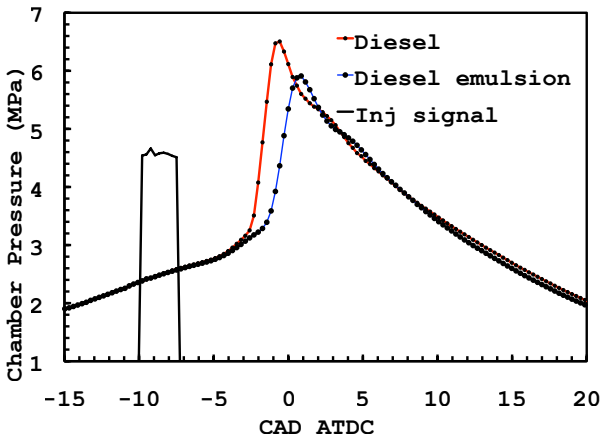

Figure 4.72: Combustion pressures for Diesel fuel (red) and D10 (blue) obtained in the optical side chamber, SOI is −10 ATDC

combustion chamber, analysis using the heat release rate, as would most usually be applied is unsuitable [182]. This is mainly due to the long connecting passage joining the two separate variable volumes, similar to an IDI system. This leads to difficulty in modeling the gas flow and the gas composition during combustion (heat release) and it is believed that some flame quenching may be taking place. The ignition delay (ID) is therefore determined using the 1st combustion pressure derivative with respect to crank angle($\mathrm{d}P/\mathrm{d}\theta$). In the following section, the θ (in CAD ATDC) at which combustion starts is stated, from which the ID in ms and CAD is given taking into account the 300μs (1.8CAD) injection delay.

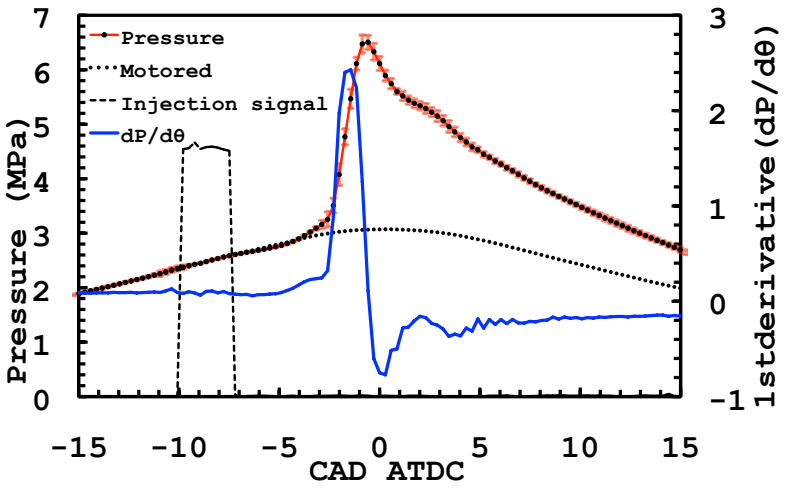

Figure 4.73: Chamber pressure with error bars (red) one standard deviation, motored pressure (broken black line), $dP/d\theta$ (blue line) and injection signal for Diesel fuel combustion in the OACC.

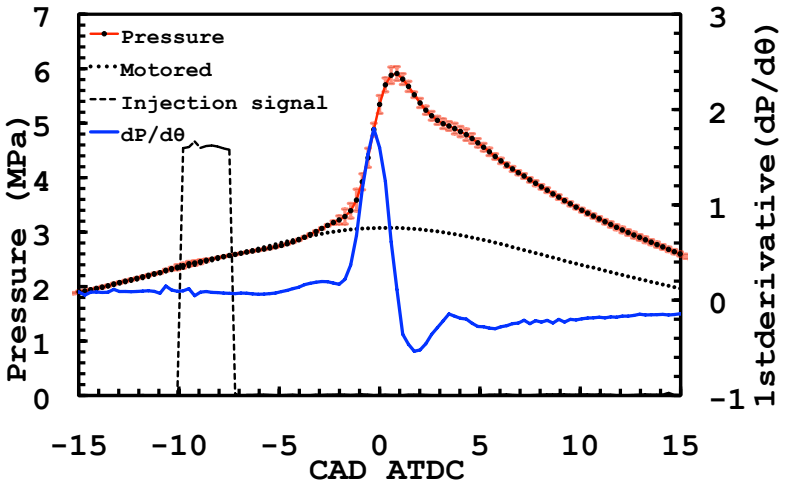

Figure 4.74: Chamber pressure with error bars (red) one standard deviation, motored pressure (broken black line), $dP/d\theta$ (blue line) and injection signal for D10 combustion in the OACC.

Fig.4.73 shows the: 1st pressure differential, $\mathrm{d}P/\mathrm{d}\theta$; the combustion and motored pressures and; the injection signal for Diesel fuel whilst Fig.4.74 shows the same for the D10 fuel. The initial depression in the combustion pressure curve away from motored pressure curve arises due to the evaporation of the injected fuel. This corresponds with a reduction in $\mathrm{d}P/\mathrm{d}\theta$. This is followed by an increase in $\mathrm{d}P/\mathrm{d}\theta$ as ignition has occurred and combustion pressure crosses the motored pressure curve. This is followed shortly lately by a much steeper change in pressure, a large positive

change $\mathrm{d}P/\mathrm{d}\theta$ as the main pre-mixed combustion event progressed..

For Diesel fuel the initial increase in $\mathrm{d}P/\mathrm{d}\theta$ occurs at -5.2CAD ATDC (0.5ms or 3.0CAD after SOI). The steep rise occurs at -2.9CAD ATDC (0.89ms or 5.3 CAD after SOI).

The emulsion shows a similar trend to the neat fuels with an rise in $\mathrm{d}P/\mathrm{d}\theta$ at -5.5CAD ATDC (0.45ms 2.7 CAD after SOI) The initial increase for the emulsion is slightly advanced when compared with its neat counterpart. This maybe a microexplosion effect, with a small proportion of the injected fuel reaching an ignitable mixture slightly earlier. It is unclear that the microexplosion phenomenon could occur so early in the cycle.

Other factors such as the increased viscosity, surface tension and thermal conductivity effects may effect the phenomenon at this point. With the emulsion fuel there is a clear reduction in $\mathrm{d}P/\mathrm{d}\theta$ just before the second steeper increase. This occurs at -2.3 CAD ATDC (1.0ms or 5.9 CAD after SOI) for the D10 fuel.This small reduction in the $\mathrm{d}P/\mathrm{d}\theta$ must be a consequence of the water content of the fuel. At the temperatures and pressures that are present at this early stage of the combustion process this is most likely due to the final evaporative effect of the water. Ignition delays are presented in graphical form in Fig.4.78.

The emulsion has shown an extended secondary ID and in reference to Fig.4.72 with both pressures shown together as well as the $\mathrm{d}P/\mathrm{d}\theta$ values in Fig.4.74 it is clear that the emulsion has lead to a reduction in the rate of pressure rise and a reduction in the peak pressure achieved when compared with it's neat fuel parent. When comparing the emulsion with the neat fuel; ID is longer; peak pressure (θ of peak) and peak $\mathrm{d}P/\mathrm{d}\theta$ is retarded (occurs at a later CAD after SOI).

Variability between the individual cycles has been considered. The error bars attached to each combustion pressure of Figs.4.73 and 4.74 are the size of one standard deviation at each sample point. The small size of the error bars suggests the variability of the combustion pressure between each cycle is low.

During all conditions tested with the external chamber there was no detectable flame-spray overlap nor was flame observed connected to the fuel spray (no FLoL) or before the injection indicating LED had gone out. This is most likely a result of the short injection period for each fuel coupled with the ambient temperature and pressure in the chamber at the time of injection. A portion of the fuel injected into the chamber is well mixed with the swirling air in the chamber before combustion starts. The mixture may not be considered to be homogenous as there will be regions of varying equivalence ratio. Examination of the combustion pressures shows the

combustion starts off pre-mixed in nature followed by an extended period which is not pre-mixed as the remaining portion of the injected fuel burns under mixing controlled limits. The varying equivalence ratio in the chamber leads to a diffusion combustion controlled by the availability of oxygen to the fuel [18].

Though the emulsion has shown an increase in the ID, the additional time to pre-mix has not lead to an increase in peak pressures or peak $\mathrm{d}P/\mathrm{d}\theta$, this is due to the energy absorbed by the dispersed water to increase its temperature. The existence of the microexplosion phenomenon may be leading to a slight reduction in the initial ID for the diesel fuel/water emulsion. It would be expected that the microexplosion would lead to an increased pressure rise rate due to the high rate of fuel air mixing. The often recorded result of an increase in pre-mixed combustion due to increased mixing rates and increased ID with emulsions leading to increased peak pressures earlier in the cycle may not be true when dealing with the combustion type in this chamber.

4.3.2 NL images

Fig.4.75 is a set of combustion images for Diesel fuel, SOI−10 ATDC. The images are taken from a representative set of images with the SINL lying very close to the average for this test case. The images show the first frame that NL was visible in, the first image in the sequence of Fig.4.75, the frame with peak NL (Fig.4.75(A)), Fig.4.75(B) shows the NL image from 10 CAD ATDC while Fig.4.75(C) is at 15 CAD ATDC. The schematic in the lower right corner includes an image scale and an example with the central axis of the sprays (green lines), the injector nozzle (light green circle) and the direction of swirl (red arrow) imposed upon it. The swirl number was estimated to be in the region of 1.45 (see Section.3.6.1).

For Diesel fuel the first NL image frame occurred at -1.16 CAD ATDC. It shows a larger region of high intensity sooting flame with fringes of this region of less intense luminosity. The first NL frame for Diesel fuel is within the period in which the peak $\mathrm{d}P/\mathrm{d}\theta$ occurred. As much of the initial combustion that occurred is not visible in the NL range, the high temperature, low sooting nature of this pre-mixed period is not detected by the camera. The Diesel fuel peak frame (Fig.4.75(A)), captured at 1.04 CAD ATDC, is 100% high intensity in the optical area. Both Fig.4.75(B and C) show a region of high intensity luminosity fringed with an area of lower intensity that fills the remanding space.

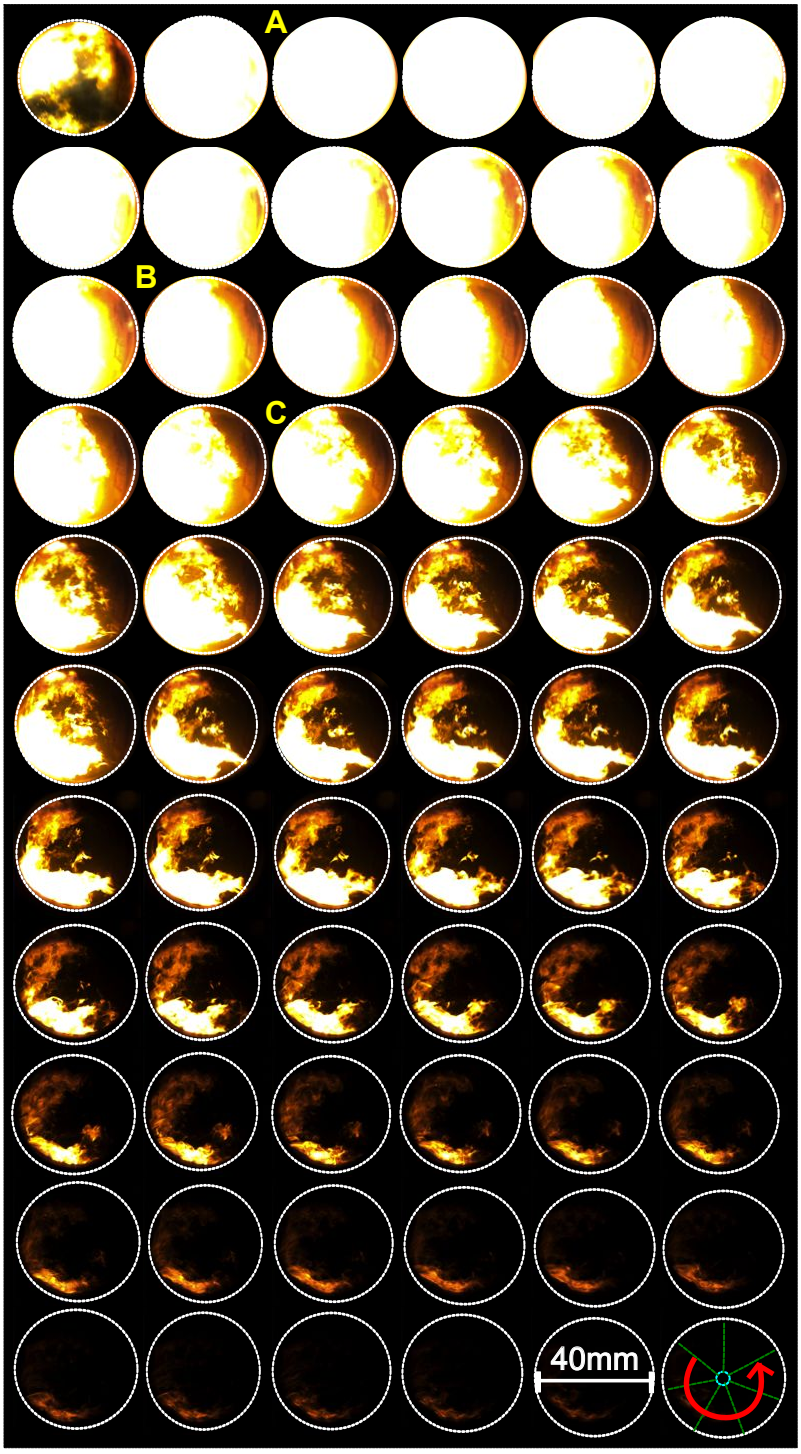

Figure 4.75: Typical combustion image sequence from natural flame emission/luminosity during Diesel fuel combustion. Used to determine the SINL.

The NL images here help highlight the understanding of the diffusion period of combustion in the chamber. Although there is no flame-spray overlap, the flame is not observed to propagate through the mixture as would be expected with a highly pre-mixed near homogeneous mixture. In the frames collected at 15 CAD ATDC it is clear that the NL combustion is occurring around the periphery of the chamber, where the air has a high degree of swirl due to the swirl ring. Fuel air mixing rates are higher, more air is available to the fuel, increasing the diffusion combustion rate when compared with the central region of the combustion volume.

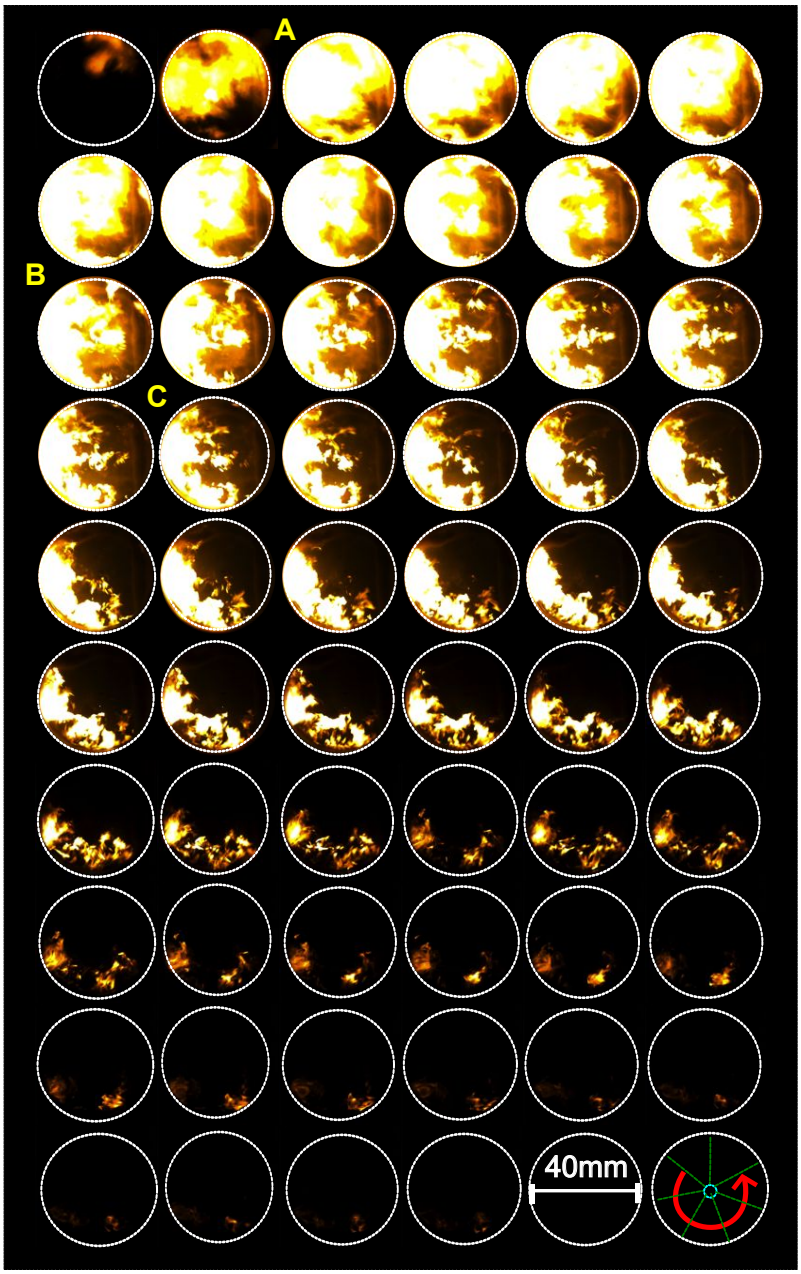

Figure 4.76: Typical combustion image sequence from natural flame emission/luminosity during D10 combustion. Used to determine the SINL.

The same set of images for the emulsified fuel are shown in Fig.4.76.

The first NL frame for the emulsion, has no areas of high intensity NL present and small portion of the optical area with low intensity luminosity. As with the neat Diesel fuel, the first NL frame coincides with the peak $\mathrm{d}P/\mathrm{d}\theta$. The emulsion peak frame (Fig.4.76(A)) exhibits a high intensity region approximately 60% of the optical area fringed by a region of lower intensity that makes up the remainder of the optical region. The entire optical area contains some luminosity with a small area of quite low luminosity observable in the lower right region of the optical area.

When comparing the emulsified fuel with the neat Diesel fuel there is a clear reduction in luminosity. The first frame showing luminosity for the emulsified fuel shows a great reduction in both the intensity of luminosity and the size of the region which contains any luminosity. This is indicative of the reduction in the rate of luminosity increase. The emulsion has decreased the initial increase in luminosity by a great amount. Continuing this relationship it is clear that the emulsification of the fuel has had a great effect on reducing the NL in the peak and 15 CAD ATDC frames.

4.3.3 SINL

Studying natural luminosity images can lead to an insight into combustion type and features. It has been particularly useful in helping to understand the pre-mixed to diffusion nature of the combustion with no flame-spray over-lap visible but an extended combustion period occurring at the periphery of the combustion chamber. They also suggest no evidence of the microexplosion phenomenon or suggest that the phenomenon may only exist in a stabilized spray lifted flame scenario (not visible here). Images such as this are highly qualitative in nature. The summing of the pixel values over an entire image provides a value for the SINL which then allows an averaging over a number of combustion events to be carried out, allowing general trends in the data to be identified that may otherwise be lost in simple image analysis. As previously stated, the SINL is still qualitative in nature but may be thought of as a quantitative comparison tool which is a function of temperature and soot concentrations. This metric, the SINL is presented for both fuels tested in Fig.4.77.

Here the SINL is compiled in the same manner as the combustion pressures using the average of 40 cycles. During experimentation it was found that the SINL repeatability was highly susceptible to changes in operating conditions such as air

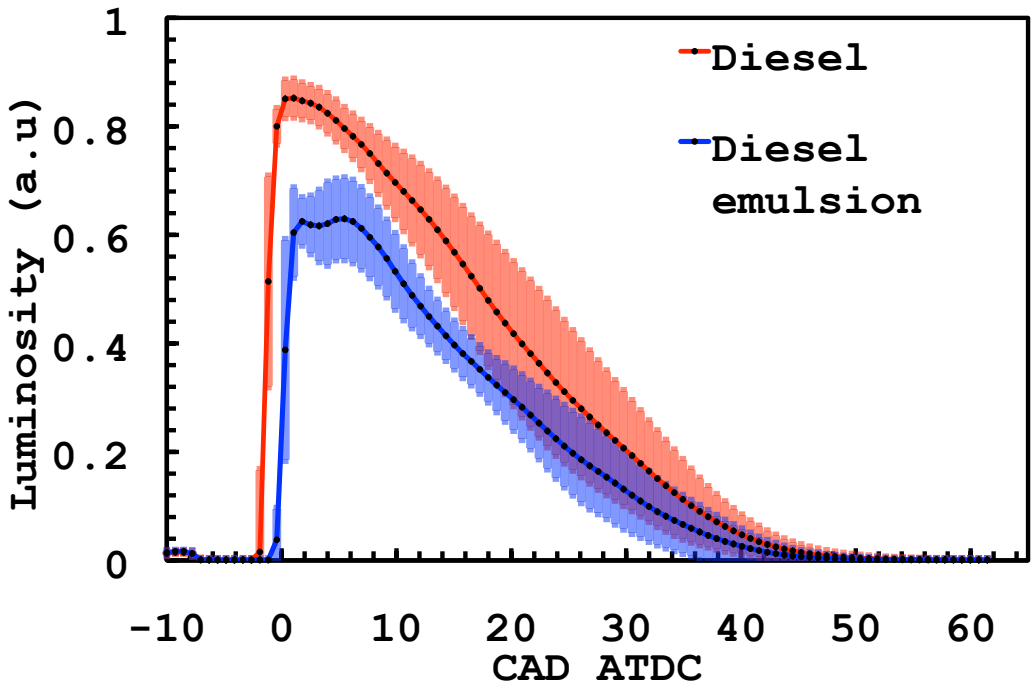

Figure 4.77: SINL for Diesel fuel (red) and D10 (blue) with error bars the size of one standard deviation for the 40 combustion cycles.

intake temperature, chamber temperature (hence the thermocouple used to ensure chamber had reached 200°C) and any adjustments to the optical set-up. The degree of repeatability is evidenced in Fig.4.77 by the error bars which are the height of one standard deviation.

The temperature of the radiating soot is paramount importance to any analysis of the NL and SINL since it will heavily impact the luminosity. The spectral emittance of soot is governed by its temperature distribution and may be approximated using the Stefan Boltzmann law to NL $\propto T^4$. Incandescent soot temperature may be approximated to the overall in-cylinder combustion temperature [212]. During data collection, air mass flow rate to the chamber was measured using an orifice plate fitted to a large settling chamber, hence the over-all equivalence ratio could be deduced (0.24 for Diesel and 0.21 for D10). With Diesel fuel modeled as $C_{10}H_{22}$, the flame temperature for both fuels was evaluated using the freely propagating flame module of LOGEsoft software [213]. The flame temperature for Diesel fuel was calculated to be 943 K whilst the D10 was 876 K. Alternatively, the mean combustion temperature achieved during combustion may be assumed to be the local stoichiometric adiabatic flame temperature for the relevant fuel-air mixtures producing H_2O and CO (CO to CO_2 oxidation was considered too slow during this combustion). This was assessed using a basic first law calculation and the enthalpy of formation of the reactants and products. The calculation yielded a

flame temperature of 1621 K for the Diesel fuel and 1548 K for the D10. Whilst the values differ depending on the technique applied, the difference between the two fuels is around 70K for both cases.

For the purpose of the analysis both sets of flame temperatures were considered to elucidate the influence on the analysis the flame temperature calculation may have had. The emission ratio was obtained using

$$Emissions\ Ratio = \frac{T_D^4}{T_{D10}^4} \tag{4.12}$$

Using the LOGEsoft flame temperatures, the ratio is 1.34, suggesting there would be a 34% increase in SINL from the D10 to the Diesel fuel (due to the increase in flame temperature). Using the first law calculation, the ratio is 1.20, suggesting a 20% increase in SINL.

Peak measured SINL for the D10 was approximately 0.6 a.u whilst for the Diesel fuel it was approximately 0.9, an increase of 50%. A 34% increase would give 0.8 a.u for the Diesel fuel, a 20% increase would give 0.72 a.u for the Diesel fuel. It may be assumed that the remainder of the increase in measured SINL is due to an increase in soot volume fraction for the Diesel fuel combustion. Based on the results and the calculations here, the increase in SINL due to soot volume fraction accounted for either 16% (LOGEsoft estimation) or 30% (first law estimation) of the increase in SINL observed.

For both fuels the ignition point as measured from the increase in the SINL appears after the ignition point as defined by the pressure data. Fig.4.78 shows the trend in ID observed in the external chamber. There is a small increase between the ID from the 2nd increase in $\mathrm{d}P/\mathrm{d}\theta$ with the emulsified fuel. The first NL emission occurs later with the emulsified fuel and is identified in Fig.4.78 as the luminosity delay.

Here the SINL metric is being used as an indexing methodology to assess total incandescent soot concentration during the combustion process. Therefore the peak value of the SINL achieved during combustion is of interest. Also to be examined are any shape features in the SINL lines. The SINL is shown in arbitrary units (a.u) which are a function of the optical set-up used, though indexing of trends may be compared, direct comparison to values of SINL from other researchers may not made.

The initial "bump" that is evident in the SINL curve for both fuels is the camera response to the illumination of the injection indicating LED which is in the corner of

the frame during recording. This universal point in all recorded video files allowed accurate alignment of the SINL as a TDC signal does with pressure data.

Peak SINL is observed during Diesel fueling with a steep increase commencing at −1.6CAD ATDC (6.6CAD or 1.1ms after SOI) to a defined peak value of approximately 0.9 a.u. The emulsified fuel shows a reduction in observed peak SINL compared with the neat Diesel fuel. The observed SINL during D10 fueling (Fig.4.77) increases from −0.4 CAD ATDC (7.8 CAD or 1.3ms after SOI) and increases with a slightly reduced rate compared the neat Diesel fuel. An initial peak is reached followed by a slight reduction with another small increase following, giving the SINL a small depression around the peak value of 0.6 a.u, a 26% decrease compared with neat diesel. The reduced peak SINL is a function of reduced temperature or reduced soot concentration. Temperature reduction which results from the evaporative effect of water content and displacement of energy content due to water addition. The influence of spray dynamics (associated with emulsion injection) on the diffusion period of combustion have been suppressed. Soot concentration reduction may result from chemical implications of the addition of water leading to the dissociation of water into OH. The oxidation of any soot produced to CO by the OH may explain the extended period of SINL around the peak and the slight depression around the peak.

Table 4.5: Peak pressure and peak SINL values and timings

Fuel	Peak pressure (MPa)	Peak pressure time (θCAD ATDC)	Peak SINL (a.u)	Pesk SINL time (θCAD ATDC)
Diesel	6.5	−0.5	0.85	0.3
Emulsion	5.9	0.8	0.6	1.8

Fig.4.78 allows a convenient reference to elucidate IDs for the both fuels. Table. 4.5 highlights the variation between the position of peak combustion pressure and peak SINL (θ CAD). It is evident that the peak pressure is always in advanced of the peak SINL. This highlights the fact that during the pre-mixed combustion period when peak pressure will occur, incandescent soot is not produced, it is a feature of the diffusion flame period, whether the flame is a stabilized spray lifted (FLoL) or as in the case here, mixing rate limited none-spray lifted flame.

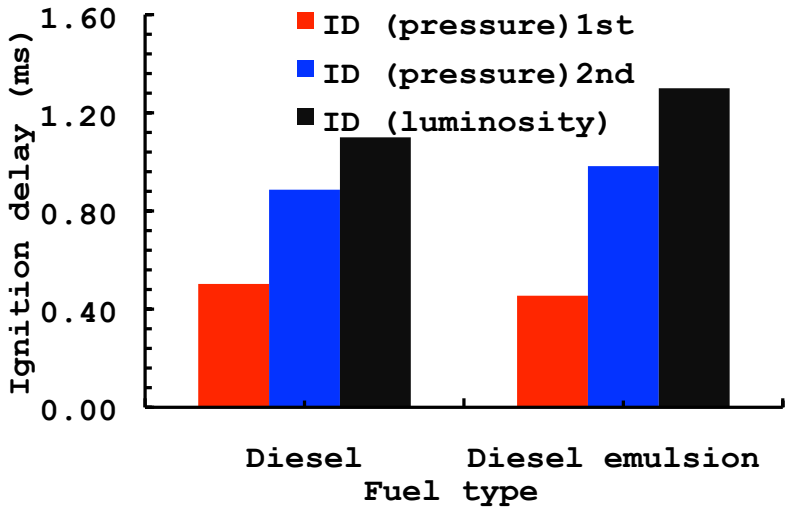

Figure 4.78: Chart showing the variation in ID (ms) for the four fuels investigated. The pressure 1st is the delay from the SOI until the first increase in $\mathrm{d}P/\mathrm{d}\theta$, pressure 2nd is the delay from the SOI until the much larger second increase in $\mathrm{d}P/\mathrm{d}\theta$, luminosity is the delay from the SOI until the first increase in NL is observed.

4.4 Summary and Conclusions

The combustion of Diesel fuel and Diesel and water emulsion containing 10% water by mass was examined in a compression ignition environment in a novel optically accessible combustion chamber. Combustion pressures were recorded in the chamber and used to determine ignition delays and to compare combustion characteristics between the fuels. High speed photography was used to collect combustion images of the natural luminosity (NL) which was then used to determine ignition delay and the qualitative indexing metric, the spatially integrated natural luminosity (SINL). The SINL was used an indicator of soot concentrations during combustion in the chamber. The following are primary observations in the study:

- Pressure ID appeared in two stages, with a primary ignition followed by a secondary ignition when the main pre-mixed combustion period started.
- The external combustion chamber was operated with no spray/flame overlap, the diffusion combustion period was not attached to spray (lifted flame), the mixing was controlled by air motion in the chamber (swirl ring). The first NL images for Diesel fuel coincided with the peak of the first pressure derivative ($\mathrm{dP}/\mathrm{d}\theta$). ID from the SINL is extended as during initial ignition and combustion starting, no incandescent soot is produced.
- The emulsion shown a slight reduction in the initial ignition delay when compared with neat diesel fuel. Emulsification of Diesel fuel extended the sec-

ondary (larger increase in $dP/d\theta$) ignition delay. There was a small reduction in the first pressure derivative prior to the secondary ignition, a result of the evaporation enthalpy of the water as it evaporated, reducing the bulk gas temperature. Water content reduced and retarded the peak pressures achieved with the emulsified fuel, again due to the water absorbing energy through a heat transfer effect and being used to raise its temperature.

- NL images and the SINL for the emulsified fuel show a large decrease when compared with the neat Diesel fuel.
- The peak SINL occurred during the diffusion flame period.

From the results, the following conclusions were reached:

- The peak pressure occurred during pre-mixed period, peak SINL followed as the diffusion period commences.
- Evidence from the pressure histories to suggest the microexplosion phenomenon occurred in the chamber is not strong.
- Due to physical mixing factors associated with spray mixing and stabilized lifted flames (FLoL) during the diffusion period being suppressed, it is concluded that the observed reduction in the SINL, which may indicate reduced incandescent soot concentration was largely due to a combination of the chemical effect of dissociation of the water and the reduction in the bulk temperature in the chamber. Influence of fuel properties on the spray and hence FLoL may not play a major role in the incandescent soot concentration when compared with these effects.
- There was no optical evidence of the microexplosion phenomenon.
- The described chamber provided a cheap, simple to operate and effective CI environment to conduct optical combustion experiments.

5. Overview, Conclusions and Future Work

5.1 Overview

This work details an experimental campaign to characterize non-vaporizing sprays of Diesel fuel and Diesel emulsions. Characterization of the fuel sprays was done:

- Optically using high speed photography.
- Hydraulically using a force transducer placed in the path of the emerging spray.

Preliminary testing was also conducted in an optically accessible combustion chamber.

All spray measurements were made in an in-house designed and constructed optically accessible high pressure chamber filled with nitrogen. Measurements were conducted at two ambient gas densities of 22.6 kg/m^3 and 34.5 kg/m^3 at 20°C which was achieved by maintaining a pressure of 20 bar and 30 bar (respectively) in the chamber. Fuel injection was achieved using a piezo type injector, coupled to a common rail injection system controlled by a LabView DAQ PC based system and a separate injector driver. The fuel injector was adapted so spray emerged from only one of it's seven holes.

Emulsions were produced with 10% water and 20% water added by mass. The emulsions were mixed using an ultrasonic mixing probe and stabilized with a mixture of two surfactants, SPAN 80 and TWEEN 80, with a HLB of 6.4. The emulsion were very stable over a two week period.

High speed images were collected using a focused shadowgraphy system utilizing a double pass, single parabolic mirror system. The point light source was provided by a novel LED system using a high power LED with an in-house made drive circuit.

Large over currents of short duration were utilized resulting in high intensity flashes. A high speed camera was used with frames rates of 30,075 fps with an effective exposure time of 3μs. Images were also collected using a diffuse backlit system. The same LED was used in a different configuration with a frame rate of 88,888 fps and an effective exposure time of 2μs. From the image sequences collected, spray cone angle, spray tip penetration and spray tip velocity was measured using Matlab.

Momentum flux of the fuel sprays was measured using a force transducer mounted in front of the injector nozzle. The transducer was fitted with a target whose face was orthogonal to the spray central axis at a distance of 0.5mm from the nozzle exit. The measurements were made in the high pressure chamber with the same conditions as the optical tests. To complete the hydraulic characterization, the total mass of fuel injected per injection, the fuel viscosity and the fuel density were measured. The momentum flux and mass measurement were used to construct an instantaneous mass rate profile, determine the nozzle discharge coefficient, the momentum coefficient, the momentum efficiency and the injection velocity.

Combustion testing of one emulsion containing 10% water was conducted. High speed imaging at 8146 fps was used to collect natural luminosity of the flame. The natural luminosity was used to calculate the spatially integrated luminosity. Combustion chamber pressure was also collected.

5.2 Conclusions

- The injection pressure was shown to have no discernible influence on the spray cone angle of the Diesel fuel sprays, in accordance with previous findings.
- The injection pressure did have an influence on the D10 and D20 spray cone angles. At an injection pressure of 500 bar, the two emulsions had a considerably smaller spray angle than the Diesel spray angle at 500 bar and for the other emulsion injections at 700 and 1000 bar.
- Increasing the ambient density was shown to result in an increase of the spray cone angle for the Diesel fuel sprays, in accordance with findings in previous works. This was also observed with the emulsion fuels with the injection pressure of 500 bar. As the injection pressure was increased to 700 and 1000 bar, the increase in the ambient density did not result in the spray angle increasing. The emulsification process appeared to suppress the effect of increasing ambient density for the injection pressures of 700 and 1000bar.

- All spray angles determined using the backlit system were smaller than the corresponding angles determined using the shadowgraphy system. The angles measured using the backlit system were more transient than the shadowgraph derived angles with a period of rapid decrease at the start and then a period of more gradual decrease approximately 250μs after SOI.

- There was no discernible difference between the Diesel fuel, D10 and D20 fuel spray tip penetration for corresponding conditions, determined using the shadowgraph image sequences. This suggests the emulsification process had no effect on the spray tip evolution. The linear dependence of the tip penetration during the early period, S$\propto t$ with a transition to a period of S$\propto t^{0.5}$ is supported.

- Backlit image sequences were used to determine the spray tip velocity for Diesel and D10 sprays. The linear dependence of the tip penetration during the early period, S$\propto t$, is not supported when a higher temporal resolution is applied. The tip accelerated from the nozzle and reached a peak velocity shortly after the SOI. The time when this peak occurred seemed to be independent of the injection pressure and ambient density for the Diesel fuel sprays but not for the D10 where an increase in the injection pressure resulted in a reduction in the time after the SOI when the peak velocity occurred.

- The momentum flux for all fuels was almost the same at corresponding conditions.

- Increasing the ambient gas density resulted in a decrease in the spray momentum flux.

- A larger mass of Diesel fuel was injected during each injection compared with the emulsions. The emulsions had a larger density and a higher viscosity than the Diesel fuel. The increase in viscosity must have reduced the mass flow rate, countering the increase in fuel density.

- Instantaneous mass flow rate profiles, suitable as input for modeling purposes were produced.

- The nozzle discharge coefficient was lower for the emulsions compared with Diesel fuel. For all conditions the nozzle was non-cavitating (geometric).

- The injection velocity of the emulsions was higher than that of the Diesel fuel for corresponding conditions.

- The injection velocity and the spray tip velocity were very different variables that should not be confused, they represent different aspects of the spray character and their peak values should not be used interchangeably.
- The momentum efficiency was introduced and used to characterize the sprays. The emulsions had a larger momentum efficiency than the Diesel fuel.
- There may be a relationship between the transitional times observed with the backlit derived spray angles and the changes in the momentum flux.

5.3 Future Work

During experimentation in the high pressure chamber, the windows were prone to considerable fouling from injected fuel deposition. With the high sensitivity of the shadowgraph system this effectively reduced the number of injections that could be sensibly done for each condition. It should be possible to adapt the chamber with extensions fitted into the window saddles so the windows would sit at a much greater distance from the injector. This may help reduce the fuel droplets depositing themselves on the windows. The number of repetitions for each condition could then be increased with the shadowgraph system.

The density ratio range over which the experimentation has been conducted is rather limited. The original design of the chamber allowed for a maximum pressure of 40bar. The chamber stress analysis could be conducted to examine the implications of increasing the pressure up to 50 bar and conducting the experiment with pressures in the chamber at 20, 30 40 and 50 bar (gas density of 22.6, 34.5, 46.0 and 57.4 kg/m^3). The injection system is capable of delivering pressures of 250 bar up to 2000 bar. The experimental conditions could be extended to include examination of the spray cone angle of the emulsions with injection pressures of 300, 400, 500 and 600 bar. It is at the lower injection pressures that the emulsification seemed to have had the greatest effect on cone angle.

The error in injection timing induced by the connection of the camera in the DAQ system should be investigated and rectified. The full spray cone development period and momentum flux could then be examined together. Some examples of high speed image collection of the spray striking the surface of the force transducer's target during momentum flux data collection, to confirm the interaction between the two, would be ideal.

During experimentation it had been intend to include a study of biodiesel (RME)

sprays and bio-diesel emulsions sprays. During development of the test, a large range of RME emulsions were examined, using different surfactants and different mixing strategies. No successful, stable RME emulsion was ever produced, with either very unstable emulsions or the emulsion thickening over a short period. Bio-diesel emulsions may be an important method for reducing the so called NO_x penalty that has been observed with bio-diesel usage. There are very few studies examining bio-diesel emulsions, particularly their stability, their spray character and optical combustion studies. Further investigation with the focus on producing a successful emulsion of RME would be advantageous.

Validation of the instantaneous mass flow rate profiles using the same conditions and injector with a Bosch rate tube or a Zuech chamber would help assess the viability of future use of the method as an alternative technique.

The LED illumination system proved to be a reliable, cheap, effective alternative to a HID lamp or a laser. Further investigation with an alternative power supply, a dedicated signal generator and a new driver circuit produced on printed circuit board with wide tracks would help improve the system. The system should be capable of even higher intensities. There is currently no data for the output intensity of this system, therefore testing with a photodiode arrangement to measure output would further improve the design and operation. The system could be extended with the addition of fibre optics and lenses for Mie scattering.

The OACC suffered from a number of design defects which made operation extremely cumbersome. It was very difficult to operate the chamber at repeatable conditions and conduct experiments with an adequate number of combustion cycles that were repeatable. A redesign of the basic concept is underway. The new design will use an externalized combustion chamber fitted to a motored single cinder engine. This system will make use of a cylinder head with the chamber built into it rather than attached to it. Diagnostics will be made at much high frame rates with filtering and intensification applied. It is hoped that the engine could operate over a considerable period of time at each condition collecting a large number of combustion cycle image sequences. The operation of the new chamber will also allow for increased injection durations so spray and flame overlap is observed.

Appendices

A. High Pressure Chamber Drawings

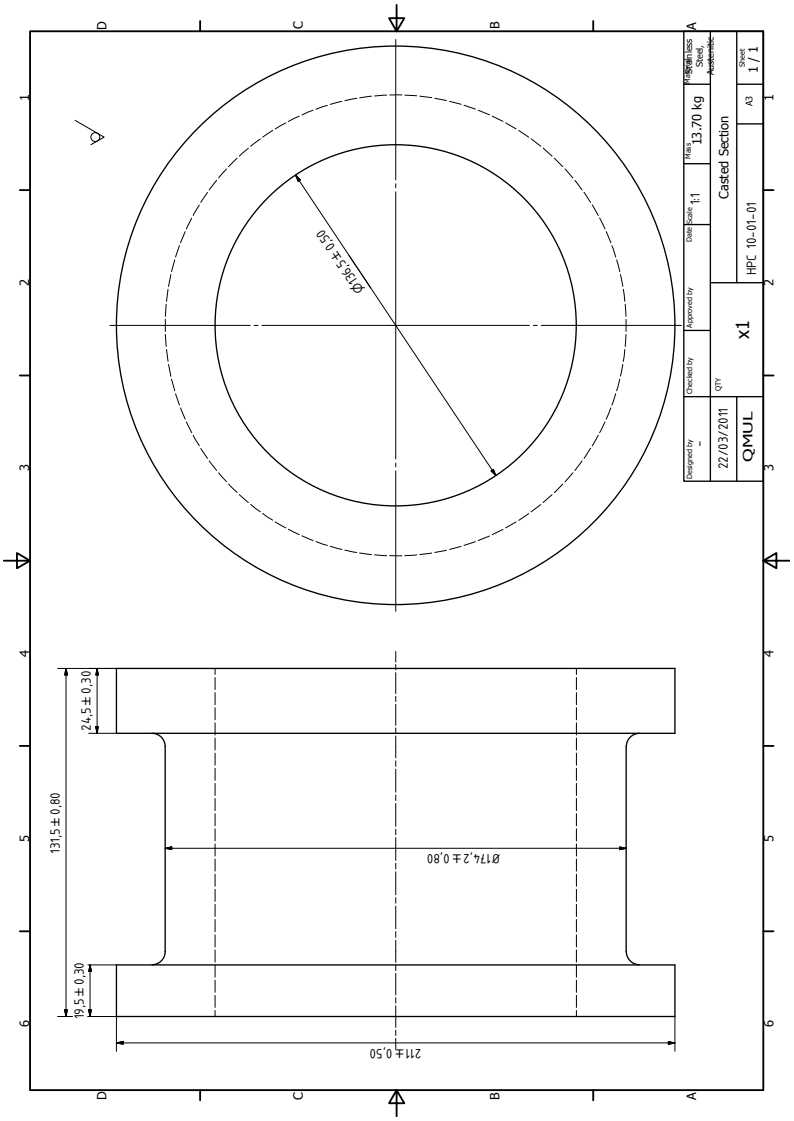

Figure A.1: High pressure chamber cast section.

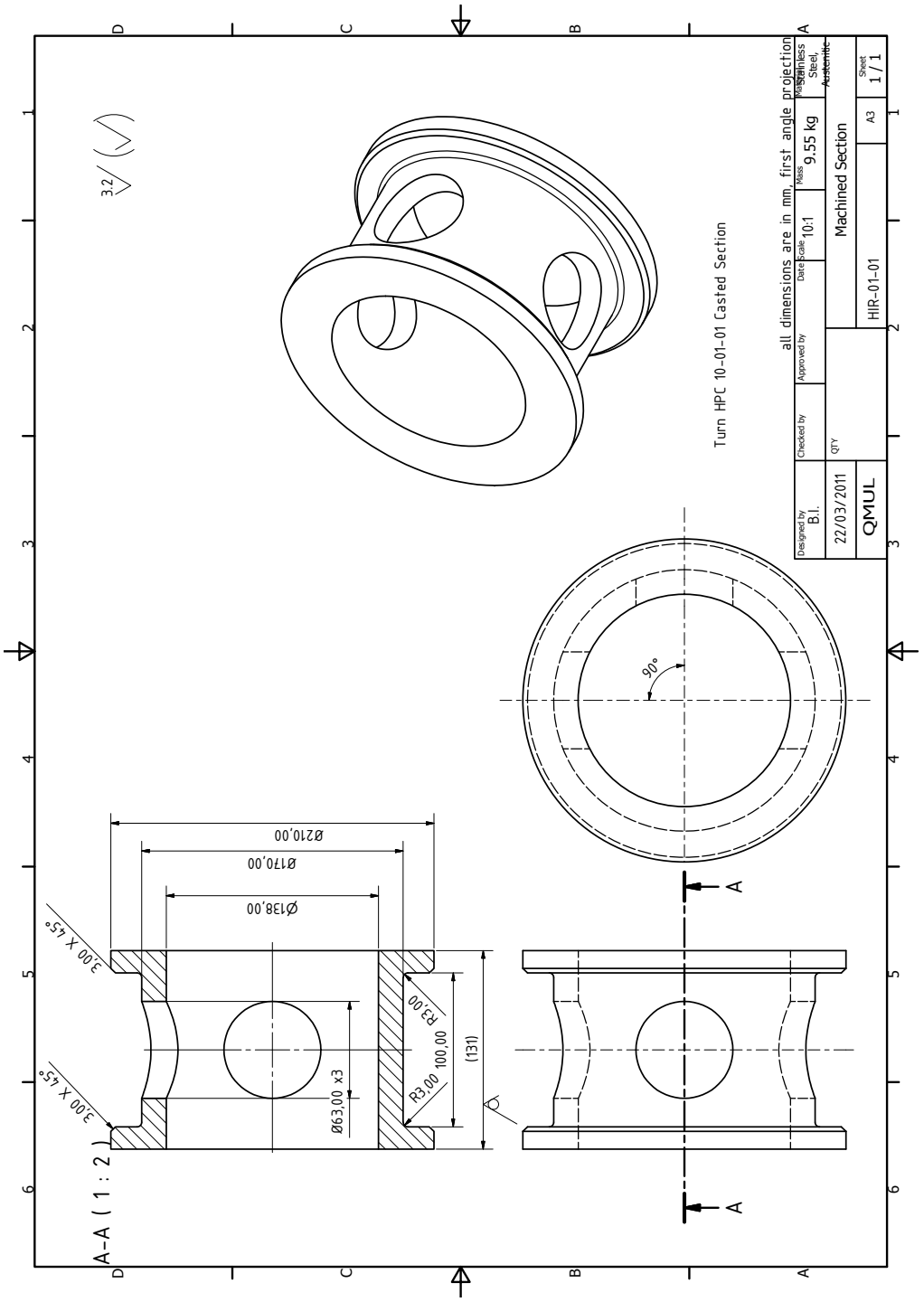

Figure A.2: High pressure chamber machined section.

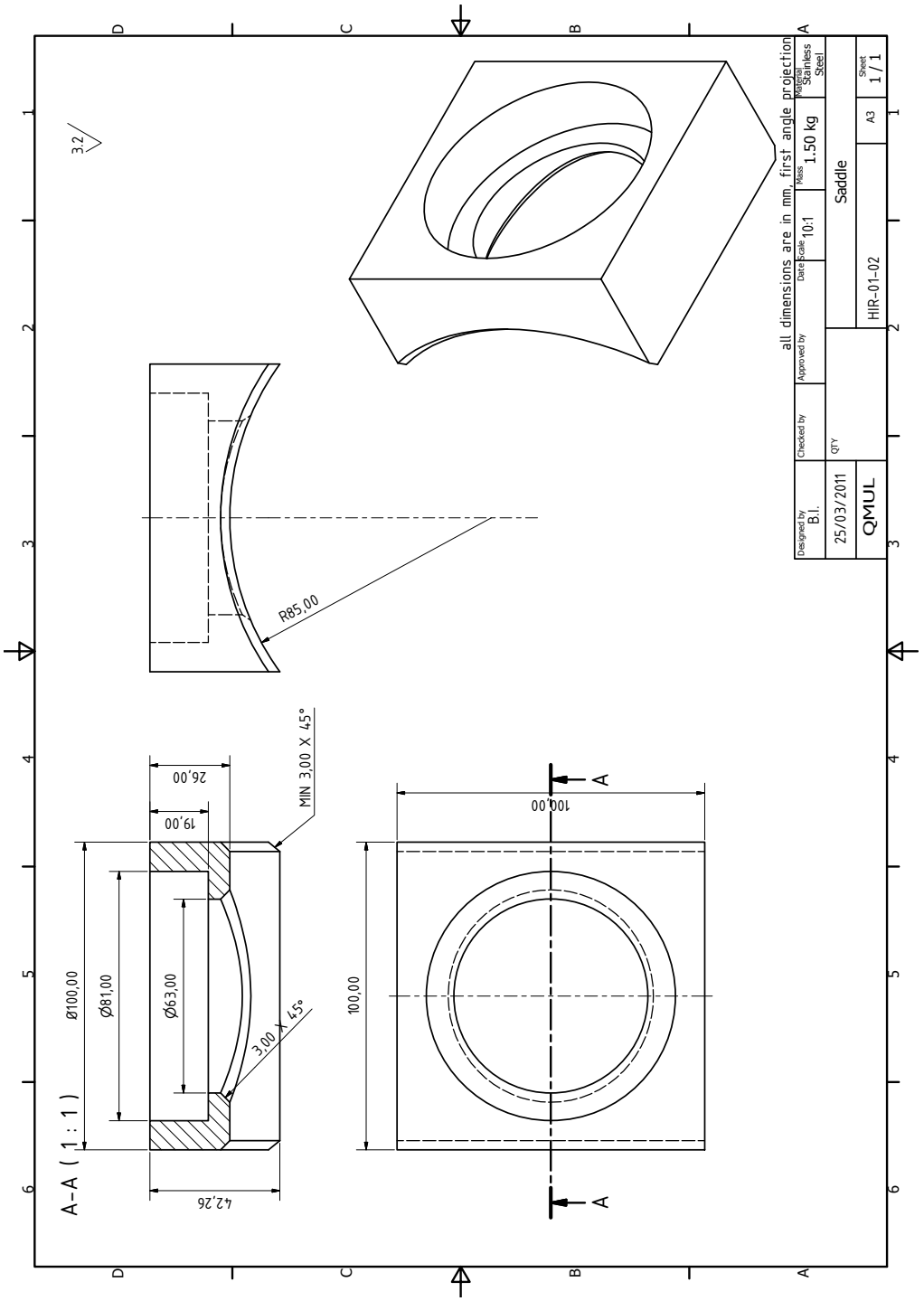

Figure A.3: High pressure chamber window saddle.

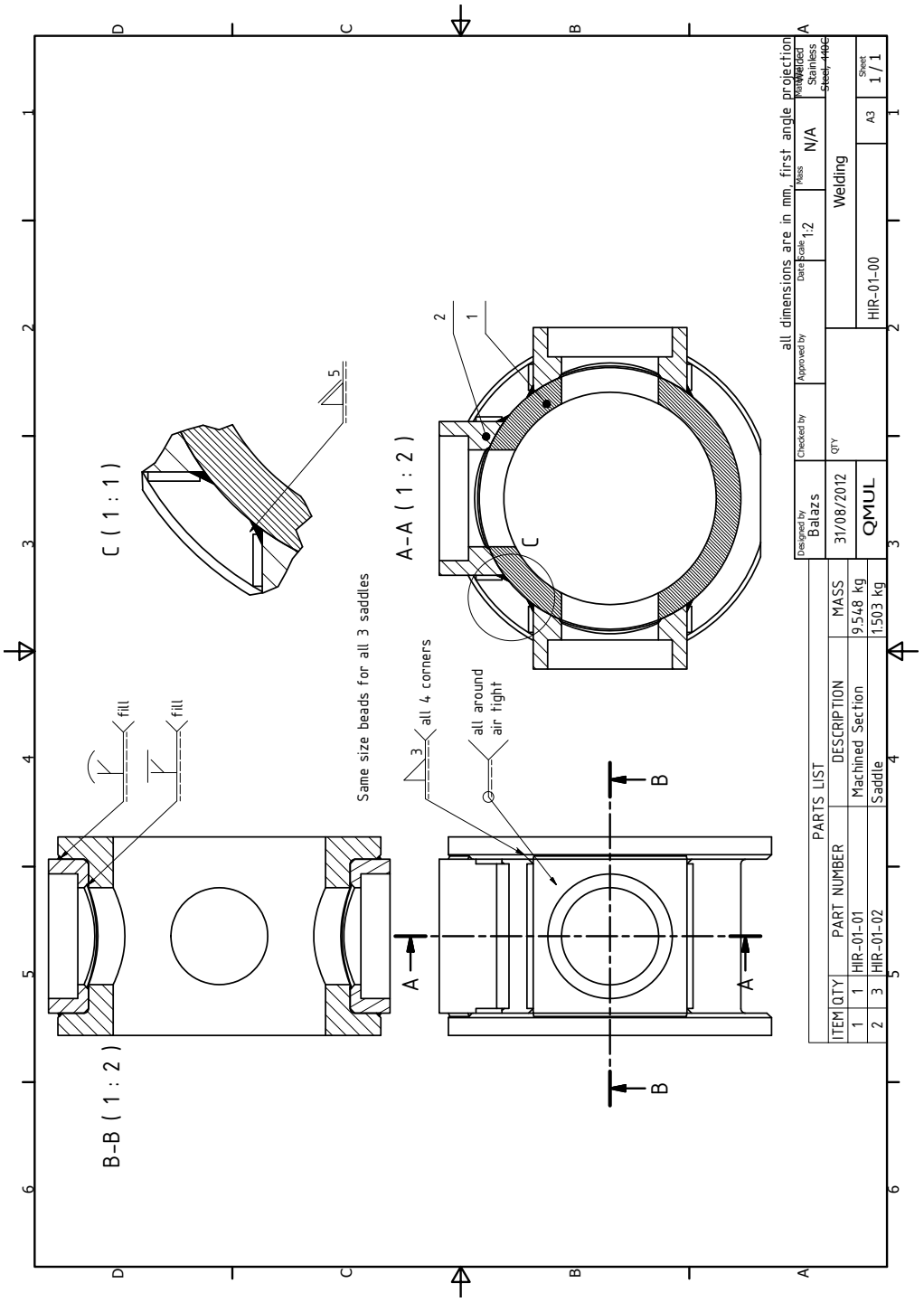

Figure A.4: High pressure chamber welding.

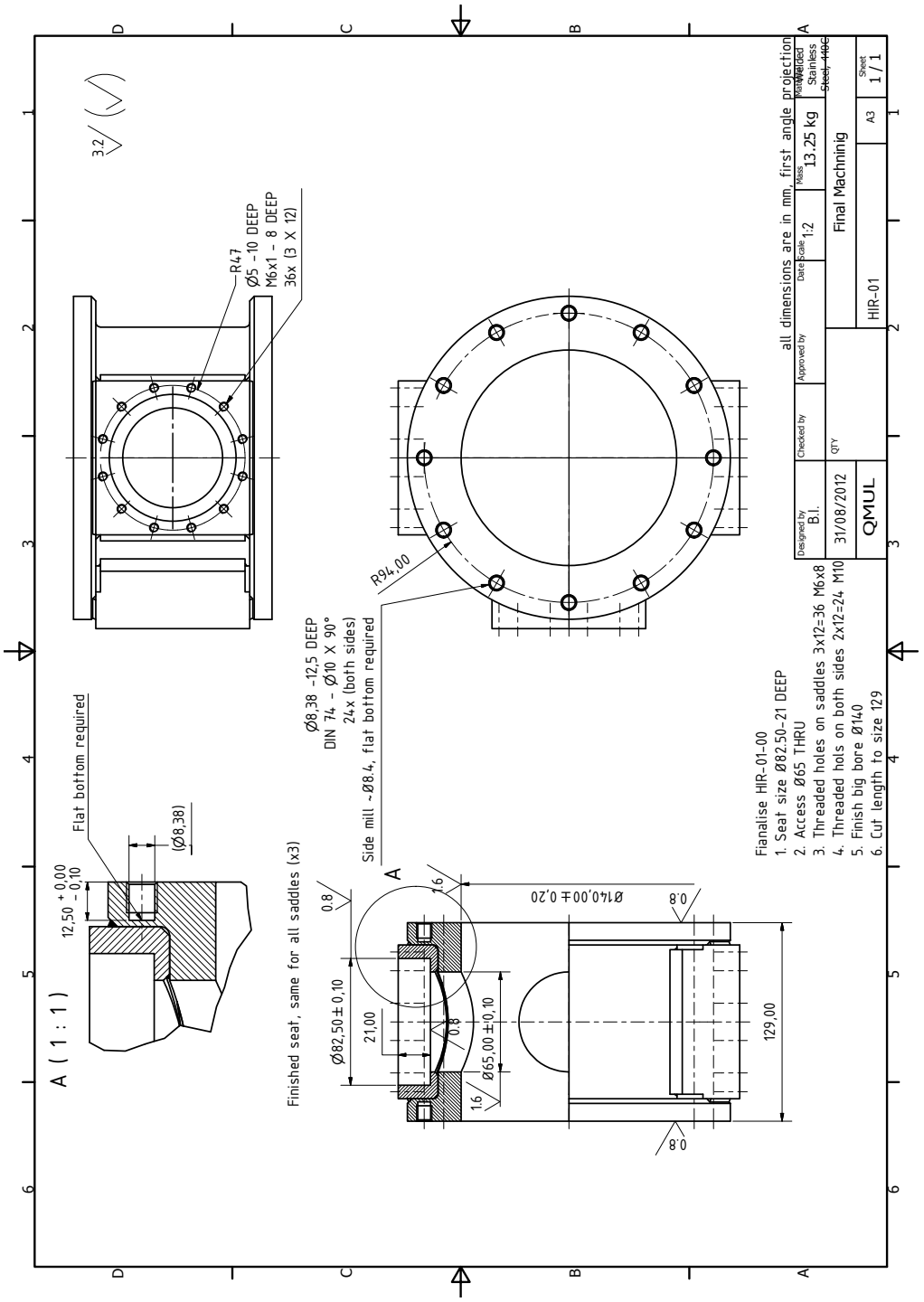

Figure A.5: High pressure chamber final machining.

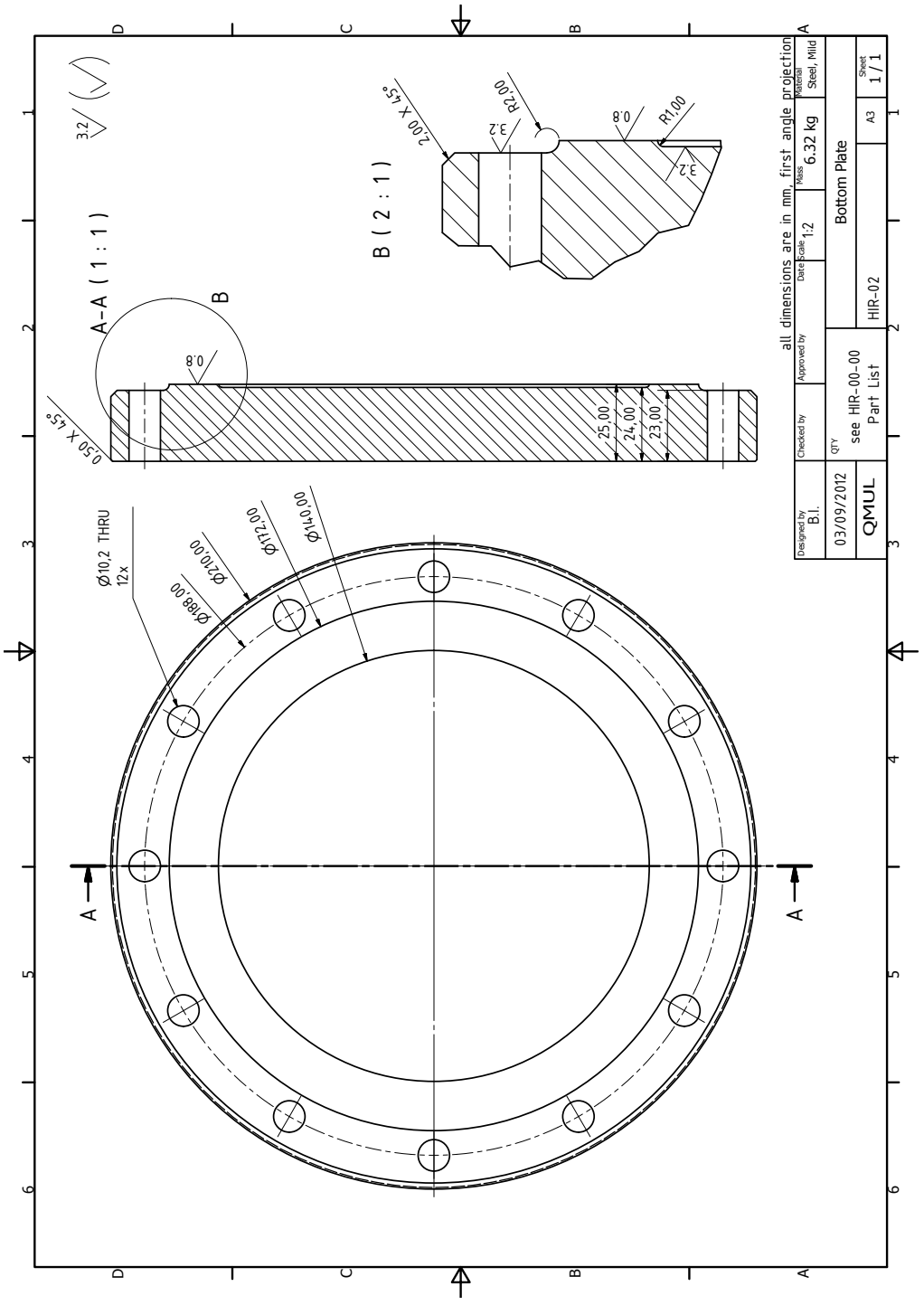

Figure A.6: High pressure chamber bottom plate.

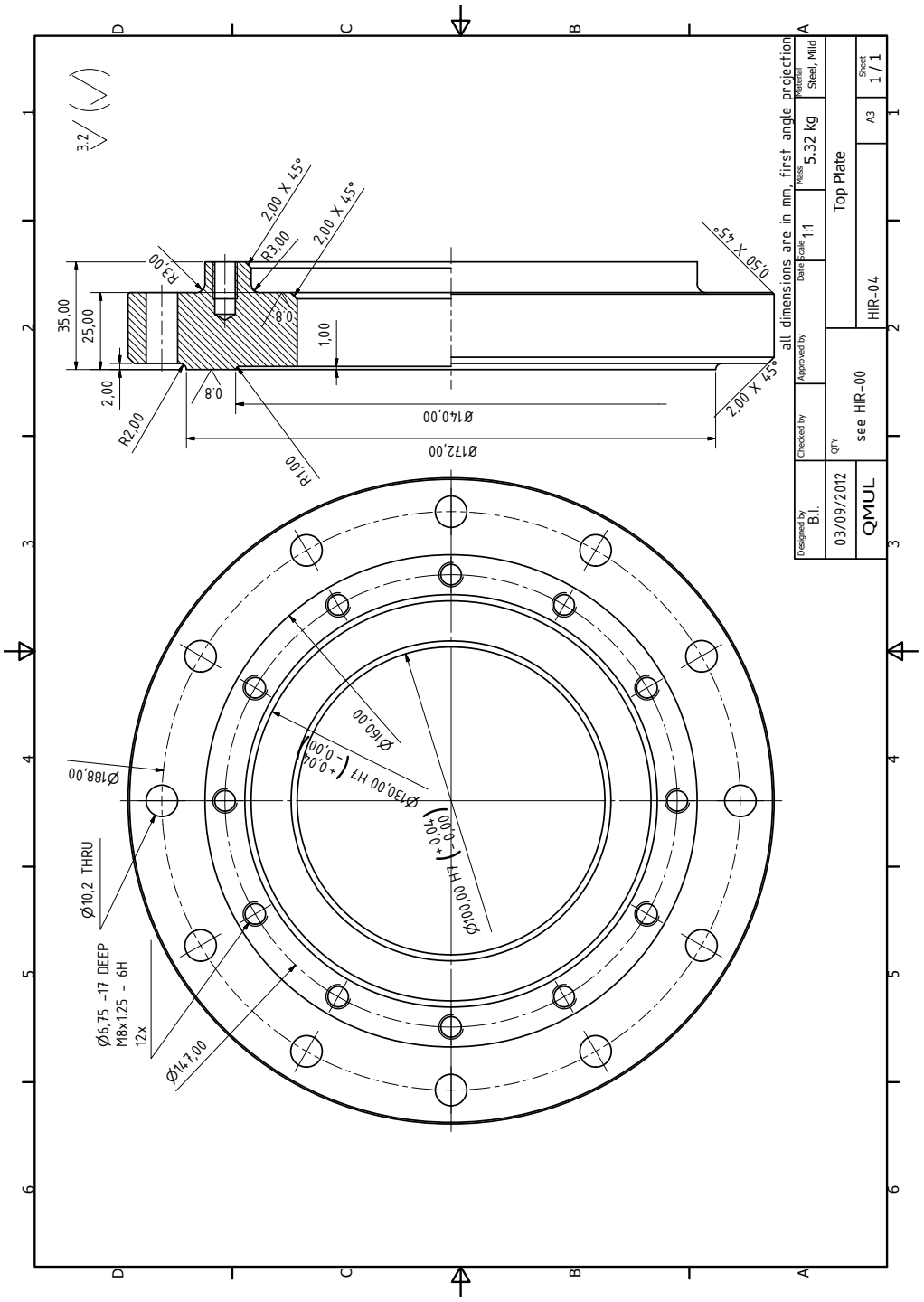

Figure A.7: High pressure chamber top plate.

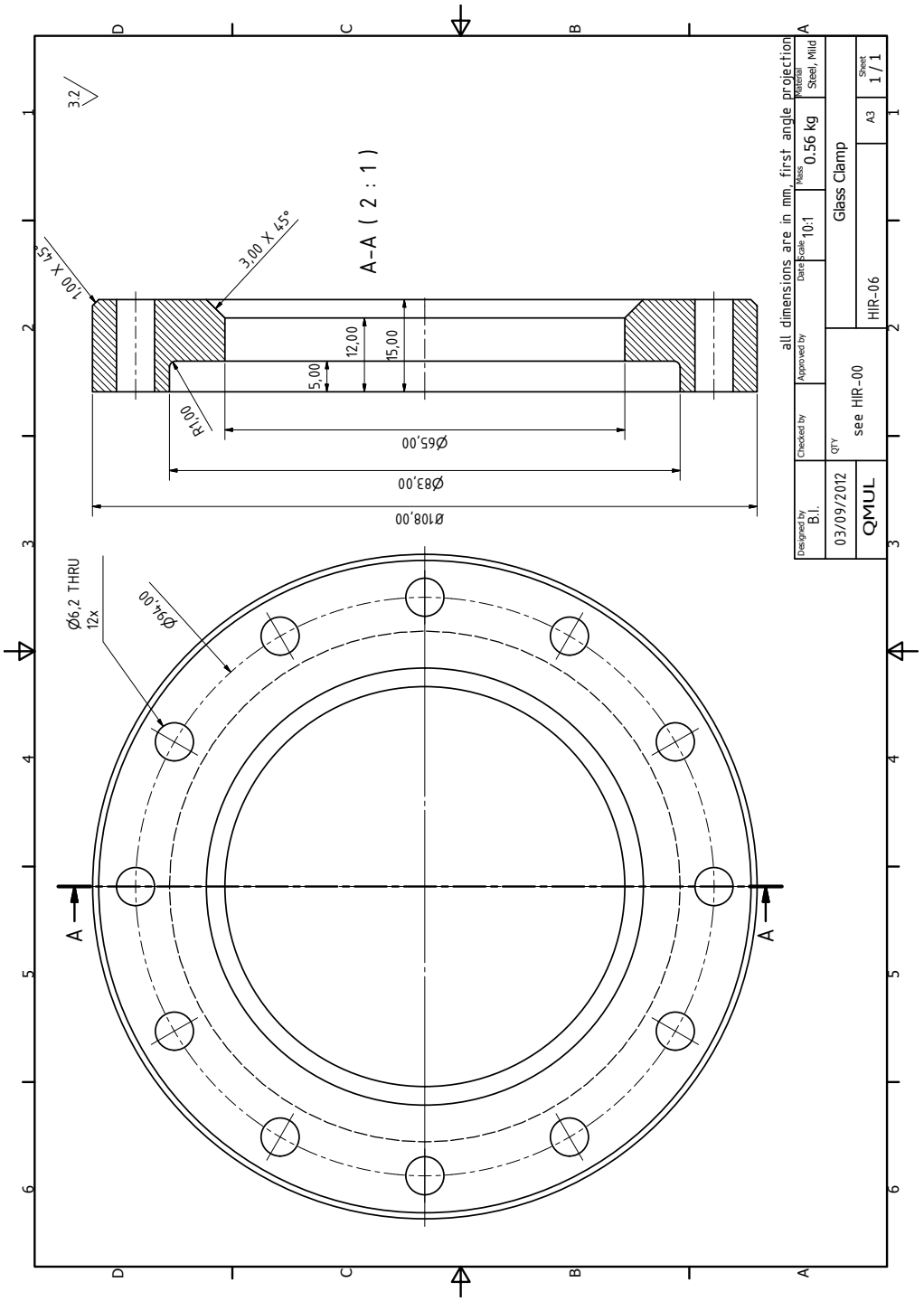

Figure A.8: High pressure chamber window clamp.

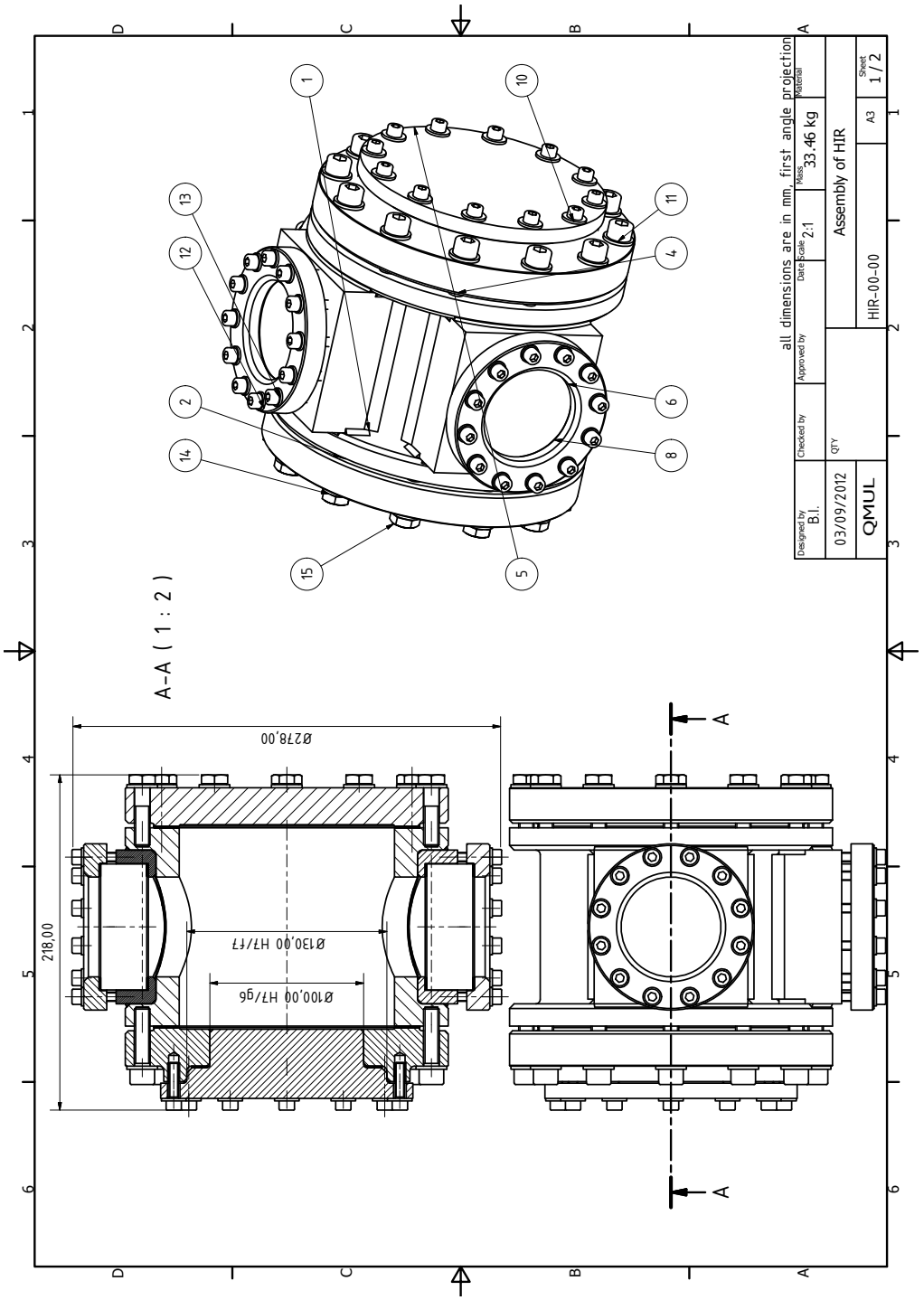

Figure A.9: High pressure chamber completed.

Stress Analysis of the High Pressure Injection Pressure Vessel

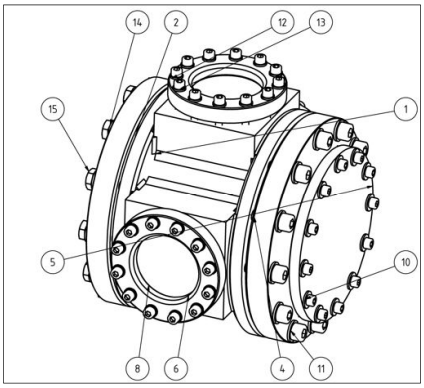

Body and Widow Seats

Thermal and Mechanical Load

Pressure: 4.0 MPa (40 bar) at ambient temperature

Material

Grade: EN 1.4301

Analysis settings

General objective and settings:

Design Objective	Single Point
Simulation Type	Static Analysis
Last Modification Date	23/08/2013, 09:24
Detect and Eliminate Rigid Body Modes	No

Advanced settings:

Avg. Element Size (fraction of model diameter)	0.1
Min. Element Size (fraction of avg. size)	0.2
Grading Factor	1.5
Max. Turn Angle	60 deg
Create Curved Mesh Elements	No
Ignore Small Geometry	No

Results

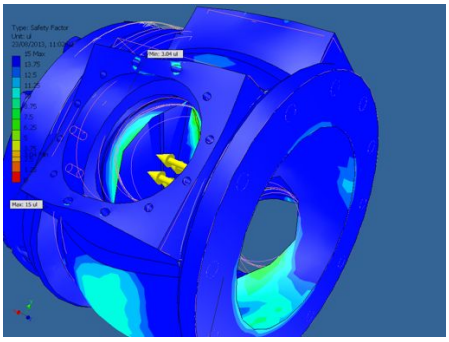

Z Displacement	-0.00479238 mm	0.00489572 mm
Equivalent Strain	0.0000000963366 ul	0.00221705 ul
1st Principal Strain	-0.00000352308 ul	0.00247547 ul
3rd Principal Strain	-0.00114635 ul	0.00000305597 ul
Strain XX	-0.00036088 ul	0.00135621 ul
Strain XY	-0.00136788 ul	0.00167363 ul
Strain XZ	-0.00122445 ul	0.00132261 ul
Strain YY	-0.000607611 ul	0.000341815 ul
Strain YZ	-0.000304315 ul	0.00027222 ul
Strain ZZ	-0.000440613 ul	0.00033135 ul
Contact Pressure	0 MPa	64.6767 MPa
Contact Pressure X	-64.6403 MPa	39.7708 MPa
Contact Pressure Y	-28.2186 MPa	45.7378 MPa
Contact Pressure Z	-31.0857 MPa	31.8978 MPa

Conclusion

The safety factor was found to be at least 3.04 everywhere in the structure under the given load and conditions. Therefore, the vessel will be able to withstand 40 bar mechanical load at ambient temperatyure.

Name	Minimum	Maximum
Volume	2699070 mm^3	
Mass	0 kg	
Von Mises Stress	0.0230316 MPa	68.0719 MPa
1st Principal Stress	-12.4944 MPa	70.0617 MPa
3rd Principal Stress	-47.5866 MPa	32.4884 MPa
Displacement	0 mm	0.013887 mm
Safety Factor	3.048715 ul	15 ul
Stress XX	-36.3724 MPa	60.2147 MPa
Stress XY	-25.8969 MPa	20.3179 MPa
Stress XZ	-18.7921 MPa	18.1793 MPa
Stress YY	-28.7198 MPa	40.9388 MPa
Stress YZ	-11.0461 MPa	12.1979 MPa
Stress ZZ	-18.8059 MPa	40.196 MPa
X Displacement	-0.000672436 mm	0.0135963 mm
Y Displacement	-0.0125675 mm	0.00411913 mm

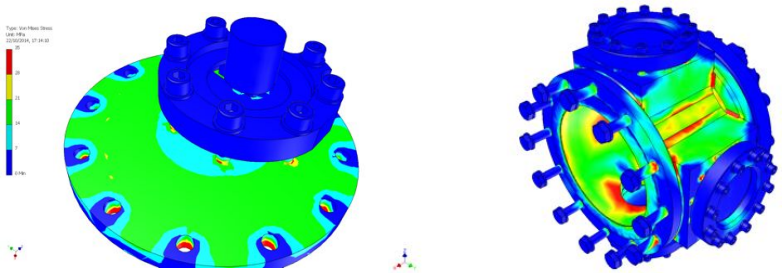

Figure A.10: High pressure chamber stress analysis.

B. LED drive circuit and mount

To achieve the high current, short duration pulsed operation of the LED a drive circuit was constructed. The circuit is shown in Fig.B.1 and is based upon the works [176, 172, 173]. The components are detailed in Table.B.1.

The two capacitors in parallel, C_1, C_2 are charged through the power supply, in this study 30V. The MOSFET driver U_1 is chosen for its TTL compatibility input. The LED cathode is connected to the the drain of T_1 whose source is connected to ground via R_2. A TTL signal is generated and synchronized by the custom LabView program running in the background of the experiment. The MOSFET power transistor T_1 is triggered by the TTL via U_1. The capacitors discharge through the LED and light is emitted. The current through the LED is controlled by the supply voltage, high pulsed currents are achieved through the use of large capacitors (C_1, C_2) with low internal resistance. The resistor R_2 acts a sense resistor across which the voltage is measured by an oscilloscope to determine an approximation of the current flow though the LED. The diode D_1 acts to protect the LED from any reverse currents during switching. Resistor R_1 acts as rudimentary protection for

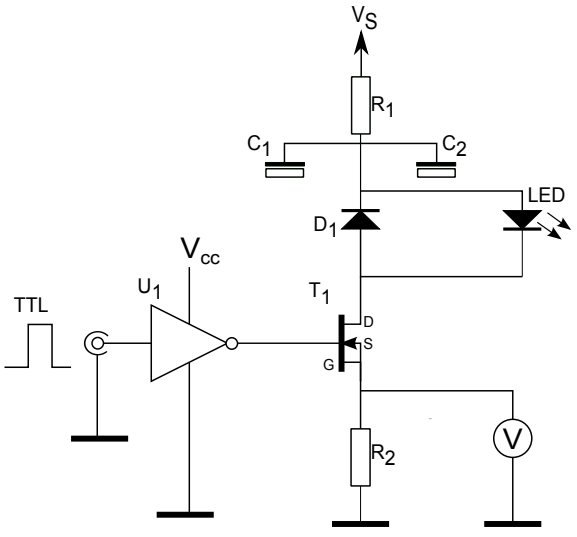

Figure B.1: LED drive circuit.

Table B.1: Components

Key	Component
R_1	Resistor 1Ω
R_2	Resistor 0.002Ω
C_1	Capacitor 2200μF elec
C_2	Capacitor 10μF poly
D_1	BYT01-400 Diode
T_1	IRFB3206GPbF MOSFET
U_1	UCC37322P MOSFET driver
V_S	Supply Voltage
V_{CC}	5 Volt
V	Oscilloscope

the LED to prevent over charging of the capacitor bank. In the works [173, 176, 172] the requirement to use short connections between the components is stressed to reduce any parasitic losses in the circuit and maintain performance. In those works, PCB were used. In this study, prototyping Veroboard was used, with the addition of thick copper wire along the tracks and connection lengths as short as possible. The power supply used was an ISO-Tech IPS-4303. The use of this power supply, which has a safety over-current protection system installed resulted in an effective cap of the maximum current thought the LED of 60A. Fig.B.2 shows a 3.25μs, 60A current pulse as measured using the oscilloscope across R_2.

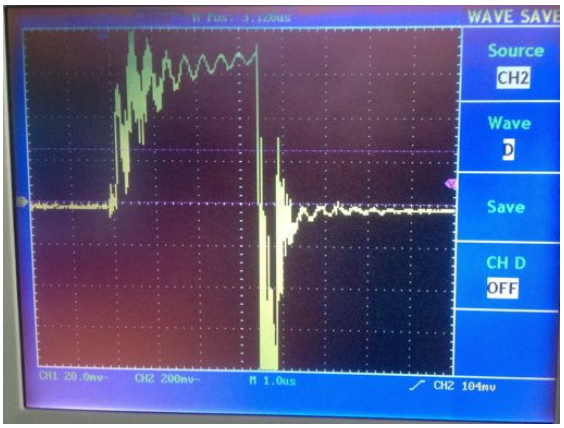

Figure B.2: Oscillascope of LED drive circuit voltage used to determine the drive current.

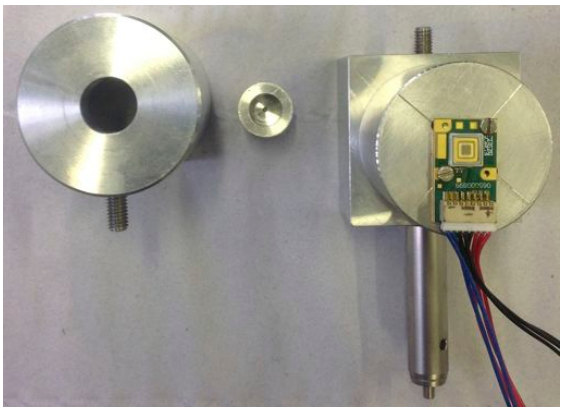

Figure B.3: LED mount.

In the work [176] this same LED is driven at a pulsed (1μs at 1KHz) 30A current, a 5 fold increase to rated. The LED was shown to increase in light emission with increasing drive current with a proportionality of approximately 0.35 beyond currents of 10A. The green CBT-40 LED is rated for 9.8A pulsed, 50% duty cycle with radiometric flux of 1.9W. This equates to an effective pulse power of 3.8W for the pulse duration. Using the 0.35 proportionality, the increase in current from 9.8A to the 60A used in this study will result in an effective pulse power of 21W.

B.1 LED mounting

The LED used is a flat type with the the emitting surface a small square in the centre of the chipset. For schlieren/shadowgraph, a small aperture point source was necessary. For the backlit, diffuse experiments this was not needed and an extended source, i.e full emission surface could be used. There was also a desire

for the LED to be used in the future for Mie scattering tests that may want to be done requiring the eventual connection to a fibre optic system. A mounting system was produced that allowed the temporary fixing of a pin hole, 1mm in diameter which when removed would except a Fibre-lite fibre optic system. When neither of these were in position, the entire emission surface was unobscured. The base of the mount utilized a Thorlabs stand and clamp for fitting to the optical bread board or the optical rail. The mounted LED is shown with the pin-hole removed and the sheath that housed the pin-hole also removed (right to left respectively) in Fig.B.3. The LED was then ready to be installed in the completed system and alignments conducted.

C. Force/Pressure transducer details

Force

KISTLER
measure. analyze. innovate.

Low Level Force Sensor

M5x0,5, –20 … 200 N

Type 9215

Patent No. US 7,548,012 B2

Highly sensitive, piezoelectric force sensor for measuring quasi-static and dynamic tensile and compression forces from a few mN upwards. The sensor has a sealed case and is suitable for both laboratory and industrial applications.

- 3 calibrated measuring ranges
- Dynamic measuring range 1 : 100 000
- Highly sensitive, for forces from 1 mN upwards
- For tensile and compression forces
- High allowable transverse force
- Low acceleration sensitivity
- High rigidity

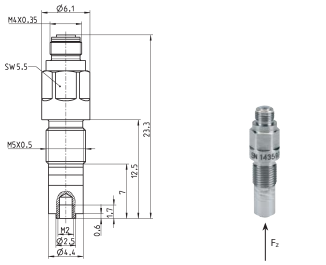

Description

The highly sensitive measuring element fitted under low preload gives the sensor very high rigidity with simultaneously low transverse force sensitivity. The sensor body has an M5x0,5 external thread and a sealed, ceramic-insulated connecting plug. The force is introduced via the M2 tapped bore at the front.

Technical Data

Measuring range	F_z	N	–20 … 200
Overload	F_z	N	–30/300
Calibrated measuring ranges			
100 %	F_z	N	0 … 200
10 %	F_z	N	0 … 20
1 %	F_z	N	0 … 2
Threshold	F_z	N	$<5 \cdot 10^{-4}$
Sensitivity	F_z	pC/N	≈–81
Linearity, all measuring ranges		%FSO	≤±1,0
Hysteresis, all measuring ranges		%FSO	≤1,0
Transverse force [1], max.	$F_{x,y}$	N	90
Transverse force sensitivity	$F_{x,y} \rightarrow F_z$	N/N	≤±0,05
Transverse force sensitivity, typical		N/N	≤±0,035
Bending moment, max.	$M_{x,y}$	N·m	0,5
Sensitivity to bending moment	$M_{x,y} \rightarrow F_z$	N/N·m	≤±3
Torque, max.	M_z	N·m	1,0
Rigidity	c_z	N/µm	≈100

Natural frequency	kHz	>50
Acceleration sensitivity		
axial	N/g	$<2 \cdot 10^{-3}$
radial	N/g	$<4 \cdot 10^{-4}$
Operating temperature range	°C	–50 … 180
Temperature coefficient of sensitivity		
20 … 100 °C	%/°C	<0,05
100 … 180 °C	%/°C	<0,07
Insulation resistance, at 20 °C	Ω	$>10^{13}$
Capacitance	pF	≈15
Connector (ceramic insulator)		M4x0,35 neg.
Degree of protection (with cable connected)	EN60529	IP65
Case material	DIN	1.4542
Weight	g	2,5
Tightening torque, max.		
M5x0,5	N·m	2
M2	N·m	0,2

[1] Point of force application at tip of force introducing cap

9215_000-487e-01.11

Figure C.1: Kistler 9215 details

D. Shadowgraph Image sets of D10 sprays

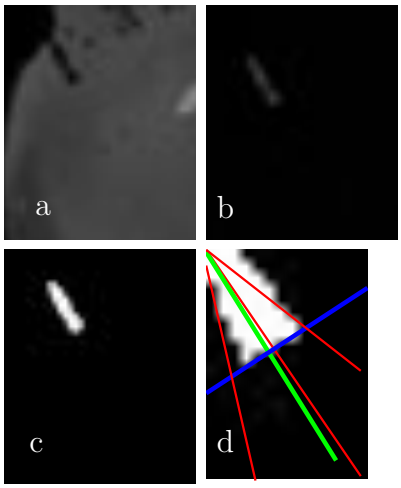

Figure D.1: Shadowgraph D10 spray image at the SOI $t = 0\mu$s (first frame containing spray). (*a*)Raw image, (*b*)Complement image, (*c*)Black and white image, (*d*)Cropped, processed measurement image.

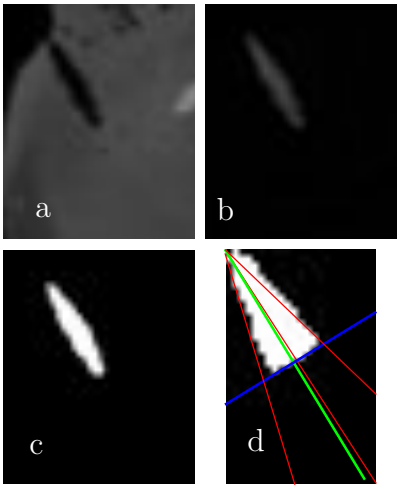

Figure D.2: Shadowgraph D10 spray image at $t = 33.25\mu$s (second frame containing spray). (*a*)Raw image, (*b*)Complement image, (*c*)Black and white image, (*d*)Cropped, processed measurement image.

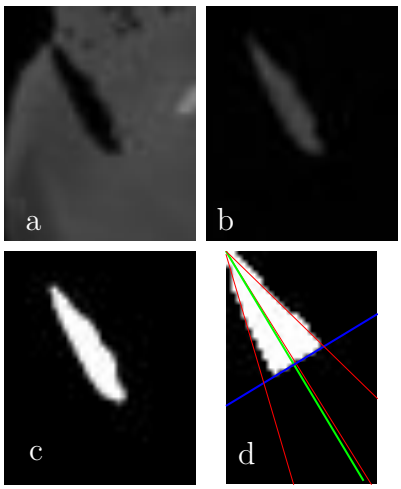

Figure D.3: Shadowgraph D10 spray image at $t = 66.50\mu$s (third frame containing spray). (*a*)Raw image, (*b*)Complement image, (*c*)Black and white image, (*d*)Cropped, processed measurement image.

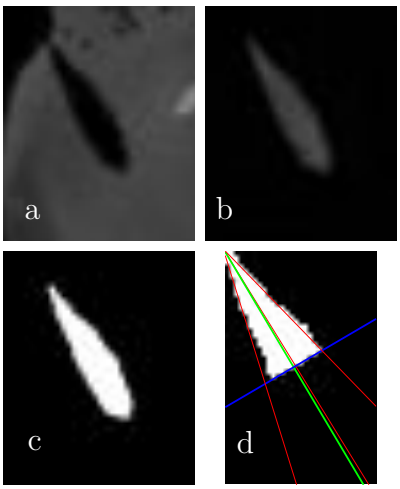

Figure D.4: Shadowgraph D10 spray image at $t = 99.75\mu$s (fourth frame containing spray). (*a*)Raw image, (*b*)Complement image, (*c*)Black and white image, (*d*)Cropped, processed measurement image

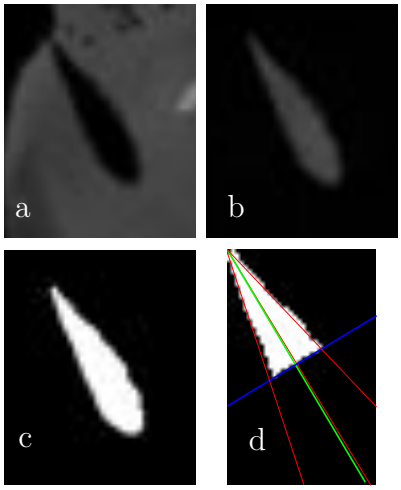

Figure D.5: Shadowgraph D10 spray image at $t = 133\mu$s (fifth frame containing spray). (a)Raw image, (b)Complement image, (c)Black and white image, (d)Cropped, processed measurement image

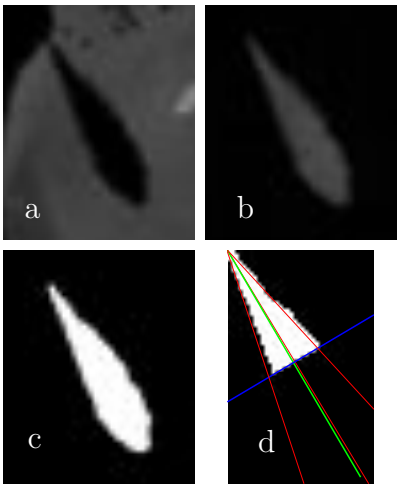

Figure D.6: Shadowgraph D10 spray image at $t = 166.25\mu$s (sixth frame containing spray). (a)Raw image, (b)Complement image, (c)Black and white image, (d)Cropped, processed measurement image

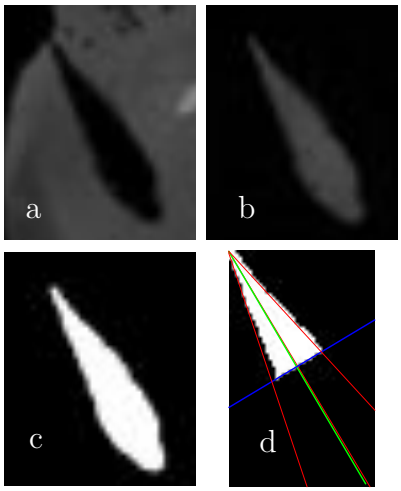

Figure D.7: Shadowgraph D10 spray image at $t = 199.50\mu$s (seventh frame containing spray). (a)Raw image, (b)Complement image, (c)Black and white image, (d)Cropped, processed measurement image

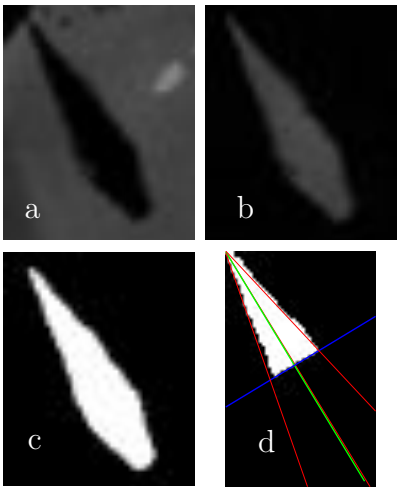

Figure D.8: Shadowgraph D10 spray image at $t = 232.75\mu$s (eighth frame containing spray). (a)Raw image, (b)Complement image, (c)Black and white image, (d)Cropped, processed measurement image

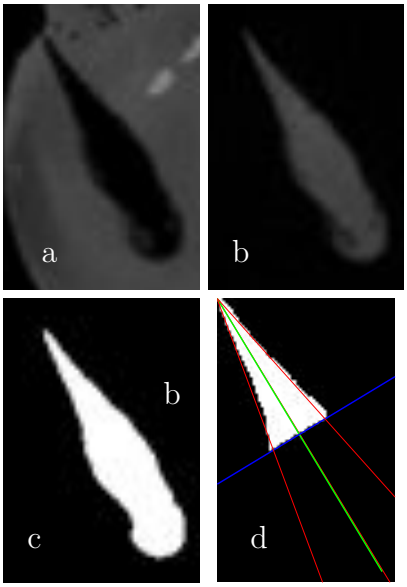

Figure D.9: Shadowgraph D10 spray image at $t = 399\mu$s (thirteenth containing spray). (a)Raw image, (b)Complement image, (c)Black and white image, (d)Cropped, processed measurement image

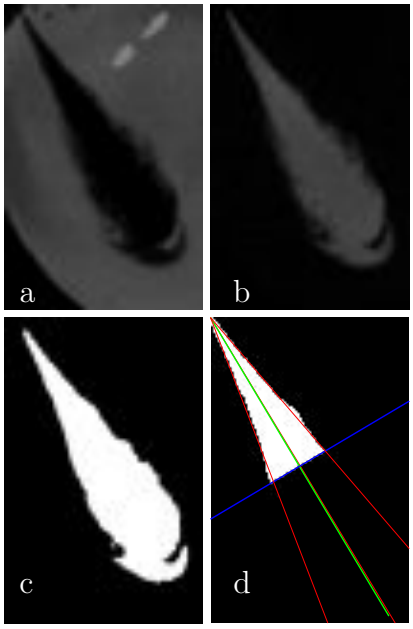

Figure D.10: Shadowgraph D10 spray image at $t = 731.50\mu$s (twenty third frame containing spray). (a)Raw image, (b)Complement image, (c)Black and white image, (d)Cropped, processed measurement image

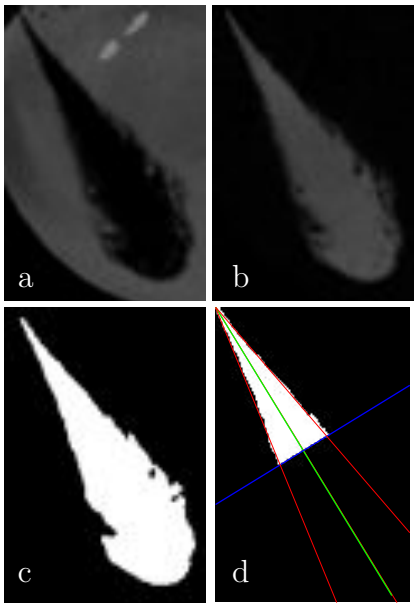

Figure D.11: Shadowgraph D10 spray image at $t = 1064\mu$s (thirty third frame containing spray). (a)Raw image, (b)Complement image, (c)Black and white image, (d)Cropped, processed measurement image

E. Shadowgraph Image sets of D20 sprays

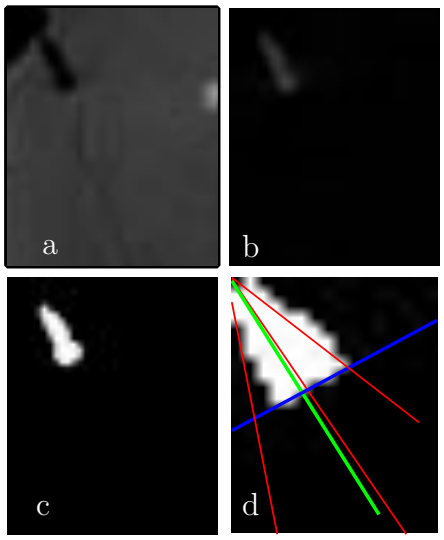

Figure E.1: Shadowgraph D20 spray image at the SOI $t = 0\mu$s (first frame containing spray). (*a*)Raw image, (*b*)Complement image, (*c*)Black and white image, (*d*)Cropped, processed measurement image.

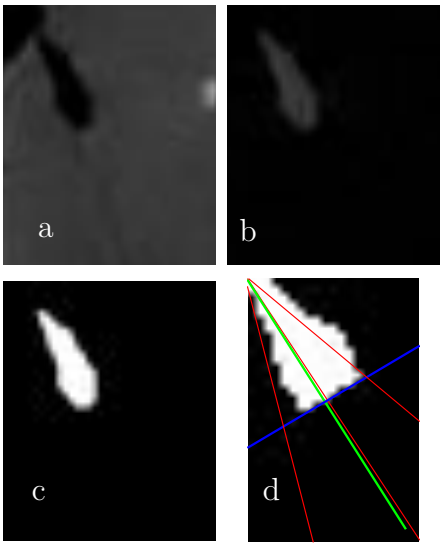

Figure E.2: Shadowgraph D20 spray image at $t = 33.25\mu$s (second frame containing spray). (*a*)Raw image, (*b*)Complement image, (*c*)Black and white image, (*d*)Cropped, processed measurement image.

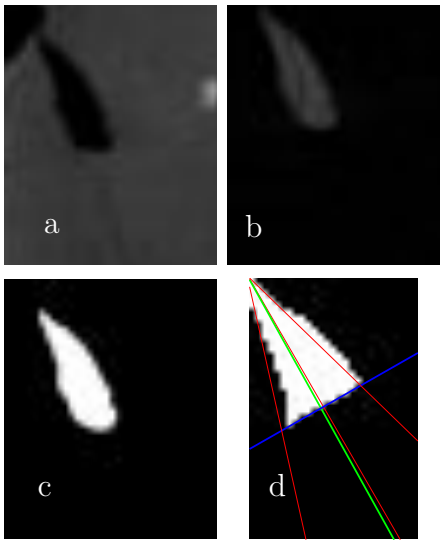

Figure E.3: Shadowgraph D20 spray image at $t = 66.50\mu$s (third frame containing spray). (*a*)Raw image, (*b*)Complement image, (*c*)Black and white image, (*d*)Cropped, processed measurement image.

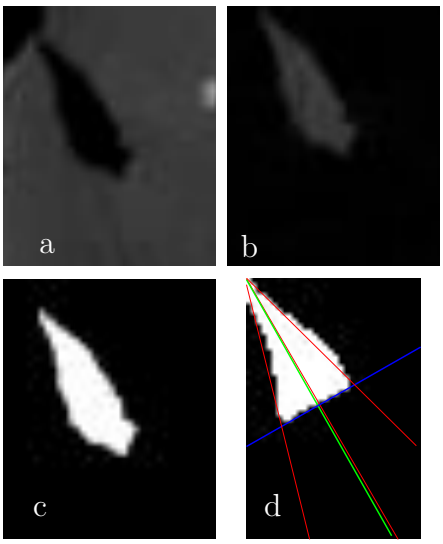

Figure E.4: Shadowgraph D20 spray image at $t = 99.75\mu$s (fourth frame containing spray). (*a*)Raw image, (*b*)Complement image, (*c*)Black and white image, (*d*)Cropped, processed measurement image

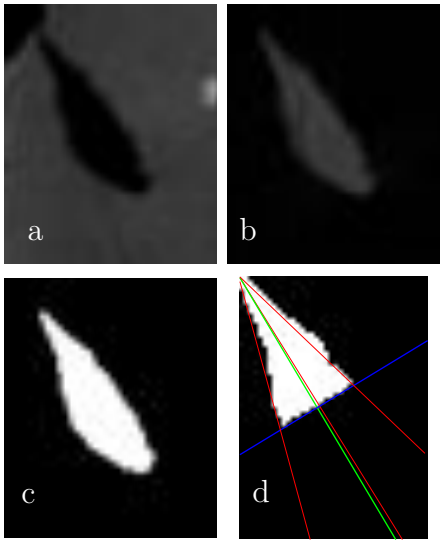

Figure E.5: Shadowgraph D20 spray image at $t = 133\mu$s (fifth frame containing spray). (a)Raw image, (b)Complement image, (c)Black and white image, (d)Cropped, processed measurement image

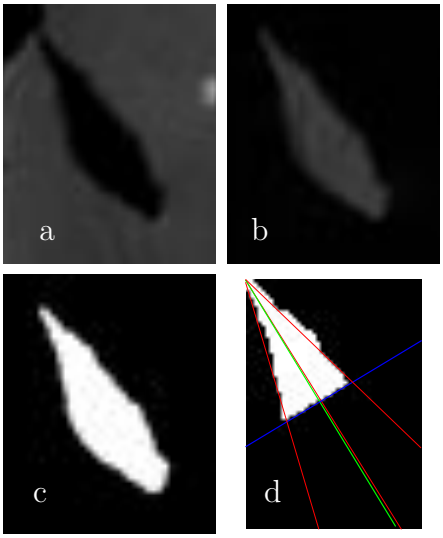

Figure E.6: Shadowgraph D20 spray image at $t = 166.25\mu$s (sixth frame containing spray). (a)Raw image, (b)Complement image, (c)Black and white image, (d)Cropped, processed measurement image

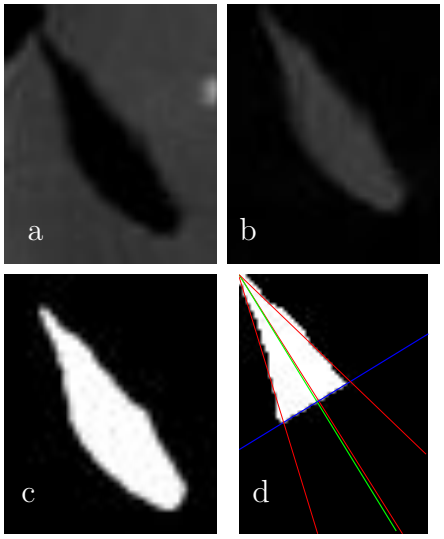

Figure E.7: Shadowgraph D20 spray image at $t = 199.50\mu$s (seventh frame containing spray). (a)Raw image, (b)Complement image, (c)Black and white image, (d)Cropped, processed measurement image

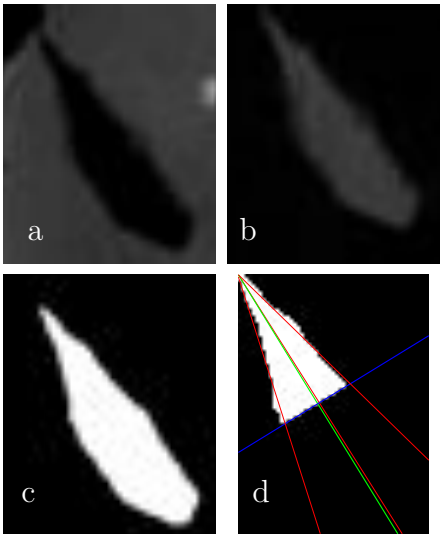

Figure E.8: Shadowgraph D20 spray image at $t = 232.75\mu$s (eighth frame containing spray). (a)Raw image, (b)Complement image, (c)Black and white image, (d)Cropped, processed measurement image

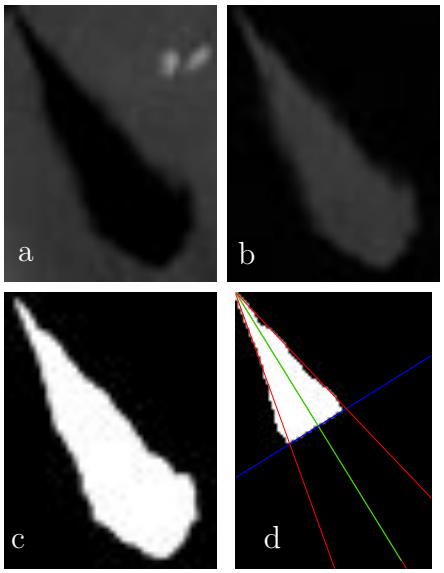

Figure E.9: Shadowgraph D20 spray image of at $t = 399\mu$s (thirteenth containing spray). (a)Raw image, (b)Complement image, (c)Black and white image, (d)Cropped, processed measurement image

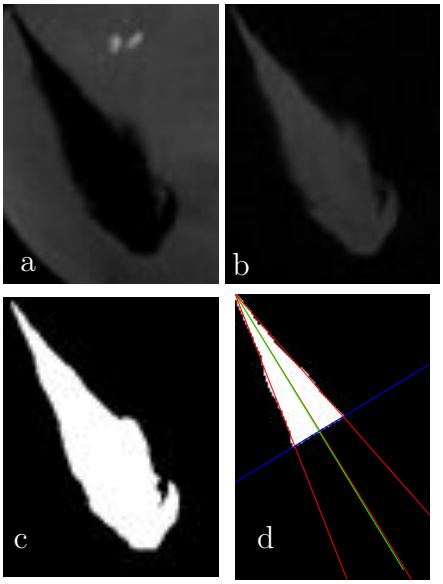

Figure E.10: Shadowgraph D20 spray image at $t = 731.50\mu$s (twenty third frame containing spray). (a)Raw image, (b)Complement image, (c)Black and white image, (d)Cropped, processed measurement image

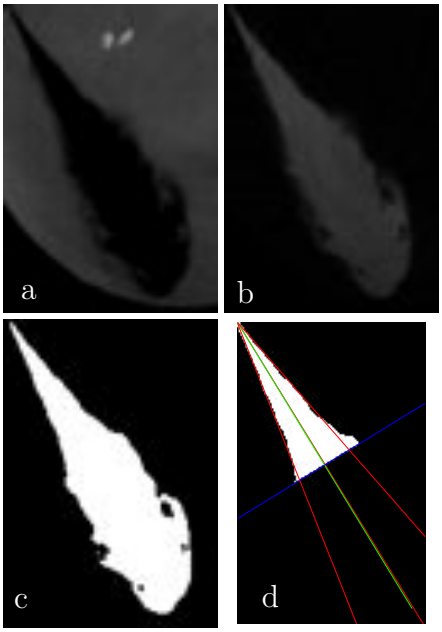

Figure E.11: Shadowgraph D20 spray image at $t = 1064\mu$s (thirty third frame containing spray). (a)Raw image, (b)Complement image, (c)Black and white image, (d)Cropped, processed measurement image

F. Backlit image sets D10

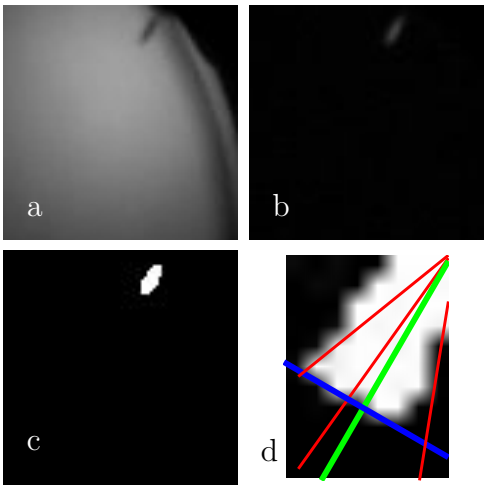

Figure F.1: Backlit D10 spray image at the SOI $t = 0\mu$s (first frame containing spray). (a)Raw image, (b)Complement image, (c)Black and white image, (d)Cropped, processed measurement image.

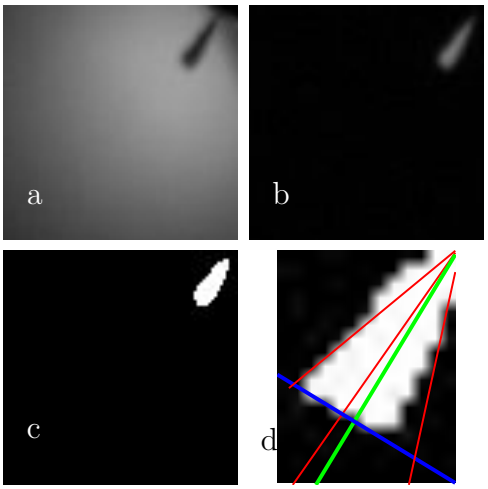

Figure F.2: Backlit D10 spray image $t = 11.25\mu$s (second frame containing spray) after the SOI. (a)Raw image, (b)Complement image, (c)Black and white image, (d)Cropped, processed measurement image.

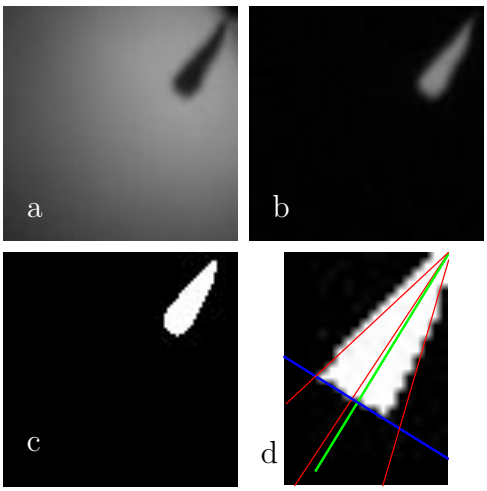

Figure F.3: Backlit D10 spray image $t = 22.50\mu$s (third frame containing spray) after the SOI. (a)Raw image, (b)Complement image, (c)Black and white image, (d)Cropped, processed measurement image.

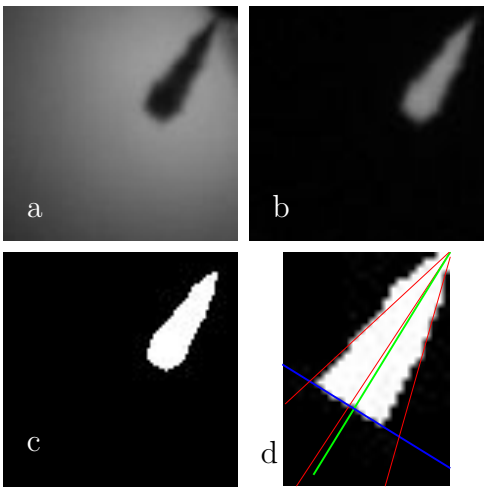

Figure F.4: Backlit D10 spray image $t = 33.75\mu$s (fourth frame containing spray) after the SOI. (a)Raw image, (b)Complement image, (c)Black and white image, (d)Cropped, processed measurement image.

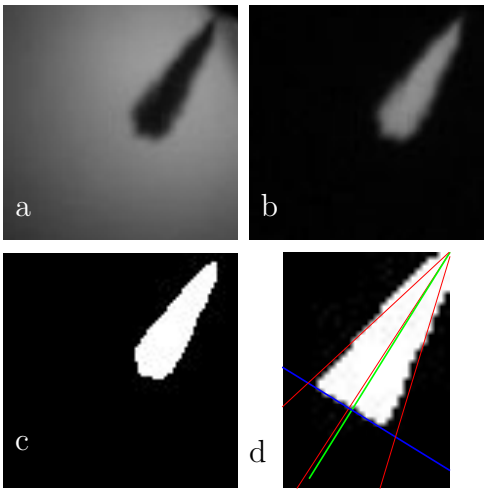

Figure F.5: Backlit D10 spray image $t = 45\mu$s (fifth frame containing spray) after the SOI. (a)Raw image, (b)Complement image, (c)Black and white image, (d)Cropped ,processed measurement image.

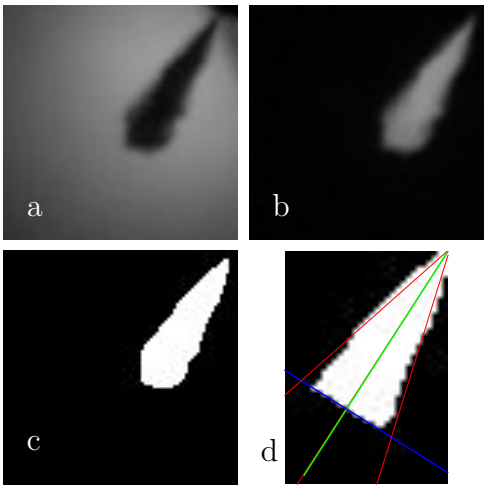

Figure F.6: Backlit D10 spray image $t = 56.25\mu$s (sixth frame containing spray) after the SOI. (a)Raw image, (b)Complement image, (c)Black and white image, (d)Cropped ,processed measurement image.

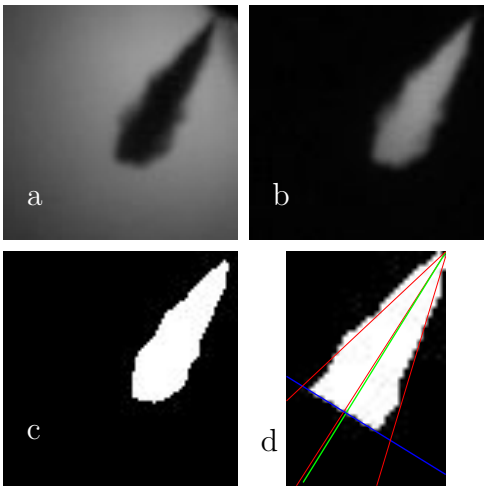

Figure F.7: Backlit D10 spray image $t = 67.50\mu$s (seventh frame containing spray) after the SOI. (a)Raw image, (b)Complement image, (c)Black and white image, (d)Cropped ,processed measurement image.

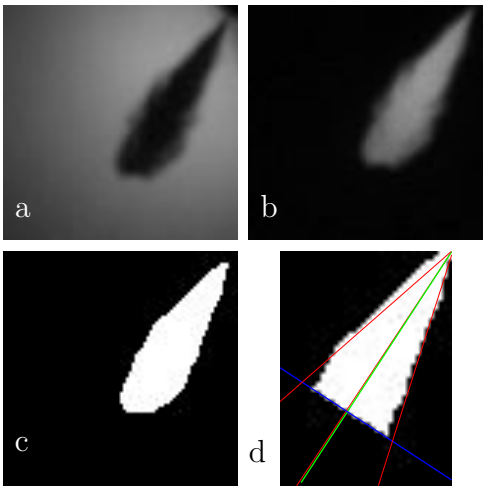

Figure F.8: Backlit D10 spray image $t = 78.75\mu$s (eighth frame containing spray) after the SOI. (a)Raw image, (b)Complement image, (c)Black and white image, (d)Cropped ,processed measurement image.

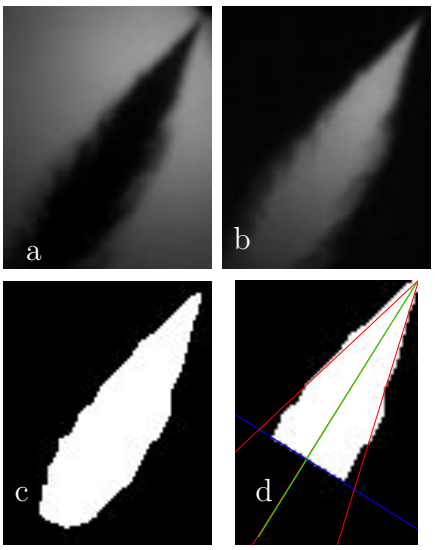

Figure F.9: Backlit D10 spray image $t = 258.75\mu$s (twenty third frame containing spray) after the SOI. (a)Raw image, (b)Complement image, (c)Black and white image, (d)Cropped, processed measurement image.

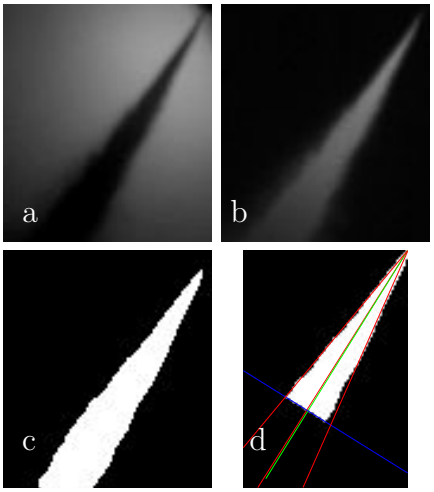

Figure F.10: Backlit D10 spray image $t = 742.50\mu$s (sixty sixth frame containing spray) after the SOI. (a)Raw image, (b)Complement image, (c)Black and white image, (d)Cropped, processed measurement image.

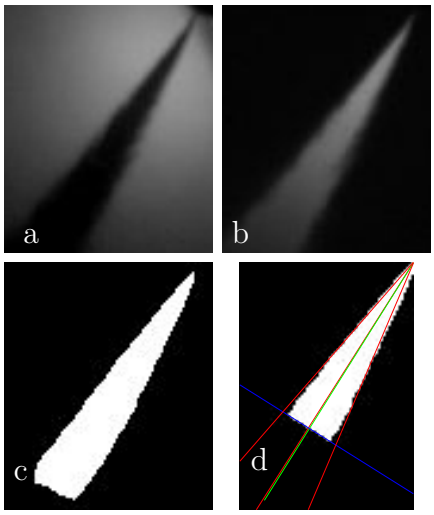

Figure F.11: Backlit D10 spray image $t = 1001.25\mu$s (eighty ninth frame containing spray) after the SOI. (a)Raw image, (b)Complement image, (c)Black and white image, (d)Cropped, processed measurement image.

G. Backlit Diesel fuel spray angle

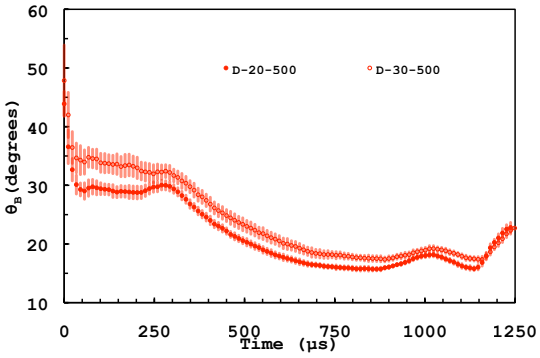

Figure G.1: Fuel injection spray angle variation with time for Diesel fuel, P_{inj}= 500 ρ_a=22.6 kg/m^3 and 34.5 kg/m^3 (P_{amb}=20 and 30bar). Determined using the near field, backlit image sequences. Error bars are the size of one standard deviation.

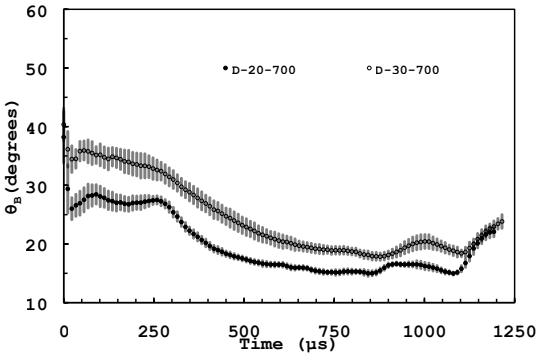

Figure G.2: Fuel injection spray angle variation with time for Diesel fuel, P_{inj}= 700 ρ_a=22.6 kg/m^3 and 34.5 kg/m^3 (P_{amb}=20 and 30bar). Determined using the near field, backlit image sequences. Error bars are the size of one standard deviation.

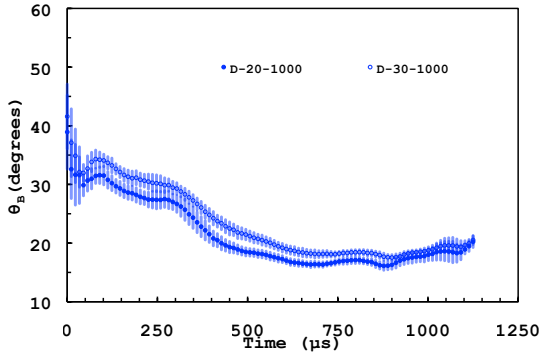

Figure G.3: Fuel injection spray angle variation with time for Diesel fuel, P_{inj}= 1000 ρ_a=22.6 kg/m^3 and 34.5 kg/m^3 (P_{amb}=20 and 30bar). Determined using the near field, backlit image sequences. Error bars are the size of one standard deviation.

H. Backlit D10 Spray angle

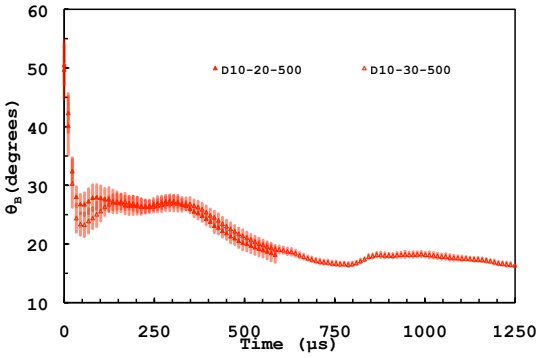

Figure H.1: Fuel injection spray angle variation with time for D10 fuel, P_{inj}= 500 ρ_a=22.6 kg/m^3 and 34.5 kg/m^3 (P_{amb}=20 and 30bar). Determined using the near field, backlit image sequences. Error bars are the size of one standard deviation.

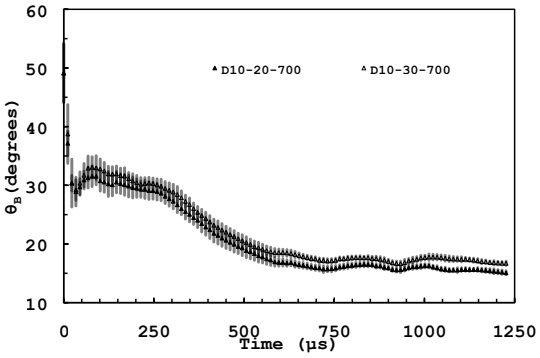

Figure H.2: Fuel injection spray angle variation with time for D10 fuel, P_{inj}= 700 ρ_a=22.6 kg/m^3 and 34.5 kg/m^3 (P_{amb}=20 and 30bar). Determined using the near field, backlit image sequences. Error bars are the size of one standard deviation

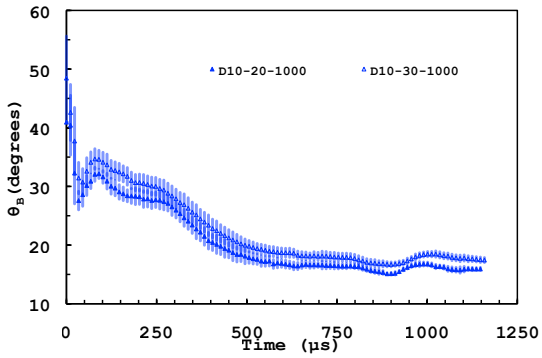

Figure H.3: Fuel injection spray angle variation with time for D10 fuel, P_{inj}= 1000 ρ_a=22.6 kg/m^3 and 34.5 kg/m^3 (P_{amb}=20 and 30bar). Determined using the near field, backlit image sequences. Error bars are the size of one standard deviation

Bibliography

[1] Q. A. Wang. Time for commercializing non-food biofuel in china. *Renewable & Sustainable Energy Reviews*, 15(1):621–629, 2011.

[2] S. Zhang, Y. Wu, H. Liu, R. Huang, P.i Un, Y. Zhou, L. Fu, and J. Hao. Real-world fuel consumption and CO_2 (carbon dioxide) emissions by driving conditions for light-duty passenger vehicles in china. *Energy*, 69(0):247 – 257, 2014.

[3] BP statistical review of world energy 2014. on-line, 2014.

[4] M. Aftabuzzaman and E. Mazloumi. Achieving sustainable urban transport mobility in post peak oil era. *Transport Policy*, 18(5):695–702, 2011.

[5] Richard A. Kerr. Peak oil production may already be here. *Science*, 331(6024):1510–1511, 2011. Times Cited: 0.

[6] Robert Marks and R. Buckminster Fuller. *The Dymaxion world of Buckminster Fuller*. Anchor Books, 1973 [c1960]., 1973.

[7] B. Mohan, W. Yang, and S. Chou. Fuel injection strategies for performance improvement and emissions reduction in compression ignition engines review. *Renewable and Sustainable Energy Reviews*, 28(0):664 – 676, 2013.

[8] EU Commision. Regulation (ec) no 443/2009 of the European Parliament and of the council. on-line, April 2009.

[9] G. Fontaras and Z. Samaras. On the way to 130 kgco2/km estimating the future characteristics of the average european passenger cars. *Energy Policy*, 38(4):1826 – 1833, 2010.

[10] C. Bampatsou and E. Zervas. Critique of the regulatory limitations of exhaust CO_2 emissions from passenger cars in european union. *Energy Policy*, 39(12):7794 – 7802, 2011.

[11] G. Fontaras and P. Dilara. The evolution of european passenger car characteristics 2000-2010 and its effects on real-world CO_2 emissions and CO_2 reduction policy. *Energy Policy*, 49(0):719 – 730, 2012.

[12] Food Department for Environment and Rural Affairs. Air pollution in the UK 2013. Technical report, Department for Environment, Food and Rural Affairs, 2013.

[13] G. M. Marcazzan, S. Vaccaro, G. Valli, and R. Vecchi. Characterisation of PM 10 and PM 2.5 particulate matter in the ambient air of Milan (Italy). *Atmospheric Environment*, 35(27):4639 – 4650, 2001.

[14] DieselNet. EU emission standards. on-line, December 2014.

[15] M. Weiss, P. Bonnel, J. Ehlwein, A. Provenza, U. Lambrecht, S. Alessandrini, M. Carriero, R. Colombo, F. Forni, G. Lanappe, P. Le Lijour, U. Manfredi, F. Montigny, and M. Sculati. Will euro 6 reduce the NO_x emissions of new diesel cars? Insights from on-road tests with portable emissions measurement systems (pems). *Atmospheric Environment*, 62(0):657 – 665, 2012.

[16] G. Fontaras, V. Franco, P. Dilara, G. Martini, and U. Manfredi. Development and review of euro 5 passenger car emission factors based on experimental results over various driving cycles. *Science of The Total Environment*, 468-469(0):1034 – 1042, 2014.

[17] Richard Stone. *Introduction to internal combustion engines*. Macmillan Educ, 2nd edition, 1992.

[18] John B Heywood. *Internal Combustion Engines Fundamentals*. McGraw-Hill series in mechanical engineering. McGraw-Hill, Singapore, international edition, 1988.

[19] F Zhao, M.-C Lai, and D.L Harrington. Automotive spark-ignited direct-injection gasoline engines. *Progress in Energy and Combustion Science*, 25(5):437 – 562, 1999.

[20] Brian E. Milton. *Thermodynamics, combustion and engines*. Chapman & Hall, 1995.

[21] S. B. Gupta, B. P. Bihari, M.r S. Biruduganti, R. R. Sekar, and J. Zigan. On use of chemiluminescence for combustion metrics in natural gas fired reciprocating engines. *Proceedings of the Combustion Institute*, 33(2):3131 – 3139, 2011.

[22] M.-Chia D Lai and P. J Dingle. *Diesel Common Rail and Advanced Fuel Injection Systems*. SAE International, 2005.

[23] P. A. Caton, L. J. Hamilton, and J. S. Cowart. Understanding ignition delay effects with pure component fuels in a single-cylinder diesel engine. *Journal of Engineering for Gas Turbines and Power-Transactions of the Asme*, 133(3):11, 2011.

[24] Bernard Challen and Rodica Baranescu. *Diesel engine reference book*. Butterworth-Heinemann, Oxford, 2nd edition, 1999.

[25] Gregory K. Lilik and Andre L. Boehman. Advanced diesel combustion of a high cetane number fuel with low hydrocarbon and carbon monoxide emissions. *Energy & Fuels*, 25(4):1444–1456, 2011.

[26] J. E. Dec. Advanced compression-ignition engines-understanding the in-cylinder processes. *Proceedings of the Combustion Institute*, 32:2727–2742, 2009.

[27] S Cheng, A, A Upatnieks, and J Mueller, C. Investigation of the impact of biodiesel fuelling on NOx emissions using an optical direct injection diesel engine. *International Journal of Engine Research*, 7:297–318, 2006.

[28] Dale R. Tree and Kenth I. Svensson. Soot processes in compression ignition engines. *Progress in Energy and Combustion Science*, 33(3):272 – 309, 2007.

[29] Ian M Kennedy. Models of soot formation and oxidation. *Progress in Energy and Combustion Science*, 23(2):95 – 132, 1997.

[30] H Richter and J.B Howard. Formation of polycyclic aromatic hydrocarbons and their growth to soot. A review of chemical reaction pathways. *Progress in Energy and Combustion Science*, 26(46):565 – 608, 2000.

[31] J. E. Dec. A conceptual model of di diesel combustion based on laser-sheet imaging. *SAE Technical Paper*, SAE Paper 970873, 1997.

[32] R J Ho, M Z Yusoff, and K Palanisamy. Trend and future of diesel engine: Development of high efficiency and low emission low temperature combustion diesel engine. *IOP Conference Series: Earth and Environmental Science*, 16(1):012112, 2013.

[33] D. Cipolat. Analysis of energy release and NOx emissions of a CI engine fuelled on diesel and DME. *Applied Thermal Engineering*, 27(11-12):2095–2103, 2007.

[34] M. Lapuerta, O. Armas, and J. Fernandez. Effect of biodiesel fuels on diesel engine emissions. *Progress in Energy and Combustion Science*, 34(2):198 – 223, 2008.

[35] G. H. Abd-Alla. Using exhaust gas recirculation in internal combustion engines: a review. *Energy Conversion and Management*, 43(8):1027–1042, 2002.

[36] M. Zheng, G. T. Reader, and J. G. Hawley. Diesel engine exhaust gas recirculation - a review on advanced and novel concepts. *Energy Conversion and Management*, 45(6):883–900, 2004.

[37] Xavier Tauzia, Alain Maiboom, and Samiur Rahman Shah. Experimental study of inlet manifold water injection on combustion and emissions of an automotive direct injection diesel engine. *Energy*, 35(9):3628 – 3639, 2010.

[38] K. A. Subramanian. A comparison of water-diesel emulsion and timed injection of water into the intake manifold of a diesel engine for simultaneous control of no and smoke emissions. *Energy Conversion and Management*, 52(2):849–857, 2011.

[39] F Bedford, C Rutland, P Dittrich, A Raab, and F Wirebeleit. Effects of direct water injection on DI diesel engine combustion. *SAE Paper No 2000- 01-2938*, 2000.

[40] M. Matti Maricq. Chemical characterization of particulate emissions from diesel engines: A review. *Journal of Aerosol Science*, 38(11):1079 – 1118, 2007.

[41] A. Lif and K. Holmberg. Water-in-diesel emulsions and related systems. *Advances in Colloid and Interface Science*, 123:231–239, 2006.

[42] M. Nadeem, C. Rangkuti, K. Anuar, M.R.U. Haq, I.B. Tan, and S.S. Shah. Diesel engine performance and emission evaluation using emulsified fuels stabilized by conventional and gemini surfactants. *Fuel*, 85(14-15):2111 – 2119, 2006.

[43] O. Armas, R. Ballesteros, F. J. Martos, and J. R. Agudelo. Characterization of light duty diesel engine pollutant emissions using water-emulsified fuel. *Fuel*, 84(7-8):1011–1018, 2005.

[44] Alain Maiboom and Xavier Tauzia. NOx and pm emissions reduction on an automotive HSDI diesel engine with water-in-diesel emulsion and EGR: An experimental study. *Fuel*, 90(11):3179 – 3192, 2011.

[45] D.H. Qi, H. Chen, R.D. Matthews, and Y.ZH. Bian. Combustion and emission characteristics of ethanol-biodiesel-water micro-emulsions used in a direct injection compression ignition engine. *Fuel*, 89(5):958 – 964, 2010.

[46] Cherng-Yuan Lin and Li-Wei Chen. Comparison of fuel properties and emission characteristics of two- and three-phase emulsions prepared by ultrasonically vibrating and mechanically homogenizing emulsification methods. *Fuel*, 87(10-11):2154 – 2161, 2008.

[47] J. W. Park, K. Y. Huh, and K. H. Park. Experimental study on the combustion characteristics of emulsified diesel in a rapid compression and expansion machine. *Proceedings of the Institution of Mechanical Engineers, Part D: Journal of Automobile Engineering*, 214(5):579–586, 2000.

[48] M. Abu-Zaid. Performance of single cylinder, direct injection diesel engine using water fuel emulsions. *Energy Conversion and Management*, 45(5):697 – 705, 2004.

[49] Mohammed Yahaya Khan, Z. A. Abdul Karim, Ftwi Yohaness Hagos, A. Rashid A. Aziz, and Isa M. Tan. Current trends in water-in-diesel emulsion as a fuel, 2014.

[50] Milton J. Rosen. *Surfactants and Interfacial Phenomena*. Wiley, New York, NY, 2nd edition, 1989.

[51] Drew Myers. *Surfaces, interfaces, and colloids : principles and applications*. Wiley-VCH, New York, 2nd edition, 1999.

[52] H. Y. ld r m Erbil. *Surface chemistry of solid and liquid interfaces*. Blackwell Pub., Oxford, UK ; Malden, MA, 2006.

[53] J. E. Dec, R. Canaan, and D.R Tree. The effect of water emulsified fuel on diesel soot formation. In *Proceedings of the 219th ACS national meeting*, March 2000.

[54] K Song, Y Lee, and Litzinger. T. Effects of emulsified fuels on soot evolution in an optically-accessible di diesel engine. *SAE Technical Paper*, 2000-01-2794, 2000.

[55] Jamil I. Ghojel and Xuan-Thien Tran. Ignition characteristics of diesel water emulsion sprays in a constant-volume vessel: Effect of injection pressure and water content. *Energy & Fuels*, 24(7):3860–3866, 2010.

[56] R. Ochoterena, A. Lif, M. Nydon, Sven Andersson, and I. Denbratt. Optical studies of spray development and combustion of water-in-diesel emulsion and microemulsion fuels. *Fuel*, 89(1):122 – 132, 2010.

[57] M. Musculus, J. Dec, D. Tree, D. Daly, D. Langer, T. Ryan, and A. Matheaus. Effects of water-fuel emulsions on spray and combustion processes in a heavy-duty di diesel engine. *SAE Technical Paper*, 2002-01-2892, 2002.

[58] M. Huo, S. lun Lin, K. Nithyanandan, H. Liu, and C. Lee. Effects of injection pressure and ambient temperature on spray characteristics of water emulsified diesel. In *ILASS Americas, 24th Annual Conference on Liquid Atomization and Spray Systems*, 2012.

[59] Y. Morozumi and Y. Saito. Effect of physical properties on microexplosion occurrence in water-in-oil emulsion droplets. *Energy & Fuels*, 24(3):1854–1859, 2010.

[60] T Kadota and H Yamasaki. Recent advances in the combustion of water fuel emulsion. *Progress in Energy and Combustion Science*, 28(5):385 – 404, 2002.

[61] Hong-Chul Park, Ki-Taek Byun, and Ho-Young Kwak. Explosive boiling of liquid droplets at their superheat limits. *Chemical Engineering Science*, 60(7):1809 – 1821, 2005.

[62] J. E. Shepherd and B. Sturtevant. Rapid evaporation at the superheat limit. *Journal of Fluid Mechanics*, 121:379–402, 1982.

[63] M Shusser and D Weihs. Explosive boiling of a liquid droplet. *International Journal of Multiphase Flow*, 25(8):1561 – 1573, 1999.

[64] H. Watanabe, Y. Suzuki, T. Harada, Y. Matsushita, H. Aoki, and T. Miura. An experimental investigation of the breakup characteristics of secondary atomization of emulsified fuel droplet. *Energy*, 35(2):806 – 813, 2010.

[65] Hirotatsu Watanabe, Yohsuke Matsushita, Hideyuki Aoki, and Takatoshi Miura. Numerical simulation of emulsified fuel spray combustion with puffing and micro-explosion. *Combustion and Flame*, 157(5):839 – 852, 2010.

[66] Haifeng Liu, Chia-fon Lee, Ming Huo, and Mingfa Yao. Comparison of ethanol and butanol as additives in soybean biodiesel using a constant volume combustion chamber. *Energy & Fuels*, 25(4):1837–1846, 2011.

[67] Alvaro Diez, Roy J Crookes, and Tovas. Experimental studies of autoignition and soot formation of diesel surrogate fuels. *Proceedings of the Institution of Mechanical Engineers, Part D: Journal of Automobile Engineering*, 2012.

[68] Incheol Jeong, Kyung-Hwan Lee, and Jaesoo Kim. Characteristics of auto-ignition and micro-explosion behavior of a single droplet of water-in-fuel. *Journal of Mechanical Science and Technology*, 22(1):148–156, 2008.

[69] Roy J. Crookes, Fariborz Kiannejad, and Marouan A.A. Nazha. Systematic assessment of combustion characteristics of biofuels and emulsions with water for use as diesel engine fuels. *Energy Conversion and Management*, 38(15-17):1785 – 1795, 1997.

[70] Marco Mattiello, Lucia Cosmai, Luigi Pistone, Federico Beretta, and Patrizio Massoli. Experimental evidence for microexplosions in water/fuel oil emulsion flames inferred by laser light scattering. *Symposium (International) on Combustion*, 24(1):1573 – 1578, 1992.

[71] Hirotatsu Watanabe and Ken Okazaki. Visualization of secondary atomization in emulsified-fuel spray flow by shadow imaging. *Proceedings of the Combustion Institute*, 34(1):1651 – 1658, 2013.

[72] Ming Huo, Shenlun Lin, Haifeng Liu, and Chia fon F. Lee. Study on the spray and combustion characteristics of water-emulsified diesel. *Fuel*, 123(0):218 – 229, 2014.

[73] Weibiao Fu, Jingsong Gong, and Lingyun Hou. There is no micro-explosion in the diesel engines fueled with emulsified fuel. *Chinese Science Bulletin*, 51(10):1261–1265, 2006.

[74] F.Y. Hagos, A.R.A. Aziz, and I.M. Tan. Water-in-diesel emulsion and its micro-explosion phenomenon-review. In *Communication Software and Networks (ICCSN), 2011 IEEE 3rd International Conference*, 2011.

[75] Urs Mathis, Martin Mohr, Ralf Kaegi, Andrea Bertola, and Konstantinos Boulouchos. Influence of diesel engine combustion parameters on primary soot particle diameter. *Environmental Science & Technology*, 39(6):1887–1892, 2005.

[76] Charles E. Roberst, David Naegeli, and Christopher Chadwell. The effect of water on soot formation chemistry. *SAE Technical Paper*, 2005-01-3850, 2005.

[77] BBC News. Why is diesel now bad news?, 2014.

[78] M.R. Turner, S.S. Sazhin, J.J. Healey, C. Crua, and S.B. Martynov. A breakup model for transient diesel fuel sprays. *Fuel*, 97:288 – 305, 2012.

[79] Gunnar Stiesch. Multidimensional models of spray processes. In *Modeling Engine Spray and Combustion Processes*, Heat and Mass Transfer, pages 119–192. Springer Berlin Heidelberg, 2003.

[80] J.I.Ramos. *Internal combustion engine modeling*. Hemisphere, c1989.

[81] C. Baumgarten. Fundamentals of mixture formation in engines. In *Mixture Formation in Internal Combustion Engine*, Heat, Mass Transfer, pages 5–46. Springer Berlin Heidelberg, 2006.

[82] R. D Reitz and F.B Bracco. On the dependence of spray angle and other spray parameters on nozzzle design and operating conditions. *SAE Technical Paper*, 790494, 1979.

[83] S.S. Sazhin, G. Feng, and M.R. Heikal. A model for fuel spray penetration. *Fuel*, 80(15):2171 – 2180, 2001.

[84] Vicente Bermudez Simon Martinez-Martinez, Fausto Sanchez and J. Manuel Riesco-Avila. *Fuel Injection*, volume Liquid Sprays Characteristics in Diesel Engines. InTech, 2010.

[85] J.M Desantes, R. Payri, F.J Salvador, and J. Gimeno. Measurements of spray momentum for the study of cavitation in diesel injection nozzles. *SAE Technical Paper*, 2003-01-0703, 2003.

[86] Kyoung-Su Im, Seong-Kyun Cheong, Christopher F. Powell, Ming-chia D. Lai, and Jin Wang. Unraveling the geometry dependence of in-nozzle cavitation in high-pressure injectors. *Sci. Rep.*, 3:–, June 2013.

[87] Adrian J Butcher, Pavlos G Aleiferis, and Dave Richardson. Development of a real-size optical injector nozzle for studies of cavitation, spray formation and flash-boiling at conditions relevant to direct-injection spark-ignition engines. *International Journal of Engine Research*, 14(6):557–577, 2013.

[88] Hyun Kyu Suh and Chang Sik Lee. Effect of cavitation in nozzle orifice on the diesel fuel atomization characteristics. *International Journal of Heat and Fluid Flow*, 29(4):1001 – 1009, 2008.

[89] R.J.H. Klein-Douwel, P.J.M. Frijters, L.M.T. Somers, W.A. de Boer, and R.S.G. Baert. Macroscopic diesel fuel spray shadowgraphy using high speed digital imaging in a high pressure cell. *Fuel*, 86(1213):1994 – 2007, 2007.

[90] I.V. Roisman, Lucio Araneo, and C. Tropea. Effect of ambient pressure on penetration of a diesel spray. *International Journal of Multiphase Flow*, 33(8):904 – 920, 2007.

[91] J.Kong and C.Bae. Effects of tapered nozzle hoe on spray characteristics of high pressure diesel injection. *ICLASS 2009*, 2009.

[92] Ozgur Oguz Taskiran and Metin Ergeneman. Experimental study on diesel spray characteristics and autoignition process. *Journal of Combustion*, 2011:20, 2011.

[93] R. Payri, F.J. Salvador, J. Gimeno, and R. Novella. Flow regime effects on non-cavitating injection nozzles over spray behavior. *International Journal of Heat and Fluid Flow*, 32(1):273 – 284, 2011.

[94] Raul Payri, S. Molina, F.J. Salvador, and J. Gimeno. A study of the relation between nozzle geometry, internal flow and sprays characteristics in diesel fuel injection systems. *KSME International Journal*, 18(7):1222–1235, 2004.

[95] E. Delacourt, B. Desmet, and B. Besson. Characterisation of very high pressure diesel sprays using digital imaging techniques. *Fuel*, 84(7-8):859–867, 2005.

[96] Xiangang Wang, Zuohua Huang, Olawole Abiola Kuti, Wu Zhang, and Keiya Nishida. Experimental and analytical study on biodiesel and diesel spray characteristics under ultra-high injection pressure. *International Journal of Heat and Fluid Flow*, 31(4):659 – 666, 2010.

[97] J. Naber and D Siebers. Effects of gas density and vaporization on penetration and dispersion of diesel sprays. *SAE Technical Paper*, 960034, 1996.

[98] H. Hiroyasu and M Arai. Structures of fuel sprays in diesel engines. *SAE Technical Paper*, 900475, 1990.

[99] Raul Payri, Antonio Garca, Vicent Domenech, Russell Durrett, and Alejandro H. Plazas. An experimental study of gasoline effects on injection rate, momentum flux and spray characteristics using a common rail diesel injection system. *Fuel*, 97(0):390 – 399, 2012.

[100] Yuan Gao, Jun Deng, Chunwang Li, Fengling Dang, Zhuo Liao, Zhijun Wu, and Liguang Li. Experimental study of the spray characteristics of biodiesel based on inedible oil. *Biotechnology Advances*, 27(5):616 – 624, 2009.

[101] Desantes J. Payri, F. and J Arrgle. Characterization of DI diesel sprays in high density conditions. *SAE Technical Paper*, 960774, 1996.

[102] J. Dernotte, F. Foucher, C. Hespel, and S. Houill. Experimental study of the effect of fuel properties on the diesel injection process. *Proceedings of the European Combustion Meeting 2011*, 2011.

[103] Jose M. Desantes, Raul Payri, Antonio Garcia, and Julien Manin. Experimental study of biodiesel blends effects on diesel injection processes. *Energy & Fuels*, 23(6):3227–3235, 2009.

[104] Chao He, Yunshan Ge, Jianwei Tan, and Xiukun Han. Spray properties of alternative fuels: A comparative analysis of biodiesel and diesel. *International Journal of Energy Research*, 32(14):1329–1338, 2008.

[105] C Grimaldi and L Postrioti. Experimental comparison between conventional and bio-derived fuels sprays from a common rail injection system. *SAE Technical Paper*, 2000-01-1252, 2000.

[106] Chang Sik Lee, Sung Wook Park, and Sang Il Kwon. An experimental study on the atomization and combustion characteristics of biodiesel-blended fuels. *Energy & Fuels*, 19(5):2201–2208, 2005.

[107] Hyung Jun Kim, Su Han Park, and Chang Sik Lee. A study on the macroscopic spray behavior and atomization characteristics of biodiesel and dimethyl ether sprays under increased ambient pressure. *Fuel Processing Technology*, 91(3):354 – 363, 2010.

[108] J. Arregle, J. V. Pastor, and S. Ruiz. The influence of injection parameters on diesel spray characteristics. *SAE*, 1999-01-0200, 1999.

[109] Rik S. G. Baert, Peter J. M. Frijters, Bart Somers, Carlo C. M. Luijten, and Wout de Boer. Design and operation of a high pressure, high temperature cell for hd diesel spray diagnostics: Guidelines and results. *SAE*, 2009-01-0649, 2009.

[110] Sergei Sazhin, Cyril Crua, David Kennaird, and Morgan Heikal. The initial stage of fuel spray penetration. *Fuel*, 82(8):875 – 885, 2003.

[111] C Crua, D A Kennaird, S S Sazhin, M R Heikal, and M R Gold. Diesel autogignition at elevated in-cylinder pressueres. *International Journal of Engine Research*, 5(4):365–374, 2004.

[112] J.M. Desantes, J.V. Pastor, J.M. Garca Oliver, and J.M. Pastor. A 1d model for the description of mixing-controlled reacting diesel sprays. *Combustion and Flame*, 156(1):234 – 249, 2009.

[113] R. Payri, F.J. Salvador, J. Gimeno, and L.D. Zapata. Diesel nozzle geometry influence on spray liquid-phase fuel penetration in evaporative conditions. *Fuel*, 87(7):1165 – 1176, 2008.

[114] W. Ethan Eagle, Steven B. Morris, and Margaret S. Wooldridge. High-speed imaging of transient diesel spray behavior during high pressure injection of a multi-hole fuel injector. *Fuel*, 116(0):299 – 309, 2014.

[115] Hyun Kyu Suh, Sung Wook Park, and Chang Sik Lee. Effect of piezo-driven injection system on the macroscopic and microscopic atomization characteristics of diesel fuel spray. *Fuel*, 86(1718):2833 – 2845, 2007.

[116] Keiya Nishida, Jiangping Tian, Yasuki Sumoto, Wuqiang Long, Kiyotaka Sato, and Masahisa Yamakawa. An experimental and numerical study on sprays injected from two-hole nozzles for DISI engines. *Fuel*, 88(9):1634 – 1642, 2009.

[117] R. Payri, S. Ruiz, F. Salvador, and J. Gimeno. On the dependence of spray momentum flux in spray penetration: Momentum flux packets penetration model. *Journal of Mechanical Science and Technology*, 21(7):1100–1111, 2007.

[118] F. Payri, R. Payri, M. Bardi, and M. Carreres. Engine combustion network: Influence of the gas properties on the spray penetration and spreading angle. *Experimental Thermal and Fluid Science*, 53(0):236 – 243, 2014.

[119] R. Payri, J. M. Garcia, F. J. Salvador, and J. Gimeno. Using spray momentum flux measurements to understand the influence of diesel nozzle geometry on spray characteristics. *Fuel*, 84:551–561, 2005.

[120] Wang Changyuan, Liu Fushui, and Li Xiangrong. Experimental research on the characteristics of dense spray of diesel engine. In *Computer Distributed Control and Intelligent Environmental Monitoring (CDCIEM), 2011 International Conference on*, pages 428–432.

[121] J. Kostas, D. Honnery, and J. Soria. Time resolved measurements of the initial stages of fuel spray penetration. *Fuel*, 88(11):2225 – 2237, 2009.

[122] Kwang-Jae Myong, Hirotaka Suzuki, Jiro Senda, and Hajime Fujimoto. Spray inner structure of evaporating multi-component fuel. *Fuel*, 87(2):202 – 210, 2008.

[123] B. Bougie, M. Tulej, T. Dreier, N.J. Dam, J.J. Ter Meulen, and T. Gerber. Optical diagnostics of diesel spray injections and combustion in a high-pressure high-temperature cell. *Applied Physics B*, 80(8):1039–1045, 2005.

[124] Dung Nguyen and Damon Honnery. Combustion of bio-oil ethanol blends at elevated pressure. *Fuel*, 87(2):232 – 243, 2008.

[125] PradiptaKumar Panigrahi and Krishnamurthy Muralidhar. Laser schlieren and shadowgraph. In *Schlieren and Shadowgraph Methods in Heat and Mass Transfer*, SpringerBriefs in Applied Sciences and Technology, Springer New York, 2012.

[126] Syed Mohammed Aminuddin Aftab, Obai Younis, and Musthak Al-Atabi. Four decades of utilizing shadowgraph techniques to study natural convection in cavities: Literature review. *IOP Conference Series: Materials Science and Engineering*, 36(1):012021, 2012.

[127] G.S. Settles. *Schlieren and Shadowgraph Techniques*. Experimental Fluid Mechanics. Springer Berlin Heidelberg, 2001.

[128] J. B. Ghandhi and D. M. Heim. An optimized optical system for backlit imaging. *Review of Scientific Instruments*, 80(5):–, 2009.

[129] J. Manin, M. Bardi, L.M. Pickett, R.N. Dahms, and J.C. Oefelein. Microscopic investigation of the atomization and mixing processes of diesel sprays injected into high pressure and temperature environments. *Fuel*, 134(0):531 – 543, 2014.

[130] R. Morgan, J.Wray, D.A.Kennaird, C.Crua, and M.R. Heikal. The influence of injector parameters on the formation and break-up of a diesel spray. *SAE Technical Paper*, 2001-01-0529, 2001.

[131] Jian Gao, Deming Jiang, and Zuohua Huang. Spray properties of alternative fuels: A comparative analysis of ethanol/gasoline blends and gasoline. *Fuel*, 86(1011):1645 – 1650, 2007.

[132] Y L Qi, B Y Xu, and S L Cai. An application of digital image processing techniques to the characterization of liquid petroleum gas (lpg) spray. *Measurement Science and Technology*, 17(12):3229, 2006.

[133] Sanghoon Kook and Lyle M. Pickett. Liquid length and vapor penetration of conventional, fischertropsch, coal-derived, and surrogate fuel sprays at high-temperature and high-pressure ambient conditions. *Fuel*, 93(0):539 – 548, 2012.

[134] R. Payri, F. J. Salvador, A. Garca, and A. Gil. Combination of visualization techniques for the analysis of evaporating diesel sprays. *Energy & Fuels*, 26(9):5481–5490, 2012.

[135] Zhijun Wu, Zhiyong Zhu, and Zhen Huang. An experimental study on the spray structure of oxygenated fuel using laser-based visualization and particle image velocimetry. *Fuel*, 85:1458 – 1464, 2006.

[136] Raul Payri, Jaime Gimeno, Michele Bardi, and Alejandro H. Plazas. Study liquid length penetration results obtained with a direct acting piezo electric injector. *Applied Energy*, 106(0):152 – 162, 2013.

[137] Brian T. Fisher and Charles J. Mueller. Liquid penetration length of heptamethylnonane and trimethylpentane under unsteady in-cylinder conditions. *Fuel*, 89(10):2673 – 2696, 2010.

[138] F. Payri, R. Payri, F.J. Salvador, and J. Martinez-Lopez. A contribution to the understanding of cavitation effects in diesel injector nozzles through a combined experimental and computational investigation. *Computers and Fluids*, 58(0):88 – 101, 2012.

[139] Mark Linne. Imaging in the optically dense regions of a spray: A review of developing techniques. *Progress in Energy and Combustion Science*, 39(5):403 – 440, 2013.

[140] Seoksu Moon, Yuan Gao, Jin Wang, Kamel Fezzaa, and Taku Tsujimura. Near-field dynamics of high-speed diesel sprays effects of orifice inlet geometry and injection pressure. *Fuel*, 133(0):299 – 309, 2014.

[141] N. Hay and P. L. Jones. Comparison of various correlations for spray penetration. *SAE*, 720776, 1972.

[142] H. Hiroyasu, T. Kadota, and M. Arai. *Supplementary Comments: Fuel Spray Characterization in Diesel Engines*, volume Combustion modeling in reciprocating engines of *General Motors symposium series*. Plenum Press, 1980.

[143] T.-C. Wang, J.-S. Han, X.-B. Xie, M.-C. Lai, N. A. Henein, E. Schwarz, and W. Bryzik. Parametric characterization of high-pressure diesel fuel injection systems. *Journal of Engineering for Gas Turbines and Power*, 125(2):412–426, 2003.

[144] Ainul Ghurri, Kim Jae-duk, Song Kyu-Keun, Jung Jae-Youn, and KimHyung Gon. Qualitative and quantitative analysis of spray characteristics of diesel and biodiesel blend on common-rail injection system. *Journal of Mechanical Science and Technology*, 25(4):885–893, 2011.

[145] J Shao, Y Yan, G Greeves, and S Smith. Quantitative characterization of diesel sprays using digital imaging techniques. *Measurement Science and Technology*, 14(7):1110, 2003.

[146] Jiaqing Shao and Yong Yan. Digital imaging based measurement of diesel spray characteristics. In *Instrumentation and Measurement Technology Conference, 2006. IMTC 2006. Proceedings of the IEEE*, pages 8–11, April 2006.

[147] Lucio Postrioti, Giacomo Buitoni, Francesco C. Pesce, and Claudio Ciaravino. Zeuch method-based injection rate analysis of a common-rail system operated with advanced injection strategies. *Fuel*, 128(0):188 – 198, 2014.

[148] T Husberg, V Manente, R Ehleskog, and S Andersson. Fuel flow impingement measurements on multi-orifice diesel nozzles. *SAE Technical Paper*, 2006-01-1552, 2006.

[149] S. Vass and H. Nemeth. Sensitivity analysis of instantaneous fuel injection rate determination for detailed diesel combustion models. *Periodica Polytechnica Transportation Engineering*, 41(1):77–85, 2013.

[150] M. Lindstrom and H Angstrom. Development of a fuel spray impulse measurement device and correlation with time resolved mass flow. *SAE Technical Paper*, 2009-01-1880, 2009.

[151] Glenn R. Bower David E. Foster. A compariosn of bosch and zuech rate injection meters. *SAE Technical Paper*, 910724, 1991.

[152] R. Payri, F. J. Salvador, J. Gimeno, and J. De la Morena. Influence of injector technology on injection and combustion development - part 1: Hydraulic characterization. *Applied Energy*, 88:1068–1074, 2011.

[153] M. Marcic. A new method for measuring fuel-injection rate. *Flow Measurement and Instrumentation*, 10(3):159–165, 1999.

[154] M. Marcic. Deformational injection rate measuring method. *Review of Scientific Instruments*, 73(9):3373–3377, September 2002.

[155] Dong Han, Yaozong Duan, Chunhai Wang, He Lin, and Zhen Huang. Experimental study on injection characteristics of fatty acid esters on a diesel engine common rail system. *Fuel*, 123(0):19 – 25, 2014.

[156] L. Ganippa, S. Andersson, and J Chomiak. Transient measurements of discharge coefficients of diesel nozzles. *SAE Technical Paper*, 2000-01-2788, 2000.

[157] Jason G. Kempenaar, Charles J. Mueller, Kim A. Shollenberger, and Krishna Lakshminarasimhan. An instrument for measuring orifice-specific fuel-injection rate from a multi-orifice nozzle. *ASME 2008 Fluids Engineering Conferences*

[158] D. K. Sangiah and L. C. Ganippa. Application of spray impingement technique for characterisation of high pressure sprays from multi-hole diesel nozzles. *International Journal of Thermal Sciences*, 49(2):409–417, 2010.

[159] Samual E. Johnson, Jaclyn E. Nesbitt, and Jeffrey D. Naber. Mass and momentum flux measurements with a high pressure common rail diesel fuel injector. *ASME 2010 Internation Combustion Engine Division fall Technical Conference*, 2010.

[160] Fuqiang Luo, Huifeng Cui, and Shaofeng Dong. Transient measuring method for injection rate of each nozzle hole based on spray momentum flux. *Fuel*, 125(0):20 – 29, 2014.

[161] Lucio Postrioti, Francesco Mariani, and Michele Battistoni. Experimental and numerical momentum flux evaluation of high pressure diesel spray. *Fuel*, 98(0):149 – 163, 2012.

[162] Lucio Postrioti and Michele Battistoni. Evaluation of diesel spray momentum flux in transient flow conditions. *SAE Technical Paper*, 2010-01-2244, 2010.

[163] Lucio Postrioti and Michele Battistoni. Analysis of diesel spray momentum flux spatial distibution. *SAE Technical Paper*, 2011-01-0682, 2011.

[164] Lucio Postrioti and Maurizio Bosi. Momentum flux spatial distibution and pda analysis of a gdi spray. *SAE Technical Paper*, 2012-01-0459, 2012.

[165] J.M. Desantes, R. Payri, F.J. Salvador, and J. De la Morena. Influence of cavitation phenomenon on primary break-up and spray behavior at stationary conditions. *Fuel*, 89(10):3033 – 3041, 2010.

[166] M.G. De Giorgi, A. Ficarella, and M. Tarantino. Evaluating cavitation regimes in an internal orifice at different temperatures using frequency analysis and visualization. *International Journal of Heat and Fluid Flow*, 39(0):160 – 172, 2013.

[167] W. H. Nurick. Orifice cavitation and its effect on spray mixing. *Journal of Fluids Engineering*, 98(4):681–687, December 1976.

[168] J.M. Desantes, R. Payri, F.J. Salvador, and A. Gil. Development and validation of a theoretical model for diesel spray penetration. *Fuel*, 85(78):910 – 917, 2006.

[169] David P Schmidt and ML Corradini. One-dimensional analysis of cavitating orifices. In *Proc. 9th Annual Conference on Liquid Atomization and Spray Systems (ILASS), San Francisco, CA*, 1996.

[170] F. Payri, V. Bermudez, R. Payri, and F.J. Salvador. The influence of cavitation on the internal flow and the spray characteristics in diesel injection nozzles. *Fuel*, 83(45):419 – 431, 2004.

[171] V. Macian, V. Bermudez, R. Payri, and J. Gimeno. New technique for determination of internal geometry of a diesel nozzle with the use of silicone methodology. *Experimental Techniques*, 27(2):39–43, 2003.

[172] S. Wilson, G. Gustafson, D. Lincoln, K. Murari, and C. Johansen. Performance evaluation of an overdriven led for high-speed schlieren imaging. *Journal of Visualization*, pages 1–11, 2014.

[173] NicolasA. Buchmann, ChristianE. Willert, and Julio Soria. Pulsed, high-power led illumination for tomographic particle image velocimetry. *Experiments in Fluids*, 53(5):1545–1560, 2012.

[174] C. Willert, S. Moessner, and J. Klinner. Pulsed operation of high power light emitting diodes for flow velocimetry. *8TH INTERNATIONAL SYMPOSIUM ON PARTICLE IMAGE VELOCIMETRY*, 2009.

[175] Christian Willert, Daniel Mitchell, and Julio Soria. Megahertz schlieren imaging of shock structure and sound waves in under-expanded, impinging jets. *Gallery of Fluid Motion, 63rd Annual APS-DFD Meeting, 2010*,

[176] C Willert, B Stasicki, J Klinner, and S Moessner. Pulsed operation of high-power light emitting diodes for imaging flow velocimetry. *Measurement Science and Technology*, 21(7):075402, 2010.

[177] ChristianE. Willert, DanielM. Mitchell, and Julio Soria. An assessment of high-power light-emitting diodes for high frame rate schlieren imaging. *Experiments in Fluids*, 53(2):413–421, 2012.

[178] Vision Research. *Phantom 7.3 Data Sheet.* Vision Research Inc, Wayne, NJ 07470, USA.

[179] Luminus Devices Inc. *Technical product data sheet CNBT-40 product range, 2011.*

[180] B. Ihracska, D. Wen, S.d Imran, D. Emberson, L. Mara Ruiz, R. Crookes, and T. Korakianitis. Assessment of elliptic flame front propagation characteristics of hydrogen in an optically accessible spark ignition engine. *International Journal of Hydrogen Energy*, 38(35):15452 – 15468, 2013.

[181] B. Ihracska, T. Korakianitis, P. Ruiz, D. Emberson, R. Crookes, A. Diez, and D. Wen. Assessment of elliptic flame front propagation characteristics of iso-octane, gasoline, (m85) and (e85) in an optical engines. *Combustion and Flame*, 161(3):696 – 710, 2014.

[182] A. M. Namasivayam. *Combustion, Performance and Emissions Characteristics of Compression-Ignition Engines Fuelled by Sustainable Fuels*. PhD thesis, Queen Mary University of London, 2011.

[183] Yung-Sung Lin and Hai-Ping Lin. Spray characteristics of emulsified castor biodiesel on engine emissions and deposit formation. *Renewable Energy*, 36(12):3507 – 3516, 2011.

[184] Dongxiang Zhang, Yuanping Lin, Anmei Li, and V.V. Tarasov. Emulsification for castor biomass oil. *Frontiers of Chemical Science and Engineering*, 5(1):96–101, 2011.

[185] Ali M.A. Attia and A.R. Kulchitskiy. Influence of the structure of water-in-fuel emulsion on diesel engine performance. *Fuel*, 116(0):703 – 708, 2014.

[186] A. Bulent Koc and Mudhafar Abdullah. Performance and NOx emissions of a diesel engine fueled with biodiesel-diesel-water nanoemulsions. *Fuel Processing Technology*, 109(0):70 – 77, 2013.

[187] A. Cucheval and R.C.Y. Chow. A study on the emulsification of oil by power ultrasound. *Ultrasonics Sonochemistry*, 15(5):916 – 920, 2008.

[188] Cherng-Yuan Lin and Li-Wei Chen. Emulsification characteristics of three- and two-phase emulsions prepared by the ultrasonic emulsification method. *Fuel Processing Technology*, 87(4):309 – 317, 2006.

[189] J Kang, C Bae, and K. O. Lee. Initial development of non-evaporating diesel sprays in common-rail injection systems. *International Journal of Engine Research*, 4(4):283–298, 2003.

[190] M. N. Svrcek, S.L. Miller, and C. F. Edwards. Effect of extreme compression on diesel spray penetration and dispersion. In *11th Triennial International Conference on Liquid Atomization and Spray Systems*, 2009.

[191] V. Macian, R. Payri, A. Garcia, and M. Bardi. Experimental evaluation of the best approach for diesel spray images segmentation. *Experimental Techniques*, 36(6):26–34, 2012.

[192] Nobuyuki Otsu. Threshold selection method from gray-level histograms. *IEEE Transactions on Systems, Man and Cybernetics*, 9(1):62–66, 1979.

[193] Avinash Kumar Agarwal and Vipul H. Chaudhury. Spray characteristics of biodiesel/blends in a high pressure constant volume spray chamber. *Experimental Thermal and Fluid Science*, 42(0):212 – 218, 2012.

[194] Guiyang Zhang, Xinqi Qiao, Xuelong Miao, Jianhai Hong, and Jinbao Zheng. Effects of highly dispersed spray nozzle on fuel injection characteristics and emissions of heavy-duty diesel engine. *Fuel*, 102(0):666 – 673, 2012.

[195] N. Neal and D. Rothamer. An optical study of the impact of swirl ratio on extended lift-off diesel combustion. In *Spring Technical Meeting of the Central States Section of the Combustion Institute*, 2012.

[196] Charles J. Mueller, Andr L. Boehman, and Glen C. Martin. An experimental investigation of the origin of increased NOx emissions when fueling a heavy-duty compression-ignition engine with soy biodiesel. *SAE Technical paper*, 2009-01-1792, 2009.

[197] Randy L. Vander Wal and Mueller Charles J. Initial investigation of effects of fuel oxygenation on nanostructure of soot from a direct-injection diesel engine. *Energy & Fuels*, 20(6):2364–2369, 2006.

[198] J. V. Pastor, R. Payri, J. Gimeno, and J. G. Nerva. Experimental study on RME blends: Liquid-phase fuel penetration, chemiluminescence, and soot luminosity in diesel-like conditions. *Energy & Fuels*, 23(12):5899–5915, 2009.

[199] Tiegang Fang and Chia fon F. Lee. Bio-diesel effects on combustion processes in an {HSDI} diesel engine using advanced injection strategies. *Proceedings of the Combustion Institute*, 32(2):2785 – 2792, 2009.

[200] Kihyun Kim, Donghoon Kim, Yongjin Jung, and Choongsik Bae. Spray and combustion characteristics of gasoline and diesel in a direct injection compression ignition engine. *Fuel*, 109(0):616 – 626, 2013.

[201] Siemens. *Siemens VDO Automotive Lynx PCR system*, 2004.

[202] H. Grosshans, E. Kristensson, R.-Z. Szsz, and E. Berrocal. Prediction and measurement of the local extinction coefficient in sprays for 3D simulation/experiment data comparison. *International Journal of Multiphase Flow*, 72:218 – 232, 2015.

[203] Jeong Heon Kim and Chang Sik Lee. Hydrodynamic effects on spectroscopic water detection in gasoline pipe flow. *Energies*, 7(6):3810, 2014.

[204] L Araneo, V Soare, R Payri, and J Shakal. Setting up a PDPA system for measurements in a diesel spray. *Journal of Physics: Conference Series*, 45(1):85, 2006.

[205] Hironobu Ueki. Heterogeneous structure in diesel fuel sprays. *Procedia Engineering*, 56:18 – 28, 2013. 5th International Conference on Thermal Engineering.

[206] G. Barroso, B. Schneider, and K. Boulouchos. An extensive parametric study on diesel spray simulation and verification with experimental data. In *SAE Technical Paper*. SAE International, 10 2003.

[207] A. Munnannur. *Droplet Collision Modeling in Multi-dimensional Engine Spray Computation*. University of Wisconsin–Madison, 2007.

[208] J. Benajes, J. V. Pastor, R. Payri, and A. H. Plazas. Analysis of the influence of diesel nozzle geometry in the injection rate characteristic. *Journal of Fluids Engineering*, 126(1):63–71, February 2004.

[209] B.A. Reid, M. Gavaises, N. Mitroglou, G.K. Hargrave, C.P. Garner, E.J. Long, and R.M. McDavid. On the formation of string cavitation inside fuel injectors. *Experiments in Fluids*, 55(1), 2014.

[210] B. A. Reid, G. K. Hargrave, C. P. Garner, and G. Wigley. An investigation of string cavitation in a true-scale fuel injector flow geometry at high pressure. *Physics of Fluids*, 22(3):–, 2010.

[211] R.D. Lockett, L. Liverani, D. Thaker, M. Jeshani, and N.P. Tait. The characterization of diesel nozzle flow using high speed imaging of elastic light scattering. *Fuel*, 106:605 – 616, 2013.

[212] Charles J. Mueller and Glen C. Martin. Effects of oxygenated compounds on combustion and soot evolution in a di diesel engine:broadband natural luminosity imaging. In *SAE Technical Paper*. SAE International, 05 2002.

[213] Loge.AB. Logesoft v1.0.